USE OF TRIPLE BEAM RESONANT GAUGES IN TORQUE MEASUREMENT TRANSFER STANDARD

A thesis submitted for the degree of Doctor of Philosophy

by

Jittakant Intiang

School of Engineering and Design, Brunel University

June 2010

Abstract

A new torque transfer standard using metallic TBTF resonant sensor was developed to overcome the overload capability problem which occurs with conventional metallic resistance strain gauges. Previous research work, however, has shown that the first prototype of the metallic TBTF resonant sensor was not suitable for use in a torque transfer standard due to its size and subsequent sensitivity to parasitic lateral forces. To maximize the benefits from this sensor, particularly overload capability and long-term stability, in the high accuracy torque measurement application area, there is a need to develop significantly smaller devices.

The aim of this thesis is to research through FEA modelling and experimental characterisation the key performance parameters required to produce a miniaturised metallic TBTF resonant sensor that provides better performance when applied in a torque measurement system. For high accuracy any torque transducer using these sensors ought to have low sensitivity to parasitic influences such as bending moments and lateral forces, which can only be achieved with reduced size. The problems with the existing design, key design issues, possible configuration and packaging solutions of the metallic TBTF resonant sensor that could be used for achieving a higher accuracy torque transfer standard are considered.

Two designs of miniaturised metallic TBTF resonant sensors, SL20 and SL12, are considered and experimentally investigated. The lateral forces are reduced by 52% for SL20 design and by 80% for SL12 design when compared to the original SL40 design. A torque transducer using the SL20 design was calibrated falling into the Torque Transfer Standard class of accuracy 1 category, uncertainty 0.8%. A torque transducer using the SL12 design was made and calibration showed a class of accuracy 0.5 category, uncertainty 0.2%.

The results from this research indicate that the SL12 design is suitable for use in a torque transfer standard. The SL12 design is optimal and the smallest size possible based on the overload capability design criteria requiring the tine cross sectional area to remain constant.

Contents

Acknowledgements

The author would like to thank Dr. Richard Rakowski of Brunel University for the support and advice during the course of the work described in the dissertation as the first supervisor and Professor Barry Jones who gave some suggestion about conducting the project as the second supervisor. The author further wishes to thank the workshop technicians of the School of Engineering and Design at Brunel University for the quality of their technical support.

The author would also like to express gratitude to ForceSenSys Ltd. (FSS) and Dr. Metti Cheshmehdoost from FSS for providing in-kind support in the form of metallic TBTF resonant sensors. Also, the author would like to thank Mr. Andy Robinson from National Physical Laboratory (NPL) for the support in calibration.

The author acknowledges the financial support of the Royal Thai government for studying in UK and The Worshipful Company of Scientific Instrument Makers (WCSIM) for their award of a 2 year scholarship.

Finally, the author would like to thank Mom and Dad for their love during my life and study in UK and my husband, Chanapon, for his continuous interest and encouragement.

List of Tables

List of Figures

Chapter 1

1. Introduction

1.1 Aims and Objectives

The aim of the research work reported in this thesis is to contribute to the development of a new torque transducer, based on a metallic triple beam tuning fork (TBTF) resonator configuration, giving high overload capability and direct frequency output signal, for implementation as a torque transfer standard. The first objective is to study the performance of the current design of TBTF resonator in order to understand the performance characteristics and drawbacks with this current design. The second objective is to apply Finite Element Analysis (FEA) in order to analyse the source of measurement errors in torque transducers and model the new design which minimise those flaws. The third objective is to fabricate the prototype of the new TBTF design according to the FEA model and examine its performance from the experimental results. The new prototype is calibrated against the national torque standard at the National Physical Laboratory (NPL) with a view to classify the accuracy of this new torque transducer. Finally, another prototype metallic TBTF resonator is fabricated and characterised, which will achieve additional performance improvements and satisfy industrial needs.

1.2 Justification of the Research

Torque is involved in almost everything in human daily life such as, tightening of wheel nuts on a car, manufacturing of caps for pill bottles and maximizing the output of a jet engine etc (*Robinson, 2007*). In manufacturing, torque value must be verified for the safety and quality of products by using torque transducers. Moreover, if companies wish to be certified as part of a quality system, their equipment must be calibrated in order to ensure that the measured value is correct, that is the basis of traceability. Measuring test equipment will be calibrated against a reference standard that itself has been calibrated in unbroken succession back to the national standard (*Rainer,* 2002). There are many kinds of reference standards such as primary standards, secondary standards, working standards etc. depending on the accuracy. The accomplishment of linking between these reference standards is succeeded by using transfer standards to transfer the measured quantity (torque) from the national standard to a reference standard, then to working standards such as calibration devices and ultimately to test devices, such as power test benches.

In torque calibration, the most common torque transfer standards widely used in laboratories and in industry are based on strain gauge sensors,

where the torque value is acquired from the electrical output signal of the strain gauge circuit. These conventional metallic resistive strain gauges produce low amplitude output signal, thus the surface strain is generally designed to approach the elastic limit of the sensing element in order to obtain a measurable value. As a result, the overload capability of the strain-gauges-based torque transducers will be limited by this factor (*Yan et al*, *2004b*). This problem with overload capability has led to the development of the new torque transfer standard using metallic resonant sensors. Evidence shows that the resonant sensor, fabricated on stiff structures will provide better overload capability than strain gauges and also increase the torque measuring range (*Yan et al, 2004b*).

Moreover, the output signal of the strain-gauge-based torque transducers is an analogue voltage signal, so an analogue-to-digital conversion unit is required if used with digital circuitry. Metallic resonant sensors directly give a frequency signal output, which is compatible with digital circuitry so the analogue-to-digital conversion unit can be eliminated for this kind of torque transducer. From this point, implementing metallic resonant sensors as a torque transfer standard is more convenient and the cost of the torque measurement system will be reduced compared to strain gauges. In addition, the resolution achievable using metallic resonant sensors would be as good as strain gauges as the frequency can be measured with high accuracy, which is very important for transfer standards. Moreover, resonant sensors provide better long-term stability since the frequency signal is not dependent on the amplitude of the electrical signals and the measurement accuracy is not limited by the signal-to-noise ratio, which occurs with an analogue signal (*Yan et al, 2004b*).

An additional consideration is that the installation of strain gauges is normally labour intensive, the metallic resonant sensor is the better option due to the convenience of mounting the sensors to the torque shaft either by laser welding or simply using the appropriate adhesive. Furthermore, the combination of photochemical etching technique and thick-film screen printing processes used in the fabrication of the metallic resonant sensor presents a low-cost manufacturing opportunity for mass batch production.

The Brunel Centre for Manufacturing Metrology (BCMM) is an organization within Brunel University that had developed sensors employing resonant metallic double-beam and triple-beam tuning forks and utilized them in many applications, such as force measurements, pressure sensors and torque transducers. The advantage of two parallel beams is that the bending and the shearing forces at the common mounting points are cancelled out when those beams move in opposition to each other. For this reason, very little vibrational energy is dissipated to the structure at the ends so that Q-value is greatly increased (*Yan et al*, *2004a*). Double-beam has some benefits, however, there is a drawback with the piezoelectric printing process which has to be made twice at the side of both of the two beams. The triple-beam resonant structure was developed in order to solve this problem so that the

piezoelectric paste can be printed on the central beam in one operation. Thus, the cost of manufacturing triple-beam resonators will be lower than for the double-beam sensor.

The metallic resonant sensors based on a triple beam tuning fork (TBTF) design, activated by the PZT material, showed promise in the measurement of torque. However, the first successful metallic TBTF resonant sensor with thick-film drive/pickup elements is too large for current force, torque and pressure sensing applications and has additional problems when assembled on a transducer shaft for use as a torque transducer. FEA models showed that the TBTF not only measure the changes in tensile/compressive strain, which is the desired measured value, but experienced shear strain and twist that affects the accuracy of the torque transducer. The predominant source for this error was due to the length of the TBTF which affects the measurement accuracy of the torque transducers. By reducing the overall length of the TBTF thus minimizing lateral force, this will improve the class of the transfer standard accuracy whilst maintaining the stiffness of the resonant sensors. Consequently, the challenge of reducing the resonant sensor dimensional footprint will be part of this dissertation.

In conclusion, using metallic resonant sensors in torque measurement transfer standard offers a number of advantages to industry due to its low cost, reliability and with high accuracy. All these factors will reduce the cost of ownership of torque transfer standards with subsequent improvements in productivity and quality.

1.3 Project Strategy

The transfer of a calibrated torque measurement from a national standard to working equipment in industry is via the torque transducer. This transfer from the lever-beam deadweight system to the torque measuring devices requires not only a high accuracy of torque transducer but also stability, repeatability and reliability. Several kinds of sensors have been used by national laboratories to obtain the best result.

The torque transducer in this project is the metallic triple-beam tuning-fork resonant sensor which was designed to replace conventional metallic resistive strain gauges because of the difficulties in the mounting technique and the poor measurable output signal. For practical applications there is a need to reduce the size of the sensor footprint. This research will compare the physical limits of size reduction by measuring key performance parameters. During the development of TBTF sensors, it would be necessary to model the characteristics of the resonator by developing a FEA model for the sensors for comparison and design development purposes. Once a model has been established, some experiments have been conducted to understand the sensors behavior with regard to the application for torque measurement. Then the viability of using TBTF technology in a torque transducer will be evaluated

and its use as a transfer standard will be determined. In addition, the uncertainty in TBTF manufacturing will be considered and minimized in order to improve the accuracy of the TBTF resonators. The strategy of this research is illustrated in figure 1.1.

1.4 The Thesis Layout

The first chapter of the thesis outlines the aims and objectives of this project with justification of the research, project strategy and the thesis layout.

Chapter 2 is the literature review of three main topics associated with this research. Torque measurement: several kinds of torque transducers with characteristics, advantages and drawbacks, and torque standards involved in the research and additional theoretical contributions to knowledge are discussed. This is followed by the general concept of resonant sensors, which considers the configuration, characteristics and some applications using resonant sensors. Lastly, the use of resonant sensors for torque application will be discussed. This section will mention the demonstrated feasibility of resonant sensors in torque measurement; the design, construction and fabrication of the current metallic TBTF resonant sensors, and the characteristics and performances of the metallic TBTF-based torque transducers.

Chapter 3 will discuss the general case of torque: the theory and background of torque, torque measurement methods, torque measuring system and the calibration of torque.

Improvement in torque transducer design will be described in Chapter 4. This chapter will evaluate previous experimental tests, FEA analysis of the existing design, problems with existing design such as temperature, lateral forces and manufacturing uncertainties. Lastly, a method of repositioning the sensor on the transducer to measure force rather than torque will be investigated, with possible solutions being proposed.

Chapter 5 and 6 will cover the miniaturisation of the metallic TBTF resonant sensors. Two designs of the miniaturised TBTF were investigated including their configurations and characteristics.

The conclusions of this research work and suggestions for future development are summarised in the last chapter.

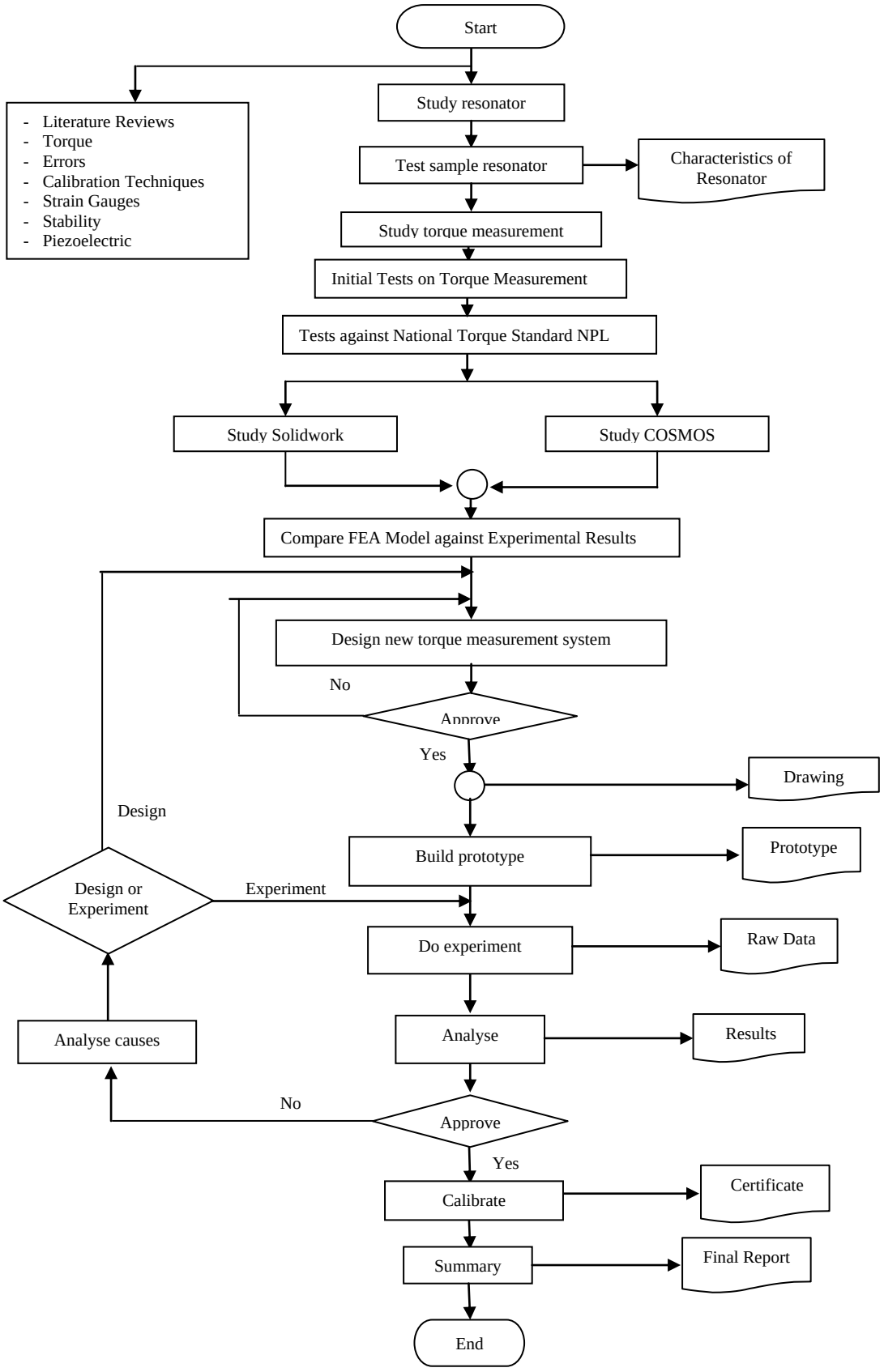

Figure 1.1 Project strategy for using a metallic triple-beam tuning-fork resonant sensor as a transfer torque standard.

Chapter 2

2. Literature Review

This chapter will present topics which are related to the research work. Torque will be discussed first, which will include torque definition, torque measurement, and torque standards. Then, the resonant sensor will be described, as this type of sensor is the underpinning technology used in the new torque transducer design. The principle of operation, important characteristics, advantages, disadvantages and some applications of the resonant sensors will be given. Lastly, implementing a torque transducer using the metallic triple-beam tuning-fork (TBTF) geometry will be explained. Previous research has shown the proof of principle but further research is required to understand and develop the required accuracy and resolution of a possible torque transfer standard using this technology.

2.1 Torque

2.1.1 Torque Definition

Torque is an important measurement quantity, which plays a significant role in assessing the quality of products. It can be loosely defined as a measure of the tendency of a force to rotate the body on which it acts about an axis, as shown in figure 2.1 (*Westbrook et. al, 1994*). The magnitude of the torque can be calculated by multiplying the force value, acting in a plane perpendicular to the axis of rotation, by the perpendicular distance from the axis to the line of action of the force (Eq. 2.1). The SI unit of torque is newton metre (Nm), which is equivalent to the torque produced by a force of 1N acting at a radius of 1m (*Adams, 1975*). This definition can be applied to both static and dynamic problems.

$$\vec{T} = \vec{F} \times \vec{r} \qquad (2.1)$$

where: $\vec{T}$ = torque

$\vec{F}$ = force

$\vec{r}$ = displacement from the axis of rotation to the line of force action

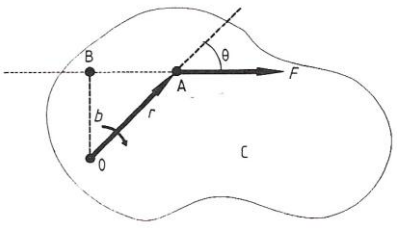

Figure 2.1 Force F acting on body C at a distance r from the point of rotation. (Westbrook et. al, 1994).

In the case of a shaft rotating with angular velocity ω and carrying power *P*, torque can also be simply calculated from

$$T = \frac{P}{\omega} \tag{2.2}$$

When a solid circular shaft, fixed at one end of length *l*, is subjected to a torque *T* (Fig. 2.2), there will occur an angle of twist θ given by

$$\theta = \frac{Tl}{JG} \tag{2.3}$$

where *J* is polar moment of inertia = $\pi r^4/2$ (solid circular shaft)
G is modulus of rigidity

The maximum shear stress τ occurs at the surface of the shaft and can be found from

$$\tau = \frac{Tr}{J} \tag{2.4}$$

where *r* is the shaft radius as shown in figure 2.2.

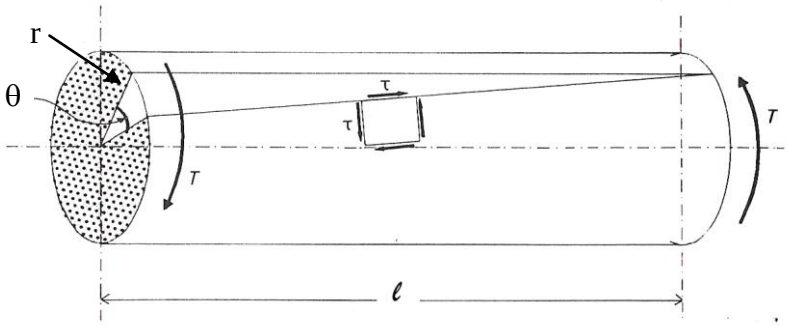

Figure 2.2 Circular shaft under torsion (Westbrook et. al, 1994).

Substituting $J = \pi r^4 / 2$, the angle of twist, θ will be

$$\theta = \frac{2Tl}{\pi r^4 G} \tag{2.5}$$

And the maximum shear stress, τ is

$$\tau = \frac{2T}{\pi r^3} \tag{2.6}$$

2.1.2 Torque Measurement

Torque measurement is essential in many commercial and industrial applications which are used to determine mechanical power, either power

required to operate a machine or power developed by the machine. Another important reason for measuring torque is to obtain load information necessary for stress or deflection analysis (*Beckwith et. al, 1993*). This information helps ensure that the design of the rotating element in products is suitable and adequate to prevent failure under shear stresses from applied torque (*Morris, 1991*).

In general, there are two types of torque application, the static system and dynamic system. In a static system, torque value is the moment that makes the object to be twisted. In a dynamic system, the force will rotate or turn the object. Measuring torque in dynamic system is more complicated than in static system because of the difficulty in signal communication between the stationary and rotating part. The method of determining torque in both systems will be explained in this chapter.

According to the theory of torque and torsion of circular shaft above, torque can be determined from the following parameters,

1. Force and displacement
2. Power
3. Angular of twist
4. Shear stress

There are many researchers such as Abbott (1966), Bass (1971), Adams (1975) etc. suggesting a variety of methods for torque measurement. Some of them use mechanical techniques, such as measuring force on a lever arm or tension in the rope, as in the prony brake. Other methods use various techniques such as optical, magnetic, electrical, or piezoelectric sensors, amongst others. Torque transducers are mostly used to detect the applied torque. In addition, torque can be simply calculated from knowing the electrical power input and speed of rotation. The following section contains brief outlines of the principle and detail of each method for torque measurement.

In 1966, Abbott proposed a Moiré fringe torque transducer (Fig. 2.3) which is an angular twist-type optical torque transducer. This method is an interesting technique for many researchers because it is a non-contact system that can be used to measure torque in dynamic application. This system consists of two Moiré fringe patterns with the equal space of the transparent and opaque areas which are concentrically mounted on the adjustable collars, which are mounted on the gauge arbors. When a torque is applied, light passes through the total transparent area of the combination, and its intensity is dependent upon the angular position between two patterns due to the twist in a stressed shaft. Light intensity is detected by a solar cell which is connected to a suitable circuit. The output signal can be a voltage, which is proportional to the illuminated area of the solar cell, which is also proportional to the transparent area of the Moiré pattern.

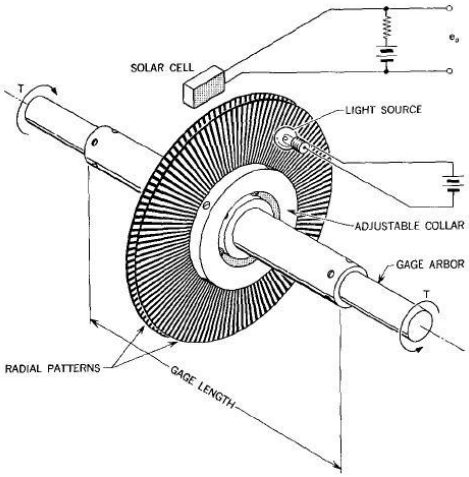

Figure 2.3 Moiré fringe torque transducer (Abbott, 1966).

Although this method gives the benefit of non-contact measurement, there is the difficulty in the adjustment of the system: light source, patterns and solar cell.

Later, torque transducer which is based on magnetostrictive technique had been developed by exploiting the fact that the permeability of magnetic materials will be changed when subjected to strain on the shaft; permeability decreases with positive strain, and increases with negative strain (*Bass, 1971*). This method measures the strain in the shaft itself. The system consists of two a.c. energized coils wound on iron cores, generating the flux paths through the shaft at ±45° coinciding with the direction of maximum strain, similar to strain gauge method, are positioned close to the shaft as shown in figure 2.4.

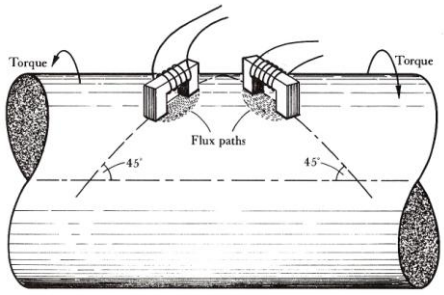

Figure 2.4 Magnetostrictive transducers in torque measurement (Bass, 1971).

This method gives non-contact measurement so there is no need for any modification to the shaft, and it is relatively compact. However, the bridge balance can be upset by any very small changes in the air gap between the coil cores and the shaft, unless these changes are identical for both coils (*Bass, 1971*).

In the same year, an inductive transducer which is used to measure the angle of twist as shown in figure 2.5 was proposed. Flange A and flange B carry a coil and an iron core respectively, to form the inductive transducer. The iron core attached to flange B will move in and out of the

coil according to the relative displacement of the two flanges due to the twist when the torque is applied.

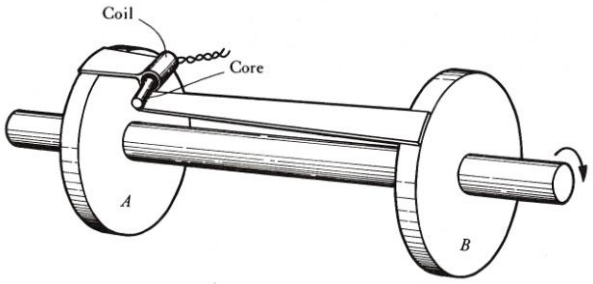

Figure 2.5 Inductive torque transducer (Bass, 1971).

Using four coil-and-core units arrangement, as shown in figure 2.6, will give better sensitivity and linearity according to Bass.

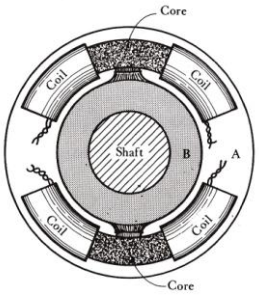

Figure 2.6 Inductive-bridge torque transducer (Bass, 1971).

Another form of angular displacement measurement using flanges is the single-toothed wheel (Fig. 2.7), which will generate voltage pulses in the inductive pick-offs C and D respectively (*Bass, 1971*). At zero torque, the voltage pulses will be simultaneously generated as the shaft rotates, as the two teeth are aligned with each other. When the torque is applied, there is an angular displacement of flange A relative to B, so a time interval between the two voltage pulses will occur which can be measured by an electronic timer.

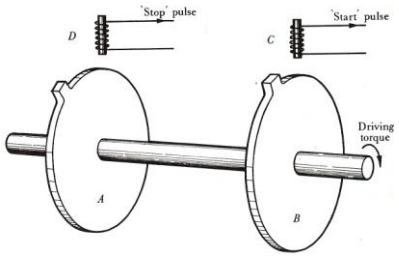

Figure 2.7 Single-toothed wheels for measuring torque (Bass, 1971).

Replacing the single-toothed wheels with multi-toothed wheels will generate voltage pulses from the pick-offs in sinusoidal form. If the two wheels are correctly aligned at no applied torque, the output signal will be in phase. When the applied torque is increased, the signals will become more out of phase therefore the phase difference can be used as a measure of torque (*Bass, 1971*).

Applying two magnetic or photoelectric transducers instead of inductive coils with the multi-toothed wheel, as shown in figure 2.8, was proposed by Adams (1975).

These toothed wheel methods eliminate errors arising from the use of slip rings, as they are non-contact measurements.

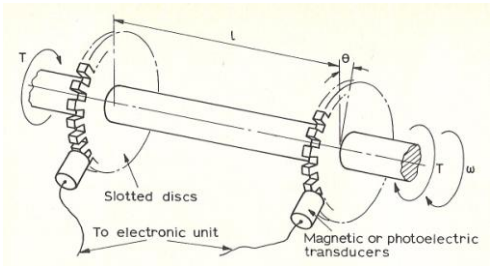

Figure 2.8 Multi-toothed wheels with magnetic or photoelectric transducers (Adams, 1975).

Adams suggested that the torque value can also be obtained from the gravity-balance method as shown in figure 2.9. The principle of this method is moving a mass (m) along an arm or varying the magnitude of the mass at a constant distance until the value of the torque, which is the product of force and distance, $F \cdot r$, equals the torque which is to be measured. In this case, the arm must be horizontal, so that the moment-arm distance is perpendicular to the line of action of the force. A measurement error may occur due to a friction torque caused by the force at a bearing supporting the shaft. Alternative arrangement to apply equal and opposite forces to give the same torque can solve this problem.

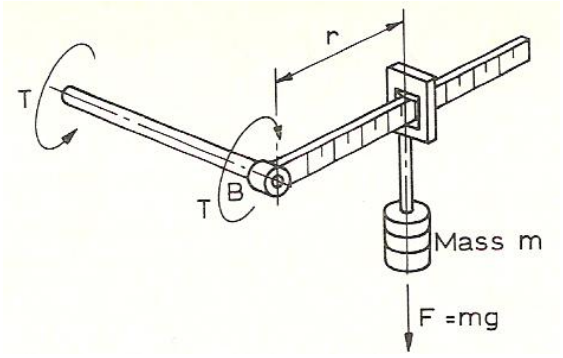

Figure 2.9 Gravity-balance method (Adams, 1975).

Moreover, a method of measuring the reaction torque on the motor support cradle either, acting as a power source or power sink, was proposed by Adams and other several authors (*Doebelin, 1966*, *Adams, 1975* and *Morris, 1991*). The principle is that transmitted torque in the shaft is equal to the reaction torque which is more easily measured than an applied torque in some situations (*Adams, 1975*). In this case, by measuring the reaction force F on the cradle, either on power source or power sink, knowing the arm length, torque value can be calculated. This method is simple but reveals an error source due to bearing friction (*Doebelin, 1966* and *Morris, 1991*) and windage torques (*Morris, 1991*)

within the motor. Figure 2.10 is the arrangement of measuring torque by torque-reaction methods suggested by Adams.

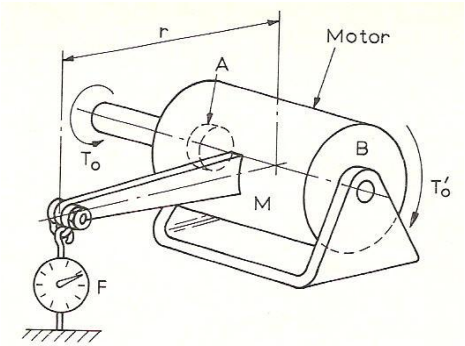

Figure 2.10 Measuring torque by torque-reaction methods (Adams, 1975).

An another optical method of a torquemeter uses a light ray, *pq*, deflected from two mirrors A and B to a stationary scale as shown in figure 2.11 (*Adams, 1975*). If there is no twist occurring in the shaft, two mirrors A and B are parallel, then the outgoing ray *rs* is parallel to the incoming ray *pq*. However, when a torque is applied, there will be twist in the shaft so that one mirror is moved out of parallel, then the outgoing ray is deflected through an angle which is the same angle of twist in the shaft, and now follows the line *r's'*. Hence the angular deflection θ of the light ray can be obtained which is proportional to the twist of, and hence the torque in, the shaft.

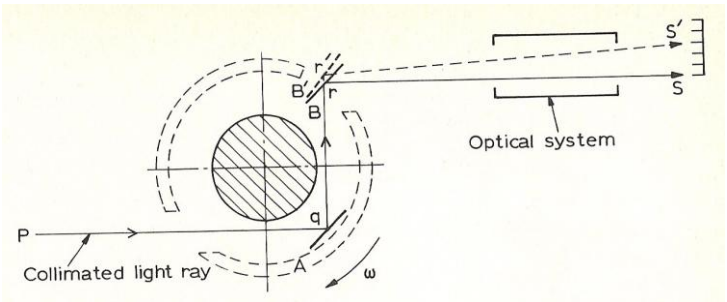

Figure 2.11 Torquemeter principle (Adams, 1975).

A torque transducer with permanent magnets and a ring core was presented by Harada and Sakamot in 1976. This torque transducer can measure torque in both the rotating state and stationary state. The configuration of the torque transducer is shown in figure 2.12. The torque shaft is fixed with two cup adapters at both terminals and there is a tape wound toroidal core inserted between the cup adapters. Several permanent magnets are attached along the periphery of each adapter in order to generate a magnetic field across the core. The applied torque is detected by measuring the magnetic field in the circumferential direction of the tape which is proportional to the twist deflection angle occurring in the shaft.

This torque transducer can measure torque in dynamic system without contact. But in the static condition, the sensitivity of the detector varies with the stopped position of the magnets fixed around the adapter.

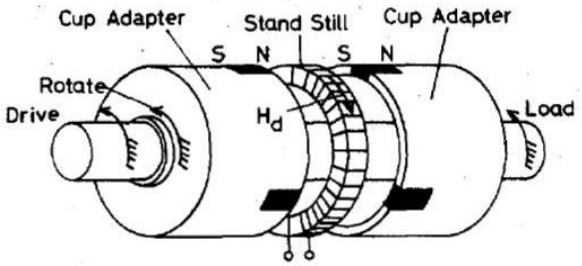

Figure 2.12 Torque transducer with permanent magnets and a ring core (Harada and Sakamoto, 1976).

The advantages in measuring the angular twist according to Westbrook and Turner are: no need of the sensors which require precise location and orientation, minimise the influence of any local variation in material properties or shaft geometry since the effect of an applied torque is integrated along the length of the shaft, and non-contact torque measurement systems can be possible with this principle if the larger displacements are available when movements of the two ends of a shaft are compared.

Collett and Hope (*1978*) suggested a simple method to determine torque by the angular displacement method as shown in figure 2.13. Each end of a rotating shaft carries a pointer and the scale respectively. When a torque is applied, the angle of twist over a given length of bar causes the pointer to move relative to the scale, which can be directly read from the scale in a static system. However, it is still possible to read the angular displacement in a dynamic application by using a stroboscope. This method is inexpensive, assuming a stroboscope to be available. In general the angular displacement is small, and the reading accuracy is consequently poor. To overcome this problem, the pointer and scale may be replaced by the similar transducer used to measure small linear displacements. However, the practical problems of using displacement transducers are associated with the satisfactory mounting of the components of the transducer on the shaft, and with making the necessary electrical connections to it (*Bass, 1971*).

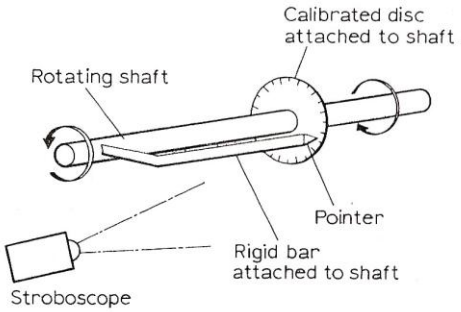

Figure 2.13 Stroboscopic torque meter (Collett and Hope, 1978).

A new torque transducer, which is employing the magnetostrictive effect, uses two stress-sensitive amorphous ribbons glued on a torsion bar, shown in figure 2.14 (*Harada et al, 1982*). Magnetoelastic magnetic anisotropy of the anisotropy constants (K_{u0}) in both amorphous ribbons lie in the opposite direction along ±45° to the shaft axis. When the torque is applied to the torsion bar, the anisotropy constants of two amorphous ribbons are different.

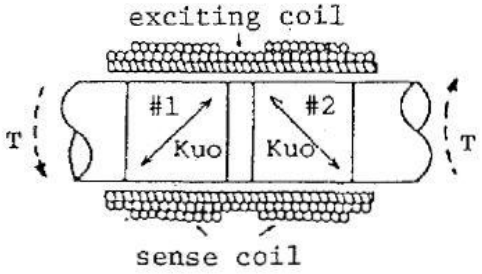

Figure 2.14 Stress sensitive amorphous ribbons torque transducer (Harada et al, 1982).

In the past, torque transducers employing magnetic phenomena had problems with the fluctuation in the output signal due to the lack of circular symmetry of the transducer structure. This new torque transducer is free from these fluctuations because of its circularly symmetric structure. Furthermore, this torque transducer is of the non-contact type and can detect both instantaneous and static torque. In addition, its structure is simple and the sensitivity is high.

Few years later, the pattern of amorphous ribbons on the torque transducer was modified into the chevron-pattern (*Sasada,Hiroike and Harada, 1984*) which exhibits wide dynamic range and good linearity is developed. Several pairs of stress-sensitive amorphous ribbons of rectangular form or of parallelogram form are glued to the shaft in a chevron-pattern as shown in figure 2.15.

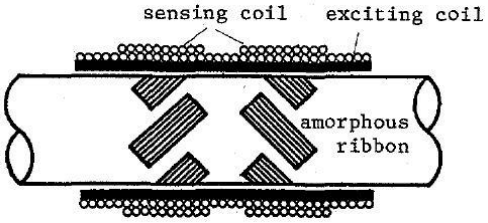

Figure 2.15 Torque transducer with stress-sensitive amorphous ribbons of chevron-pattern (Sasada,Hiroike and Harada, 1984).

If the electrical power and rotation speed in a dynamic system were known, the torque value can be determined from equation 2.2. Devices used for power measurement are commonly referred to as dynamometers. According to Nakra and Chaudhry (1985), it can be classified into three types; driving type dynamometer, transmission type dynamometer and absorption type dynamometer, depending on the machine arrangement (Fig. 2.16).

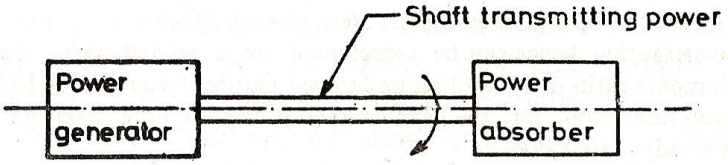

Figure 2.16 Dynamometer arrangement (Nakra and Chaudhry, 1985).

The principle of each dynamometer will be briefly given here. The detail about dynamometers can be found in the power measurement section in many textbooks.

Driving type dynamometer: The power driven by the motor can be obtained from the dynamometer itself or the dynamometer is the power generator like an electric motor.

Transmission type dynamometer: The power being transmitted through the device is measured by transimission type dynamometer. It is neither a power generator nor a power absorber.

Absorption type dynamometer: The absorption type dynamometer will absorb the mechanical energy after it is measured.

This torque measurement using power has the benefit of no need for the mechanical intervention in the system. However, dissipated power and the operating status of the machinery can contribute to the large errors in the calculation (*Rainer, 2002*).

In 1991, Morris had developed the optical technique that uses two black and white striped wheels instead of multi-toothed wheels as shown in figure 2.17 (*Morris, 1991*). When no torque is applied, the two pulse-trains of reflected light from the wheels, transmitted back to a receiver by a second pair of fibre-optic cables, are in phase with each other and move out of phase when the torque is increased. This method is inexpensive and is satisfactory for many applications due to their small physical size.

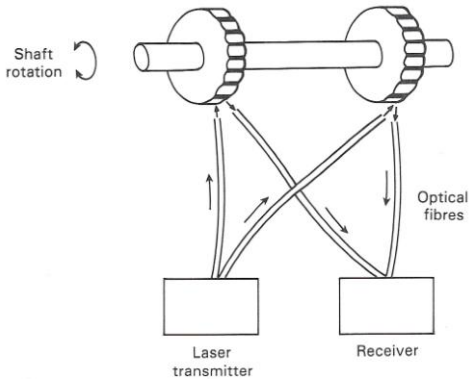

Figure 2.17 Optical torque measurement (Morris, 1991).

Prony brake is another method that Morris suggested to measure torque in a rotating shaft (*Morris, 1991*). It consists of a rope wound around the shaft with one end of the rope being attached to the spring balance and

measures force F_s whilst the other end carries a standard mass, m giving a load to the rope (Fig. 2.18). Then the effective force, F_e, exerted by the rope on the shaft is given by

$$F_e = mg - F_s \tag{2.7}$$

And the effective radius, R_e is the sum of the radius of the shaft, R_s and the rope, R_r.

$$R_e = R_s + R_r \tag{2.8}$$

Then the torque in the shaft, T, can be calculated from

$$T = F_e \times R_e \tag{2.9}$$

This method is well-known for measuring torque. However, a water cooling system is needed because a lot of heat is generated due to the friction between the rope and shaft, and this makes the system more expensive.

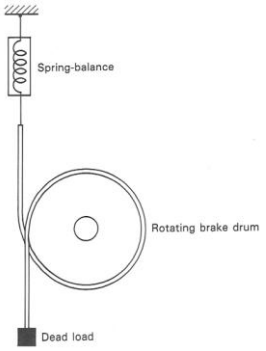

Figure 2.18 Prony brake (Morris, 1991).

A year later, a new type of magnetoelastic torque transducer was published by Garshelis (1992) utilizing a circularly polarized ring thus having the ability to be used as a non-contact torque transducer. The system configuration for this kind of torque transducer is shown in figure 2.19.

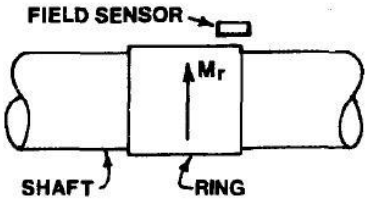

Figure 2.19 Torque transducer utilizing a circularly polarised ring (Garshelis, 1992).

It consists of two elements which are a magnetostrictive ring and a Hall effect or similar magnetic field intensity sensor. The ring is attached to a shaft and the sensor is mounted in proximity to one end of the ring. The

ring has been made to have continuously constant magnetisation from its manufacture or assembly. When the torque is applied, the ring is stressed so the magnetic anisotropy is altered along one of the principal stress directions. In this condition, the ring magnetisation will be reoriented from purely circular direction to a more or less steep helix, depending on the magnitudes of the torque. The ring acts as a hollow cylindrical magnet so the electrical output signal from a Hall effect, or similar field vector sensing device, near one end of the ring measures the torque value on the shaft.

The benefits of this kind of torque transducer are: the ability to use as a non-contact torque transducer, avoiding the complexities associated with conventional magnetoelastic torque transducer constructions which need external sources and means for magnetic excitation such as electronic circuitry, and finally the overall size can be reduced. However, there is a concern about the stability of the remanent circular magnetization in the ring over time under varying temperature conditions and with usage.

A modified torque transducer is constructed to replace a single circularly polarized ring by using two oppositely polarized rings (*Garshelis and Conto, 1994*). The construction of this torque transducer is shown in figure 2.20.

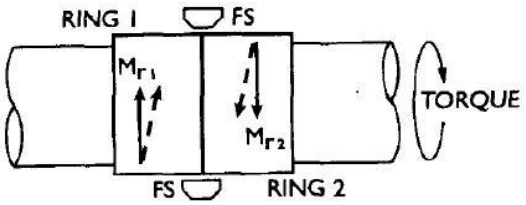

Figure 2.20 Torque transducer utilizing two oppositely polarized rings (Garshelis and Conto, 1994).

Two concentric rings, having oppositely directed circular magnetizations, are used and two field sensors (FS) are located in a diametrically opposite position. For this arrangement, the two rings are subjected to the same torque and the axial field so that the total detected field is free of the ambient magnetic fields found with single ring transducers. Moreover, an output signal is independent of all such fields due to the use of two field sensors. However, a minor reduction in sensitivity to torque measurement is obtained.

Another example of utilizing the magnetostrictive effect uses five coils wound onto a common five-armed core (Fig. 2.21) was proposed in 1994. The centre coil acts as the primary winding of a transformer, and the other four circumferentially positioned coils act as secondary winding and connected together in a Wheatstone bridge arrangement similar to strain gauge method. The currents induced in the four secondaries are equal in the case of no torsion so the bridge out-of-balance voltage is zero. When the torque is applied, the permeability will be changed equally but opposite amount in the tension and compression directions, which gives

the amplitude of the resulting bridge output voltage proportional to the applied torque (*Westbrook and Turner, 1994*).

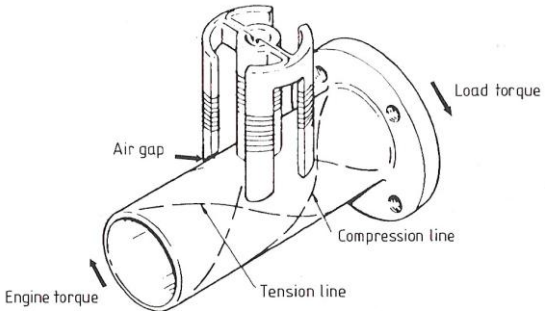

Figure 2.21 Magnetostrictive torque sensor (Westbrook and Turner, 1994).

The problems, according to Westbrook and Turner, of this torque sensor are associated with the inhomogeneity of the shaft material, sensitivity to changes in the sensor/shaft gap, thermal effects and variations in the sensor output due to changes in the shaft rotation speed.

The strain gauge torque transducer, which measures the strain in an elastic element built into the shaft, is the most common torque transducer and widely used in many laboratories and in industry according to Westbrook and Turner (*1994*). Four strain gauges are mounted around the circumference of the shaft as a Wheatstone bridge circuit. At each side of the shaft, two strain gauges are arranged at ±45° to the shaft axis and the adjacent gauges are placed at an angle of 90° from each other as seen in figure 2.22.

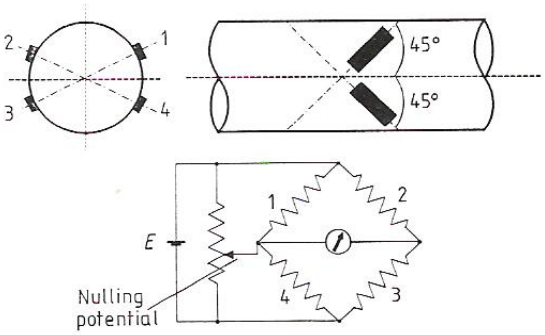

Figure 2.22 Strain gauges for shaft torque measurement (Westbrook and Turner, 1994).

When torque is applied to the shaft, shearing strain occurs in the two directions inclined by 45° from the axial line, thus one pair of gauges which are mounted parallel to each other will have tensile strain which increase the resistance of the circuit, while the other pair will decrease in resistance due to compression strain. Then the output voltage which is proportional to torque value is read with a measuring instrument.
This arrangement is fully temperature compensated, therefore it can be used in a wide range of temperatures (*Westbrook and Turner, 1994*) and is also insensitive to bending or axial stresses (*Bass, 1971*). It is the most

common method for torque measurement in recent years because there is no friction torque introduced in the system, as occurred in the cradled shaft bearing and prony brake (*Morris, 1991*). Strain gauge transducers can be applied in both static and dynamic measurements having excellent linearity, hysteresis, reproducibility and long-term stability (*Westbrook and Turner, 1994*).

However, if the shaft is lightly loaded, the generated strain is not sufficient for strain gauges to provide on adequate output signal. Moreover, there is difficulty with connecting the bridge to its power-source and display equipment (*Bass, 1971*). A set of slip rings can be used for power and/or data transmission system but it can be unreliable when operated in a dirty environment (*Westbrook and Turner, 1994*). The noise level in variation of contact resistance may be the same order of magnitude as the signal itself (*Collett and Hope, 1974*). Precise positioning of the strain gauges on the shaft axis is very difficult to achieve and makes this transducer relatively expensive (*Morris, 1991*).

Surface Acoustic Wave (SAW) sensor, which is made of a piezoelectric material with etched aluminium electrodes, can be used to measure torque (*Wolff et al, 1996*). These transducers have an interdigital configuration determining the wavelength of the wave (Fig. 2.23). An alternating voltage is applied to these transducers creating the waves on the surface of the piezoelectric substrate and then reflected by a similar array.

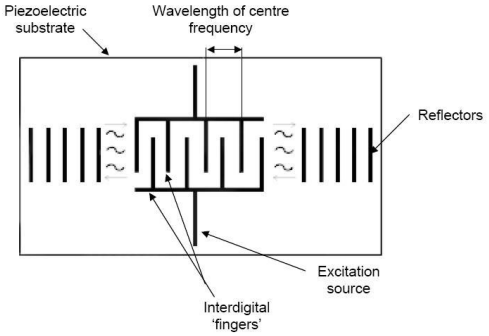

Figure 2.23 Configuration of SAW sensor (Wolff et al, 1996).

SAW torque transducer uses two sensors mounted at ±45° to the axis of the shaft and at 90° to each other (Fig. 2.24). If the torque is applied, the natural frequency of each sensor will be changed due to the twist in the shaft. The torque value is determined from the difference between the two natural frequencies.

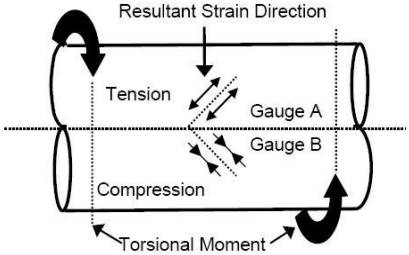

Figure 2.24 SAW sensor in torque measurement (Wolff et al, 1996).

SAW sensors can operate in the high frequency range so that the radio signals can be used for interrogating the sensor in a dynamic system and they are easily compatible with other SAW sensors making use of multi-sensor systems in measuring many parameters at the same time.

In 1998, a piezoelectric torque sensor operating in a non-contacting mode is proposed (*Hammond and Lec, 1998*). The shaft is attached with the sensing element, a piezoelectric torque sensor, on the surface as shown in figure 2.25. When the torque is applied, the material properties of the piezoelectric will change with the stresses and strains occurring in the shaft due to twist. For this reason, the resonant frequency of the piezoelectric plate will be changed according to the applied torque.

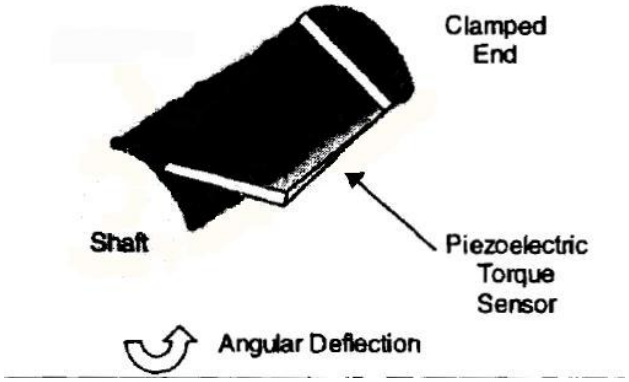

Figure 2.25 Piezoelectric torque sensor (Hammond and Lec, 1998).

The advantages of this piezoelectric torque sensor are; small size, selectivity, sensitivity, low-cost manufacturability and performing in on-line conditions (*Hammond and Lec, 1998*).

A Magnetostrictive type Torque Sensor (MTS), using an inverse magnetostrictive effect, shown in figure 2.26, is presented by Wakiwaka and Mitamura (*2001*). The torque sensor comprises of eight detecting cores, which are set up with the detecting coils around the circumference of the shaft and one exciting coil enclosing the shaft. When the torque is applied, the magnetic field in the shaft is changed so the output voltage is changed proportionally to the applied torque.

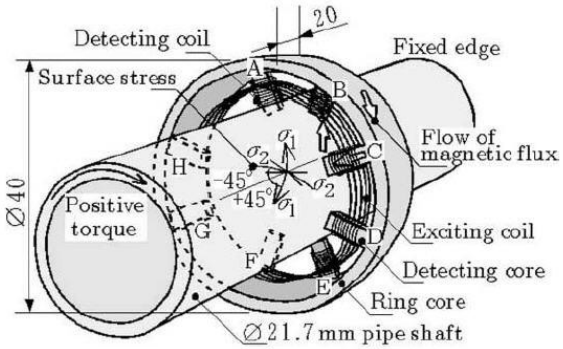

Figure 2.26 New magnetostrictive type torque sensor (Wakiwaka and Mitamura, 2001).

This magnetostrictive torque sensor can be used in dynamic torque applications. Moreover, the large hysteresis property normally associated

with the magnetostrictive type torque sensor can be decreased with this new sensor configuration.

Figure 2.27 is a commercial torque transducer of HBM uses the torque-reaction method. It is very frequently used to determine power, the viscosity of a medium via the supporting force of a motor in an agitator (*Schicker* and *Wegener, 2002*). A force transducer is installed at the end of the lever arm to measure the force acting on it when the torque is applied. The length of the lever arm was known so the torque value can be simply determined from equation 2.1.

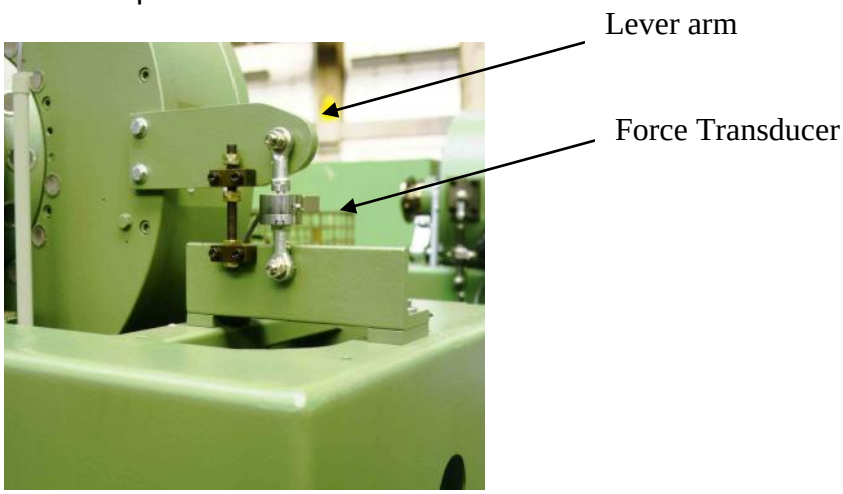

Figure 2.27 A lever arm with a force transducer at the end (Schicker and Wegener, 2002).

The disadvantages of this method are the changes in the length of the pendulum over time and expansion of the lever arm due to temperature changes, which can cause measurement errors. Moreover, the mass moment of inertia of the large masses makes it a significant problem in a dynamic system.

Figure 2.28 shows the measurement of the angular twist of a stainless steel wire gauge inserted between the drive and the load (*Antonio,Achille and Stefano, 2006*). Two optical reflective sensors, D_1 and D_2 are used to detect the black strips mounted on two rings at each end of the torsion spring wire. The applied torque is measured in electronic signal via the optical reflective sensors which generate a current when the black strips cross the detection area. This torque transducer is low cost, reliable and accurate.

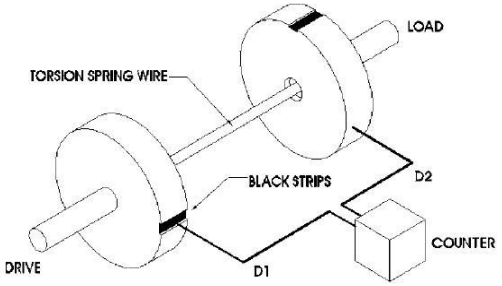

Figure 2.28 The angle twisted type torque transducer (Antonio,Achille and Stefano, 2006).

2.1.3 Torque Standard

Section 2.1.2 clearly shows the great efforts made over the years by researchers to develop cheap, reliable methods to measure torque. However, nearly all the papers cited do not give values for measurement accuracy, resolution, stability, or the ability of the sensor to withstand overload situations (ruggedness/stiffness). The whole range of transduction technologies (strain gauge, magnetostrictive, magnetoelastic, optical, inductive, SAW, etc.) need some electronic interfacing and conditioning and then the output signal needs to be shown how to be equated to torque in units of Nm.

In order to validate the reliability of the measuring device to measure torque accurately, the torque transducer must be calibrated against a reference standard. The torque measuring device may only be the torque transducer or a whole measurement chain that includes the signal detection, amplifier electronics and an instrumental display unit.

Calibration is a method to determine the relationship between the measured value of the output quantity (from the transducer/electronics) and a known input quantity (*Schicker and Wegener, 2002*). The reference standard used in any calibration must be traced back to the national standard in an unbroken chain. In metrology, traceability to the base SI unit is very important to ensure that the measured value is correct.

From the definition of torque, which is the product of force and distance, torque can be traceable to the fundamental units of mass, length and time as shown in figure 2.29. The hierarchy of metrology is as follows; primary standard, secondary standard, calibration machine and measuring instrument. The accomplishment of linking between the levels of this hierarchy is succeeded by using transfer standards.
Each country has its National Standard laboratories. In England these are held at National Physical Laboratory reference to UKAS. In Germany, Physikalisch-Technische Bundesanstalt (PTB) which is the national metrological institutes has the legal duty to hold the national standard and a reference standard is reserved for DKD accredited calibration laboratories. It is necessary that the accuracy of the reference is higher than the accuracy that needs to be demonstrated in the equipment being calibrated. A factor of 2 to 5 is recommended as the difference between each level of accuracy (*Schicker and Wegener, 2002*).

Basically, there are three techniques used in torque calibration. They are lever-arm-mass system, torque reference transducer and force reference transducer.

Lever-arm-mass system or deadweight system is used at the present time in all calibration laboratories for the high accuracy technology. In this system, the torque transducers are calibrated with a calibrated dead weight hanging from the end of a stiff beam. If the exact length of the beam from the axis of rotation to the hanging point is known, the resulting torque can be computed easily by multiplying the load force by the length

of the beam (*Herceg, 1976*). There are two different designs of mounting torque transducers to be calibrated. They are horizontally mounted and vertically mounted torque calibration machines.

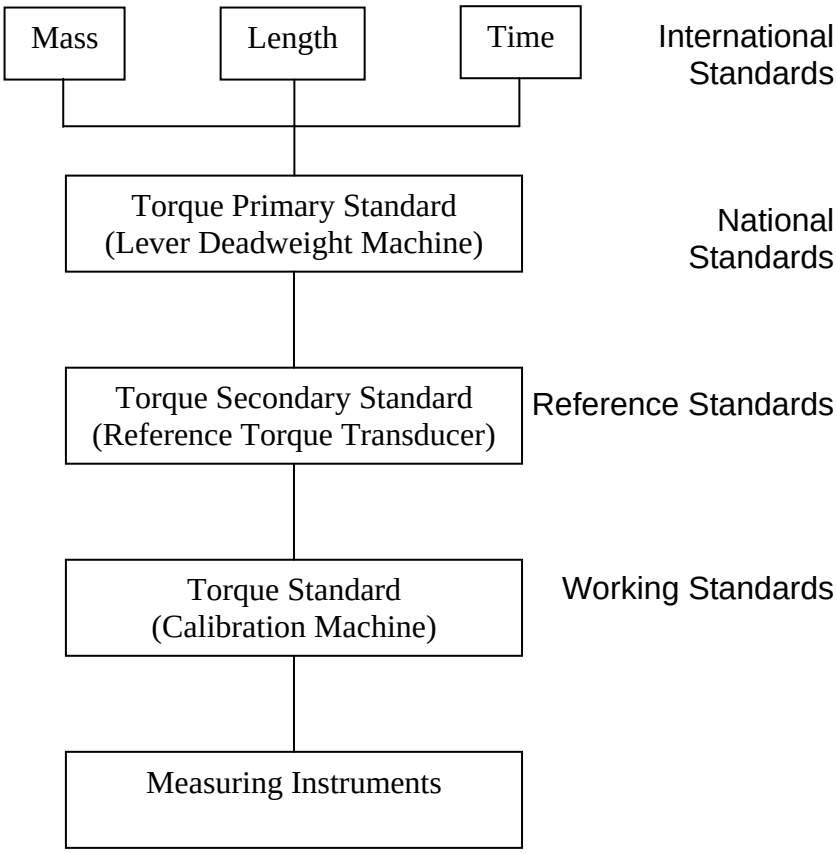

Figure 2.29 Traceability chart of torque measurement.

Horizontal torque calibration machines are more popular because it is the most simple and direct way to apply torque (*Robinson, 2007*). However, this design has many disadvantages. Firstly, a bending moment can affect the torque transducer if a force is produced from a single weightstack (*Robinson, 2007*). To overcome this problem, a spurious torque must be counteracted by an equivalent torque in the opposite direction (180° apart). Two identical arms attached to the torque transducer 180° apart will be used and the equal weights are suspended from each arm (*Herceg, 1976*). Secondly, the weight loading depends on the earth's gravitational field so the local gravity must be measured in calibration laboratories (*Davis, 2002 and Schicker and Wegener, 2002*). In addition, the length of the lever arm must be accurate which depends on whether it is aligned precisely horizontally or not (*Schicker and Wegener, 2002*). The Centre for Metrology and Accrediation (MIKES) in Finland has presented the new construction of its 2kNm Torque Standard Machine to solve this problem (*MIKES metrology annual report, 2005*). The control system, which has two functions, is introduced in order to fulfil this requirement. The first control is based on the force loading to the lever. It will drive the beam to the horizontal level when the level has tilted due to loading. The second function is distance control, which has been

realised using a laser sensor. It will be changed from force measurement to distance control when removing the load. Moreover, the imprecise relative axial location between the torque transducer and the point of applied torque produces unbalanced forces in the system (*Davis, 2002*). Furthermore, the effective weight of the beam can give significant error if the hanging weight is not normal to the beam (*Herceg, 1976*). This requirement can be verified by observing the output signal of the measuring system. The position that the weights are suspended exactly perpendicular to the beam will show the highest peak of the output reading whilst the signal will be smaller on either side of the peak when the torque transducer body is rotated slowly and slightly against the torque load (*Herceg, 1976*).

The Physikalisch-Technische Bundesanstalt (PTB) in Germany occupies the most sophisticated of this type of static torque calibration machine (Fig. 2.30). This machine can operate in two measuring ranges which are from 2 Nm to 1kNm with a reported uncertainty of 2×10^{-5}, and from 0.2Nm to 5Nm with a reported uncertainty of 1×10^{-4}.

Figure 2.30 PTB 1kNm torque standard machine (PTB, 2009).

Another design is the lever-deadweight system with a vertically mounted transducer. The advantages are that the lever beam construction is balanced, the location of the central fulcrum point is accurate and the bending moment on the torque transducer is zero (*Davis, 2002*). This kind of system is adopted to be used as the first national torque standard (Fig. 2.31) in UK. It was designed and manufactured by the National Physical Laboratory (NPL) and would then be used to calibrate transfer devices to disseminate the unit of torque within industry. The maximum capacity of the torque calibration machine is 2 kNm with an uncertainty of ±0.002% (k=2).

According to the analysis of Smith, it reveals that the error sources are mainly from the length measurement of the lever beam and the suspension wire connections from the lever beam to the deadweight hanger (*Davis, 2002*). Moreover, converting the vertical force generated by the weightstacks into a horizontal force in order to transfer torque to the lever beam, is complicate (*Robinson, 2007*). However, this problem can be solved by using a proper arrangement of boron fibre tapes used for suspending the deadweights, and a pulley air bearing supporting the lever beam which is designed to rotate independently of the torque

transducer when applying both clockwise and anti-clockwise torque loading (*Robinson, 2007*).

Figure 2.31 NPL torque standard machine (Robinson, 2007).

The second technique in torque calibration is using a force reference transducer with a lever arm (*Schicker and Wegener, 2002*). Apart from using the deadweight mechanism to apply force, a hydraulic system can be an alternative choice for many laboratories to use as a torque calibration machine (*Davis, 2002*). The Laboratoire National d'Essais (LNE) in France is one of many laboratories that use this kind of machine. The hydraulic rams are attached to the upper lever beam to generate force and the force transducers mounted on the lower beam are used to measure the reaction force. The 200kNm torque calibration machine with the uncertainty of 1×10^{-3} at LNE is illustrated in figure 2.32.

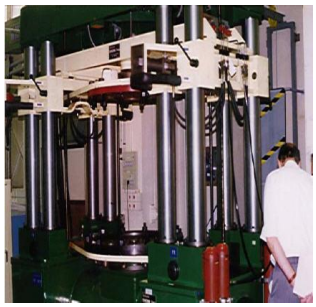

Figure 2.32 LNE torque machine (Davis, 2002).

Figure 2.33 The 1.1 MNm torque standard machine of PTB (PTB, 2005).

PTB is also developing a torque standard machine with a vertical measuring axis (Fig. 2.33). The measuring range is up to 1.1 MNm with a measurement uncertainty of 0.1%.

The forces, acting on the equal-armed double lever arm with mechanical spindle drives in the lower machine platform used to generate torque, are measured by means of the pair of tension-compression force transducers. The mechanical disturbances such as bending moments and transverse forces generated during loading by asymmetries are minimized by using additional drives (*PTB, 2005*).

Using a torque reference transducer is another method to calibrate torque. Any mechanism can be used to generate torque in this system. The torque reference transducer is used to measure torque and then this value directly compared to the torque transducer being calibrated. (*Schicker and Wegener, 2002*)

This method has many advantages such as it is convenient for using in on-site calibration on a test bench, due to regarding its transportability. Moreover, there is no need for complicated arrangement of weights which makes it possible for torque measurement to be made with a high level of automation. (*Schicker and Wegener, 2002*)

However, the friction occurring in the bearing between the reference torque and the torque transducer can cause an error in measurement results. Using air bearings to ensure that the mechanism it is free of friction can overcome this problem. (*Schicker and Wegener, 2002*)

A torque transfer machines (TTM) using this method is illustrated in figure 2.34 and belongs to the Centro Nacional de Metrologia (National Metrology Center, CENAM) in Mexico. It can calibrate torque up to 2 kNm with an uncertainty of 5×10^{-4}.

Figure 2.34 2 kNm Torque Transfer Machines (CENAM, 2006).

2.2 Resonant Sensors

Sensors which are rugged, reliable, low cost and compatible with computer controlled systems, which are dependent on digital processing, are increasingly required in all industrial sectors. Historically, most sensors have been based upon the measurement of electrical parameters, which give an analogue output signal. Utilising these sensors in control systems, which require digital signals, an analogue-to-digital

conversion unit is required. This additional stage involves some degree of complexity with an inevitable penalty in terms of reliability and cost of the system (*Jordan, 1985, Myrvoll, 2003*). Consequently, resonator sensors have been developed to replace those sensors as they can produce an intrinsic digital output signal (*Jordan, 1985*), making them very attractive in the precision measurement field. In early 1960, these resonant sensors have been presented, but with complex structures. Later, around 1982, they have been introduced again with more simple structures and ease of fabrication in mind (*Jordan, 1985*).

2.2.1 Introduction

Resonant sensors or frequency output sensors are devices with vibrating elements that are designed to exhibit the resonator's natural frequency or relative phase of oscillation in a mechanical structure (*Jordan, 1985, Langdon, 1987, Elwenspoek and Wiegerink, 2001 and Beeby et al., 2004*). The resonance frequency of the resonator sensors will change when subject to the measured quantity that alters the stiffness, mass, or shape of the resonator (*Beeby et al., 2004*). Figure 2.35 is a block diagram of a typical resonant sensor.

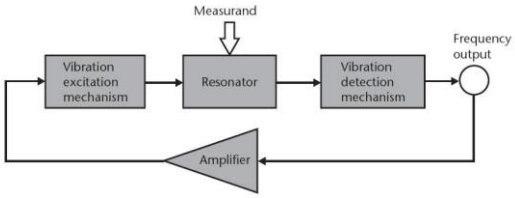

Figure 2.35 Block diagram of a resonant sensor (Beeby et al., 2004).

There are several configurations of the resonating elements such as beams, diaphragms or membranes, the "butterfly" structure, the "H" structure, tubes, cylinders, strings, rods, or micro machined pieces of quartz (*Elwenspoek and Wiegerink, 2001, Myrvoll, 2003*). Figure 2.36 illustrates some examples of these vibrating elements.

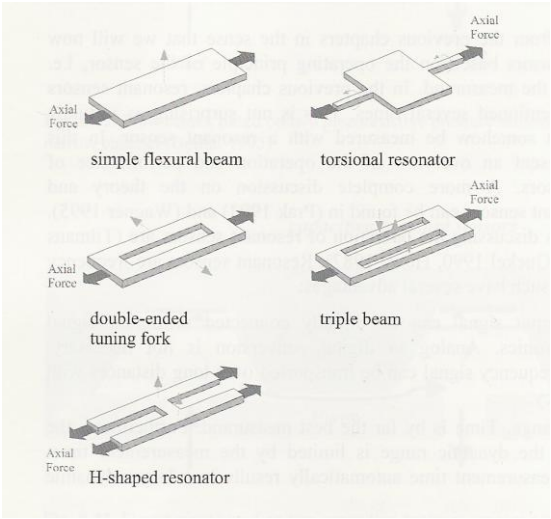

Figure 2.36 Various structures used in resonant microsensors (Elwenspoek and Wiegerink, 2001).

Each of these shapes can also have several types of vibrations, e.g. transversal, longitudinal, torsional, and lateral. Generally, there are several vibrational modes occurred with every type of vibration. The resonant sensors are designed such that one of these modes dominates and the resonance frequency of this mode is made dependent on the measurand (*Elwenspoek and Wiegerink, 2001*).

2.2.2 Fabrication Technology

In general, the resonators can be fabricated by either bulk micromachining or surface micromachining, and also the combinations of both technologies (*Tilmans, et al., 1992*).

Bulk micromachining is associated with the etching of a piece of material into a three-dimensional structure (*Tilmans, et al., 1992*). The thickness range may cover from 200 to 500 μm *(Varadan, et al., 2001)* and the lateral size ranges from 75 to 200 mm *(Gardner, et al., 2001)*. This technique can be divided into wet etching which uses liquid etchants, and dry etching which uses vapor and plasma etchants *(Varadan, et al., 2001)*.

Surface micromachining is different from the bulk micromachining because this technique does not shape the bulk wafer but instead builds structures on the surface of the wafer by using thin films deposition of 'sacrificial layers' and 'structural layers' and later removing the sacrificial layers in order to release the mechanical structures (*Tilmans, et al., 1992, Varadan, et al., 2001*). The dimensions of the structures obtained from this technique can be several orders of magnitude smaller than the previous technique. This technique could also be performed using both wet and dry etching methods (*Varadan, et al., 2001*).

The resonators can be fabricated from a variety of materials including metals and non-metallic such as crystal, quartz and silicon. In high-frequency applications, resonators made of piezoelectric material are preferred (*DeVoe, 2001*).

2.2.3 Coupling Mechanisms

There are several mechanisms used for coupling the resonator to the measurand, such as strain effect, shape coupling effect and mass effect. In mechanical sensing applications, the most common mechanism is to apply a strain across the structure. It is achieved by mounting the resonator in a suitable location on a sensing structure that deflects due to the application of the measurand. The output of the resonator, which is its natural frequency, is increased when the stiffness of the resonator is increased due to the applied strain from the deflection of the sensing structure. Force sensors, pressure transducers, and accelerometers apply this principle (*Beeby, et al., 2004*).

Another similar method to the strain effect is the shape coupling effect. The principle of this method is not related to the strain but it is about the changes in the geometry of the resonator due to the measurand, which leads to a shift in the resonant frequency (*Beeby, et al., 2004*).

Coupling the measurand to the mass of the resonator is implemented if the resonator is used to measure a liquid or gas. There are several methods for this coupling, such as surrounding the structure by a liquid or gas, coating the resonator in a chemically sensitive material and depositing material onto the resonator. The resonant frequency will be decreased when the mass of the resonator is increased. This decrease in frequency can be caused by the effective inertia of the resonator being increased due to the presence of the surrounding liquids or gases, as in density and level measurement, or by the absorption of molecules of a particular gas into the sensitive material coated on the gas sensor (*Beeby, et al., 2004*).

2.2.4 Vibration Excitation and Detection Mechanisms

The other components of a resonant sensor are the vibration drive mechanism, which excites the vibrations in the structure, and detection mechanisms, which senses these vibrations. These mechanisms are very important because they are used to determine the resonance frequency of the resonator sensors (*Tilmans, et al., 1992, Elwenspoek and Wiegerink, 2001*). The efficiency of excitation of a particular mode of vibration depends on the driving load distribution along the beam length that should be symmetric with respect to the centre of the beam because it is impossible to excite an anti-symmetric mode theoretically (*Tilmans, et al., 1992*). There are number of techniques used to drive the mechanical vibrations of the sensing elements such as coils, magnets, piezoelectric elements and techniques utilizing fiber optics, depending on the material properties of the vibrating element (*Myrvoll, 2003*). Six pairs of excitation and detection mechanisms have been proposed (*Tilmans, et al., 1992, Elwenspoek and Wiegerink, 2001*).

2.2.4.1 Electrostatic Excitation and Capacitive Detection

The principle of electrostatic excitation is that it uses the attractive force between the two plates or electrodes of a capacitor which are the resonator sensor and the substrate as the driving load (*Tilmans, et al., 1992, Elwenspoek and Wiegerink, 2001)*. When the capacitance between a charged capacitor fluctuates, there will be current flows through a biased capacitor, which is sensed by capacitive detection mechanism (*Elwenspoek and Wiegerink, 2001*).

This scheme is very attractive in term of easy fabrication of the resonators and integration with electronics (*Tilmans, et al., 1992*). The problem with this method is the damping of the squeeze film in the narrow gap between the substrate and the resonator (*Elwenspoek and Wiegerink, 2001*). Another disadvantage is due to the small capacitance value which gives a very small output signal. In this case, the detection

signal of the mechanical resonance will be obscured by electrical feedthrough and/or parasitic capacitances (*Tilmans, et al., 1992, Elwenspoek and Wiegerink, 2001*). Introducing of on-chip buffering and/or amplification is necessary for solving this problem (*Tilmans, et al., 1992*). For precision measurement, very stable voltages and amplitudes of vibration are required as the resonance frequency highly depends on the polarization voltage and the instability (*Tilmans, et al., 1992*).

2.2.4.2 Magnetic Excitation and Detection

An external magnetic field can be used for magnetic excitation and detection mechanisms. Lorentz force results from an electrical current flowing through the resonator sensors and used as the driving force (*Tilmans, et al., 1992, Elwenspoek and Wiegerink, 2001*). When the beam vibrates, the magnetic flux passing through the current loop will change due to a change in area of the current loop that will induce a voltage in the loop, providing the detection signal (*Tilmans, et al., 1992*). These mechanisms are suitable for metallic resonators. However, if a non-metallic material is used, the piezoelectric drivers can be used for this purpose (*Langdon, 1987*). Rosemount had used a metal resonator, which was magnetically driven, instead of using a quartz device because of long-term drift and hysteresis problems occurred in the quartz resonator itself (*Cucci, 1982*). However, some applications are not suitable to use a metallic resonator such as measuring density in corrosive fluids so a non-metallic material is chosen (*Jordan, 1985*).

The fabrication of this method is relatively simple but there are several problems such as very small signals and the difficulty of integrating the magnet in the sensor that requires the positioning of a magnet close to the resonator (*Tilmans, et al., 1992, Elwenspoek and Wiegerink, 2001*). There is also compressive axial stress induced in the resonators due to thermal expansion between the resonators and the support because of the dissipation of the heat by conducting a current through the resonator (*Tilmans, et al., 1992, Elwenspoek and Wiegerink, 2001*). This effect results in a lowering of the resonance frequency (*Tilmans, et al., 1992*).

2.2.4.3 Piezoelectric Excitation and Detection

Piezoelectric excitation and detection are based on the inverse piezoelectric effect and the direct piezoelectric effect, respectively which is widely used for resonators made of quartz because this material can be piezoelectric itself (*Tilmans, et al., 1992, Elwenspoek and Wiegerink, 2001*). If the resonators are not made of quartz, other materials such as zinc oxide (ZnO) or aluminium nitride (AIN) will be used in the form of thin films sandwiched between two electrodes for use in silicon-based resonators. (*Tilmans, et al., 1992, Elwenspoek and Wiegerink, 2001*). These electrodes must be deposited and patterned on the surface of the resonator at the location which is carefully designed to maximize the excitation and detection signal (*Beeby, et al., 2004*). The geometry of the electrodes should also be carefully designed for drive efficiency (*Beeby, et al., 2004*). In the inverse piezoelectric effect, an electric field such as a voltage is applied to these electrodes, therefore thickness and lateral dimensions of the film are changed (*Tilmans, et al., 1992*, *Elwenspoek*

and Wiegerink, 2001). In this case, a bending moment produced by the lateral deformation is used to excite the resonators (*Elwenspoek and Wiegerink, 2001*). Conversely, a dielectric displacement in the material, resulted from a mechanical stress or strain through the direct piezoelectric effect, can be detected as an electric current in an external circuit (*Tilmans, et al., 1992*).

The advantage of using piezoelectric materials is that it enables to maintain the vibration in the structure by a simple drive circuit (*Jordan, 1985*). Furthermore, crystal materials such as quartz and silicon are particularly interesting materials to produce the resonator sensors because of their high accuracy and repeatability properties with low cost of manufacture and low power consumption (*Langdon, 1987*).

Although ZnO is a very attractive material for using in these mechanisms because of its strong piezoelectric coupling efficiency (*Tilmans, et al., 1992*) there are some problems with piezoelectric transduction used ZnO thin film. For example, it has sensitive to humidity, light and the history of thermal treatment. Furthermore, the Q-factor is reduced because of the deposition of a ZnO layer on the resonator which also increases the temperature sensitivity due to differences in thermal expansion (*Tilmans, et al., 1992, Elwenspoek and Wiegerink, 2001*). Moreover, encapsulation of the ZnO layer in silicon nitride layers, to avoid zinc contamination and protect the ZnO layer against the different etchants used, is necessary because ZnO is not an IC-compatible material. In low frequencies applications (< 1 MHz), the fabrication process is more complicated because special configurations are required. When considering the properties of the piezoelectric layer after heat treatment at high temperature (1000-1150 °C), there is a possibility that the epitaxial growth of silicon may be excluded. Encapsulating the piezomaterial in a passivation layer can increase the resistance of the piezoelectric layer to the sacrificial layer etchant and also the protection against the etchant (*Tilmans, et al, 1992*).

2.2.4.4 Electrothermal Excitation and Piezoresistive Detection

Electrothermal excitation and piezoresistive detection mechanisms can be produced by using the same material in the same processing steps. Thermal expansion of a resistive material caused by a heat source on top of a beam generated by an electrical current giving rise to a temperature gradient along and normal to the beam is used as the principle of the excitation mechanism. A temperature gradient normal to the beam creates a bending moment due to thermal expansion, which is used to excite the resonators. The order of the thermal wave affects the relation between the induced mechanical bending moment and the frequency, which is related to the optimal point of the operation. The detection mechanism is based on piezoresistive effect which is detected by piezoresistors, made of the same material as that used for excitation (*Tilmans, et al., 1992, Elwenspoek and Wiegerink, 2001*).

This method is very attractive because standard IC processing technologies can be used to fabricate the resonators. The problems are that the sensitivity of this system is low. Furthermore, the thermal compressive axial forces introduced from the static heat dissipated in the sensors will affect the resonance frequency (*Tilmans, et al., 1992, Elwenspoek and Wiegerink, 2001*). To solve this problem, good control of the heat flow to the surroundings is required (*Tilmans, et al., 1992*).

2.2.4.5 Optothermal Excitation and Optical Detection
In order to avoid any electrical voltages at the sensor, optothermal excitation and optical detection mechanisms were developed. Optothermal excitation uses similar mechanism to electrothermal excitation except that the heat source is provided by the absorption of light by silicon or an absorbing layer e.g., aluminium. Several techniques have been proposed for optical detection, such as intensity modulation by means of a shutter, use of an optical proximity or displacement sensor, or integrating interferometry using the surface of the vibrating beam and the end of a glass fiber as mirrors (*Tilmans, et al., 1992, Elwenspoek and Wiegerink, 2001*).

This scheme is very attractive for applications because there is no reliable electrical solution under extreme environmental or hazardous conditions. However, the integration with the optical (fibre) system makes the realization more complicated even the fabrication of the resonator is relatively simple. Furthermore, thermally induced axial forces resulted in the dependence of the frequency on the optical drive power (*Tilmans, et al., 1992*).

2.2.4.6 Dielectric Excitation and Detection
A dielectric thin film sandwiched between a top and bottom electrode is used for dielectric excitation. The principle is that when a voltage is applied across the electrodes, an electrostatic force occurs and results in the lateral deformation of a dielectric thin film. This lateral deformation will cause bending moments that are used to drive the resonator sensors. For detection mechanism, the changes of the capacitance of a dielectric capacitor if the dielectric is deformed will be detected (*Elwenspoek and Wiegerink, 2001*).

Although this method seems promising it gives extremely small signals. Materials with a very high permittivity, such as PZT, are used to overcome this problem (*Tilmans, et al., 1992, Elwenspoek and Wiegerink, 2001*).

The various excitation and detection mechanisms used with resonators are summarized in Table 2.1.

There are several criteria that have to be determined for the suitability of the excitation and detection mechanisms. First of all, the performance and behaviour of the resonators must be considered (*Beeby, et al., 2004*), also information about the fabrication process, such as cost, yield

and through-put, and the availability of the technology (*Tilmans, et.al., 1992, Beeby, et al., 2004*), the kind and number of materials used for fabrication, which including aging of material properties, fatigue, yield strength, stress relaxation and differential thermal expansion (*Tilmans, et al., 1992*), and signal-to-noise ratio and other interference signals e.g., electrical feedthrough which can obscure the mechanical resonance (*Tilmans, et al., 1992*). Regarding the material used for resonator fabrication, a single-crystalline material with homogeneous structure is the ideal material (*Tilmans, et al., 1992*).

Table 2.1 Summary of Excitation and Detection Mechanisms.

Excitation	*Detection*
Electrostatic	Capacitive
Magnetic*	Magnetic*
Piezoelectric*	Piezoelectric*
Electrothermal*	Piezoresistive*
Optothermal*	Optical*
Dielectric	Dielectric

* These methods can be used with silicon resonators (*Beeby, et al., 2004*).

Secondly, it is important to consider the electrical circuit used to excite the sensor or measure the output signal such as the magnitude of the drive forces generated, coupling factor (or drive efficiency) and sensitivity of the detection mechanism (*Myrvoll, 2003, Beeby, et al., 2004*). For example if the electromagnets used as exciters and pickups are mounted too close to the sensor, the output frequency may not be stable (*Myrvoll, 2003*). However, if the distance between the sensor and the drivers/pickups is too far, the frequency will be constant because the effect of damping is not measurable (*Myrvoll, 2003*). Moreover, the sensors final environment needs to be considered and whether the resonators can be used in an Integrated Circuit (IC) environment or not (*Tilmans, et al., 1992, Beeby, et al., 2004*). Lastly, the overall design of the structure, including shielding, minimization of parasitic loads and on-chip electronics for buffering requires special attention (*Tilmans, et al., 1992*).

The electrical power needed to drive high-Q resonator sensors is extremely low. In small quartz devices with piezoelectric drive, the power dissipated in the resonator itself is usually insignificant in comparison with that dissipated in the oscillator and output circuits. The operation of resonator sensors in conjunction with ultra-low power drive electronics opens up the possibility of powering sensors from sources other than conventional electrical supplies, such as solar cells, fibre optic links and environmental sources such as pressure and temperature gradients. Many opportunities therefore exist for developing independently powered sensors to enhance safety and reliability (*Langdon, 1987*).

When considering to the excitation and detection mechanisms, the resonators can be divided into two approaches: one-port resonators and two-port resonators (Fig. 2.37).

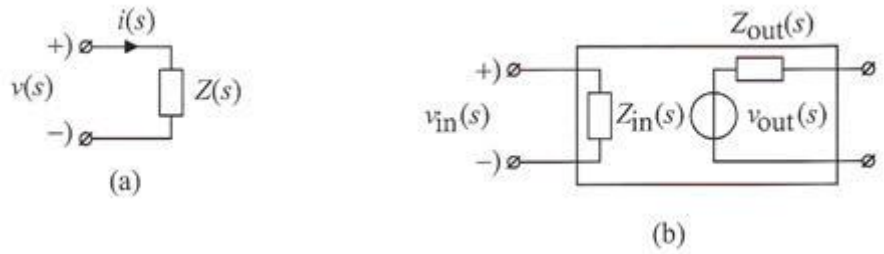

Figure 2.37 (a) One-port resonator (b) two-port resonator (Elwenspoek and Wiegerink, 2001).

One-port resonator uses a single element which combines the excitation and detection of the vibrations in the structure as shown in figure 2.37(a). The problem with this approach is that the mechanical resonance can be obscured from the parasitic parallel loads (*Elwenspoek and Wiegerink, 2001, Beeby, et al., 2004*).

Two-port resonator is different from one-port because it uses separate elements for excitation and detection of the structure (Fig. 2.37 (b)). However, they experience a similar effect that the mechanical resonance can be obscured. In the case of two-port resonator, this effect is caused by the electrical cross-talk between the driving and detection ports as a result of capacitive and/or resistive coupling, rather than the parasitic loads as in the one-port resonator (*Elwenspoek and Wiegerink, 2001, Beeby, et al., 2004*).

2.2.5 Resonator Design Characteristics

2.2.5.1 Quality Factor (Q-Factor)

The mechanical quality factor (Q-factor) is the parameter which represents the energy losses of the resonator or in other words, a measure of the mechanical damping in a system. The damping effects acting on the system will limit the magnitude of maximum amplitude at its resonant frequency when a structure approaches resonance. The Q-factor can be defined from the energy involved in the system. It is simply defined as being proportional of the total energy stored in the vibration to the energy lost per cycle due to the damping effects present and can be derived from equation 2.10 (*Tilmans, et al., 1992, Elwenspoek and Wiegerink, 2001, Beeby, et al., 2004*).

$$Q = 2\pi\left(E_M \big/ E_C\right) \tag{2.10}$$

where E_M is the total energy stored in the system
E_C is the energy lost per cycle

The Q-factor is commonly determined from the response characteristics of the resonator which is the steady-state frequency plot of a resonator excited by a harmonic force with constant amplitude because it cannot be determined directly (*Tilmans, et al., 1992, Elwenspoek and Wiegerink, 2001*). It can be calculated from Figure 2.38 using

$$Q = \frac{f_0}{\Delta f} \tag{2.11}$$

where f_0 is the resonance frequency with maximum amplitude response (a_{max})

Δf is the half-power bandwidth of the frequency response (at -3dB)

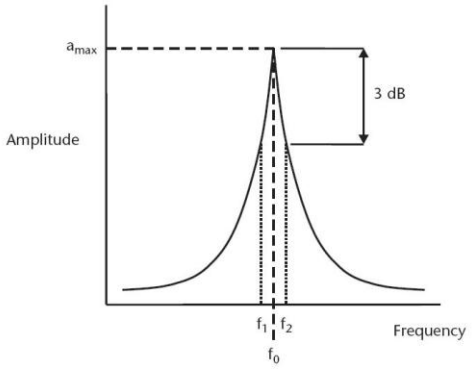

Figure 2.38 A typical characteristic of a resonant system (Beeby, et al, 2004).

It is clearly seen from the above equation that Q is a measure of the sharpness or the frequency selectivity of the resonator (*Tilmans, et al., 1992*).

A high Q-factor implies low energy losses in the system and good frequency stability. Therefore it has several advantages for resonator design characteristics. The shape of the resonant frequency with high Q-factor can be observed from the sharpness of the resonance curve. Increasing this sharpness, or in other word Q-factor, enables the resonant frequency to be more clearly distinguishable from non-resonant vibrations or parasitic mode of vibrations (Fig. 2.38) and also improves the performance and resolution of the resonator. For this reason, the operating electronics can be simpler since the magnitude of the signal from the vibration detection mechanism is greater than that of a low-Q system. A high Q-factor also ensures a minimal effect of the electronic circuitry on the oscillation frequency. In addition to those advantages, a high Q offers more possibility of excitation mechanism from alternative sources, e.g., solar energy, because the energy required to maintain the vibrations at constant amplitude is kept low which reduces heat generation. A high Q also shows that the resonant structure is well isolated from its surroundings, hence the influence of external factors will be minimized and its sensitivity to mechanical disturbances is low

(*Tilmans, et al., 1992, Elwenspoek and Wiegerink, 2001, Beeby, et al., 2004*).

Damping Mechanisms
The damping mechanisms cause the energy loss of the resonators that limit the Q-factor of the sensors. There are three distinguishable mechanisms of energy loss: (1) losses into the surrounding (fluid) medium ($1/Q_a$) caused by acoustic radiation and viscous drag, (2) losses into the mount used to support the resonator due to motion of the mount ($1/Q_s$), and (3) losses inside the material of the resonator ($1/Q_i$) from intrinsic damping. The relation between these effects and the Q-factor is shown in equation 2.12. The Q-factor can be maximized by minimizing these effects (*Tilmans, et al., 1992, Elwenspoek and Wiegerink, 2001, Beeby, et al., 2004*).

$$\frac{1}{Q} = \frac{1}{Q_a} + \frac{1}{Q_s} + \frac{1}{Q_i} \tag{2.12}$$

(1) Losses into the surrounding medium
Energy losses associated with $1/Q_a$ occur due to the interactions of the oscillating resonator with the surrounding fluids. There are several loss mechanisms and associated effects such as: squeezed film damping, acoustic radiation, gas damping and viscous damping. The nature of the gas, surrounding gas pressure, size and shape of the resonator, the direction of its vibrations, and its proximity to adjacent surfaces influence the magnitude of each loss mechanisms and associated effects.

Squeeze-film damping effect
If the flexural vibrating resonator is close to another stationary surface, squeeze-film damping effect occurs due to a pressure built-up in the intervening space. If the gap spacing approaches or becomes less than the width of the vibrating beam, the squeeze-film damping effect becomes significant but this effect can be reduced by operating the resonator in a suitable vacuum or making ventilation holes in the vibrating beam (*Tilmans, et al., 1992, Elwenspoek and Wiegerink, 2001, Beeby, et al., 2004*).

Acoustic radiation damping effect
Radiation of sound waves propagating in a direction normal to the surface will be significant if the acoustic wavelength becomes equal to or less than a typical dimension of the resonator (*Tilmans, et al., 1992*).

Gas and Viscous damping effect
The overall quality factor depending on the air-pressure will be described here. There are three main pressure regions that will be considered. The shape and material properties of the resonator have influences over the transition points of these regions. The way of supporting the resonator is also another influence (*Tilmans, et al., 1992*).

At low pressure of between 1 and 100 Pa when the surrounding gas molecules act independently of one another, the molecular damping occurs due to the collisions between the molecules and the resonator's surface as it vibrates and exchange momentum according to their relative velocities. The magnitude of this effect is dependent on the surrounding fluid pressure and close proximity of the oscillating structure to adjacent surfaces (*Tilmans, et al., 1992, Beeby, et al., 2004*).

At pressure near atmospheric pressure or above 100 Pa, where molecules can no longer act independently and the surrounding gas must be considered as a viscous fluid, the viscous damping is the dominating mechanism. The Stokes drag force for a body in uniform motion through a viscous fluid is one contribution that causes this effect. Another contribution is called shear wave effect, which is due to the fluid traveling over the surface of the resonator and forms a boundary layer around the vibrating structure. This shear wave results in transverse vibrations which travel into the fluid medium, and is dependent on the frequency of vibration, density and viscosity of the fluid medium (*Tilmans, et al., 1992, Beeby, et al., 2004*).

At pressures < 1 Pa the quality factor is independent of the pressure so it is mainly determined by losses into the support and by the intrinsic losses. Vacuum encapsulation of the resonator in a batch fabrication process, therefore, is necessary in order to obtain high Q-factor. However, temperature remains as a disturbing load, therefore, the design of packaging must be considered in order to reduce differential thermal expansion effects. The fabrication process of sealed resonators based on selective epitaxial growth of boron-doped single-crystalline silicon, high boron etch stops and selective electrochemical anisotropic etching was demonstrated by Ikeda et al. (*1988*). An alternative way is based on sacrificial layer etching and reactive sealing techniques. The hydrofluoric (HF) anodic etching and silicon fusion bonding is another method of fabricating sealed resonators (*Tilmans, et al., 1992*).

Several aspects have to be considered in deciding which technology is suitable to manufacture resonators. For example, selective epitaxy and HF anodic etching are the preferred methods for resonators made of single-crystalline silicon because of its superior material properties associated with aging, drift, hysteresis, fatigue, creep and yielding (*Tilmans, et al., 1992*).

Selective epitaxy method is more complicated and less flexible because it precludes the sealing of more than one resonator in a single cavity as the sealing cap always closely surrounds the resonator. For very thin resonators (<1 μm), this method will be difficult to control and reproduce as a result of the high deposition rate (300 nm/min). Low-pressure chemical vapour deposition (LPCVD) polysilicon which has low deposition rate (about 7 nm/min) is the preferred method for very thin resonators. However, this method is less attractive because of its long deposition times due to its low deposition rate. For this reason, LPCVD is impractical

to manufacture a resonator with thickness more than 2-3μm (*Tilmans, et al., 1992*).

(2) Losses into the mount used to support the resonator
Structural damping effect, $1/Q_s$, can be minimized by designing a balanced resonant structure, operating in a higher-order mode, supporting the resonator at its nodes, and employing a decoupling system between the resonator and its support (*Tilmans, et al., 1992, Elwenspoek and Wiegerink, 2001, Beeby, et al., 2004*).

The principle of balanced resonant structure provides a reaction to the structure's vibrations within the resonator. Multiple-beam style resonators are an example of this design, as they incorporate inherent dynamic moment cancellation when operated in a balanced mode of vibration. Double-ended tuning fork (DETF) and triple-beam tuning fork (TBTF) shown in figure 2.39 are well-known structures of this multiple-beam style (*Tilmans, et al., 1992, Elwenspoek and Wiegerink, 2001, Beeby, et al., 2004*).

DETF consists of two beams aligned alongside each other with equal width vibrating 180° out of phase, thereby cancelling moment reactions at the beam roots which results in a reduction of energy losses (*Tilmans, et al., 1992, Elwenspoek and Wiegerink, 2001, Beeby, et al., 2004*).

The TBTF structure provides another way of cancelling moments and shear forces at the clamped ends. It consists of three beams aligned alongside each other, the centre tine being twice the width of the outer tines. The middle beam and the two outer beams vibrate 180° out of phase. This structure can be fabricated with planar micromachining technologies and the excitation/detection of the flexural transverse vibrations is not difficult as in the DETF, which requires in-plane excitation/detection schemes (*Elwenspoek and Wiegerink, 2001, Beeby, et al., 2004*).

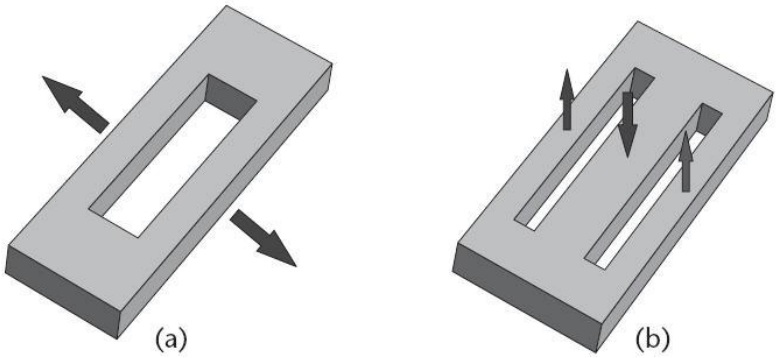

Figure 2.39 Structures and optimum modes of operation of two balanced resonators: (a) DETF and (b) TBTF (Beeby, et.al, 2004).

A dynamically balanced resonator design provides many benefits: high Q-factor therefore high resolution of frequency, high degree of immunity to environmental vibrations, immunity to interference from surrounding

structural resonances, and long-term performance since the influence of the surrounding structure on the resonator is minimized. However, unequal loading of the beams can result in the natural frequencies of the beams separating, which lower the Q-factor and eventually produces bistable operation of the device in an oscillator circuit (*EerNisse and Paros, 1983*).

The coupling mechanism between the resonator and its support is considered from Newton's Third Law that every action has an equal and opposite reaction. When observing a fixed-fixed beam vibrating in its fundamental mode, the reaction to the beam's vibrations is provided by its supports. This reaction causes energy to be lost from the resonator due to the deflection of the supports. This effect can be reduced by operating in a higher-order mode, e.g. second mode. This mode of vibration possess a node halfway along the length of the beam, hence the beam will vibrate in anti-phase either side of the node, and the reactions from each half of the beam will cancel out at the node. The magnitude of each reaction at each support for this mode is less than for mode 1. Although using of higher order modes can minimize the structural damping effect their sensitivity to applied stresses is reduced (*Beeby, et al., 2004*).

Employing a decoupling system between the resonator and its support by mechanically isolating the resonator from the mount can be done by using a large mass and an isolator beam, as applied for a single beam. This component acts as a soft spring-mass system with a natural frequency much lower than the frequency of the beam and of the support. In order to efficiently clamp the edge of the resonating beam, the mass has to be large. The loss of energy of this design is reduced because the moment and shear reactions are isolated from the support. Another way of decoupling is applying a frame around the resonator. This method is used for a torsional resonator which it can vibrate in a torsional mode. The principle of minimizing the energy losses into the support by this method is to have a high ratio between the resonant frequencies of the resonator and the mounting frame (*Tilmans, et al., 1992*).

(3) Losses inside the material of the resonator

The amplitude of vibrations still decays with time, even if the external damping mechanisms $1/Q_a$ and $1/Q_s$ are removed. This illustrates that the Q-factor of a resonator is ultimately limited by the energy loss mechanisms within the resonator material ($1/Q_i$). The vibrations of the resonators can be attenuated by several internal loss mechanisms such as: magnetic effects (magnetoelastic hysteresis), thermal effects (thermoelastic intermal friction), and atomic reconstructions (dislocations, stress relaxation at grain boundaries), scattering by impurities and phonon interaction (*Tilmans, et.al, 1992, Beeby, et.al, 2004*). Single-crystal materials, such as quartz and single-crystalline silicon are more attractive materials than amorphous or polycrystalline because of their lower intrinsic losses, more stable properties, low hysteresis and creep, and higher intrinsic Q-factor. However, the damping properties of materials still need investigating (*Tilmans, et al., 1992*).

2.2.5.2 Nonlinear Behaviour and Hysteresis

Nonlinear behaviour can adversely affect the accuracy of a resonant sensor so it is undesirable. This effect is presented in all resonant sensors and becomes apparent at higher vibration amplitudes when the resonator's restoring force becomes a nonlinear function of its displacement. There are two examples of this behaviour, hard spring and soft spring effects (Fig. 2.40), depending on the type of clamping. The hard spring effect occurs in a fixed-fixed beam, where the resonant frequency increases when a tensile force is applied. In this case, the magnitude of this effect depends on the boundary conditions of the beam. Another effect occurs in the beam which is not clamped firmly. It exhibits the soft spring effect that the resonant frequency falls with increasing tensile force. In this case, the geometry of the resonator affects the magnitude of the effect (*Beeby, et al., 2004*).

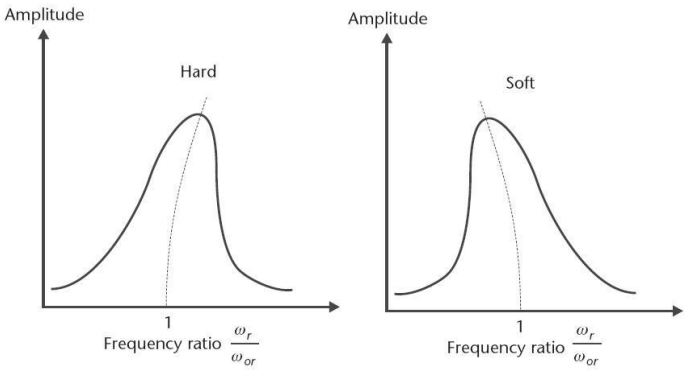

Figure 2.40 The hard and soft nonlinear effects (Beeby, et al., 2004).

In the case of an undamped structure, the equation of motion for an oscillating applied force is

$$m\ddot{y} + s(y) = F_0 \cos\omega t \tag{2.13}$$

where m is the mass of the system
F is the applied driving force
ω is the frequency
y is the displacement
s(y) is the nonlinear function.

The nonlinear relationship, s(y), can be represented by the cubic term (Eq. 2.14).

$$s(y) = s_1 y + s_3 y^3 \tag{2.14}$$

Placing (2.14) in (2.13), dividing through by m, and simplifying gives

$$\ddot{y} + s_1/m\left(y + s_3/s_1 y^3\right) = \frac{F_0}{m}\cos\omega t \tag{2.15}$$

s_1/m equals ω_{or}^2 (ω_{or} is the resonant frequency for small amplitudes of vibration) and s_3/s_1 is denoted by β. The restoring force acting on the system is therefore represented by

$$R = -\omega_{or}^2 \left(y + \beta y^3 \right) \tag{2.16}$$

The nonlinear behaviour depends on β as presented in the following three cases:

(1) $\beta = 0$, the restoring force is a linear function of displacement
(2) $\beta > 0$, the system shows the hard spring effect
(3) $\beta < 0$, the system shows the soft spring effect

The resonant frequency in the nonlinear behaviour exhibits a quadratic dependence upon the amplitude, as shown in

$$\omega_r = \omega_{or} \left(1 + 3/8 \, \beta y_0^2 \right) \tag{2.17}$$

From an experimental analysis of the resonant frequency and maximum amplitude for a range of drive levels, the variable β can be found by applying (2.16).

As the nonlinear behaviour becomes apparent when the amplitude of vibration is increased, it therefore depends on the energy supplied by the resonator's drive mechanism and the Q-factor of the resonator. If the resonator is driven too hard or has high Q-factor, the amplitudes at minimum practical drive levels will be excessive and that can result in undesirable nonlinear behaviour. Driving a resonator in a nonlinear region, then changes in amplitude due to amplifier drift, the resonant frequency will be shifted and it will be indistinguishable from shifts due to the measurand. Consequently, the analysis of a resonator's nonlinear characteristics can determine drive mechanism suitability and its associated operating variables (*Beeby, et al., 2004*).

In addition, high Q-factor also enhances the chance of hysteresis occurring in the resonators (*Elwenspoek and Wiegerink, 2001*). If the amplitude of vibration exceeds a critical value, a nonlinear system can exhibit hysteresis that the amplitude has three possible values at a given frequency (*Elwenspoek and Wiegerink, 2001, Beeby, et al., 2001*). By measuring the Q-factor of the resonator at small amplitudes and applying

$$Q = \frac{\omega_{or}}{2h}, \tag{2.18}$$

the critical value can be determined by applying

$$y_0^2 > \frac{8h}{3\omega_{or}|\beta|} \tag{2.19}$$

where h is the damping coefficient.

Apart from the nonlinear and hysteresis behaviours, the ultimate frequency resolution or stability of the sensor will be limited by noise or other instabilities of the vibrational amplitude (*Tilmans, et al., 1992*, *Elwenspoek and Wiegerink, 2001*). Several factors such as temperature sensitivity and variations, stability or electrical components of the feedback oscillator, stability of the environment, and the quality factor of the resonator are used to determine the short-term resolution or stability of the resonator. While in the case of long-term resolution or stability, creep and stress relaxation are relevant. In high-precision sensors, the response time is another parameter that should be considered and it is expected to be small compared to the time required for counting the frequency shift (*Tilmans, et al., 1992*).

Moreover, the shift in the resonance frequency not only occurs when the axial force changes but may be due to the changes in geometrical deformation of the resonant sensors. Nevertheless, this effect is small compared to the effect of the measured value but it will have an important consequence if the resonator is subjected to creep. The level of this effect depends on the creep behaviour. If the resonator sensor is subjected to creep occurring under a constant state of stress, its resonant frequency will only be slightly affected but creep will seriously limit the performance of the sensor when the input load of the gauge causes an elongation (*Tilmans, et al., 1992*).

Error readings can also be caused by a possible relaxation of the residual stress in the materials during operation. Low residual strain/stress levels (small tension) and slender vibrating elements can minimize the chance of buckling and allow long beams to be fabricated resulting in a large gauge factor. On the other hand, a large tension and increased mode number will decrease the gauge factor and the sensitivity of the device (*Tilmans, et al., 1992*).

2.2.6 Advantages and Disadvantages

The advantages of resonator sensors or frequency output sensors are that they present extremely rugged, simple construction and long-term stability (*Jordan, 1985, Myrvoll, 2003*). Moreover, the most important benefit over conventional analogue sensors is that they create a digital output signal through the mechanical characteristics of the device itself which is directly compatible with digital signal processing electronics in computer controlled systems (*Elwenspoek and Wiegerink, 2001, Myrvoll, 2003*). Consequently, analogue to digital conversion is not necessary, which makes the resonant sensors particularly attractive in present day digital measurement and control (*Myrvoll, 2003*). Furthermore, frequency signals can be transported over long distances with high accuracy (*Elwenspoek and Wiegerink, 2001*), and also shows high sensitivity and resolution, and consumes low power (*EerNisse and Paros, 1983, Tilmans, et.al, 1992*). In addition, their semi-digital output presents higher

reliability, lower error rates, lower susceptible to degradation of transmitted signals by electrical interference, lower dependence on change in electrical characteristics with time and eliminates problems such as intensity fluctuations associated with analogue signals (*Langdon, 1987, Tilmans, et.al, 1992*). Considering the fabrication technology, micromachining can be used for batch fabrication with possible on-chip electronics. For this reason, the cost of manufacturing resonant systems will be reduced and reproducibility can be improved (*Tilmans, et al., 1992*).

However, the measurement sensitivity and reliability of using resonator sensors is very dependent on how to maintain and measure the prime mode of vibration of the mechanical structure. In order to achieve this requirement, the influences of material consistency and manufacturing tolerances, and the knowledge of the modes of vibration must be fully understood by applying sophisticated mathematical modelling techniques (*Jordan, 1985*). For complex resonator shapes, where the frequencies of the different modes of vibration are very close to each other and have different sensitivities to the axial load, the interference of unwanted modes with the desired mode can be minimized by decreasing the dynamic range or measurement window of the sensor, where the frequency will be a single-valued function of the axial load. If a large dynamic range is required, the resonator structure should be simple and also the excitation and detection elements should be designed and placed so that the unwanted modes are not excited or detected (*Tilmans, et al., 1992*).
Furthermore, the frequency of resonators is intrinsically a function of temperature because the elasticity and density of materials are temperature dependent (*Langdon, 1987*). In addition, both material properties such as Young's modulus and the resonator dimensions are temperature dependent so a shift of the resonance frequency is induced from a temperature change which is a major source of error. Differential thermal expansion effects within the composite resonator or between the resonator and the supporting structure also strongly degrade the performance of the device. To solve this problem, electronic temperature compensation (on-chip temperature sensor), accurate temperature regulation of the sensor environment or employing a differential resonator design need to be considered. The latter method can minimize many errors from variations in the reference clock frequency, aging of material properties, even-order nonlinearity effects and mounting or package-induced stresses. In order to reduce the mounting strains, stress-free assembly techniques or mechanical decoupling zones are used (*Tilmans, et al., 1992*).

In addition, a perturbation of potential or kinetic energy in a mechanical structure has influence on the resonance frequency of the resonator. The potential energy perturbation is caused by changing the stiffness of the resonator due to the changes of the shape, or by mechanically straining the resonator. For the kinetic energy perturbation, it is caused by a change of the resonator mass or by changes of the density of the

surrounding medium. To avoid this perturbation, the resonator should be hermetically sealed in an evacuated or inert cavity in order to provide a stable environment (*Tilmans, et al., 1992*).

2.2.7 Applications

Resonator sensors are commercially available for the measurement of mass flow, density, level, gas, viscosity, rotation rate, pressure, force and acceleration (*Jordan, 1985, Beeby, 2004*). Langdon (*1987*) described many resonator applications, applying different techniques to measure the required value of interest. For example, varying stress or tension in a mechanical structure of the resonator sensors can lead to the changes of its vibrational resonance frequency such as in pressure sensor or load cell. Moreover, changing its mass by surrounding it by a liquid or gas also causes the frequency to change, as in liquid and gas density or liquid level application. In addition, a viscosity sensor or combined viscosity and density sensor can be constructed by using other time dependent measurement methods, such as measuring decay time of the vibration in a mechanical resonator, when it is immersed in a liquid, which depends on the viscosity of the surrounding medium. Flow velocity can also be measured with the resonator sensor, when it is immersed in a moving fluid, by measuring the time difference between signals from displacement sensors attached at different points, resulting from the momentum of the vibration transferred from one part to another by fluid flow. In applications requiring highly reliable temperature measurement such as in nuclear reactors, small tuning forks resonators excited remotely by acoustic waveguides are used (*Langdon, 1987*).

The future trend in using resonator sensors for multi-function sensor systems is also possible (*Jordan, 1985*). For example, the output signal of the resonator sensors does not only respond to the required parameter but also to other parameters, such as temperature. From this point, the designer must be very careful in designing a sensor, which maximises the response to the required parameters whilst minimising the unwanted parameters. However, this may provide additional opportunities for acquiring a sensor which can be responsive to many parameters at the same time for the price of one (*Langdon, 1987*).

2.3 Resonant Sensors for Torque Application

Torque measuring devices are implemented in several applications such as in process control, automotive industries etc.. Potentiometer, capacitive, inductive, magnetic or optical angular position sensor can be used to measure torque, which is translated into a mechanical movement of a torsion bar (*Beckley, et al., 2002*). Moreover, metallic resistance strain gauges fixed on to a weak link (e.g. a torsion bar) is used to detect the surface strain on the torsion bar produced by torque (*Whitehead, et al., 1997, Beckley, et al., 2002, Yan, et al., 2005a*). Strain-gauge-based torque sensors experience many problems such as low output signals,

poor signal-to-noise ratio, labour intensive installation, low overload capability, and drift (*Whitehead, et al., 1997, Yan, et al., 2004b*). For this reason, resonant-based sensors are an attractive alternative technology that has been developed to overcome those problems (*Whitehead, et al., 1997*).

2.3.1 Metallic TBTF Resonant Sensors

2.3.1.1 Introduction

Metallic triple-beam tuning-fork (TBTF) resonant sensors have been developed to measure torque as their resonant frequency will increase with increasing torque. This sensor consists of three beams aligned alongside each other and coupled at their roots. The advantage of triple-beam over the single beam structure is that this design is inherently more dynamically balanced. Consequently, it dissipates less energy through its supports and possesses an intrinsically high mechanical Q-factor (*Yan, et al., 2003a*). When compared to the double-beam resonator, it provides the extra space to place the drive and pick-up elements on the resonator and also permits the coplanar deposition along the width direction on the top surface of the beam, in order to generate out-of-plane vibration. For this reason, this design is more convenient and less time-consuming in terms of fabrication, because the double-beam design requires the deposition of the piezoelectric material along the thickness direction on the side of the beam to generate lateral anti-phase in-plane motion, that requires two steps of printing process (*Yan, et al., 2004b*). Nevertheless, if the piezoelectric elements are deposited along the width direction, the double-beam resonator can also be operated in out-of-plane motion mode but with reduced Q-factor (*Barthod, et al., 2003*).

Whitehead implemented metallic TBTF resonator fabricated from Ni-Fe alloy 42, which is excited by a thick-film printed lead zirconate titanate (PZT) element on one tine and a second PZT attached to another tine detects the resonant frequency. The Q-factor is about 300. Its basic configuration in a closed-loop configuration is shown in figure 2.41.

Figure 2.42 illustrates a torque transducer which is based on this type of resonant sensors. Two TBTF resonators are mounted onto the torsion bar machined from 17-4 PH stainless steel at ±45° relative to the axis of the bar. Although two devices are mounted, only one TBTF resonator is used for torque measurement. The reason for mounting two devices is to allow the symmetry of the sensor which is essential for optimum operation as a torque sensor (*Whitehead, et al., 1997*).

The metallic TBTF resonator that has been used in this current research project is based on the configuration that was proposed by Yan, et.al (*2003a*). The following sections will describe the TBTF resonator and its development, torque transducer implementing this type of TBTF resonator and some demonstrated feasibility of its performance.

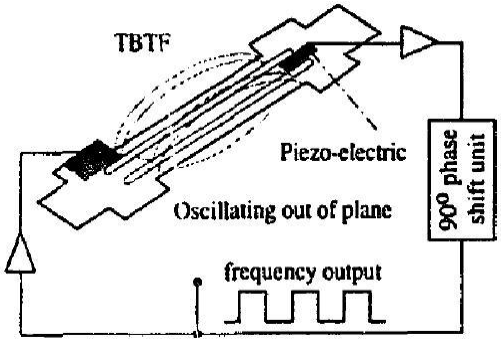

Figure 2.41 Basic TBTF in a closed-loop configuration (Whitehead, et al., 1997).

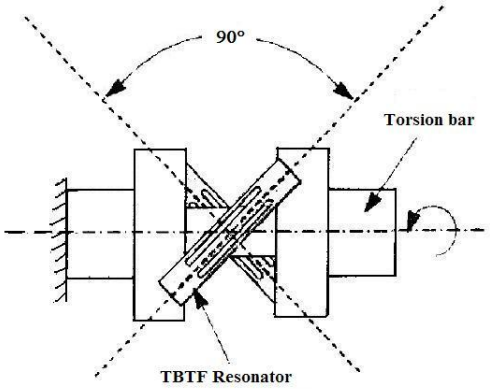

Figure 2.42 Schematic of a TBTF-based torque sensor (Whitehead, et al., 1997).

2.3.1.2 Resonator Design

The metallic TBTF resonator with thick-film printed piezoelectric drive and pickup elements proposed by Yan, et al, is shown in figure 2.43 (*2003a*). It consists of three parallel beams (tines) and joined to the substrate at each end. Its resonating element has a length of 15.5mm, a thickness of 0.25mm, a central beam width of 2mm which is twice of the two outer beams (1mm) and the distance between the beams is 0.5mm. The resonance frequency is about 6.2kHz with Q-factor of 3100.

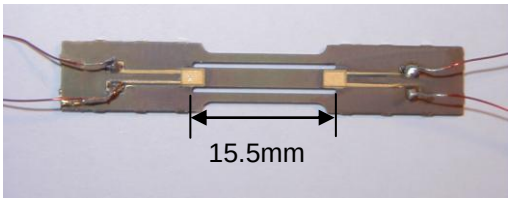

Figure 2.43 Photograph of metallic resonator (Yan, et al., 2003a).

In figure 2.44, the large electrically earthed regions are introduced on to the substrate surrounding the drive and detect electrodes in order to minimise cross talk between the drive and detect element (*Yan, et al., 2003b*).

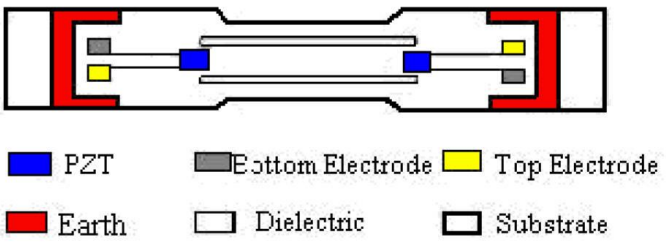

Figure 2.44 A plan view of the resonator structure with PZT driving and detecting elements with large earthed regions (Yan, et al., 2003b).

Finite Element Analysis (FEA) has been performed to observe the vibration mode with stress distribution and eigenfrequencies of the resonator as shown in figure 2.45.

It can be seen that the third mode of vibration is the mode that the central tine vibrates in anti-phase with the two outer tines. This mode is the optimum mode because the shearing forces and bending moments at the decoupling zone are cancelled out resulting only little vibrational energy is dissipated into the supporting structure at each end of the resonator, which improves the Q-factor and the performance of the resonator.

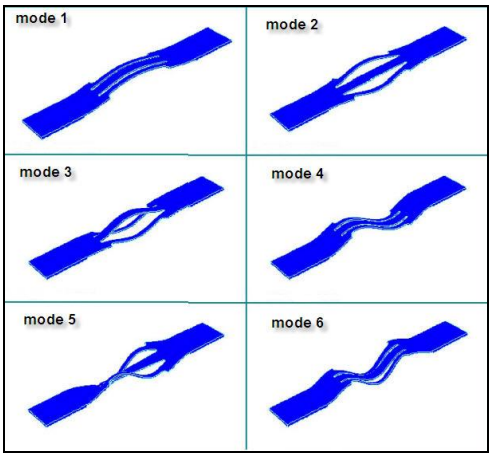

Figure 2.45 Six vibration modes of the resonator modeled by FEA (Yan, et al., 2004a).

Moreover, FEA has been employed to optimise the positioning of the thick-film piezoelectric elements on the structure. The PZT elements were printed at each end of the central beam because the maximum stresses exist at these regions when it operates in the favoured mode of vibration (3rd mode) from FEA (Fig. 2.46). For this reason, the degree of mechanical coupling between the active piezoelectric layer and the resonator for generation of both driving forces and sensing signals is maximised. The temperature operation of the PZT elements in its current formation is up to 120°C (*Yan, et al., 2005b*). The PZT element at one end drives the vibrations, whilst the PZT element on the other end detects them (*Yan, et al., 2004a*).

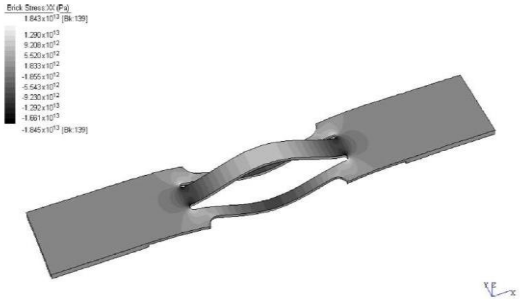

Figure 2.46 A stress distribution along the resonator in mode 3 (Yan, et al., 2004a).

The operating resonant frequency of this TBTF resonator is determined from the transverse vibrations of a prismatic beam in the x-y plane (Fig. 2.47a) which is assumed to be a plane of symmetry for any cross section.

When considering internal and inertial actions upon a free-body diagram of an element of length dx as shown in figure 2.47b, the dynamic equilibrium condition for forces in the y direction when the beam is vibrating transversely is considered to be

$$V - V - \frac{\partial V}{\partial x} dx - \rho A dx \frac{\partial^2 \upsilon}{\partial t^2} = 0 \qquad (2.20)$$

where V is the shearing force
ρ is the density of the material
A is the cross-sectional area of the beam
υ is the transverse displacement of a segment of the beam

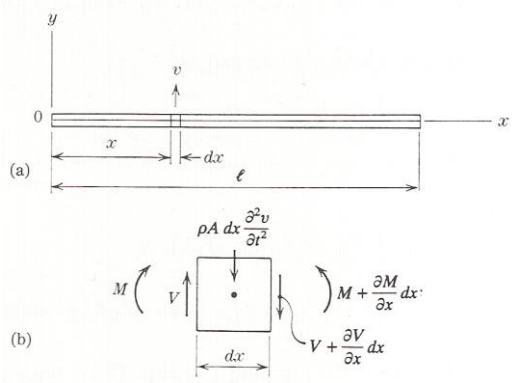

Figure 2.47 Transverse vibration of prismatic beams (Weaver, et al., 1990).

And the moment equilibrium condition gives

$$-V dx + \frac{\partial M}{\partial x} dx \approx 0 \qquad (2.21)$$

where M is the bending moment and $V = \frac{\partial M}{\partial x}$.

Substitution of V into equation (2.20) produces

$$\frac{\partial^2 M}{\partial x^2} dx = -\rho A dx \frac{\partial^2 \upsilon}{\partial t^2} \qquad (2.22)$$

From elementary flexural theory

$$M = EI \frac{\partial^2 \upsilon}{\partial x_2} \qquad (2.23)$$

where E is modulus of elasticity
I is second moment of area

$$I = \frac{\left(W * H^3\right)}{12} \tag{2.24}$$

where W is the width of the beam
H is the thickness of the beam

Substitute (2.23) in (2.22), therefore

$$\frac{\partial^2}{\partial x^2}\left(EI\frac{\partial^2 \upsilon}{\partial x^2}\right)dx = -\rho A dx \frac{\partial^2 \upsilon}{\partial t^2} \tag{2.25}$$

If the beam is uniform, the flexural rigidity EI is constant, so:

$$EI\frac{\partial^4 \upsilon}{\partial x^4}dx = -\rho A dx \frac{\partial^2 \upsilon}{\partial t^2} \tag{2.26}$$

Or

$$\frac{\partial^4 \upsilon}{\partial x^4} = -\frac{1}{a^2}\frac{\partial^2 \upsilon}{\partial t^2} \tag{2.27}$$

where $a = \sqrt{\frac{EI}{\rho A}}$

When a beam vibrates transversely, the deflection at any location varies harmonically with time, as follows:

$$\upsilon = X\left(A\cos\omega t + B\sin\omega t\right) \tag{2.28}$$

Substitution of (2.28) into equation (2.27) results in

$$\frac{d^4 X}{dx^4} - \frac{\omega^2}{a^2}X = 0 \tag{2.29}$$

Introducing $\frac{\omega^2}{a^2} = k^4$ so

$$\frac{d^4 X}{dx^4} - k^4 X = 0 \tag{2.30}$$

By writing $X = e^{nx}$, thus:

$$e^{nx}\left(n^4 - k^4\right) = 0 \tag{2.31}$$

Consequently, the values of n are found to be $n_1 = k,\ n_2 = -k,\ n_3 = jk,\ n_4 = -jk,$ where $j = \sqrt{-1}$.

As a result, the general form of (2.30) becomes

$$X = Ce^{kx} + De^{-kx} + Ee^{jkx} + Fe^{-jkx} \tag{2.32}$$

which may be written in the following form

$$X = C_1 \sin kx + C_2 \cos kx + C_3 \sinh kx + C_4 \cosh kx \tag{2.33}$$

This is a typical normal function for transverse vibrations of a prismatic beam. Different boundary conditions at the ends of the beam will determine these constants C_1, C_2, C_3 and C_4 which lead to the frequencies and mode shapes for free vibrations.

In the case of this TBTF sensor, the beam will be analyzed as the fixed ends beam (Fig. 2.48) so the boundary conditions for this case are

$$(X)_{x=0} = 0 \qquad \left(\frac{dX}{dx}\right)_{x=0} = 0 \qquad (X)_{x=l} = 0 \qquad \left(\frac{dX}{dx}\right)_{x=l} = 0$$

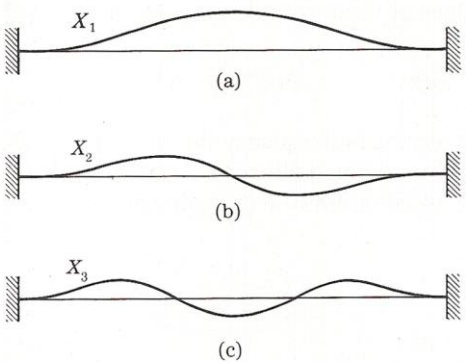

Figure 2.48 First three mode shapes of beam with fixed ends (Weaver, et al., 1990).

Rewrite equation 2.33 in the following equivalent form:

$$X = C_1(\cos kx + \cosh kx) + C_2(\cos kx - \cosh kx) + C_3(\sin kx + \sinh kx) + C_4(\sin kx - \sinh kx) \tag{2.34}$$

From the above boundary conditions of the fixed ends beam (Eq. 2.34), the first two conditions will be satisfied if $C_1 = C_3 = 0$, so that

$$X = C_2(\cos kx - \cosh kx) + C_4(\sin kx - \sinh kx) \tag{2.35}$$

From the two latter conditions the following equations are obtained:

$$C_2(\cos kl - \cosh kl) + C_4(\sin kl - \sinh kl) = 0 \tag{2.36}$$
$$C_2(\sin kl + \sinh kl) + C_4(-\cos kl + \cosh kl) = 0 \tag{2.37}$$

A solution for the constants C_2 and C_4 (different from zero) can be obtained only when the determinant of the coefficients in Eqs. (2.36) and (2.37) equal to zero. As a result, the following frequency equation can be obtained.

$$\left(-\cos kl+\cosh kl\right)^2-\left(-\sin^2 kl+\sinh^2 kl\right)=0 \qquad (2.38)$$

Or

$$\cos kl\cosh kl=1 \qquad (2.39)$$

The consecutive roots of this equation are shown as the example in the following table:

Table 2.2 A few of the lowest consecutive roots of the frequency equation of beam with free and fixed ends.

k_0l	k_1l	k_2l	k_3l	k_4l	k_5l
0	4.730	7.853	10.996	14.137	17.279

The nonzero roots can be obtained from the formula

$$k_il\approx\left(i+\frac{1}{2}\right)\pi \qquad (2.40)$$

The frequencies for the beam can be determined from the equation

$$f_i=\frac{\omega_i}{2\pi}=\frac{k_i^2a}{2\pi} \qquad (2.41)$$

where i is the mode of vibration.

Substituting of $a=\sqrt{\frac{EI}{\rho A}}$ into (2.41) results in

$$f_i=\frac{k_i^2}{2\pi}\sqrt{\frac{EI}{\rho A}} \text{ or } f_i=\frac{(k_il)^2}{2\pi l^2}\sqrt{\frac{EI}{\rho A}} \qquad (2.42)$$

It is clearly seen that the resonant frequency of the resonant sensor is dependent on the geometric dimension and properties of the material used to fabricate the resonator according to equation 2.42.

In this case, the resonating element has a length of 15.5mm, a thickness of 0.25mm and beam widths of 2. The elastic modulus of the stainless steel 430S17 is 200GPa and the density is 7800 kg/m^3. The constant k_1l = 4.730 is used as the mode shape of the vibration of this resonator associated to the third mode of vibration of beam. Consequently, the resonance frequency of this resonator from theory can be obtained from

equation 2.40 which is about 5.4kHz. This value is different from the experimental value because the frequency calculation from theory is based on the assumptions that: the parental material is uniform so the Young's modulus and density are uniform throughout the material sheet, and the dimension of the sensors i.e. tines dimensions are identical (*Cheshmehdoost, 1992*).

In addition, the FEA calculated resonant frequency is different from the experiment because it ignores the presence of the PZT elements which will increase the value by increasing the stiffness of the resonator, and the firing process during printing process which will decrease the frequency by decreasing the Young's modulus of the resonator material (*Yan, et al., 2004a*). Also for etched elements the cross-sectional area is not uniform.

2.3.1.3 Fabrication

Many kinds of material are used to fabricate the resonant sensors such as the piezoelectric, silicon and metal. Although the piezoelectric resonator has high Q value ($Q > 10^4$), it has high temperature coefficient and low yield strength. Also silicon material suffers from a large temperature coefficient. The other suitable materials are metals with high yield strength such as stainless steel and Fe-Ni alloys. A major drawback of the Fe-Ni alloy is the slight changes in the iron-nickel ratio or the presence of the impurities can cause large changes in the temperature coefficient of the frequency. Adding chromium to these iron alloys can reduce sensitivity to the composition. However, it is difficult to produce the material with desired characteristics. Moreover, it requires heavy cold working which seriously limits the size (*Cheshmehdoost, 1992*).

The important characteristics of a suitable material used for fabrication of the resonant sensors are; high mechanical Q, low temperature coefficient, low hysteresis and high yield strength. Furthermore, the availability and machinability are other important requirements that should be considered in selecting the material (*Cheshmehdoost, 1992*).

The resonator used in this research was fabricated from 430S17 stainless steel thin sheet. This material is suitable for deposition of dielectric and firing processes. It was machined by using a simultaneous double-sided photochemical etching technique which uses a photoresist and etchants to corrosively machine away selected areas for fabricating sheet metal components. This technique has several advantages such as inexpensive conventional process, accurately and economically producing highly complex parts with very fine detail, offering economical alternatives to laser cutting, inexpensive tools, quickly producing (it can make a part in hours after receiving the drawing), allowing for easy changes in mass production, applying on any commercially available metal or alloy, of any hardness and not creating sharp edges (*Yan, et al., 2003b, Wikipedia, 2009*).

The layout of the resonator was defined by the top pattern and the bottom was etched in a standoff distance for ease of mounting. The thickness of the substrate is 0.5mm with a standoff distance leaving the section of resonating element 0.25mm thick in order to allow the resonator to be mounted horizontally on a flat surface without affecting the vibration of the tines. The process of fabrication is illustrated in figure 2.49.

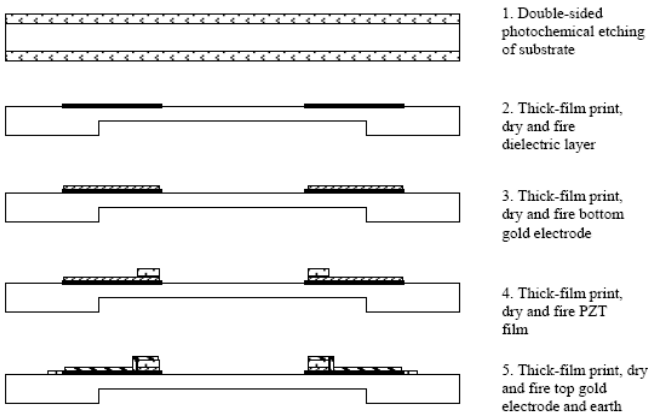

Figure 2.49 Schematic of resonator fabrication process (Yan, et al., 2004a).

Thick-film standard screen printing process is implemented to print the required material on the defined driving and sensing regions that have been predicted from FEA. This technology typically deposits thick layers of material between 50 μm and 100 μm when compared to the thin-film (1 μm and 3 μm) (*Yan, et al., 2003b)*. For this reason, it provides larger excitation forces and detection signals than alternative thin film piezoelectric materials because the magnitude of the piezoelectric element output depends on the piezoelectric properties of the deposited layer, its thickness and the magnitude of the stress generated by the applied measurand or the voltage applied for driving (*Yan, et al., 2003b and Yan, et al., 2004a)*. As a consequence, the piezoelectric properties of the thick film are also improved over the thin film.

In the thick-film screen printing process, the paste is spread over the surface of a patterned screen and a squeegee is drawn bringing it down into contact with the substrate by pressing the paste through the open areas in the screen. The screen snaps back to its original position as the squeegee passes, and the paste remains deposited on the substrate surface. The thick-film deposition process is demonstrated in figure 2.50.

The order for the printing process is as following: dielectric, bottom gold electrode, PZT film and top gold electrode layer with their own screens respectively. From the schematic of the fabrication process, the PZT layer is sandwiched between two electrodes thereby forming a capacitor structure for generating the piezoelectric behaviour. The widest layer on the substrate is dielectric, whilst the gold top electrode is smaller than the PZT pattern in all directions to prevent short circuit. The dielectric layer

was required to isolate the bottom electrode from the resonator substrate in order to enable polarization of the PZT layer (*Yan, et al., 2003b*).

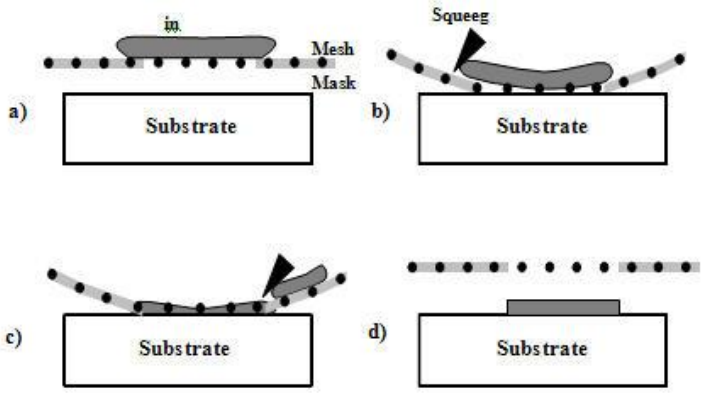

Figure 2.50 Thick-film deposition process.

For this resonator, a dielectric composition ink, ESL 8986, was used for the dielectric layer which has an approximate thickness of 25μm. A gold cermet ink, ESL 8836, was used for the bottom and top electrode layers with 25μm thickness for each layer. The PZT paste was prepared from 6μm average grain size, 95% PZT-5H powder, 5% lead borosilicate powder, and approximately 5ml ESL 400 organic vehicle per 20g powder mix. The lead borosilicate was used to bond the film to the substrate and also the active particle together. The purpose of the organic vehicle is to produce the correct viscosity of paste for printing. The thickness of PZT layer is approximate 50μm (*Yan, et al., 2003b*).

Next, the deposited substrate proceeds to the drying and firing process. An infra-red dryer is used to dry the printed film which retains a rigid pattern on the substrate at this stage and is immune to smudging so that another layer can be printed directly onto the dry film. The drying temperature is about 140°C. Then the printed film is fired on a belt furnace for 1 hour, being held at temperature of 850°C for 20min which has been found to sinter the particles adequately (Fig. 2.51). At this stage, the film is firmly attached to the substrate so that further screen-printed layers can be added as required (*Yan, et al., 2003b*).

After finishing the printing process, the next step is polarisation because the PZT is ferroelectric material that must be polarized in order to activate the piezoelectric behaviour of the PZT elements (*Beeby, 2004*). It is achieved by applying a strong electric field to the PZT elements at high temperature, where the individual micro crystals are partially aligned with the direction of the field (*Gautschi, 1936*). The polarization process is conducted by conventional electrically wire bonding, connecting the elements in parallel and poling them across the electrodes with a dc voltage up to 200 V for 1 hour at 130°C in order to align the dipoles within the PZT material and enable it to exhibit its piezoelectric properties. For the PZT layer thickness of 50 μm, an electric field of strength generated during the polarising process is 4 MV/m (*Yan, et al., 2003a*). The direction

of the resulting spontaneous polarization and the corresponding piezoelectric properties persist after the electric field is switched off (*Gautschi, 1936*). If a temperature exceeding the Curie point of the PZT is reached, its piezoelectric properties will be lost. Therefore, there is a temperature limit that the PZT can be exposed to. In addition, another effect that should be considered is the pyroelectric effect, where the piezoelectric coefficients of the PZT also vary with temperature (*Beeby, 2004*). The PZT is the most common commercially available piezoelectric ceramic for actuator and sensor applications because it exhibits very high piezoelectric coupling coefficients and can be used up to about 200°C (*Gautschi, 1936*).

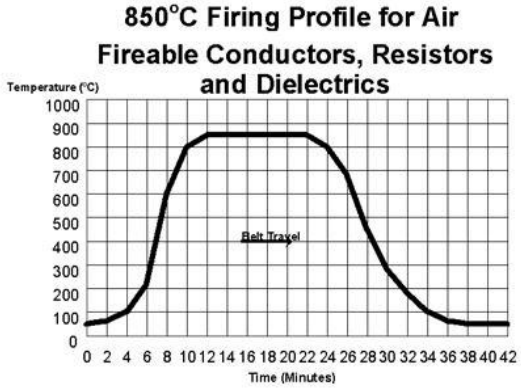

Figure 2.51 Firing cycle.

2.3.1.4 Resonator operation

After completing the polarisation process, each individual sensor will be cut from the steel sheet in order to investigate the resonator characteristics. At this stage, the appropriate method of cutting needs to be implemented in order to avoid inflicting damage to the resonators. Then, wires are connected from the bottom and top gold electrode at each end of the resonator for drive and pick-up mechanism via a low temperature, conventional soldering technique as indicated in figure 2.52.

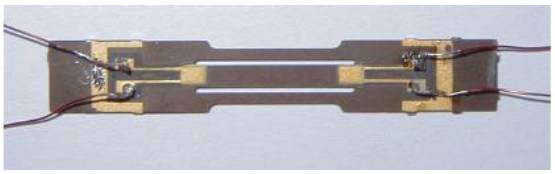

Figure 2.52 Photograph of the metallic resonator (Yan, et al., 2003b).

Open-loop configuration

Firstly, the resonator was tested in an open-loop configuration when it operated in air without any contact to any physical structure. The main objective of this testing is to observe the vibration modes and also confirm successful operation of the driving and sensing mechanisms of the PZT elements on the resonator.

In an open-loop system, a Hewlett-Packard 89410A Vector Signal Analyser was connected to the PZT element at one end of the resonator in order to drive a periodic chirp AC signal of 1 V peak-peak with the tracking generator scanning over one frequency range. The drive voltage

level affects the Q-factor of the resonator as decreasing drive voltage can increase the Q-factor and obscure the spurious modes so that the performance of the resonator is improved in terms of efficiency. The reason for this may be attributed to damping caused by high drive levels causing energy losses through acoustic and radiative heat by large amplitude of vibration of the tines (*Cheshmehdoost, 1992*). The output signal from the pick-up PZT element on the other end of the resonator was amplified using a Kistler Type 5011 charge amplifier and fed back to the Vector Signal Analyser in order to analyse the frequency response of the resonator as shown in figure 2.53.

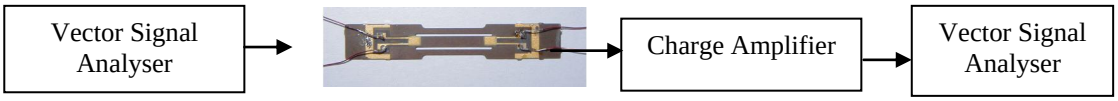

Figure 2.53 The open-loop configuration for testing the resonator.

The vibration mode of the resonator was shown in the frequency response wave form on the signal analyser as shown in figure 2.54. The highest peak is the dominant resonance of the resonator, which corresponds to the calculated third mode of vibration from the FEA simulations and the other resonances are visible at different frequencies but with much smaller amplitudes. The resonator acts as an electromechanical band-pass filter rejecting both mechanical and electrical noise at frequencies outside its resonant bandwidth (*Yan, et al., 2005a*). The blown-up inset is the third mode frequency response.

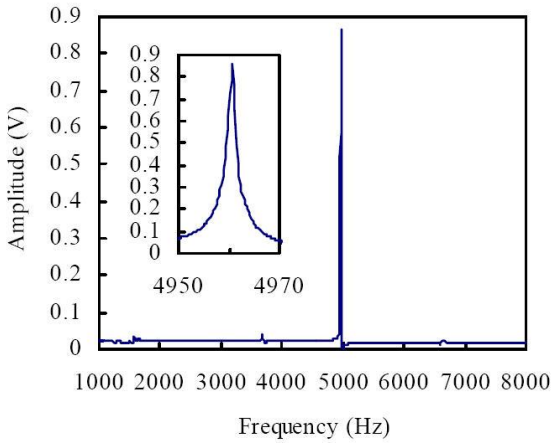

Figure 2.54 Amplitude-frequency response of the resonator (Yan, et al., 2003b).

The calculated Q-factor of the triple-beam resonator (>3000) is higher than the Q-factor of other resonating devices having different structures. For example, the Q-factor of the silicon single beam resonator with PZT thick-film drive/detection elements (*Beeby et al., 2001*) is only 70. A Q-factor of 400 was obtained for a silicon triple beam resonator with thin film drive and detection (*Yan, et al., 2003b*). Other published results show a Q-factor of 140 for a metallic double-beam-tuning-fork resonator with bulk PZT elements (*Barthod et al., 2003*) and a Q-factor of 740 for a metallic triple-beam-tuning-fork resonator with bulk PZT drive and detection

(*Randall et al., 1997*). A high Q-factor means good stability of operation and it is very important in closed-loop operation because it simplifies the feedback control electronics, gives better identification of resonant frequency resulting in a high resolution for measurement, better sensitivity, and also implies low losses of the vibration energy from the resonator to the external structure, thus requires low power to maintain the resonance (*Yan, et al., 2004b and Yan, et al., 2005a*).

Closed-loop configuration

The resonator was tested again in a closed-loop feedback configuration at atmospheric pressure as shown in figure 2.55. This time, the PZT sensing element was connected to a charge amplifier circuit, followed by a High-Pass (HP) filter used to eliminate mains current-noise, a phase-locked loop for maintaining the resonance, a digital 90-degree phase shift circuit for adjusting the right phase relation between the pickup and the drive, a Low-Pass (LP) filter introduced to change the square wave to a sine wave to drive the resonator, and a second stage of amplification, all on one circuit board. As a consequence, the drive PZT element was fed back by the output signal from the second stage amplification to maintain the frequency resonance in the required favourable mode of oscillation.

From a closed-loop operation, the direct digital frequency output of the resonator was acquired as shown in figure 2.56.

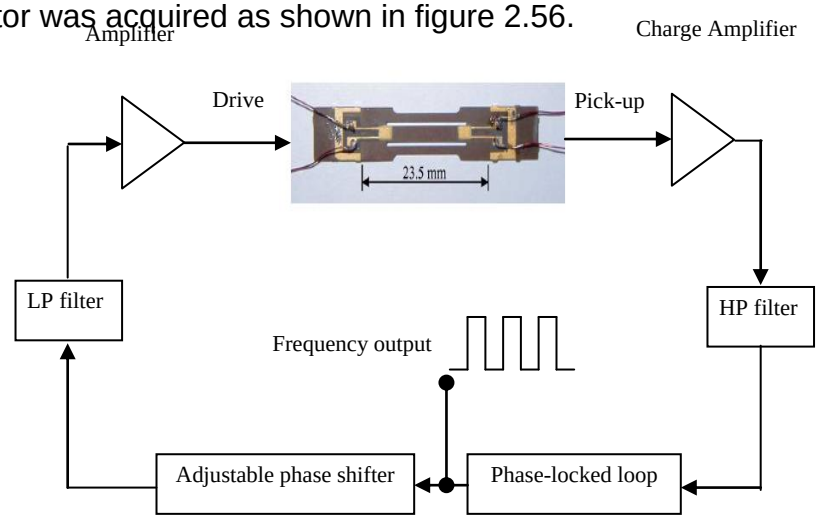

Figure 2.55 A feedback closed-loop configuration.

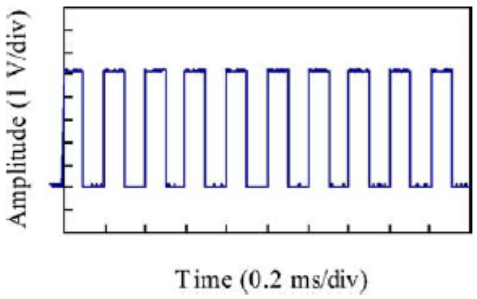

Figure 2.56 Frequency output of the resonator in closed-loop (Yan, et al., 2003b).

An alternative design with mounting holes at the ends was also demonstrated by Yan, et.al. as illustrated in figure 2.57a (*2004b*). This device was also fabricated from the same material and same etching process as the previous two designs but with both top and bottom masks to pattern the resonator layout in order to yield a symmetric profile for the resonator edges. The holes were incorporated for mounting the resonator to the sensing structure by bolts directly. This design shows that no other resonances in the applied frequency range appear due to the effective design of the resonator (Fig. 2.57b).

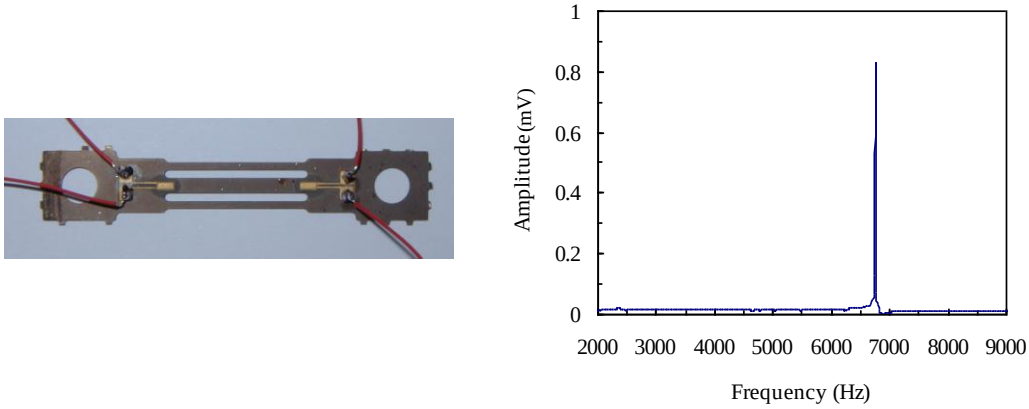

(a) Sensor with mounting hole (b) Response curve

Figure 2.57 Metallic TBTF resonator with holes at the ends (Yan, et al., 2004b).

2.3.1.5 Advantages

The presented resonator has shown a good mode selectivity with a high Q-factor (about 3100) operating in air when compared with other reported resonators of similar structures, which leads to high sensitivity and low power consumption (*Yan, et al., 2003a*, *Yan, et al., 2004a*). The combination of the two batch-fabrication processes, photochemical etching and screen printing, provides the opportunity for this device to be easily mass-produced at low cost for use in a wide range of measuring systems, e.g. load cell, weighing machines, torque transducers and pressure sensors. (*Whitehead, et al., 1997, Yan, et al., 2003b*, *Yan, et al., 2004a*)

The new resonator can be used on stiff structures, have high overload capacities, low power consumption, frequency output for digital processing, and offer prospects for wireless-batteryless operation (*Whitehead, et al., 1997, Yan, et al., 2004b*). According to their frequency output signal, these devices are also easily integrated into digital systems without analogue-to-digital conversion, having higher resolution than alternative strain gauge sensors, having good long-term stability because it is not dependent on the amplitude of the electrical signals, and immune to noise (*Yan, et al., 2004b, Beeby, et al., 2004*).

2.3.2 Metallic TBTF-based Torque Transducers

For many years metallic resistance strain gauges have been used as the principal sensors for measuring torque on a shaft. Torque transducers based on metallic resistance strain gauges can seldom withstand overloads of more than double the rated full-range torque (*Fleming, 1982*). Despite the small signal outputs, the mounting of strain gauges is normally labour intensive. A new torque transducer was proposed using metallic TBTF resonant sensor with thick-film PZT drive and pickup elements. (*Yan, et al., 2005a*).

To apply the metallic TBTF resonator torque measurement, two resonators are spot-welded on the shaft machined from 17-4PH stainless steel, which is the standard torque shaft material for many torque applications, at ±45° relative to the axis of the shaft on either side of the shaft and the resonators are perpendicular to each other. Two square blocks with grooves at 45° to the axis of the shaft were introduced in order to mount TBTF resonators on these surfaces. The resonators can be bonded to the sensor structures using laser welding, mechanical fixing, for example by bolt and screw, or appropriate glue (*Yan, et al., 2004b*). Figure 2.58 shows the configuration of torque transducer based on this metallic TBTF resonator according to Yan, et al. (*2005a*).

When the torque is applied to the shaft, the principal shear stresses occur at 45° to the axis of the shaft. The compressive stress exists in one direction while in another direction detects tension stress. However, two resonators presented here are only mounted along the tensile direction, therefore TBTF torque transducer in this measurement can measure torque in one direction (*Yan et al., 2005a*).

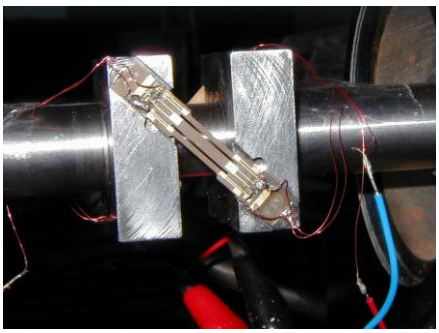

Figure 2.58 Torque transducer with TBTF metallic resonators (Yan et al., 2005a).

The response of the torque transducer is shown in figure 2.59 which is from one of the two resonators when applying torque up to 20 Nm with 2 Nm steps for 5 cycles. The variability in the fabrication of the resonators and in mounting arrangements results in the difference of the load sensitivity from one resonator to another one (*Yan, et al., 2005a*). The condition in the test room was heated up to 28.5°C and then cooled down naturally to 23.8°C in order to investigate the temperature effect to the resonators. Consequently, the temperature coefficients have been evaluated in a temperature range from 23°C to 29°C. The frequencies

and temperatures were recorded at the same time in this experiment. The experimented TBTF typical characteristics from the resonator with the highest sensitivity are summarized in Table 2.3.

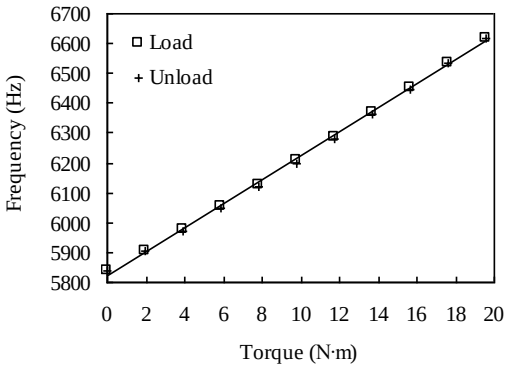

Figure 2.59 Response of one TBTF torque transducer (Yan et al., 2005a).

Table 2.3 Typical characteristics of experimented TBTF torque transducer (Yan et al., 2005a).

Initial frequency	5837 Hz
Sensitivity	40 Hz/Nm
Applied torque range	0-20 Nm (f.s.)
Stability	0.03% (of f.s.)
Repeatability	0.1% (of f.s.)
Hysteresis	1.2% (of f.s.)
Non -linearity	2.1% (of f.s.)

2.3.3 Demonstrated Feasibility

Even though most characteristics of TBTF torque transducer are considered, it is still insufficient to justify the performance of this torque transducer for implementation as the torque transfer standard according to the national standard. There are many parameters or factors that should be strictly paid attention to such as the method used to investigate the torque transducer, the equipment used in obtaining the data, the environmental condition during the measurement, the measurement parameters that should be considered, and the calculation method of these parameters.

Considering the method used to investigate the performance of the torque transducer by Yan et al, (*2005a*), it did not conform to the national standard method applied for verifying a torque measuring device. The equipments used in the measurement have to be standard level and have reliable accuracy. During the measurement, the environmental condition should be controlled according to the standard. Moreover, the parameters that will be determined should be sufficient to evaluate the performance of the torque transducers. Finally, the calculation method of each parameter should be standard and include the uncertainty calculation which is the most important value in measurement.

Apart from the above reasons, many industries require small sensors in their applications. As a result, the challenge has been to reduce the size of the metallic TBTF resonant sensors in order to meet their requirements while maintaining the accuracy of the sensors. In addition, miniaturisation of the sensors also provides more benefit in terms of reducing the cost of fabrication.

The detail of miniaturisation and calibration of the metallic TBTF resonant sensors will be demonstrated and discussed in the following chapter.

Chapter 3

3. Torque

This chapter will be devoted to the topic of torque, which is the quantity of interest in this research work. The theory and background understanding of torque will be discussed first, then several torque measurement methods will be described. Torque measuring systems will be considered next. Lastly, calibration of torque transducers and instruments, which is the main focus of this research will be explained.

3.1 Torque Measuring System

A torque measuring system is represented in figure 3.1. It consists of a transducer which is a device converting the desired measured value into a convenient form of signal, such as an electrical signal, a display which is an instrument used to interpret the signal to the observer, and a means of transmitting the signal from the transducer to the observer. When considering the word 'transducer', some authorities refer to devices with an electrical output whilst non-electrical devices are referred to 'primary element' or 'measuring element' (*Bass, 1971*).

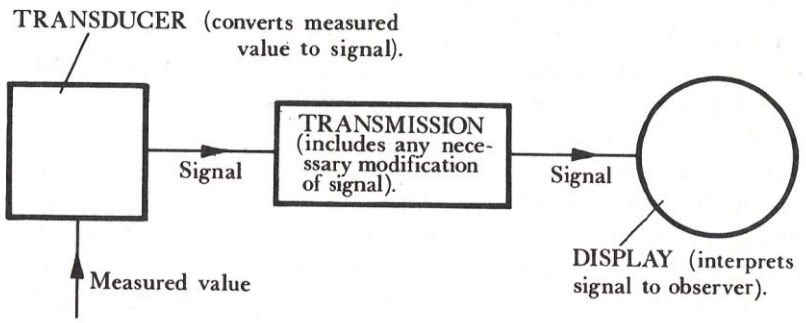

Figure 3.1 Generalized measuring system (Bass, 1971).

Conveniently, the measuring systems can be regarded as shown in figure 3.2. If the box represents the whole system of figure 3.1, the input quantity is the measured value or the measurand, and the output is the response observed from the display (*Bass, 1971*).

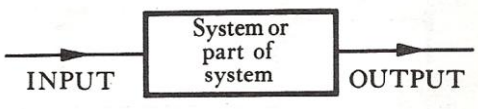

Figure 3.2 Measuring system box (Bass, 1971).

The measured valued shown on the indicator is an analogue or a digital display. The latter one requires less concentration of the observer, since the measurement can be read directly as a number. The measuring equipment enables the user to make measurements with greater accuracy (*Bass, 1971*).

There are two systems for measuring torque; static and dynamic systems. Static measuring system is when the torque transducers are installed on fixed shafts. Dynamic system uses torque transducers installed on rotating shafts. It is more difficult to transmit the electrical signal from the rotating shaft to a stationary instrument station in dynamic measurement.

Torque transducers or torque cells are devices converting an applied torque into an electrical output signal. They consist of measuring body and a sensor (*Dally, et al., 1993*). The structure of each torque transducer can be different in the form of signal transmission and measuring body design (*Schicker and Wegener, 2002*).

3.1.1 Measuring Body Designs

There are several kinds of measuring body shapes commonly in use at the present time; solid, hollow, square-section, spokes and cages as shown in figure 3.3. Importantly, their surfaces where strain occurs due to torque must be smooth for mounting sensors (*Schicker and Wegener, 2002*).

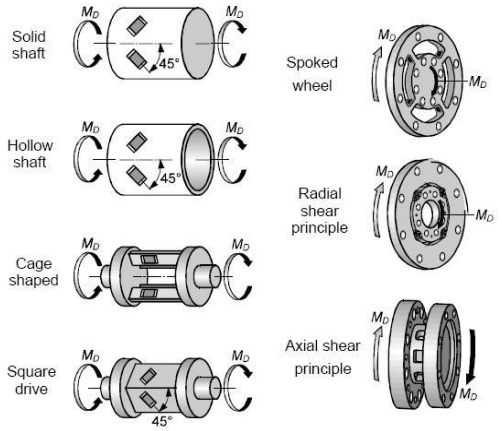

Figure 3.3 Commonly used measuring body shapes (Schicker and Wegener, 2002).

3.1.2 Measurement Signal Transmission

There are two ways of supplying power and transmitting the measurement signal generated on the rotor in the case of using strain gauges. They are transmission via slip rings and contactless transmission (*Schicker and Wegener, 2002*).

3.2 Torque Measurement Methods

There are several methods used to measure torque. They are calculating torque from electrical power, measuring reaction torque, and measuring in-line torque. The first method is related to the determinations of the

power developed or absorbed by rotating machinery. The latter two methods use force or torque transducers to obtain the torque value.

3.2.1 Calculation from Electrical Power

Torque can be calculated from equation 2.2, if the electrical power and the shaft speed are known as already discussed in Chapter 2 (*Schicker and Wegener, 2002*).

3.2.2 Measuring Reaction Torque

The principle of this method is that in-line torque equals to reaction torque and it is a method frequently used to determine power (*Schicker and Wegener, 2002*). There are two techniques to measure reaction torque by using either force transducer or torque transducer.

3.2.2.1 Measuring the reaction force on a lever arm

Considering the motor M delivering an output torque (T_o) as indicated in figure 2.10, a reaction torque (T_o') occurred to the motor casing is measured more easily than the torque T_o in the shaft. The force (F) acting on the lever arm at distance r is measured by any force-measuring methods and used to calculate torque as in equation 2.1.

3.2.2.2 Reaction torque transducers

Figure 3.4 is an example using this technique. For this application, the torque transducer used to measure the reaction torque is directly located between the motor housing and the container (*Schicker and Wegener, 2002*).

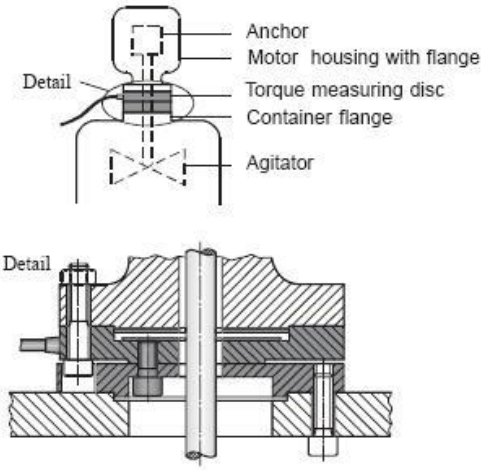

Figure 3.4 Viscosity measurement based on reaction torque measurement (Schicker and Wegener, 2002).

3.2.3 Measuring In-line Torque

The configuration of the in-line torque measurement is shown in figure 3.5. The torque transducer used to measure torque is based on several principles that will be discussed next.

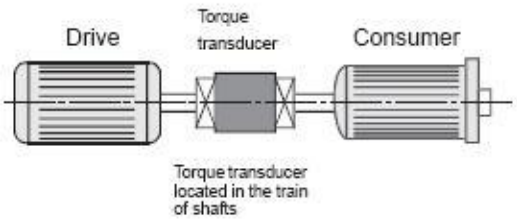

Figure 3.5 The in-line torque measurement configuration (Schicker and Wegener, 2002).

3.2.3.1 Measuring strain methods

An example of using torque transducers attached to the shaft surface for measuring torque by directly detecting strain occurring in the shaft is shown in figure 3.6. Four strain gauges are positioned at 45° to the axis of the shaft in order to experience the tensile and compressive principle strains produced by torque. The output of the strain gauges is in electrical form and it will be changed proportional to the applied torque (*Bass, 1971*, *Collett and Hope, 1974*).

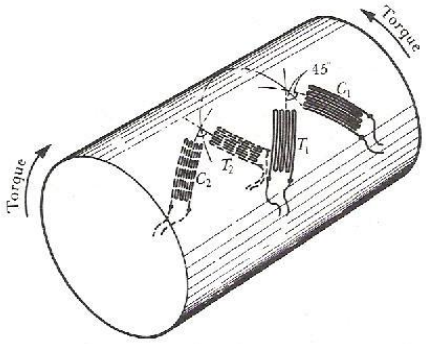

Figure 3.6 Torque measurement by strain gauges (Bass, 1971).

The previous method requires fitting the torque transducers onto the shaft. The magneto-strictive method is an alternative way that operates without any attachments or modification to the shaft as already discussed in figure 2.4, Chapter 2.

3.2.3.2 Deflection of elastic elements methods

This method (Fig. 3.7) is more common and indirectly measures strain by determining the relative angular deflection (θ) of a parallel length of shaft at some distance apart (l). The torque in the shaft can be computed from the shaft twisting equation 2.3 (*Bass, 1971, Adams, 1975*).

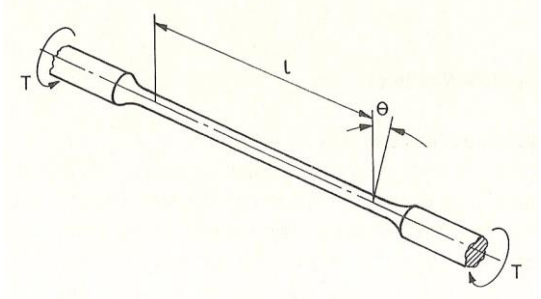

Figure 3.7 Deflection of elastic elements (Adams, 1975).

In the case of a torque wrench as shown in figure 3.8, the bending of the bar OP gives a deflection of the pointer Q on OP relative to the scale AB when the torque is applied. Torque value will be calculated from the following formula:

$$T = F(l + r) \tag{3.1}$$

where T is torque value
F is force acting on the handle of the torque wrench
l is the torque wrench length
r is the radius of the boss at O

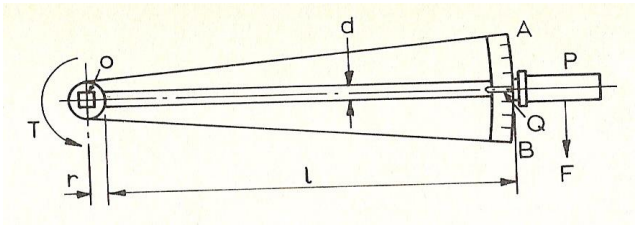

Figure 3.8 Obtaining torque value in the case of torque wrench (Adams, 1975).

3.3 Calibration of Torque

In order to ensure that the transducers still work accurately and their sensitivities have not changed with time they must be calibrated periodically (*Dally, 1993*). This requirement is required for every company wishes to be certified to ISO 9000 (*Schicker and Wegener, 2002*).

Calibration is the process of determining the relationship between the measured value of the output quantity and the input quantity (*Schicker and Wegener, 2002*). This can be done by comparing the indicated readout of a measuring system with a known input values from the reference standard, or a standard with a higher-grade standard (*Bass, 1971*). The reasons of calibrating the measuring instruments are: to ensure readings from the instrument are consistent with other measurements, to determine the accuracy of the instrument readings, and to establish the reliability of the instrument (*Howarth and Redgrave, 2003)*. The accuracy of the measuring instrument should be checked at frequent intervals (*Sirohi and Dadha, 1991*). Figure 3.9 is a block diagram of a typical calibration arrangement.

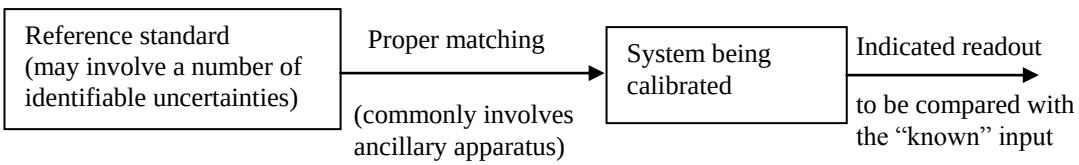

Figure 3.9 Block diagram showing calibration procedure (Beckwith, Marangoni and Lienhard, 1993).

3.3.1 Calibration Procedure

For calibration, there are five kinds of calibration procedure which are primary calibration, secondary calibration, direct calibration with known input source, indirect calibration, and routine calibration (*Nakra and Chaudhry, 1985*).

3.3.1.1 Primary calibration

Primary calibration is the procedure that a device or system is calibrated against primary standards. That device is employed as a secondary calibration device after primary calibration (*Nakra and Chaudhry, 1985*).

3.3.1.2 Secondary calibration

Secondary calibration is termed for a procedure that a secondary calibration device is used to calibrate another device of lesser accuracy (*Nakra and Chaudhry, 1985*).

3.3.1.3 Direct calibration

Direct calibration with known input source procedure gives the same order of accuracy as primary calibration. Therefore, devices that are calibrated by this method can be used as secondary calibration devices (*Nakra and Chaudhry, 1985*).

3.3.1.4 Indirect calibration

Indirect calibration uses two different devices to measure a certain physical quantity and see the equivalence of them (*Nakra and Chaudhry, 1985*).

3.3.1.5 Routine calibration

Routine calibration is used to check the accuracy and proper functioning of an instrument periodically. The known standards that can be accurately reproducible are used in this procedure (*Nakra and Chaudhry, 1985*).

3.3.2 Standards

A primary standard, or a secondary standard, or a known input source can be employed for comparison and it must possess an accuracy at least ten times higher than the instrument to be calibrated (*Sirohi and Radha, 1991*).

The standard used in calibration has to be checked against a standard of higher grade, which itself has been calibrated in unbroken chain of comparisons to the appropriate national standard (*Bass, 1971, Schicker and Wegener, 2002*). This process is called traceability and is illustrated in figure 3.10. The aim of the traceability is to ensure that the measurement result or the value of a standard is correct (*Schicker and Wegener, 2002*).

In the UK, the National Physical Laboratory (NPL) is the organization which is charged with the care and maintenance of UK national

standards, and also carries out calibration checking against primary standards (*Bass, 1971*).

There are different types of standards and they can be classified as international standards, primary standards, secondary standards, and working standards according to their function and type of application (*Nakra and Chaudhry, 1985*).

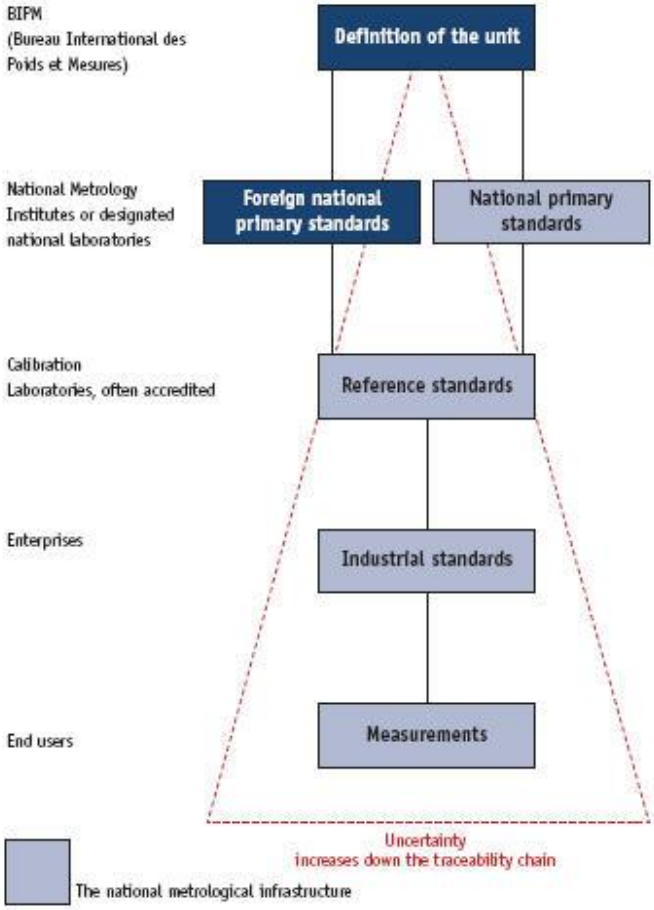

Figure 3.10 The traceability chain (Howarth and Redgrave, 2003).

3.3.2.1 International standards

International standards represent the highest possible accuracy and they are not available to an ordinary user for purposes of day-to-day comparison and calibrations (*Nakra and Chaudhry, 1985*). These standards are maintained at the International Bureau of Weights and Measures at Sevres near Paris (*Renganathan, 1999*).

3.3.2.2 Primary standards

Primary standards are maintained by National standards laboratory in different parts of the world and not available for use outside the national laboratories (*Renganathan, 1999*). They are used to calibrate or verify and certify secondary reference standards not for working standards (*Nakra and Chaudhry, 1985*).

3.3.2.3 Secondary standards
Secondary standards are maintained by the a particular laboratory and used as basic reference standards in different laboratories. They are easily accessible to the ordinary user for checking and calibration of working standards (*Nakra and Chaudhry, 1985 and Renganathan, 1999*).

3.3.2.4 Working standards
Working standards are commercial devices with high accuracy that are checked and certified against either the primary or secondary standards. They are widely used for calibrating general laboratory instruments, carrying out comparison measurements, or checking the quality of products (*Nakra and Chaudhry, 1985*).

3.3.3 Torque Calibration

In torque measurement, it is related to force measurement so torque standards are not necessary. Force and length standards are sufficient to define torque (*Doebelin, 1966*).

Torque transducers can be calibrated by using testing machine, deadweight machine, force reference transducers or transfer transducers with lever arm, or torque reference transducers or transfer transducers (*Dally, 1993*, *Schicker and Wegener, 2002*).

Using testing machine
The testing machine is used to apply load to the torque transducer mounted in the machine. The comparison is made between the output from the transducer and the load indicated by the testing machine (*Dally, 1993*).

Using deadweight machine
This technology is based on the lever-arm-mass system and is currently widely used in all calibration laboratories at the present time for the high and highest level of accuracy (*Schicker and Wegener, 2002*). The known input is provided by a calibrated standard weights applied to the end of a stiff beam which is directly connected to the transducer. This mechanism acts as the moment arm. Consequently, the resulting torque can be computed by multiplying the load force by the length of the moment arm. In this case, the exact length of the arm from the center of rotation to the suspension point of the deadweight must be known. Moreover, the hanging weights must be normal to the beam (*Herceg, 1976*). The output from the transducer is then compared with the known input (*Dally, 1993*).

This method presents some difficulties regarding to the design of the machine. Firstly, the standard weight used in this machine is dependent on the earth's gravitational field which varies with location and altitude so the local acceleration in calibration laboratories must be known (*Dally, 1993, Schicker and Wegener, 2002*).

Secondly the lever arm must be aligned precisely horizontally in order to quantify the length accurately (*Schicker and Wegener, 2002*).

Furthermore, the beam must be extremely stiff in order to prevent the deflection from hanging weights. However, the beam could contribute significant effective weight, thus a spurious torque must be counteracted by an equivalent torque in the opposite direction. Two identical arms attached to the torque transducer 180° apart, which produce equal weights suspended from each arm, are used to overcome this disadvantage (*Herceg, 1976*).

Using force reference transducers or transfer transducers
This method combines a force reference transducer or transfer transducer with a lever arm system (*Schicker and Wegener, 2002*).

Using torque reference transducers or transfer transducers
Utilising two transducers connected in series can be employed if the testing machine is not available. One transducer is a standard and the other one is the calibrated transducer. The torque reference transducer is used to provide the reference torque which can be generated by any mechanism. This generated torque is measured with the torque transfer transducer or reference transducer (*Schicker and Wegener, 2002*). The comparison is made between the output from the calibrated transducer and the load indicated by the torque reference transducer (*Dally, 1993*). The reference transducer must be more accurate than the desired smallest measurement uncertainty of the transducer being calibrated in order to acquire the high degree of precision (*Schicker and Wegener, 2002*).

The difference between a reference transducer and a transfer transducer used in torque calibration can be determined from the role of the transducer plays when the measured quantity is transferred into the application.

A reference transducer is used to directly calibrate the transducer remains in the test bench. It transfers torque value to a transducer by reproducing its reference torque from calibration (*Schicker and Wegener, 2002*).

A transfer transducer is used to transfer its calibrated reference torque from the national standard to a reference standard, then to working standards such as calibration devices or another measuring device or application. This torque transfer transducer has been calibrated only in the laboratory (*Schicker and Wegener, 2002*).
3.3.3.1 Standard method for the calibration of torque measuring devices
British Standard BS 7882:1997 was the first standard document about the method for the calibration and classification of torque measuring devices. The latest update version is BS 7882:2008. There are also a German standard DIN 51309:2005 which was published in 1998 and a Chinese calibration standard JJG995:2005. At the moment, a British standard BS

7996 is being written for continuous calibration of torque measuring devices (*Pratt, 2008*).

When compared between BS 7882:2008 and DIN 51309:2005, they use the same classification system but there is much more work involved in a calibration to DIN 51309 which increases the calibration time (*Pratt, 2008*). In this project, the British standard BS 7882:2008 will be used as the standard method and the detail will be mentioned.

The scope of the British Standard BS 7882:2008 is to specify requirements for the calibration and classification of torque measuring devices. The method of calibration, calculation of the results, calculation of uncertainties, and the classification of torque measuring devices in static mode are described in this standard.

3.3.3.2 Preliminary procedure

Reference standard used in torque calibration shall conform to Table 3.1. All definitive measurements, such as mass, length, time and temperature shall be traceable to national standards.

Table 3.1 Uncertainty of calibration torques

Class of torque measuring device to be calibrated	Maximum permissible uncertainty of calibration torque applied [A)] %
0.05	±0.01
0.1	±0.02
0.2	±0.04
0.5	±0.10
1.0	±0.20
2.0	±0.40
5.0	±1.00

[A)] Using a coverage factor of k = 2 to give a confidence level of approximately 95%

An ambient temperature of torque calibration should be within the range 18°C to 28°C and shall not vary by more than ±1°C during calibration. Before commencing the calibration, all torque measuring devices and associated components of the torque measurement system, and all parts of the equipment used in calibration shall be allowed for temperature stabilization. In this case, a thermometer is placed close to the reference torque measuring device and the calibrated torque measuring device. The temperature at the beginning and end of each measurement series should be recorded. After switching on the electrical torque measuring devices and associated components, they shall be allowed to warm-up for the period stated by the manufacturer or at least 15 minutes in case of no recommendation.

The lower limit of calibration ($T_{\min}$) must be determined in order to ensure that the classification is consistent with the resolution of the torque indicator (r). It is calculated from the equation 3.2.

$$T_{\min} = a \times r \tag{3.2}$$

where a is the constant value according to the class of the torque measuring device and has the following values:

- 4000 for a class 0.05 torque measuring device
- 2000 for a class 0.1 torque measuring device
- 1000 for a class 0.2 torque measuring device
- 400 for a class 0.5 torque measuring device
- 200 for a class 1.0 torque measuring device
- 100 for a class 2.0 torque measuring device
- 40 for a class 5.0 torque measuring device.

The resolution of the indicating device shall be converted to units of torque. The calibration shall not be performed below this lower limit.

The calibration range is selected at least five approximately equally spaced, increasing values of torque from 20% to 100% of maximum applied torque. If the calibration is required below 20%, the steps of 10%, 5%, and 2% of maximum applied torque may be used but they must be greater than the calculated lower limit of the calibration range.

If a torque measuring device requires the measurement of both increasing and decreasing values of torques, a single series of decreasing values (the same value as increasing values) is applied at the end of the last series of increasing torques.

The torque measuring device shall be calibrated in either three different mounting positions (each rotated 120° about the measurement axis), or in four different mounting positions for the transducers with square drives (each rotated 90° about the measurement axis) for classes 0.05 and 0.1. For all other classes, the device shall be calibrated at least two different mounting positions at least 90° apart.

Figure 3.11 – 3.16 show examples for the calibration of torque measuring devices according to type of torque measuring device and class.

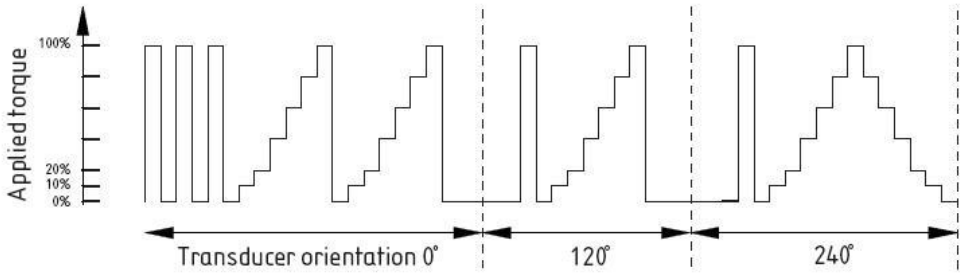

Figure 3.11 Example of preloading and calibration sequences for a torque measuring device with round shaft drives, six increasing and decreasing torques, classes 0.05 to 5.0.

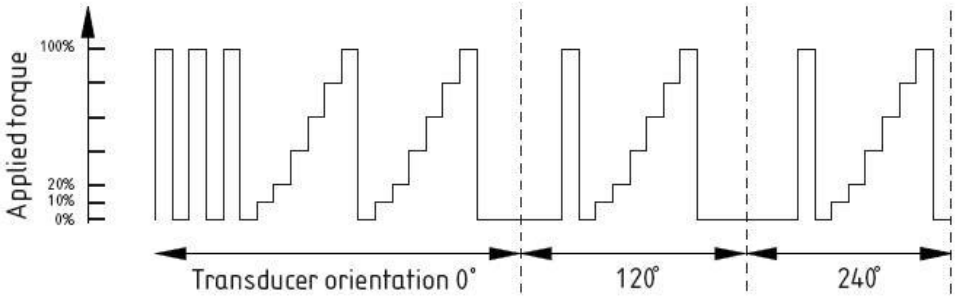

Figure 3.12 Example of preloading and calibration sequences for a torque measuring device with round shaft drives, six increasing torques only, classes 0.05 to 5.0.

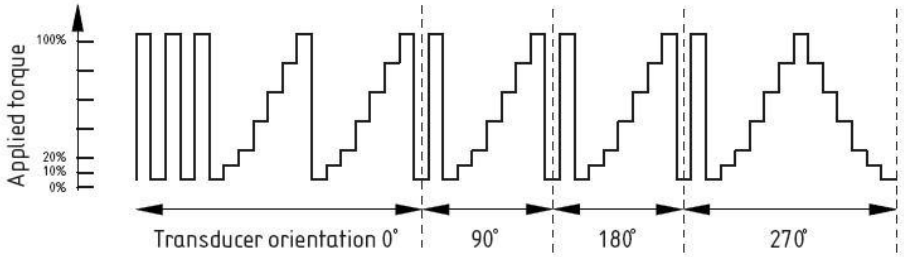

Figure 3.13 Example of preloading and calibration sequences for a torque measuring device with square drives, six increasing and decreasing torques, classes 0.05 to 5.0.

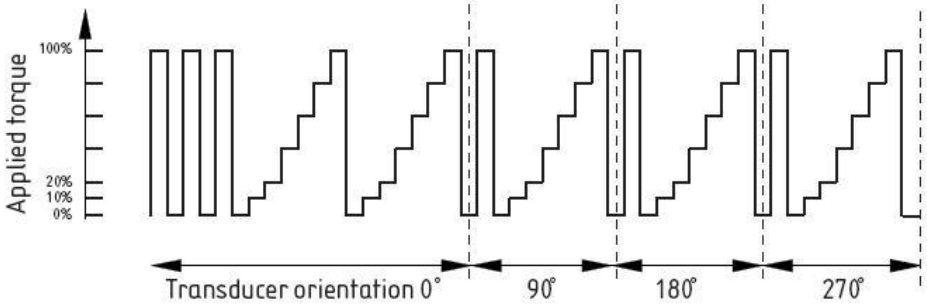

Figure 3.14 Example of preloading and calibration sequences for a torque measuring device with square drives, six increasing torques only, classes 0.05 to 5.0.

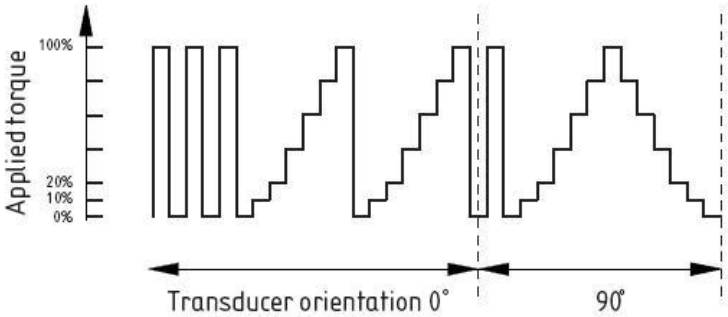

Figure 3.15 Example of preloading and calibration sequences for a torque measuring device, six increasing and decreasing torques, classes 0.2 to 5.0.

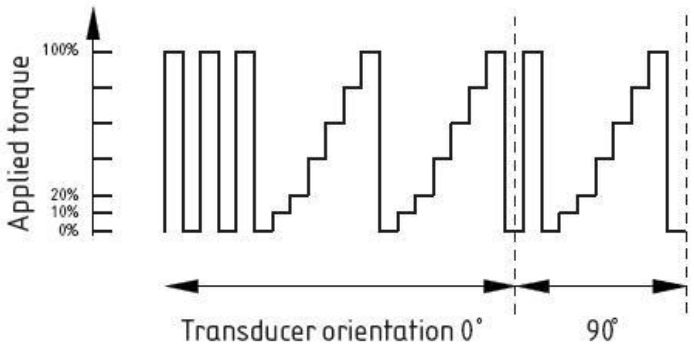

Figure 3.16 Example of preloading and calibration sequences for a torque measuring device, six increasing torques only, classes 0.2 to 5.0.

The torque measuring device should be preloaded at least three times in succession to the maximum applied torque before calibration in order to warm-up the mechanisms of torque measuring system.

3.3.3.3 Calibration procedure

3.3.3.3.1 After preloading, apply two series of increasing torques (at least five values) to the torque measuring device in required direction (clockwise or anti-clockwise) without change of the mounting position.

3.3.3.3.2 Record the reading of the indicator after each application or removal of a torque. The interval between successive application and removal of torques shall be as uniform as possible. The indicator reading may be tared to zero at the beginning of each measurement series.

3.3.3.3.3 Record the readings of the indicator with zero torque applied to the torque measuring device before and after each application of a series of torques. For the determination of relative residual deflection, record the residual deflection reading after the torque is completely removed.

3.3.3.3.4 Change the mounting position of the torque measuring device according to its class and type. After that, preload the torque measuring device once to maximum applied torque then apply a further series of increasing torques.
3.3.3.3.5 Repeat 3.4.3.3.2 and 3.4.3.3.3 at all required orientations.

3.3.3.3.6 Where relative reversibility is required, a single series of decreasing values shall be applied at the end of the last series of increasing torques.

3.3.3.4 Calculation of results

3.3.3.4.1 Determination of deflection (d)
Deflection is the subtraction of the indicator reading for the initial zero torque from the indicated reading for each applied torque and the final zero torque in the measurement series.

3.3.3.4.2 Determination of relative repeatability (R_1)

Relative repeatability is the closeness of the agreement between the results of two successive measurements from the same applied torque, carried out under the same conditions of measurement. Repeatability (the difference between series 1 and 2) is expressed as a percentage of the mean deflection for the first and second series of applied torque as shown in equation 3.3 for each value of increasing torque.

$$R_1 = \frac{(d_1 - d_2)}{\bar{d}_{R1}} \times 100 \qquad (3.3)$$

where:

$\bar{d}_{R1}$ is the mean deflection for a given torque which can be obtained from equation 3.11;

d_1 and d_2 are the deflections for a given increasing torque (series 1&2).

$$\bar{d}_{R1} = \frac{d_1 + d_2}{2} \qquad (3.4)$$

3.3.3.4.3 Determination of relative reproducibility (R_2)

Relative reproducibility is the closeness of the agreement between the results of successive measurements from the same applied torque, carried out under changed conditions of measurement. For each value of applied increasing torque, the reproducibility is calculated from equation 3.5 and expressed as a percentage of the mean indicated deflection for the given torque.

$$R_2 = \left[\frac{(d_{\max} - d_{\min})}{\bar{d}_{R2}} \right] \times 100 \qquad (3.5)$$

where:

R_2 is the relative reproducibility;

$d_{\max}$ is the maximum deflection for a given increasing torque from all series;

$d_{\min}$ is the minimum deflection for a given increasing torque from all series;

$\bar{d}_{R2}$ is the mean deflection calculated from the first series at each orientation.

The value of $\bar{d}_{R2}$ has different value depending on the number of orientations as follows:

a) for two orientations

$$\bar{d}_{R2} = \frac{d_1 + d_3}{2} \qquad (3.6)$$

b) for three orientations

$$\bar{d}_{R2} = \frac{d_1 + d_3 + d_4}{3} \quad (3.7)$$

c) for four orientations

$$\bar{d}_{R2} = \frac{d_1 + d_3 + d_4 + d_5}{4} \quad (3.8)$$

where:
d_1, d_3, d_4, d_5 are the deflections for a given increasing torque from the first series at each orientation.

3.3.3.4.4 Determination of relative error of interpolation (E_{it})
Relative error of interpolation (E_{it}) is the difference between the value of the mean deflection for a given value of increasing torque and the corresponding calculated value of deflection for the given torque which is obtained from a mathematically fitted curve. This value is only determined where the deflection is expressed in other units than torque. At each increasing calibration torque, it is calculated and expressed as a percentage of the computed deflection for the given increasing torque using equation 3.9.

$$E_{it} = \left[\frac{\left(\bar{d}_{R2} - d_{comp} \right)}{d_{comp}} \right] \times 100 \quad (3.9)$$

where:
E_{it} is the relative error of interpolation;
d_{comp} is the computed deflection for the given increasing torque.

3.3.3.4.5 Determination of relative residual deflection (R_0)
Relative residual deflection (R_0) is the maximum residual deflection obtained from all the applied series of torques. It is expressed as a percentage of the mean indicated deflection at maximum applied torque by using equation 3.10.

$$R_0 = \frac{d_{0\max}}{\bar{d}_{R2\max}} \times 100 \quad (3.10)$$

where:
R_0 is the relative residual deflection;
$d_{0\max}$ is the maximum residual deflection;
$\bar{d}_{R2\max}$ is the mean deflection at maximum applied torque.

3.3.3.4.6 Determination of relative reversibility (R_3)
Relative reversibility (R_3) is the difference between the deflection obtained from the last given torque series applied in an increasing mode and the deflection obtained from the same given torque applied in a decreasing mode. This relative reversibility is expressed as a percentage of the deflection for the given torque from the last applied series of torques, applied in an increasing mode as shown in equation 3.11.

$$R_3 = \frac{\left(d_{dec} - d_{inc}\right)}{d_{inc}} \times 100 \qquad (3.11)$$

where:
R_3 is the relative reversibility;
d_{inc} is the deflection for the application of the last series of a given increasing torque;
d_{dec} is the deflection for the application of the corresponding decreasing torque.

3.3.3.4.7 Determination of relative error of indication (E_i)
Relative error of indication (E_i) is the error of indication and it is only determined where the deflection is in units of torque. It is the mean indicated deflection for a given value of increasing torque minus the corresponding value of applied torque. equation 3.12 is used to calculate this value in percentage of the true value of applied torque.

$$E_i = \frac{\bar{d}_{R2} - T_a}{T_a} \times 100 \qquad (3.12)$$

where:
E_i is the relative error of indication;
T_a is a given increasing calibration torque.

3.3.3.5 Classification of torque measuring devices
The calibration results are analysed and compared with Table 3.2 in order to establish the devices classification. At each calibration torque, the values calculated for each parameter shall not exceed the value given in Table 3.2 for the selected classifications. There are 7 classes of the devices to be classified according to the accuracy. Class 0.05 is the highest performance, and class 5 is the lowest.

If the deflection is expressed in units of torque and increasing torques have been applied, the classification shall be determined from relative repeatability, relative reproducibility, relative residual deflection, and relative error of indication. If the deflection is expressed in other units, the relative error of interpolation is used in the classification instead of the relative error of indication. The relative reversibility parameter shall be determined in addition if decreasing torques have also been applied. The

overall class of the device is determined from the lowest performing parameter.

Table 3.2 Criteria for classification of torque measuring devices

Class	Maximum permissible values of the torque measuring device (%)					
	R_1	R_2	E_{it}	R_0	R_3	E_i
0.05	± 0.025	± 0.05	± 0.025	± 0.01	± 0.062	± 0.025
0.1	± 0.05	± 0.10	± 0.05	± 0.02	± 0.125	± 0.05
0.2	± 0.10	± 0.20	± 0.10	± 0.04	± 0.250	± 0.10
0.5	± 0.25	± 0.50	± 0.25	± 0.10	± 0.625	± 0.25
1.0	± 0.50	± 1.00	± 0.50	± 0.20	± 1.250	± 0.50
2.0	± 1.00	± 2.00	± 1.00	± 0.40	± 2.500	± 1.00
5.0	± 2.50	± 5.00	± 2.50	± 1.00	± 6.250	± 2.50

3.3.3.6 Uncertainty of the calibration results

In torque calibration, there are about 8 uncertainty contributions as follows:

u_1 - the standard uncertainty associated with the calibration torque;

u_2 - the standard uncertainty associated with the reproducibility of the device;

u_3 - the standard uncertainty associated with the repeatability of the device;

u_4 - the standard uncertainty associated with the resolution of indicator;

u_5 - the standard uncertainty associated with the residual deflection of the device;

u_6 - the standard uncertainty associated with the temperature of the device;

u_7 - the standard uncertainty associated with the error of interpolation when units other than those of torque are used;

u_8 - the standard uncertainty associated with the reversibility of the device.

Calculation of calibration torque uncertainty, u_1

u_1 is the standard uncertainty associated with the torques generated by the calibration machine. This value should be obtained from the calibration certificate of the calibration machine.

Calculation of reproducibility uncertainty, u_2

u_2 is the standard deviation associated with the population of incremental deflections obtained during the calibration and obtained by using equation 3.13.

$$u_2 = \frac{0.5R_2}{\sqrt{2}} \tag{3.13}$$

where R_2 is the relative reproducibility.

Calculation of repeatability uncertainty, u_3

u_3 is the uncertainty contribution due to the repeatability of the measured deflection and is calculated as follow:

$$u_3 = \frac{0.5R_1}{\sqrt{3}} \tag{3.14}$$

where R_1 is the relative repeatability.

Calculation of resolution uncertainty, u_4

Each deflection value is calculated from two readings (the reading with an applied torque minus the reading at zero torque). Because of this, the resolution of the indicator needs to be included twice so a standard uncertainty is calculated by using equation 3.15.

$$u_4 = \frac{r}{\sqrt{6}} \tag{3.15}$$

where r is the resolution of the indicator.

If the initial reading of each series is tared to zero, a standard uncertainty of $r/\sqrt{12}$ can be used.

Calculation of residual deflection uncertainty, u_5

u_5 is the uncertainty component due to the variation in the relative residual deflection R_0 and obtained from equation 3.16.

$$u_5 = \frac{0.5R_0}{\sqrt{3}} \tag{3.16}$$

Calculation of temperature uncertainty, u_6

u_6 is the contribution due to the variation of temperature throughout the calibration, together with the uncertainty in the measurement of the calibration temperature. It can be obtained by using equation 3.17. The sensitivity of the device to temperature needs to be determined:

$$u_6 = \frac{K\Delta t}{2\sqrt{3}} \tag{3.17}$$

where:

K is the device's relative temperature coefficient expressed as a percentage of maximum applied torque per degree Celsius, derived either by tests or from the manufacturer's specifications;

Δt is the calibration temperature range, allowing for the uncertainty in the measurement of the temperature.

Calculation of error of interpolation uncertainty, u_7

u_7 is the uncertainty contribution due to the relative error of interpolation and is calculated from equation 3.18.

$$u_7 = \frac{0.5E_{it}}{\sqrt{6}} \tag{3.18}$$

For torque measuring devices where the deflection is in torque units, the calibration uncertainty is that of the torque value given by the error of indication when the deflection of the device is a specific torque value. For devices where the deflection is in other units, the calibration uncertainty is that of the torque value calculated from the interpolation equation, at any measured deflection.

Calculation of reversibility uncertainty, u_8

u_8 is the uncertainty component due to the relative reversibility R_3. equation 3.19 is used to obtain this value.

$$u_8 = \frac{0.5R_3}{\sqrt{3}} \tag{3.19}$$

Calculation of combined standard uncertainty, u_c

At each calibration torque, a combined standard uncertainty u_c is calculated by combining the individual standard uncertainties mentioned above using equation 3.20.

$$u_c = \sqrt{\sum_{i=1}^{n} u_i^2} \tag{3.20}$$

where:

u_i is the standard uncertainty associated with the readings;

n is the number of uncertainty contributions u_i.

Calculation of expanded uncertainty, U

Then it is multiplied by the coverage factor, k, associated to the required confidence level in order to give an expanded uncertainty value, U (equation 3.21). Normally, k = 2 which is corresponded to 95% confidence level is used.

$$U = k \cdot u_c \tag{3.21}$$

The advantages of a calibration to BS 7882:2008 are as follows (*Pratt, 2008*):

1. The end user can easily use a device which has already been classified without correcting the reported error.

2. It is convenient to compare products of different manufacturers.
3. It increases the confidence of the end user to make the measurement because the classification allows the device to reproduce its results under different conditions of use.

This standard allows for devices to be independently calibrated of the indicator they are used with, providing that the indicators have a valid Certificate of Calibration.

CHAPTER 4

4. Improvements in Torque Transducer Design

This chapter will evaluate previous experimental tests on a torque transducer with 40mm long TBTF resonant sensors, as described in 2.3.2. FEA analysis of existing transducer design will be described. Moreover, temperature, lateral forces and manufacturing uncertainties, which cause problems with existing design are mentioned. The last section will propose two possible solutions for increasing the accuracy of a torque transducer based on TBTF resonant sensors.

4.1 Problems with Existing Design

4.1.1 Temperature

Torque transducers can also be regarded as electronic instruments which are sensitive to environmental conditions. Hence the environmental conditions must be kept constant, otherwise the accuracy and ability to function as a torque transducer can be reduced (*Schicker and Wegener, 2002*).

Temperature effect is one of many environmental errors and it may affect both the measuring system and the measurand (*Herceg, 1976*). There are two kinds of temperature effects; temperature effect on the zero signal (TK_0) and temperature effect on the sensitivity (TK_C). Both temperature effects result in different characteristic curve as shown in figure 4.1. TK_0 results in a parallel shift and TK_C results in a change of slope (*Schicker and Wegener, 2002*).

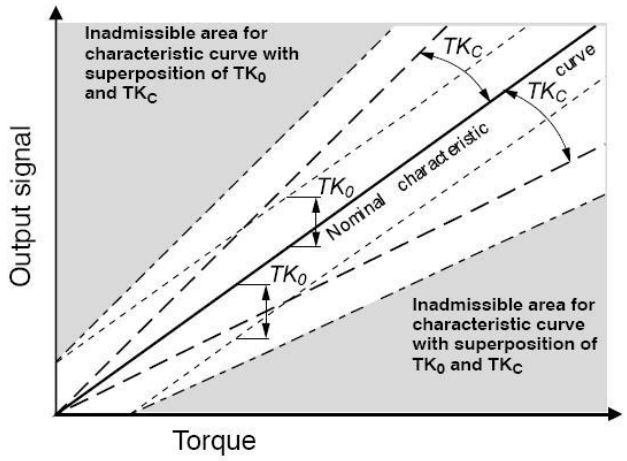

Figure 4.1 Temperature effect on the zero point, TK_0 and on the sensitivity, TK_C (Schicker and Wegener, 2002).

Temperature distribution is another factor that should be considered as changing or non-uniform distribution exhibits stronger influence than static or uniform distribution. A cooling system can be used to minimise the non-uniform distribution by directly cooling the component which is generating the heat. However, the cooling system must have symmetry as it can cause an additional non-uniform distribution. Thermal shielding on the torque transducer can also be used to minimise this effect (*Schicker and Wegener, 2002*).

The thermal expansion effect should be taken into account for a torque transducer that determines torque indirectly from a measurement of strain. This is because every object alters its dimension when the temperature changes. This effect does not produce any mechanical stress in the material if the object is free to move, or the object has a complete uniform temperature over its full length. In systems which have parts with different thermal expansions joined together, free thermal expansion is prevented, therefore thermal stresses occur in the system (*Hoffmann, 1989*).

The thermal expansion coefficient (α) is dependent on the material and the temperature and can be obtained from

$$\alpha = \frac{l_2 - l_1}{l_1} \cdot \frac{1}{\Delta\vartheta} = \frac{\Delta l}{l_0 \cdot \Delta\vartheta} \text{ in} \left[\frac{\text{m/m}}{\text{K}}\right] = \left[\frac{1}{\text{K}}\right] \tag{4.1}$$

where:

$l_1 = l_0$ = initial length before temperature change, i.e. reference length

l_2 = final length after temperature change

Δl = change in length due to change in temperature

$\Delta\vartheta$ = temperature change, positive for heating, negative for cooling.

Under zero load condition, the response to temperature is reversible and the temperature effects disappear when the original temperature conditions at the measuring point return (*Hoffmann, 1989*).

If the object experiences both temperature changes and mechanical loading, the measurement result will be the sum of mechanical strain and thermal strain. Unfortunately, it is impossible to separate these two strains (*Dally, Riley and McConnell, 1993*). Therefore, the indicated strain is error. Use of self-temperature compensating sensors can minimise this effect. Nonetheless this method is optimum for flat mounting surfaces, whilst deviations may occur with curved surfaces (*Hoffmann, 1989*).

For the torque transducer based on TBTF resonant sensor, there may be thermal expansion errors between the sensor and the torsion shaft if they are made from different material. In order to reduce this effect, the material used for the sensor and the torsion shaft should be the same. Alternatively, applying electronic compensation can also be used. However, it should be noted that the properties of electronic components

are only thermally stable within certain temperature limits (*Schicker and Wegener, 2002*).

4.1.2 Lateral Forces

Lateral force is one of the parasitic loads, which acts on the torque transducer in addition to the intended measured quantity (Fig. 4.2). Ideally, torque transducers should be designed so that the error from parasitic loads has no effect on the measurement signal. However, there is still an error on torque signal if the parasitic load is very large. This error is unpredictable due to the manufacturing tolerance variations. The parasitic load can be caused by external forces and moments acting on the torque transducer, or by the mounting conditions (*Schicker and Wegener, 2002*).

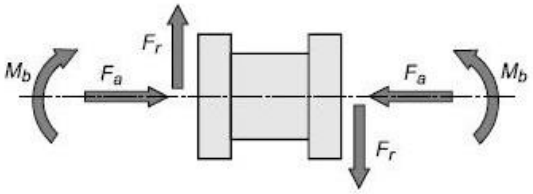

Figure 4.2 Parasitic loads: axial force F_a, lateral force F_r, bending moment M_b (Schicker and Wegener, 2002).

Torque transducers can be used for measurement if the lateral forces do not exceed the lateral limit force. If the limit is exceeded, there may be some effect on the measurement signal or the ability of the transducer to measure may be permanently damaged (*Schicker and Wegener, 2002*).

TBTF sensor performance is known to work well under tensile stress as occurring in a load cell. In designing a torque transducer, the TBTF resonant sensor was mounted at 45° to the axis of the torsion shaft. Therefore, the two attached faces of the TBTF resonant sensor are parallel and in-plane with each other when no load is applied. When a torque is applied, the angle actually changes from 45° as the material strains resulting in different forces acting on the TBTF resonant sensor. There will be tensile strain, which is the quantity being measured, and shear strain which occurs as the co-linear sides of the mounting surfaces move away from each other. Thus different amounts of tension are created in the two outer tines and the middle tine (Fig. 4.3). It is likely that this could have an effect on the accuracy of the reading.

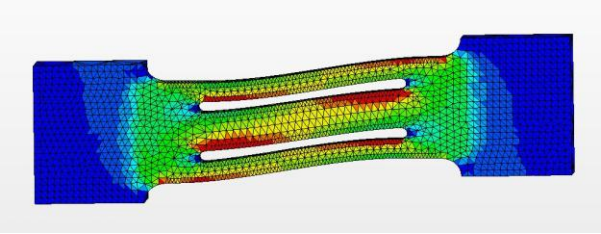

Figure 4.3 TBTF with distortion configuration (DeGolier, 2007).

From the FEA analysis, it can be indicated that the TBTF not only measures the changes in tensile/compressive strain at a 45^{o} angle to the axis of the shaft caused by torque but also experiences some shear strain and twist that will affect the final accuracy of the torque transducer. This effect could be minimized by implementing an alternative mechanical alignment of the sensor or reducing the overall size, whilst maintaining the stiffness of the sensor. These two possible methods will be described later.

4.1.3 Manufacturing Uncertainties

Uncertainties exist in all steps of the manufacturing process, which result in different performance characteristics of each individual device and low yield. These uncertainties can severely affect the performance of devices because tolerance ranges of the manufacturing processes can be relatively large and improvement of process accuracy is usually very expensive. The device performance is random because design parameters changing within tolerance ranges are random variables. The final output may fail to meet the acceptable range if the tolerances are large. Modifying the process or design to increase the yield can be achieved by tightening tolerances. However, cost or technical challenges of manufacturing processes are increased (*Shavezipur, et al., 2008*).

For example, figure 4.4 illustrates the cross-section of the middle tine of two TBTF resonant sensors. It is clearly seen from the images that the there is the uncertainty in the etching manufacturing process of the resonators occurred at the edge of the cross-section of the middle tine. This uncertainty results in different cross-sectional area for both resonators. According to equation (2.40), $f_i = \frac{(k_i l)^2}{2\pi l^2}\sqrt{\frac{EI}{\rho A}}$, the cross-sectional area, A, is one of many parameters which has an affect on the resonance frequency of the resonator. Therefore, any dimensional deviation can result in the variation of the frequency from one resonator to another. The effect of this variation will be shown in Chapter 5 which is about the miniaturisation of metallic TBTF resonant sensors.

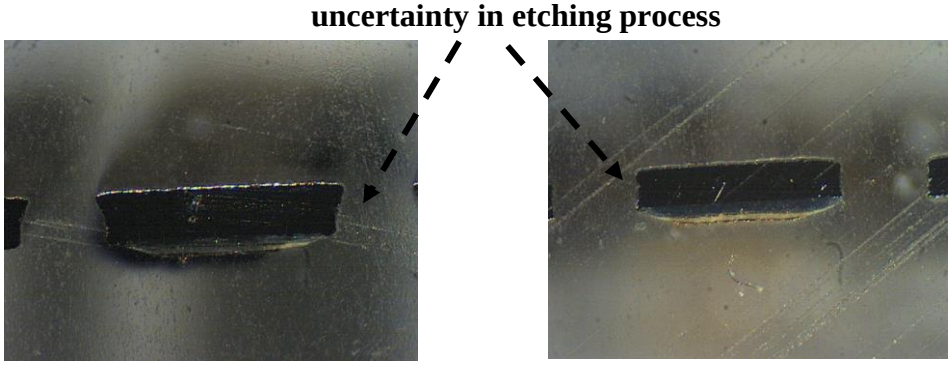

Figure 4.4 Uncertainty in resonator's beam etching process.

4.2 Possible Solutions

4.2.1 Repositioning to Measure Force

A spoked pinned wheel configuration (Fig. 4.5) was analysed to be used instead of cylindrical shaft in order to reduce the effect of lateral forces. The TBTF resonant sensor was mounted at 90° to the shaft axis instead of 45°. This design eliminates the lateral force as it allows the TBTF resonant sensor to experience only tensile force through the spoke.

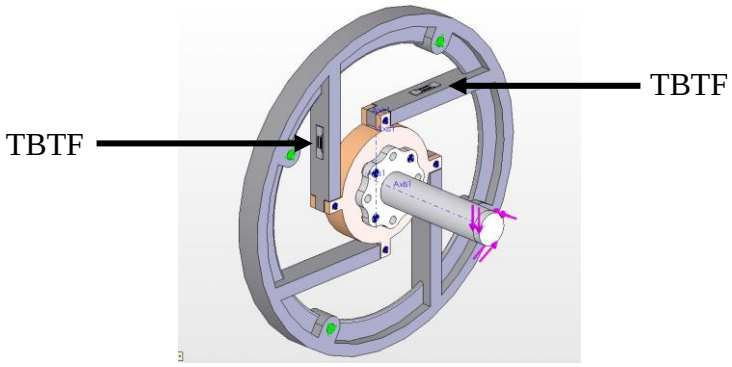

Figure 4.5 A spoked pinned wheel configuration with TBTF (DeGolier, 2007).

4.2.2 Reducing Size of Metallic TBTF Resonant Sensors

For high accuracy any torque transducer using TBTF resonant sensors ought to have low sensitivity to lateral forces. This effect could be minimized if it was possible to reduce the overall size of the TBTF resonant sensors.

Three TBTF resonant sensors with different size were investigated. They are SL40, SL20 and SL12 as shown in figure 4.6 (SL-Sensor Length include mounting). The first phase of the miniaturisation process was achieved by simply reducing the overall length by 50% from 40mm (SL40) to 20mm (SL20). The latest version of the sensor (SL12) has the overall length 12mm which is reduced by 70% from the original size. In trying to reduce the size of the sensor there is a danger that the piezoactuator might not be able to excite the stiffer tines, so PZT printing is a physical limitation in size reduction. The strategy adopted for the miniaturisation process was to maintain the tine cross-sectional area, roughly at 0.4 mm^2, therefore the connector and mounting geometry were reduced whilst maintaining the area of the PZT elements.

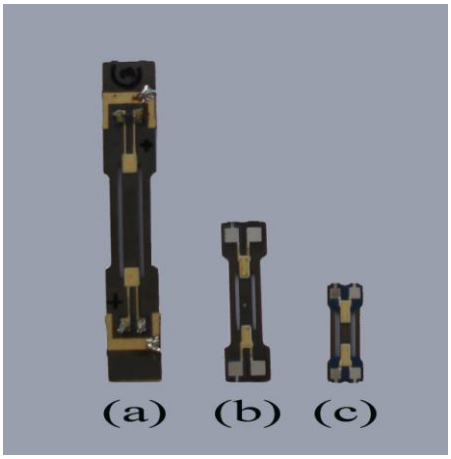

Figure 4.6 Metallic TBTF resonant sensors with different size.
(a) SL40: overall length is 40mm.
(b) SL20: overall length is 20mm.
(c) SL12: overall length is 12mm.

The effect of lateral force on the performance of the metallic TBTF resonant sensor was investigated by using FEA. COSMOSWorks software, which is a commercial implementation of FEA will be used for FEA analysis. The dimension of the modeled sensors is the same as the real prototypes. The PZT elements were not included in the model for the purpose of a simpler mesh, shorter meshing and computing times. After preparing the geometry, the type of analysis is selected. Static type was chosen for this analysis. Then material properties, loads and restraints are defined. The material was assigned to be stainless steel 430S17 type which is the same as used to fabricate the metallic TBTF resonant sensors. The bottom face of the sensor was fixed at one end and the lateral force was applied at the edge of the sensor as shown in figure 4.7. The lateral force was applied from 20-100N at 20N step in order to compare the results at each load. The next step is splitting the model geometry into small entities which are called finite elements. This step is called meshing. The solution from the analysis is approximated by assembling the solutions from individual elements. The solid mesh was used for this model, the mesh quality is set to be high and the mesh size was automatically created from the software which is 0.441136 mm, 0.361277 mm and 0.284518 mm for SL40, SL20 and SL12 respectively. This function will provide acceptable discretisation errors, while keeping solution times reasonably short. Now the model is ready for FEA analysis.

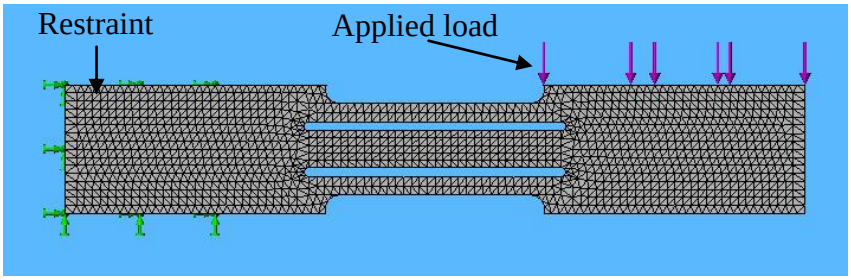

Figure 4.7 Load/Restraint configuration of SL40.

For this investigation, the average von Mises stress value on each tine of the sensor will be used to indicate the effect from the lateral force. In an ideal situation, the average stress value should be the same for all three tines. Unfortunately, this is impossible due to the unavoidable error in meshing process of FEA software. However, the closeness of the average stress value between the outer tine and the middle tine can be used as the indicator for this evaluation. Actually, the metallic TBTF resonant sensor is designed to work in tension/compression mode as implemented in a load cell application. If the sensor only experienced the tension/compression force, the average stress value between the outer and middle tine should be very close. But when used as a torque transducer, the sensor experiences any lateral force as well as the tension/compression force, therefore the average stress value between the outer and middle tine will be different. The difference will be increased when the sensor experiences more lateral force. The effect from the lateral force can be minimised if the size of the sensor is reduced and that can be proved by using FEA analysis results.

Figure 4.8 shows the stress distribution results of SL40 at 20N lateral force after running FEA analysis. Figure 4.9 and 4.10 show the stress distribution for SL20 and SL12 sensors.

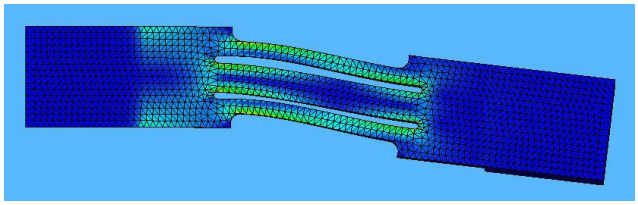

Figure 4.8 The stress results of SL40 from 20N lateral force.

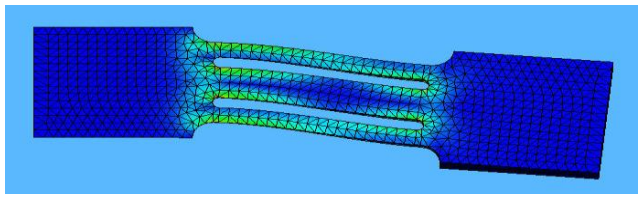

Figure 4.9 The stress results of SL20 from 20N lateral force.

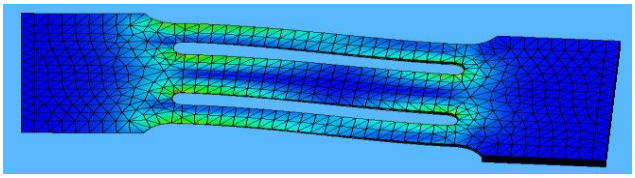

Figure 4.10 The stress results of SL12 from 20N lateral force.

The von Mises stress value on each tine of the sensor was measured and the average value was then calculated. Figure 4.11 is the graph showing the average stress value on each tine at 20N lateral force of SL40 sensor. Figure 4.12 and 4.13 show the same results for SL20 and SL12 sensors respectively. The difference between the average stress value on the outer tine and the middle tine for SL40 sensor is 36%. The difference is reduced to 24% and 16% for SL20 and SL12 sensors respectively.

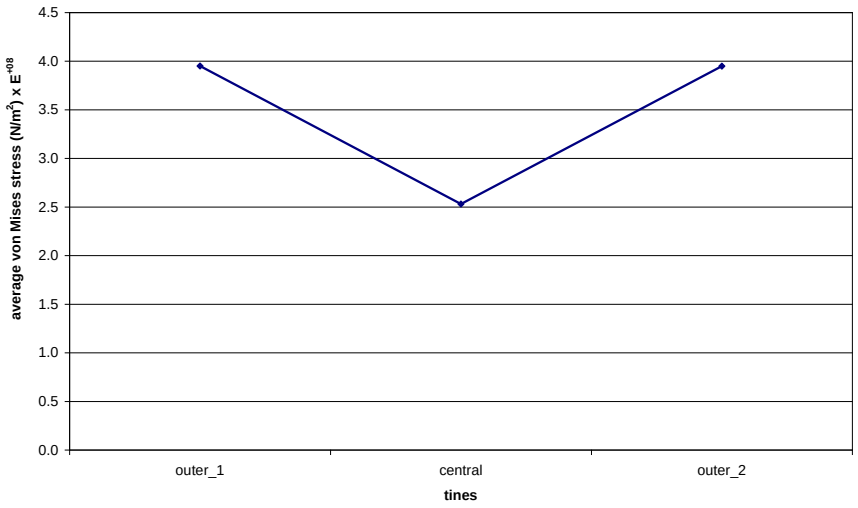

Figure 4.11 The average von Mises stress on each tine of SL40 sensor at 20N shear force.

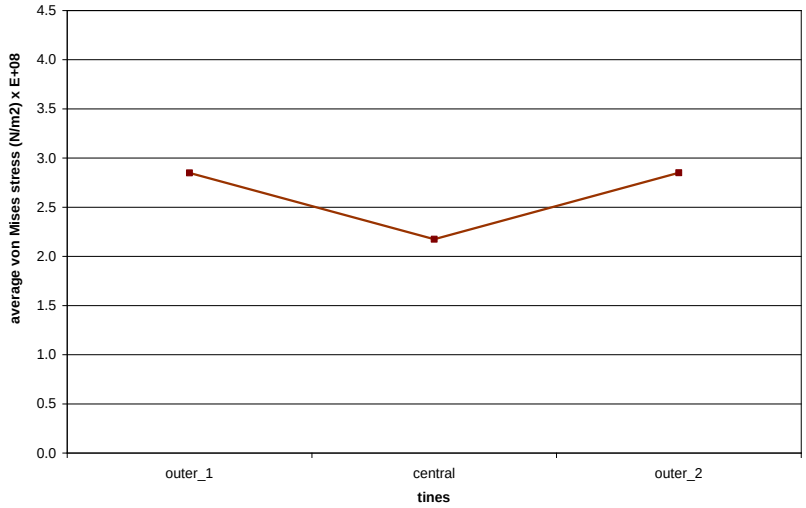

Figure 4.12 The average von Mises stress on each tine of SL20 sensor at 20N shear force.

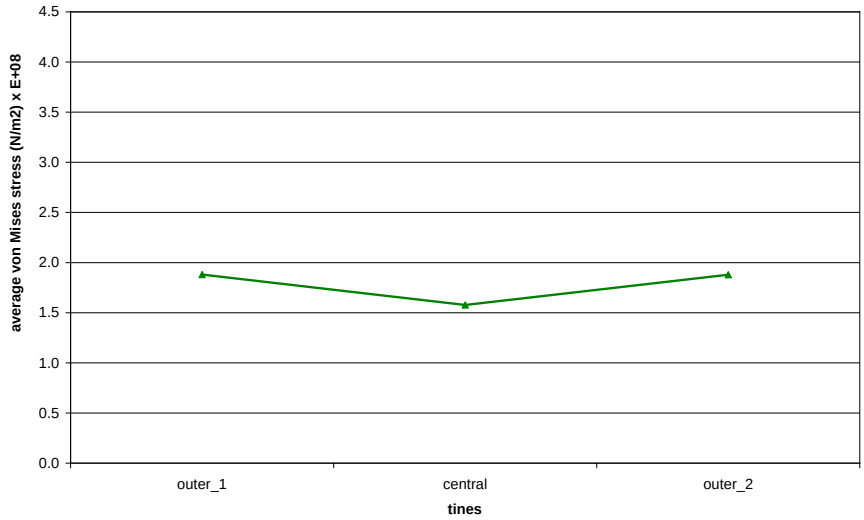

Figure 4.13 The average von Mises stress on each tine of SL12 sensor at 20N shear force.

Figure 4.14 shows the average stress value on each tine of all three sensors at 20N shear force. It is clearly seen that the difference of the average stress value on the outer tine and the middle tine is reduced when the sensor is smaller. The difference in average stress value between the outer tine and the middle tine compared to the first prototype SL40 sensor is a reduction of 52% for the SL20 sensor and reduced by 80% for SL12 sensor.

Figure 4.15 illustrates the completed FEA analysis results of the lateral force effect which shows the difference of average von Mises stress between outer and middle tine for all three sensors at applied 20-100N lateral force. It is clear that when the size of the sensor is reduced, the difference in the average stress distribution on the three vibrating beams is decreased concluding that reducing the overall size can satisfy the requirement to improve the accuracy of the torque transducer with TBTF resonant sensors.

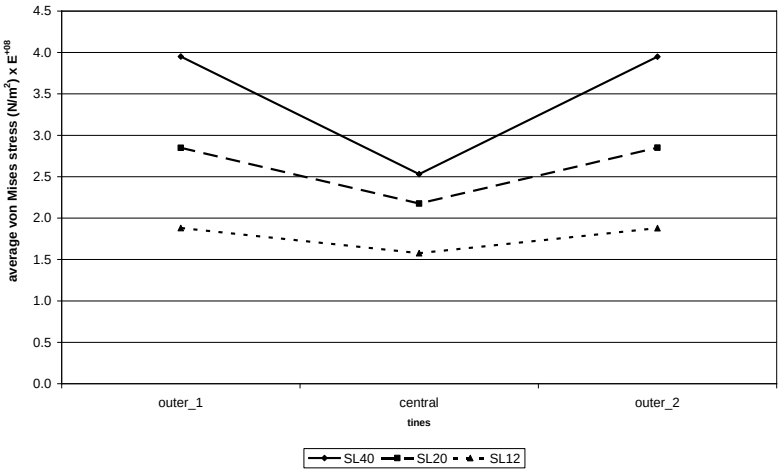

Figure 4.14 FEA results of the average von Mises stress on three tines for the SL40, SL20, and SL12 sensors with an applied 20N shear force.

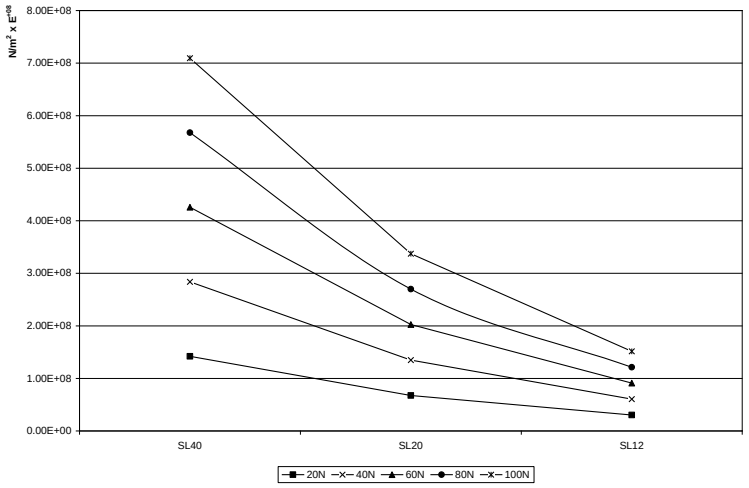

Figure 4.15 FEA results of the difference of the average von Mises stress between the outer and central beams for SL40, SL20, and SL12 sensors at applied 20-100N shear force.

In conclusion, measurement errors due to lateral forces, which would degrade the accuracy of such a torque transducer, were reduced by 52% for SL20 and by 80% for SL12 when compared to the original 15.5mm length vibrating tine (SL40).

CHAPTER 5

5. First Miniaturisation of Metallic TBTF Resonant Sensors

The first successful metallic TBTF resonant sensor (SL40) with thick-film drive/pickup elements with 15.5mm vibrating tine length and 40mm overall length of the sensor is too large for current torque sensing applications. To improve torque measurement accuracy and resolution, research is undertaken to investigate the performance impact of progressively reducing the tine length dimension. Additionally if the footprint of the new resonant sensor is smaller so the cost of fabrication per device is lower because there are more devices per plate as explained in Chapter 4, the accuracy of a smaller resonant sensor is higher because it is less sensitive to lateral forces than the larger one, when a torque is applied to the shaft. Moreover, a small size of sensor is required in retrofit applications which have limited space for installing torque transducers, say, between a motor and a pump.

The objective of this chapter is to describe the progress in the research, development and design of two miniature metallic TBTF resonant sensors, SL20 and SL12. Only the summary of key findings will be shown. The configuration and characteristics of these two miniaturized TBTF sensors, their performance in a torque transducer, and the calibration results of torque transducers with these sensors are also included.

5.1 Design 1 (SL20)

5.1.1 Configuration

First miniaturised metallic TBTF resonant sensor (SL20) has a configuration as shown in figure 5.1. The engineering drawing is shown in Appendix A.1.

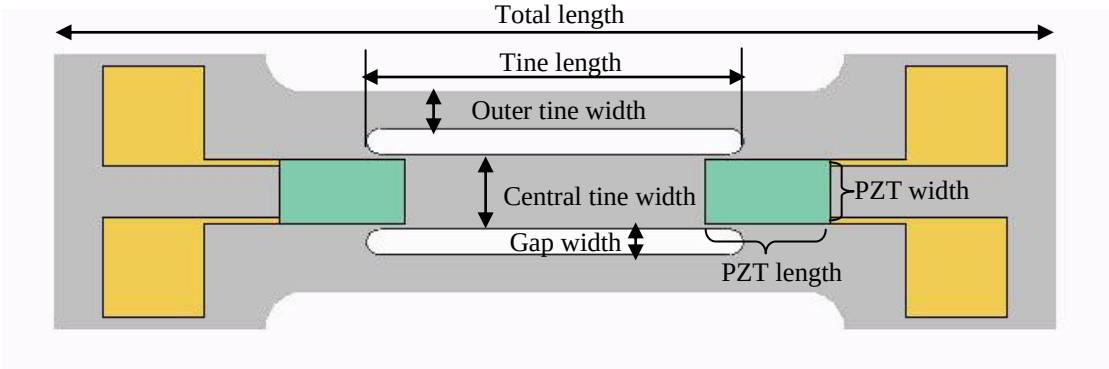

Figure 5.1 Configuration of SL20 metallic TBTF resonant sensor.

5.1.2 Fabrication

The substrate of the sensor was photochemically etched from a 0.7 mm-thick 430S17 stainless steel thin sheet with a top pattern defining the resonator layout and a bottom pattern etched in a standoff distance leaving the resonating element 0.25 mm thick. This material was chosen due to its suitability for thick film deposition and firing processes. The substrate was then cleaned using acetone in order to prepare for the thick-film printing process. The dielectric layer was deposited at the defined driving and sensing regions on the top surface of the resonator by using a standard screen-printing process. Later the consecutive layers of ground tag, bottom gold electrode, piezoelectric paste and top gold electrode were deposited with their own screens respectively. The dielectric layer is required for good isolation from the metallic substrate to enable polarisation of the piezoelectric layer at a later stage. The ground tag layer was deposited for excellent bonding in wiring stage. The bottom and top gold electrode were printed for the purpose of polarisation process. Gold material was used for the electrodes because of its long-term stability (*Torah, et al., 2004*). Moreover, implementing gold electrode can increase the piezoelectric properties of the film by preventing any silver migration into the film during the firing stage if silver is used for the electrodes. The migration of silver reduces the level of applied electric field to the PZT therefore the amount of dipole alignment is reduced (*Torah, et al., 2005*). Thick-film PZT elements were screen-printed on the central tine in order to be used for driving and detecting the tuning fork resonance. Current TBTF resonant sensors use a PZ29 piezoelectric paste, made by 95% PZ29 powder, 5% lead borosilicate powder, and approximately 5 ml ESL 400 organic vehicle per 20g powder mix. This material exhibits high levels of piezoelectric activity and has a low Curie temperature (*Torah, et al., 2005*). Each layer was allowed to stand in air for 10 minutes in order for the ink to level off and settle before drying. Then the printed film was dried for 10 minutes at 140°C. Once the printed film was dried, the thick-film layers will proceed to the firing stage in a high temperature oven. Firing in high temperature will improve the density and mechanical quality of the film because it increases the sintering between the PZT particles themselves and the binding material (*Torah, et al., 2005*).

The combination of processes used in the resonator fabrication, photo-etched TBTF sensors with drive and pick-up piezoelectric elements printed directly onto the device surface, presents low-cost manufacturing opportunities for mass batch production. Figure 5.2 shows a plate of SL20 metallic TBTF resonant sensors etched from a 90 $\times$ 70 mm stainless steel 430 S17 alloy. There are 20 sensors; 4 groups of 5 sensors per plate. Each plate was named e.g. plate A, plate B, plate 1, plate 2, etc. and each sensor was numbered from the top-left hand side as shown in figure 5.2. For example, if the sensors of plate A were identified, they are A1, A2, A3,…, A20. In the case of plate 1, the sensors were identified as plate(no.); 1(1), 1(2), 1(3),…, 1(20). Extra tracks and pads were printed at each end of the sensor (Fig. 5.2) for the purpose of simplifying the polarisation stage and in-situ characterisation of individual

sensors and any other pre-checking steps required before the sensors are cut out of the plate.

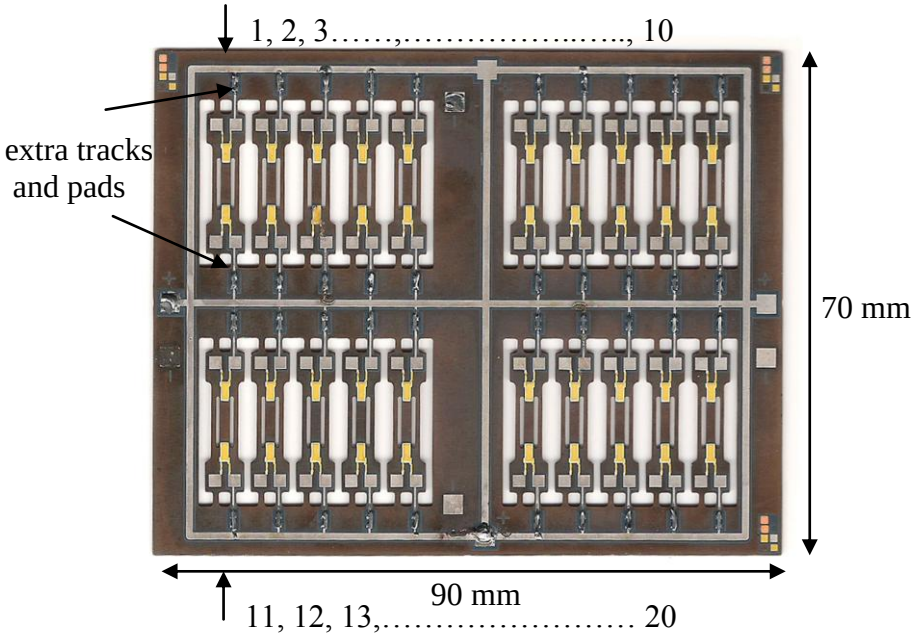

Figure 5.2 Batch production of SL20 metallic TBTF resonant sensors.

The dimension of SL20 sensors was measured at the Experimental Techniques Centre (ETC) Brunel University. The total length was measured by using the calibrated steel ruler (UKAS Inst No 06277) as shown in figure 5.3.

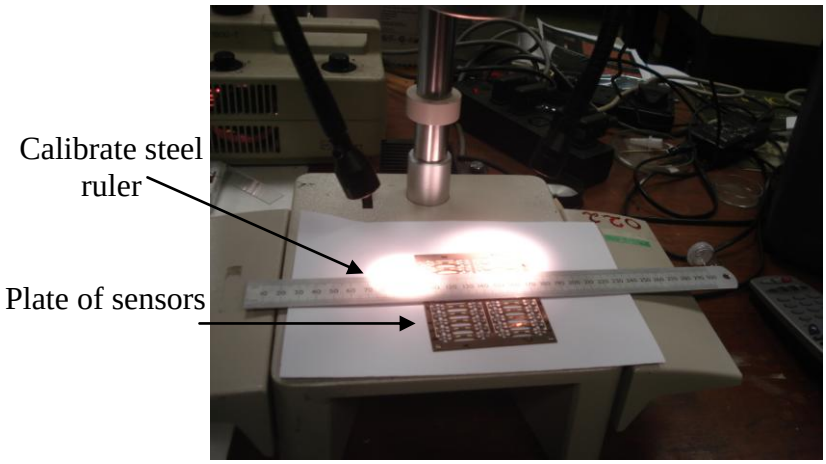

Figure 5.3 Measuring total length of SL20 sensor with the calibrated steel ruler at ETC.

The Microscope model Nikon was used to take pictures of the sensors in order to obtain the information about the tine, gap, and PZT dimension. Figure 5.4 illustrates the measuring setup for this measurement. The examples of the pictures taken from the sensors are shown in figure 5.5. The dimension of the sensors required was measured from the pictures by comparing to the calibrated scales.

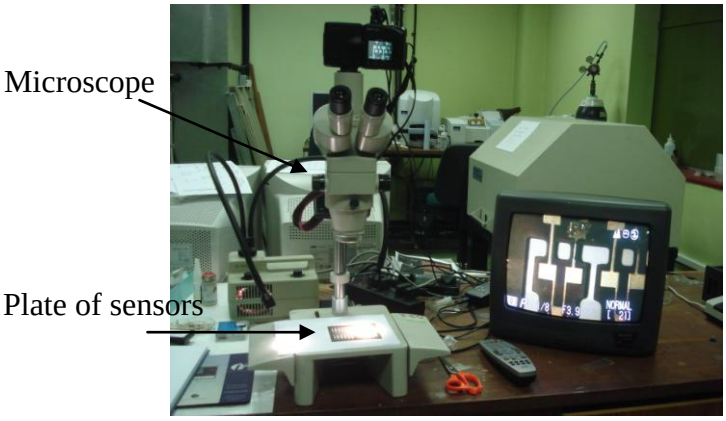

Figure 5.4 Measuring dimension of sensors by using Microscope.

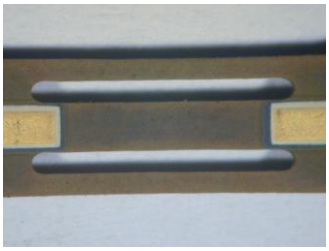

(a) tine and gap

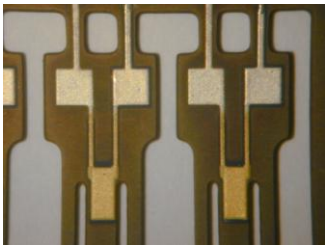

(b) PZT width and length

Figure 5.5 Picture of SL20 sensors and calibrated scale taken from the Microscope.

The thickness of the substrate and the resonating tine can be obtained by using a micrometer or measuring from the picture taken from the Microscope. Figure 5.6 shows the picture of sensor taken for measuring the thickness of the tine.

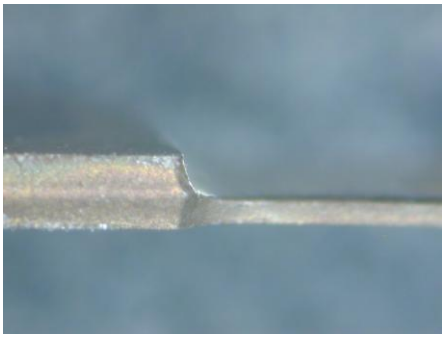

Figure 5.6 Picture of SL20 sensor for thickness measurement.

The tine length of the sensor can also be measured by using High resolution Scanning Electron Microscopy (SEM) model ZEISS SUPRA 35 FEG (Field Emission Gun). The sensor was placed in the machine and the dimension was measured directly from the display screen as shown in figure 5.7.

The dimension can be read directly from the display screen or measured from the taken picture as in the microscope method. Figure 5.8 shows the SEM photograph of printed thick-film on SL20 sensor.

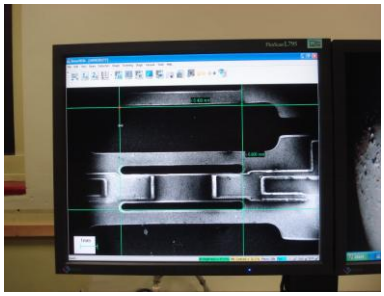

Figure 5.7 Measuring the tine length of SL20 sensor with SEM.

The thickness of the printed thick-film was measured by SEM method.

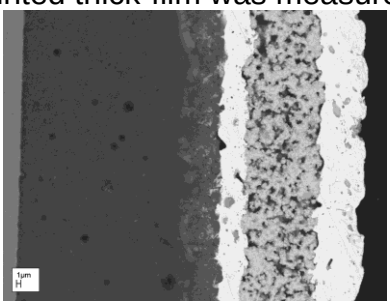

Figure 5.8 SEM photograph of printed thick-film on the SL20 sensor.

The dimension of 16 SL20 resonant sensors was measured and summarised as shown in Table 5.1.

Table 5.1 Dimension of SL20 TBTF resonant sensor.

Parameter	*Design Dimensions*	*Actual Dimensions*
Total length	20 mm	19.8±0.3 mm
Tine length	7.5 mm	7.2±0.4 mm
Central tine width	1.3 mm	1.3±0.1 mm
Outer tine width	0.65 mm	0.61±0.06 mm
Gap width	0.5 mm	0.6±0.1 mm
Tine thickness	0.25 mm	0.27±0.08 mm
PZT width	1 mm	1.0±0.2 mm
PZT length	2.5 mm	2.5±0.1 mm
PZT thickness	40 μm	38±4 μm

5.1.3 Polarisation

After firing, the PZT elements required polarisation in order to create the required piezoelectric characteristics. The electric poling field, temperature, and time, are three main parameters that should be considered for this process (*Torah, et al., 2005*). In the poling process, the PZT elements were electrically connected to a high voltage dc power supply and preheated to the required temperature. After the temperature is stabilised, the dc electric field was applied across the electrodes for the required poling time. At the end of the poling period, the sensors were allowed to cool to room temperature with a continuously applied electric field. This stage is needed to obtain a balanced poling process in order to enable observations of any changes in piezoelectric properties

independent of poling levels (*Torah, et al., 2004*). Then the electric field was removed and the sensors are ready for use in the required applications. Figure 5.9 illustrates the effect of the poling process on piezoelectric materials (*Prudenziati, 1994*). Figure 5.9(a) is called the virgin stage, where the dipoles within the piezoelectric material are aligned in a random manner. The material at this stage is piezoelectrically inactive because the effect on the individual crystallites average is zero. Figure 5.9(b) depicts the saturated state which is the stage when the electric field was applied across the piezoelectric material. At this stage, the dipoles are reoriented and aligned in the direction of the electric field. The final stage is a state of remnant polarisation which occurs after removing the electric field (Fig. 5.9(c)). The amount of remnant polarisation within the material depends on the poling conditions and therefore varies with the magnitude of the applied electric field and also the time and temperature (*White and Turner, 1997*).

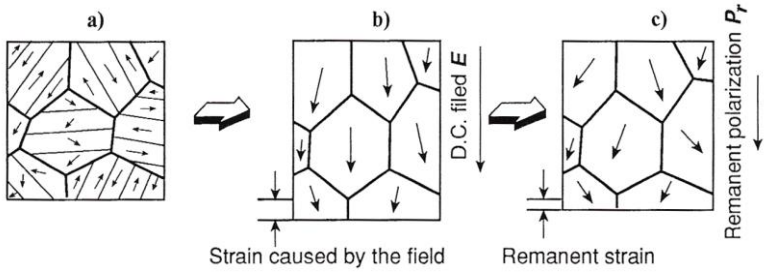

Figure 5.9 The effect of poling process for piezoelectric ceramics (Prudenziati, 1994).

In some cases, small black spots with a large hole in the center appeared on the thick-film surface of the sensors after removing them from the environmental chamber and after the polarization process, as demonstrated in figure 5.10. This could have occurred due to a high-energy dielectric breakdown event as a result of an existing pore at this location. These events only occurred with the thick film that had been exposed to a high DC bias (>300V) under hot and humid conditions during the polarisation process. There is some temporary dielectric recovery if the high voltage bias is removed or the film is dried out (*Stewart, et al., 2006*). The sensitivity of the film to humidity can be reduced by submerging the printed film into a heated mineral oil that will extract moisture from the pores in the film and seal them off (*Lou-Moller, et al., 2006*).

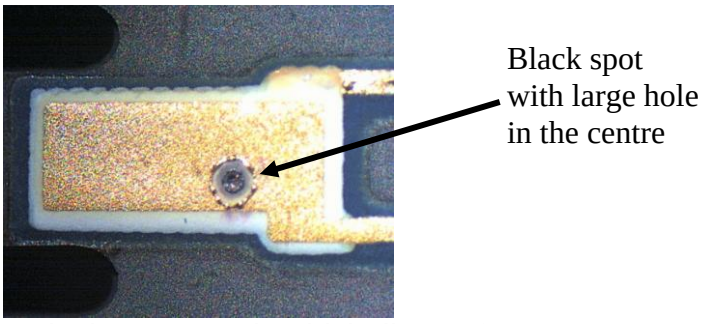

Figure 5.10 Black spots on the thick-film surface.

The effect of increasing the applied poling voltage of SL20 TBTF resonant sensors was investigated. All sensors were polarised in five different conditions which is at 180°C for 5 hours but with different applied poling voltage ranging from 200V to 300V. The Q-value of each sensor was measured and the average value was obtained for each poling voltage as shown in Table 5.2. The maximum temperature that can be used in polarisation process depends on the melting temperature of a solder used in electrical wire connection. Figure 5.11 demonstrates the relation between the applied poling voltage and the Q-value for this investigation. The Q-value is sharply increased when the poling voltage is increased from 200V to 225V then it is dropped at 250V. After that, it is gradually increased when the poling voltage is up to 300V. Nevertheless, the poling voltage should not be more than 300V because the electric breakdown event could occur as mentioned above. The reduction in Q-value may be due to the intrinsic porosity of the PZT elements that can be obtained from the following relationship (*Lou-Moller, et al., 2006*):

$$p = \left(1 - \frac{\rho}{\rho_t}\right) \tag{5.1}$$

where p is the porosity,

ρ is the measured density which is calculated from the weight and the geometric dimension of the PZT film,

ρ_t is the theoretical density of the material.

Table 5.2 Different poling condition of SL20 TBTF resonant sensors.

Condition	*Voltage (V)*	*T (℃)*	*Time (hours)*	*Q-value*
1	200	180	5	395
2	225	180	5	745
3	250	180	5	521
4	275	180	5	695
5	300	180	5	765

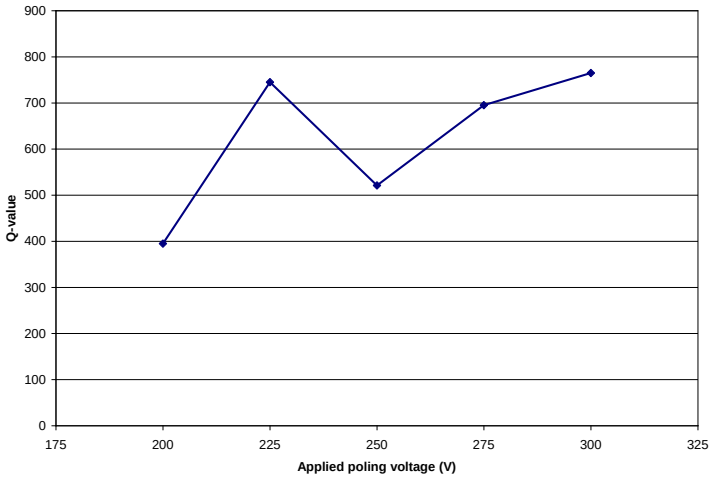

Figure 5.11 Poling voltage investigation at 180℃ for 5 hours of SL20 resonant sensors.

The poling condition that was finally used for SL20 TBTF resonant sensors is 285±15V, 200°C, and 2 hours. The temperature was increased from 180°C to 200°C because increasing poling temperature will increase the piezoelectric activity because the dipole alignment is improved as the PZT material is softer creating the permanent dimensional change required from polarisation (*Torah, et al., 2005*). The duration time was reduced from 5 hours to 2 hours because experimental work showed that the devices poled at higher temperature still achieve the same level of the piezoelectric characteristics. (*Dargie, et al, 1998*).

5.1.4 Initial Checks

The final part of the fabrication process is to characterise and pre-check the sensor performance. Each individual sensor may be checked while it is still in the plate or after cutting from the plate. The sensors can be cut by using a guillotine or a laser cutting machine. If the guillotine is used, the sensors must not be cut too close to the edge of sensors, because the cutting force may cause the sensors to bend and possibly crack the piezoelectric elements on the sensors. Therefore, a skilled operator is needed. Figure 5.12 illustrates the guillotine used for cutting the TBTF sensors at Brunel University.

Figure 5.12 Guillotine at Brunel University.

Another much better method to cut out the sensors is to use a laser cutting machine, which is more convenient and less damaging to the sensors than the guillotine. The process of cutting out all the sensors takes about 8 minutes per plate without wired sensors or 30 minutes with soldered wires, according to the information provided by the laser company. This normal cutting process is only suitable for single part production or small batch production. However, in commercial qualities, motor driven axes and CNC control will reduce the cutting time per plate to just over 1 minute. Figure 5.13 shows the laser cutting machine at Rofin-Baasel UK Ltd.

Wiring the sensors is another important step as it can cause some damage to the sensors. Electrical wires were soldered onto the soldering pads connected to the bottom and top electrode of the drive and pick-up PZT elements of the sensors. The temperature, soldering time, and

volume of solder are important parameters that should be controlled in order to get a good solder joint. If the volume of solder used in the soldering process is too much, the gold layer would be dissolved into the solder droplet resulting in a broken track (Fig. 5.14). In some cases even what looked like a 'good' solder joint had a contact resistance of around 4kΩ. This would imply a 'dry' joint with any silver being lifted by the flux.

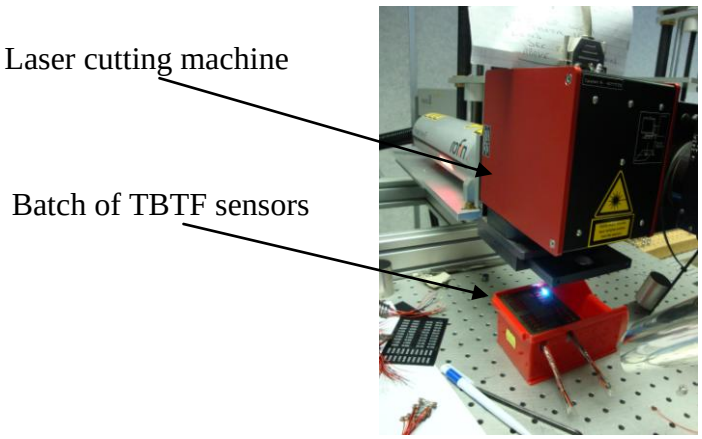

Figure 5.13 Laser cutting machine:PowerLineF20 at Rofin-Baasel UK Ltd.

Figure 5.15 shows the scratch on the printed film due to mishandling of the sensors. This scratch can adversely affect to the piezoelectric properties as well as the sensor performance. Therefore, packaging or coating the sensors with suitable material is recommended to prevent this damage happening.

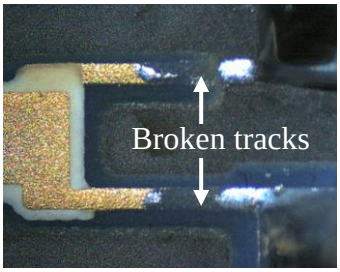

Figure 5.14 Damaged tracks.

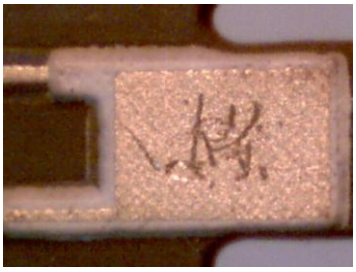

Figure 5.15 Scratch on printed film.

The sensor was firstly tested in an open-loop configuration in order to observe the vibration modes and confirm successful operation of the driving and sensing mechanisms. TBTF resonant sensor was designed to oscillate in a mode that the central tine vibrates in anti-phase with the two outer tines, as described in section 2.3.1.2, in order to minimise mechanical energy losses from the sensor.

In the open-loop configuration, the PZT element at one end of the sensor was driven by an AC periodic chirp signal of 0.5 V_{rms} from a Hewlett-Packard 89410A vector signal analyser, which swept the frequencies around the resonance frequency of the sensor. The PZT element on the other end was connected to a Kistler 5011 Charge Amplifier. Then the output from the charge amplifier was fed back to the signal analyser for

frequency response analysis of the sensor. Figure 5.16 shows the set-up of the open-loop configuration.

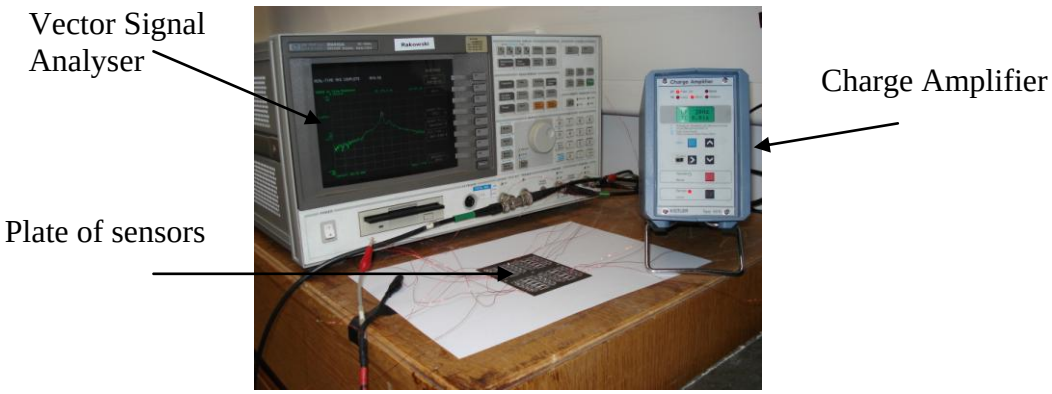

Figure 5.16 Experimental set-up for open-loop configuration.

The amplitude-frequency response for the third mode of vibration of one SL20 resonant sensor displayed on the Vector Signal Analyser is illustrated in figure 5.17. The resonance frequency was measured to be about 26kHz and Q-value was calculated to be 4002.

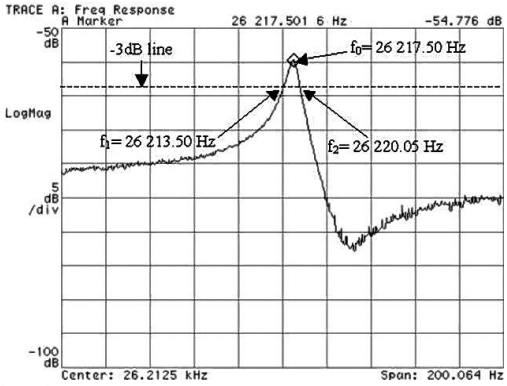

Figure 5.17 Amplitude-frequency response of SL20 sensor from Vector Signal Analyser.

The resonance frequencies of SL20 resonant sensors from 12 plates were measured and shown in Appendix A.2. The resonance frequencies of the sensors varied from one to another within the same plate and from different plates. This variation is due to the uncertainties in sensors manufacturing process as already described in Chapter 4. The resonance frequencies between 12 plates varied from 20-27 kHz with a standard deviation of 1230. When considering only one plate (e.g. plate A), the resonance frequencies are between 23kHz and 27kHz with a standard deviation of 1570. Figure 5.18 – 5.20 are three examples of the resonance frequency variation of plate B, plate 1, and plate 2 from 12 plates. The resonance frequencies of sensors on plate B are clearly divided into two groups where the sensor B1 -B10 have higher resonance frequencies than the sensors B11 – B20. The resonance frequencies of sensors on plate 1 are increasing from 1(1) to 1(20). The resonance frequencies of the sensors on plate 2 have the same pattern as the sensors on plate B but the resonance frequencies of 2(1) – 2(10) are

lower than 2(11) – 2(20). This pattern of variation which occur to the sensors on plate B and 2 can be linked to the etching process that causes the dimension of the sensors to vary from one row to another row.

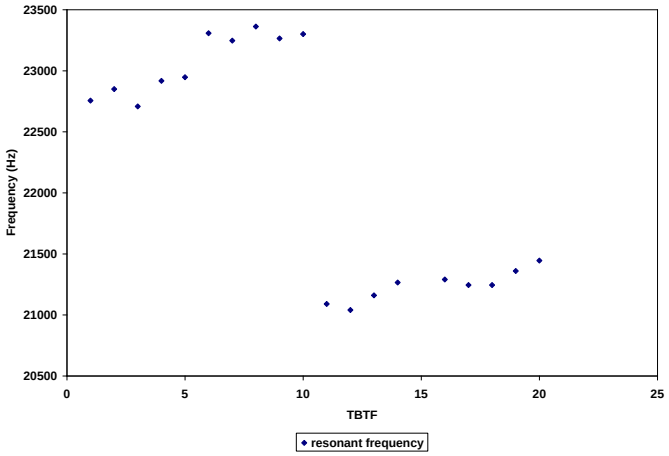

Figure 5.18 The resonance frequency of SL20 TBTF resonant sensors on plate B.

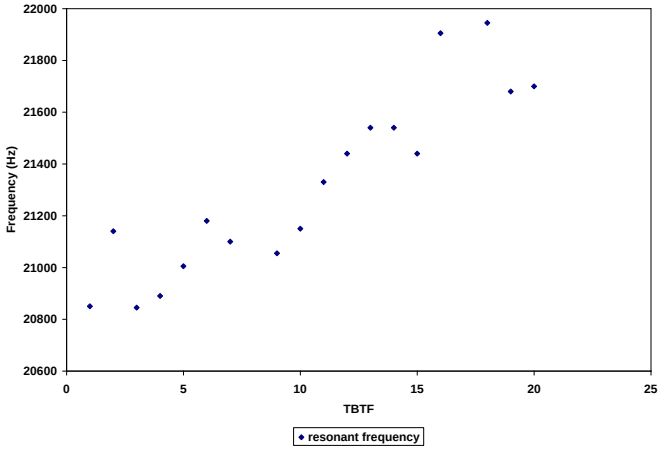

Figure 5.19 The resonance frequency of SL20 TBTF resonant sensors on plate 1.

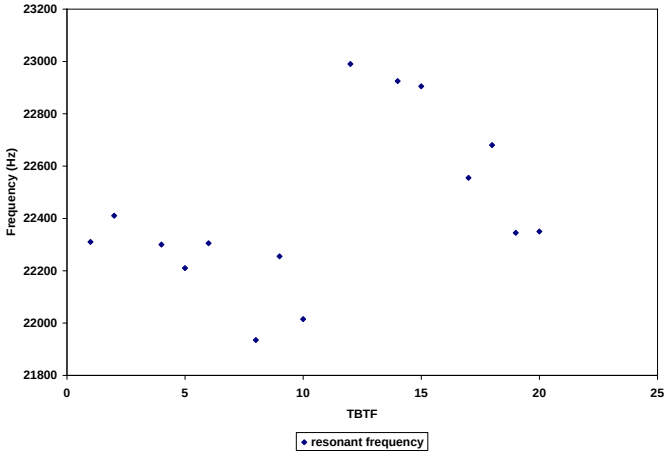

Figure 5.20 The resonance frequency of SL20 TBTF resonant sensors on plate 2.

Later the Q-value variation with position was also considered. Table 5.3 illustrates the Q-value of sensors from plate B. Sensor B15 was damaged during the fabrication process therefore there is no signal obtained. The results show that the Q-value is inconsistent. This may be due to the PZT powder dispersing unevenly throughout the paste used in the thick-film printing process on the sensors (*Torah, et al., 2004*).

Table 5.3 Resonance frequency and Q-value of SL20 resonant sensors on plate B.

TBTF	*f (Hz)*	*Q-value*	*TBTF*	*f (Hz)*	*Q-value*
B1	22755	1138	B11	21090	844
B2	22850	415	B12	21040	701
B3	22707.5	649	B13	21160	353
B4	22917.5	509	B14	21265	2127
B5	22947.5	918	B15	N/A	N/A
B6	23307	1554	B16	21290	2129
B7	23247	1550	B17	21245	1416
B8	23362	934	B18	21245	2125
B9	23265	2327	B19	21360	1424
B10	23300	1165	B20	21445	1072

5.1.5 Characteristics

Two TBTF resonant sensors having different size, SL40 and SL20, were investigated in order to better understand the sensor characteristics which are dependent on the dimension of TBTF sensor. The experiments conducted in the laboratory at Brunel University were stability, repeatability and temperature tests. Firstly, stability test, which is the ability of a measuring system to maintain constant its measurement characteristic with time was investigated. For this investigation the environmental conditions, such as temperature, humidity and pressure, have to be constant. This was achieved by using a climatic test chamber Montford Mini-Mech-B set to 25°C as shown in figure 5.21.

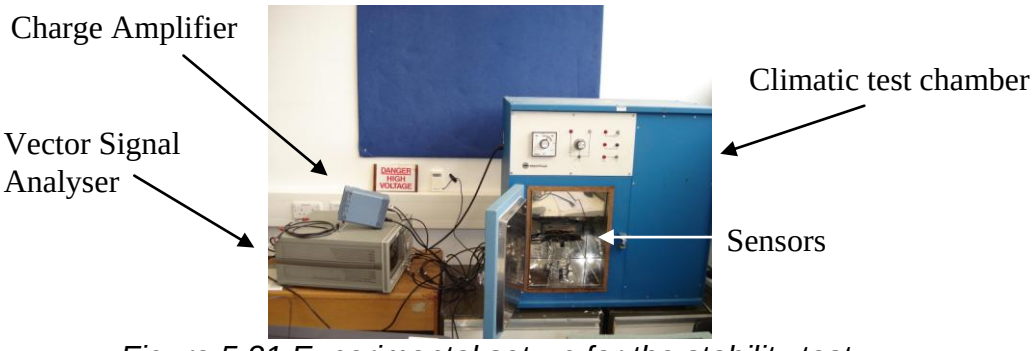

Figure 5.21 Experimental set-up for the stability test.

The sensors were operated in the open-loop configuration. Over a period of 48h the amplitude-frequency response was recorded in unequal time steps as shown in Table 5.4. The default frequency resolution for this experiment was 0.5Hz.

Table 5.4 Stability test of SL40 and SL20 resonant sensors

Hours	*f (kHz)*	
	SL40	*SL20*
2	4.6210	26.1875
4	4.6205	26.1865
20	4.6210	26.1875
22	4.6205	26.1865
24	4.6205	26.1865
26	4.6205	26.1865
46	4.6210	26.1880
48	4.6210	26.1870

Figure 5.22 displays the test result of both sensors over a period of 48h. The standard deviation of the measurement for SL40 and SL20 sensors is about 0.3Hz and 0.6Hz respectively.

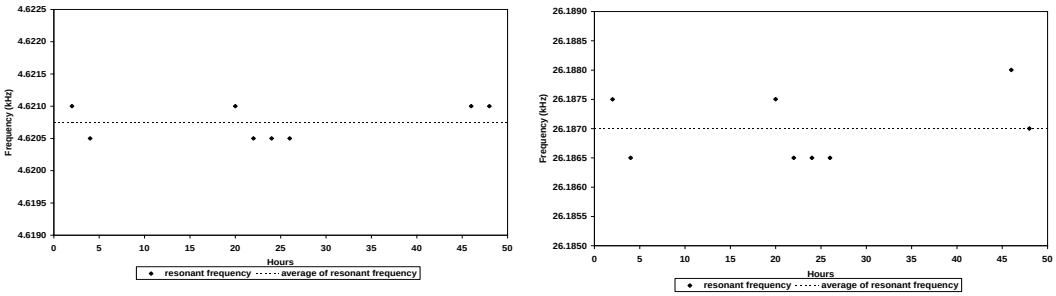

(a) SL40 resonant sensor *(b) SL20 resonant sensor*

Figure 5.22 Stability test of SL40 and SL20 resonant sensors (48 hours).

Then, repeatability investigation, which illustrates the measurement precision under conditions of repeated measurements over a short period, was investigated. The experimental set-up was similar to that for the stability investigation, except that the period of measurement was shortened to about 5 minutes and the resolution was adjusted to 0.1Hz. The frequency values were repeatedly measured 20 times and the mean value was calculated for each resonator. The experimental results are shown in Table 5.5.

Table 5.5 Repeatability test of SL40 and SL20 resonant sensors.

No.	*f (kHz)*		*No.*	*f (kHz)*	
	SL40	*SL20*		*SL40*	*SL20*
1	4.6211	26.1906	11	4.6211	26.1898
2	4.6211	26.1898	12	4.6211	26.1901
3	4.6211	26.1900	13	4.6211	26.1895
4	4.6211	26.1904	14	4.6211	26.1904
5	4.6211	26.1898	15	4.6211	26.1904
6	4.6211	26.1904	16	4.6211	26.1898
7	4.6211	26.1904	17	4.6211	26.1904
8	4.6211	26.1906	18	4.6211	26.1904
9	4.6211	26.1900	19	4.6211	26.1898
10	4.6211	26.1897	20	4.6211	26.1904

Figure 5.23 shows the repeatability test results for SL40 and SL20 resonant sensors. The standard deviation of SL40 resonant sensor for this test is less than the resolution of 0.1Hz. For SL20 resonant sensor, the standard deviation is calculated to be about 0.3Hz.

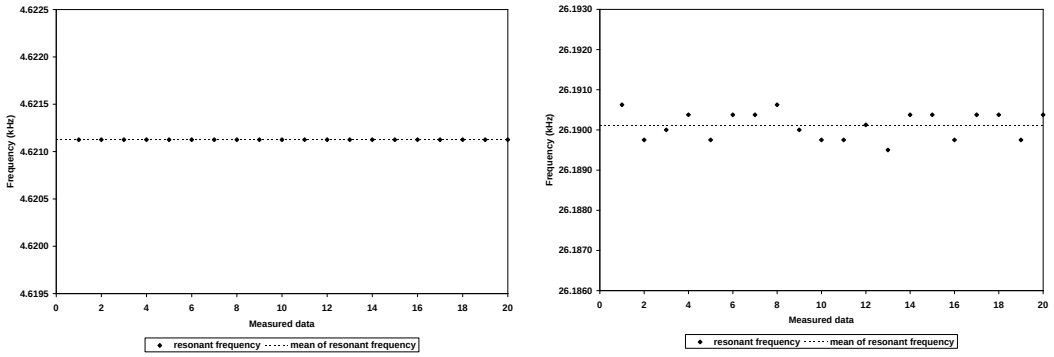

(a) SL40 resonant sensor *(b) SL20 resonant sensor*

Figure 5.23 Repeatability test results for SL40 and SL20 resonant sensors.

In industrial monitoring applications, a temperature range requires for a satisfactory measurement capability is between -30°C up to 85°C. To increase the application field of the resonant sensor by having even larger temperature ranges requires that the compensated temperature range should be as large as possible. On account of this the temperature characteristic needs to be known so that strategies for temperature compensation can be employed. The experimental set-up was similar to that for the stability and repeatability tests. The drive and pickup PZT elements of the sensor were connected by two coaxial cables to the open-loop electronics outside the climatic test chamber. The temperature was increased from -30°C to 90°C in steps of 30°C. At each temperature point the frequency response of the respective sensor was recorded after two hours delay, required to establish stable conditions inside the climatic test chamber. Table 5.6 shows the measurement results for this investigation.

Table 5.6 Temperature test of SL40 and SL20 resonant sensors.

T (°C)	*f (kHz)*	
	SL40	*SL20*
-30	4.6575	26.3100
0	4.6375	26.2300
30	4.6175	26.1700
60	4.5925	26.0725
90	4.5700	25.9800

Figure 5.24 shows the temperature characteristic of both sensors without any kind of temperature compensation. The temperature sensitivity is approximate 0.7Hz/^{o}C for SL40 resonant sensor and 2.7Hz/^{o}C for SL20 resonant sensor.

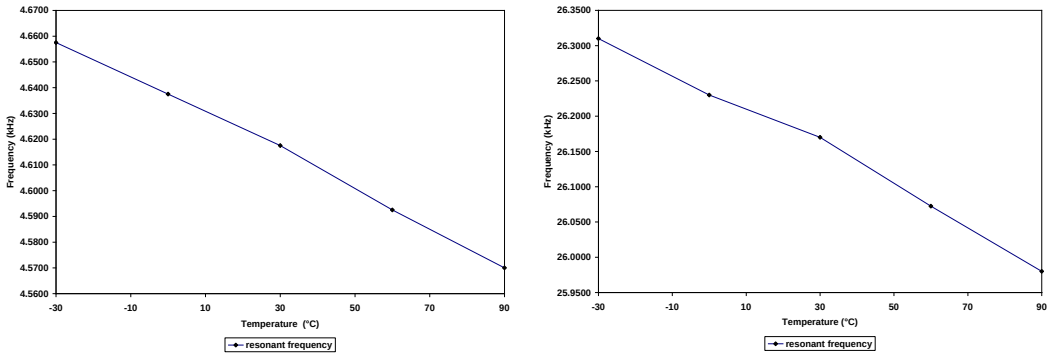

(a) SL40 resonant sensor *(b) SL20 resonant sensor*

Figure 5.24 Temperature test results for SL40 and SL20 resonant sensors.

Table 5.7 summarises the characteristics which include the stability, repeatability, and temperature performance of SL40 and SL20 TBTF resonant sensors. The SL40 resonant sensor appears to show better performance than SL20 resonant sensor. When consider to the temperature performance, SL20 sensor is more sensitive to the temperature than SL40. This may cause poor stability and repeatability due to the temperature effect. If the temperature compensation is applied, the performance of SL20 resonant sensor could be improved. However, since the sensor has been designed for a 10% change in frequency at full load, the % change on full scale figures show that the SL20 performs slightly better than the SL40.

Table 5.7 Characteristics of SL40 and SL20 TBTF resonant sensors.

TBTF	*f_0*	*10% of f_0*	*Stability*		*Repeatability*		*Temperature*	
	(kHz)	*(Hz)*	*SD*	*%*	*SD*	*%*	*Hz/^oC*	*%*
SL40	4.62	462	0.27	0.06	< 0.1	< 0.02	0.7	0.15
SL20	26.18	2618	0.60	0.02	0.35	0.01	2.8	0.11

5.1.6 Torque Transducer Based on SL20 Resonant Sensor

Next stage is to apply the metallic TBTF resonant sensor in a torque measuring application. To be used as torque transducer, the torque shaft for SL20 sensor was designed as shown in figure 5.25. The drawing of torque shaft for SL20 sensor is shown in Appendix A.3.

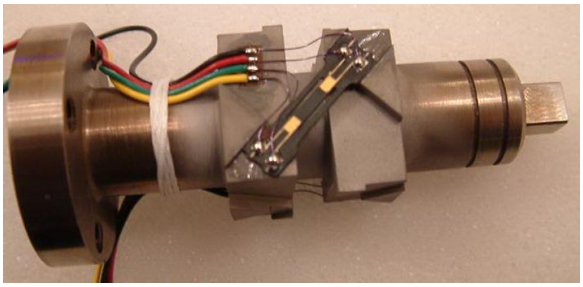

Figure 5.25 Torque transducer with SL20 metallic TBTF resonant sensor.

The TBTF resonant sensor may be attached to the torque shaft by gluing, laser-welding or the combination of both methods. The last method

begins with gluing the sensors onto the torque shaft in order to firmly align the sensors for the next stage which is the laser-welding. Pre-gluing stage can reduce the error from misalignment of the sensors during the welding process.

There are four parameters in setting up the laser welding machine. They are voltage (V), pulse time (ms), focus, and frequency (Hz). The voltage is used to control energy penetration into the object. The pulse time is used to determine the heat conduction. The focus is related to the laser spot size. The frequency is used to control the speed of a seam weld.

Figure 5.26 shows the effect of adjusting the voltage, pulse time, and focus. If the voltage is increased, deeper penetration occurrs. If the pulse time is increased, the welding result will be deeper and larger. If the focus is increased, the welding size is larger but shallower. Adjusting the focus results in stronger or weaker welding power will cause the welding size to be varied. In order to achieve a uniform weld, the focus should be maintained.

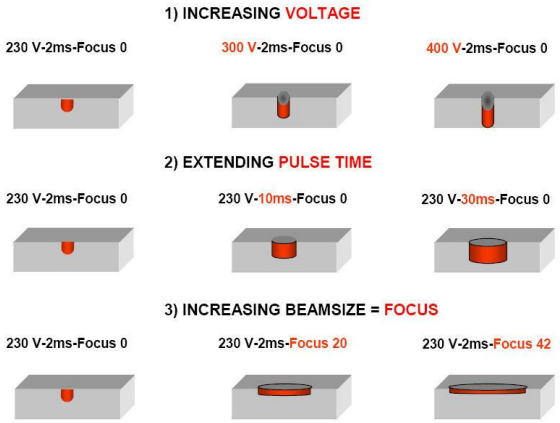

Figure 5.26 Physics of laserspots (Rofin-Baasel UK Ltd.).

Furthermore, there are many factors that should be taken into account in laser-welding process. Firstly, the direction of laser beam should be applied at perpendicular to the surface, otherwise the welding result can be different even the voltage, pulse width, and focus are kept constant. It is because the density of energy is reduced as the heated area is larger. Moreover, larger spot size will create more heat dissipation that may affect to the other parts of the object.

Secondly, the welding should be taken place where the two parts touch each other as much as possible. The gap between two parts can cause deformation at the weld spot. Greater contact will minimise the melted volume so that a lower power can be applied. If the gap is big, the pulse time or the focus should be increased so that the welding size is enlarged in order to melt and join two items together. In some cases, the laser welding wire can be used as the medium joining two items together if the gap is very big (Fig. 5.27).

Figure 5.27 Implementing the laser welding wire in laser welding.

In addition, a higher percentage of overlap between each welding spot gives better weld performance as shown in figure 5.28. However, time-consuming and cost of laser welding will be increased. Consequently, these two factors should be taken into account in deciding the appropriate percentage of overlapping.

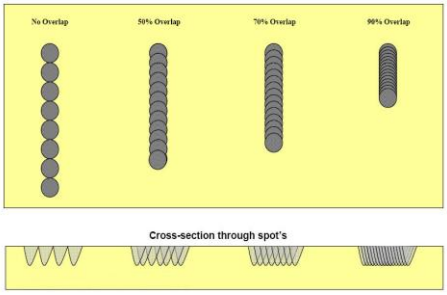

Figure 5.28 Different overlapping of the welding spot (Rofin-Baasel UK Ltd.).

Different materials and geometries of the object require different setting parameters in the laser-welding machine. Therefore, an experiment was conducted in order to find the optimum condition for each application. The laser-welding machine model Desktop was used for this experiment (Fig. 5.29).

The voltage, pulse time, and focus were adjusted as shown in Table 5.8. The experimental results of this investigation were illustrated in figure 5.30 - 5.33.

Figure 5.29 Laser-welding machine model Desktop (Rofin-Baasel UK Ltd.).

Table 5.8 Laser welding investigation.

Setting	*Voltage (V)*	*Pulse Time (ms)*	*Focus*
1	200	1	0
2	220	1.5	0
3	240	2	2
4	240	2	5
5	240	3	8
6	240	5	8
7	240	8	10
8	240	8	14
9	240	10	14
10	240	12	14

Figure 5.30 shows the setting 1 to 4 from top to bottom. Interestingly, there was damage at the edge of the welding area for setting 3. All parameters were increased for this setting, therefore too much energy was concentrated on a small area (Focus = 2). The focus was increased for setting 4 in order to allow the energy dissipated into the bigger area that shows a better result.

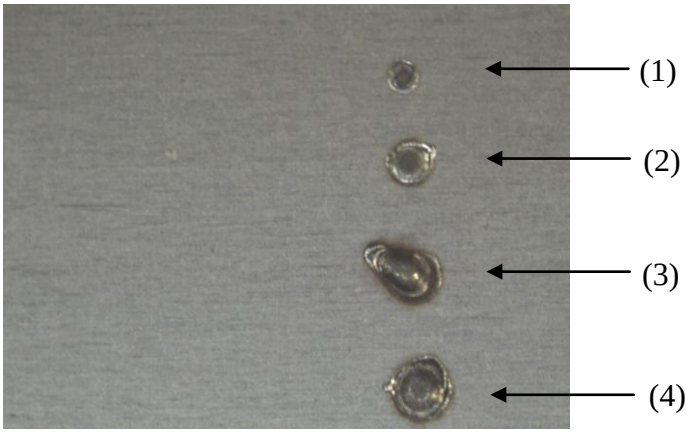

Figure 5.30 Setting 1 – 4.

Further investigation was undertaken by increasing the pulse time and the focus but keeping the voltage constant (Fig. 5.31). The welding size for setting 6 is bigger than setting 5 due to the increased pulse time. Then the pulse time and focus were increased for setting 7. There is a hole and additional damage as a result of the high energy applied on a small area.

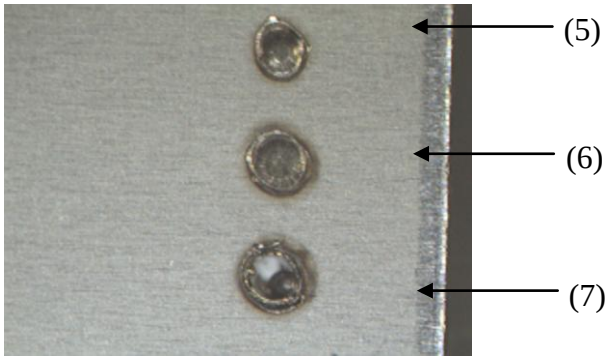

Figure 5.31 Setting 5 – 7.

From the previous experiment, increasing the focus can solve the above problem. Therefore, the focus was increased to 14 and the result is better as shown in figure 5.32. For the setting 9, the pulse time was increased but no significant result.

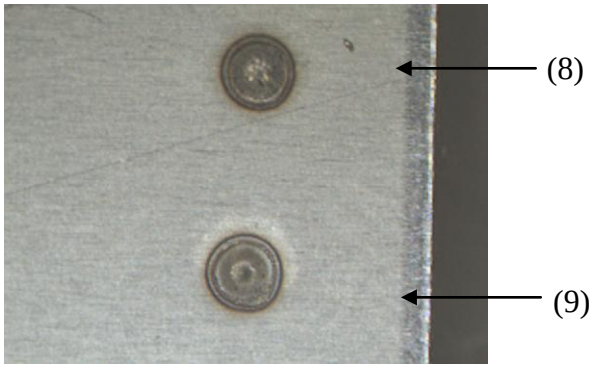

Figure 5.32 Setting 8 and 9.

When the pulse time was increased to 12ms for setting 10, then full penetration occurred to the object as seen in figure 5.33.

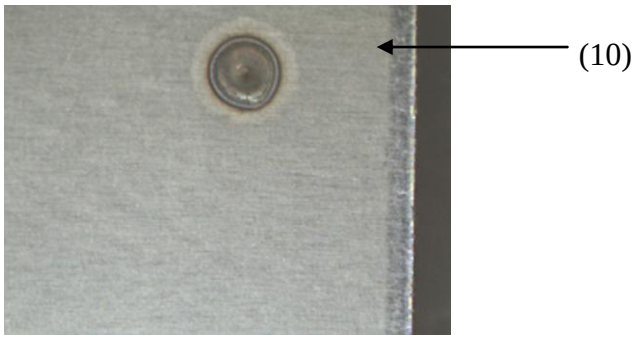

Figure 5.33 Setting 10.

The experiment clearly indicates that identifying the optimum setting for each application mainly depends on three parameters; voltage, pulse time, and focus. Consequently, some empirical work should be conducted before commencing the laser-welding process in order to prevent damage to the sensor and torque transducer.

After laser-welding the sensors onto the torque shaft, the resonance frequency and the Q-value of 4 sensors mounted onto 2 shafts were measured in order to check the performance of the sensors after laser-welding process. Moreover, a comparison of the resonance frequency and the Q-value before and after laser-welding process was made, as shown in Table 5.9.

The resonance frequencies of sensors are increased after laser-welding because the stiffness of the sensors is increased due to the tension between the sensors and the edge of the mounting area on the shaft. When considering the Q-value, the sensors mounted on shaft indicate higher value after laser-welding which is due to the firm mounting of the

sensors results in strong vibration and also prevents the energy losses from the resonating elements into the surrounding area.

Table 5.9 Resonance frequency and Q-value of torque transducer based on SL20 TBTF resonant sensors before and after laser-welding.

Shaft	*TBTF*	*f(kHz)*		*Q-value*	
		before	*after*	*before*	*after*
2	B1	25.1025	26.3944	1255	1552
3	C2	25.9150	26.4020	1091	1320
3	C4	26.5500	26.5525	1185	1397
3	D2	24.7925	25.2195	1006	1050

5.1.7 Testing of Torque Transducer Based on SL20 Resonant Sensor

The characteristics such as stability, repeatability, linearity, and temperature test of two torque transducers based on SL20 resonant sensors, C2 and D2, were examined in an industrial torque calibration laboratory. Initial tests were undertaken in the open-loop configuration to measure the resonance frequencies and obtain the Q-value as shown in figure 5.34. The results for the C2 and D2 devices in open-loop configuration are indicated in Table 5.10.

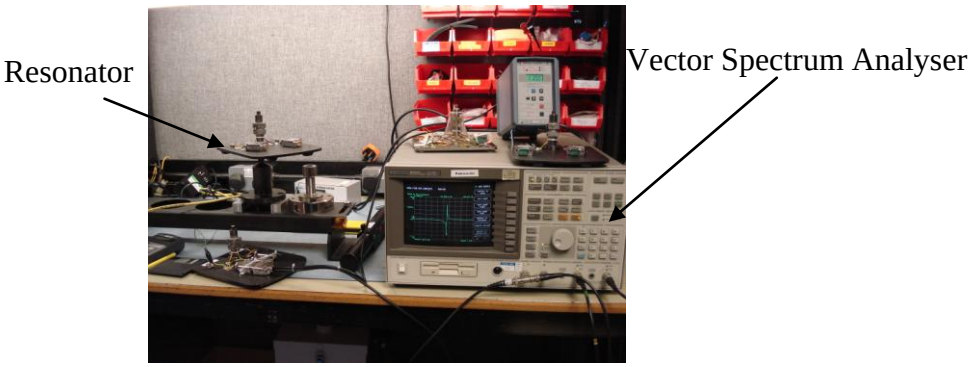

Figure 5.34 Measuring natural frequency with Vector Spectrum Analyser.

Table 5.10 Resonance frequencies and Q-values of SL20 resonant sensors mounted onto torque shafts.

TBTF	*f (kHz)*	*Q-value*
C2	26.4019	1320
D2	25.2195	1050

5.1.7.1 Stability Test

A stability test was conducted by using a calibration rig and standard weights (Fig. 5.35). Basically, the resonance frequencies of the sensors were monitored at zero torque for 15 minutes, then full load torque (27.5 Nm) was applied to each sensor and the resonance frequencies were monitored for further 15 minutes. This cycle was repeated 3 times for all sensors under test. The data for this investigation is shown in Appendix A.4.

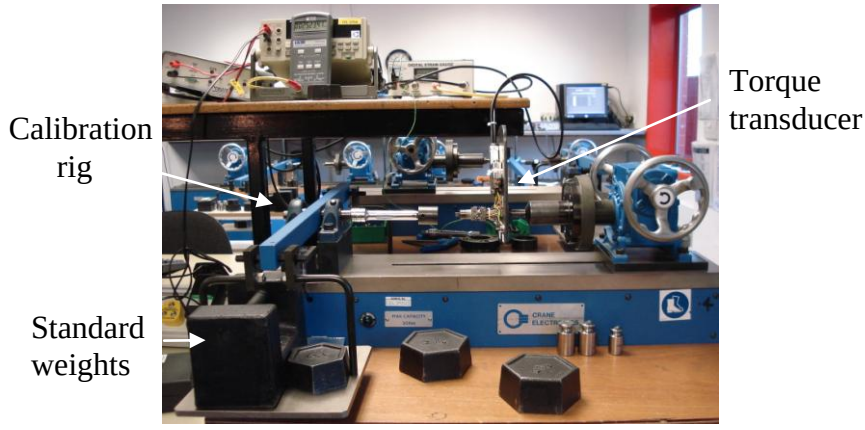

Figure 5.35 Stability test of torque transducer based on SL20 sensor.

Figure 5.36 shows the stability graph of C2 torque transducer with the standard deviation of 0.3Hz at both 0 Nm and 27.5 Nm.

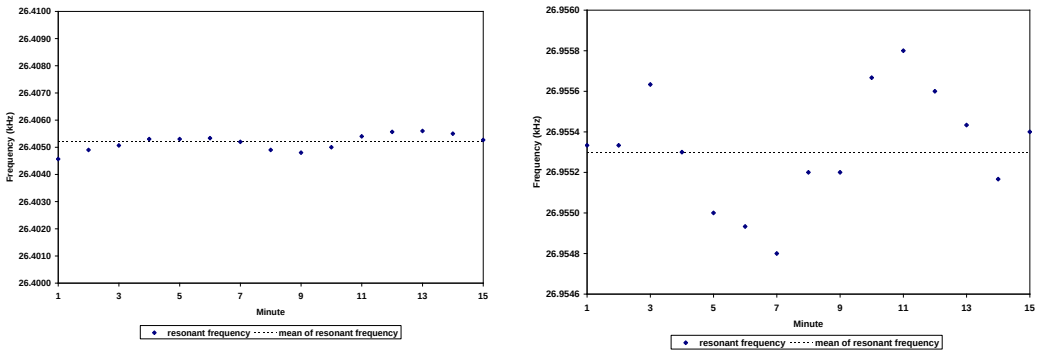

(a) at 0 Nm *(b) at 27.5 Nm*

Figure 5.36 Stability test for torque transducer based on SL20 resonant sensor, C2.

Figure 5.37 shows the stability graph of D2 torque transducer with the standard deviation of 0.6Hz and 0.7Hz at 0 Nm and 27.5 Nm respectively.

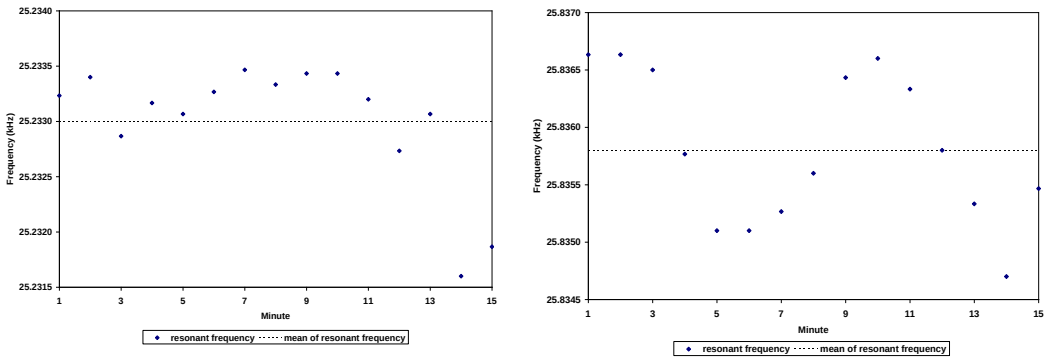

(a) at 0 Nm *(b) at 27.5 Nm*

Figure 5.37 Stability test for torque transducer based on SL20 resonant sensor, D2.

5.1.7.2 Repeatability Test

The next experiment is the repeatability test which was carried out in the same location as the stability test. A torque wrench, which was already

calibrated to the National Torque Standard, was used to apply load for this test as shown in figure 5.38. The capacity of the torque wrench is 75 Nm with resolution 0.01 Nm.

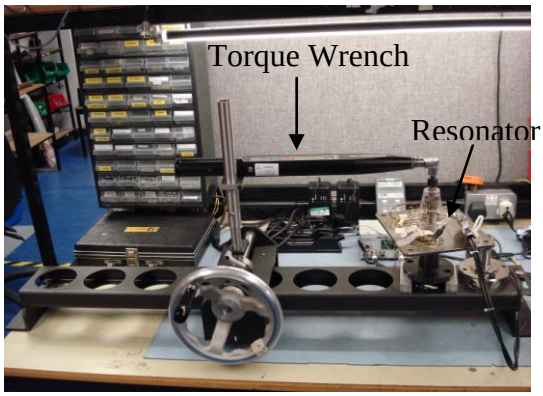

Figure 5.38 Repeatability test of torque transducer based on SL20 resonant sensor.

Each SL20 resonant sensor was monitored at zero torque, then a full load of 25 Nm was applied and resultant resonance frequency was monitored. This cycle is repeated 30 times. The data for this test is shown in Appendix A.5 and the corresponding graphs are shown in figure 5.39 and figure 5.40. At zero torque the standard deviation was calculated to be 2.1Hz and 1.5Hz whilst the standard deviation at 25Nm was calculated to be 1.2Hz and 3.2Hz for C2 and D2 torque transducers respectively.

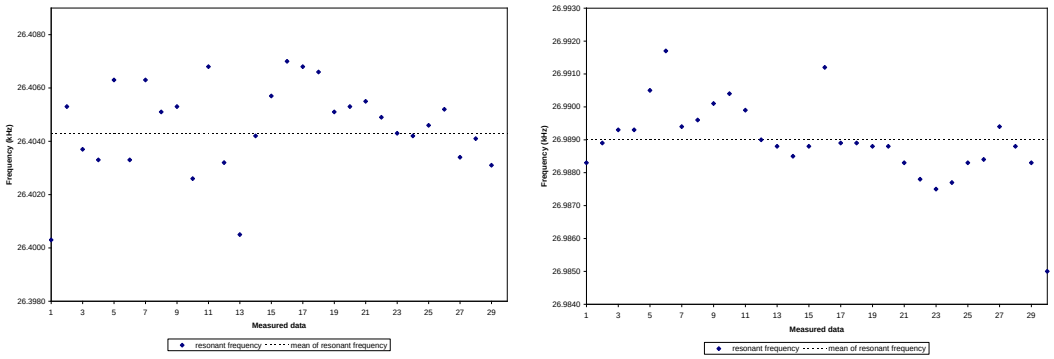

(a) at 0 Nm *(b) at 25 Nm*

Figure 5.39 Repeatability test for SL20 torque transducer (C2).

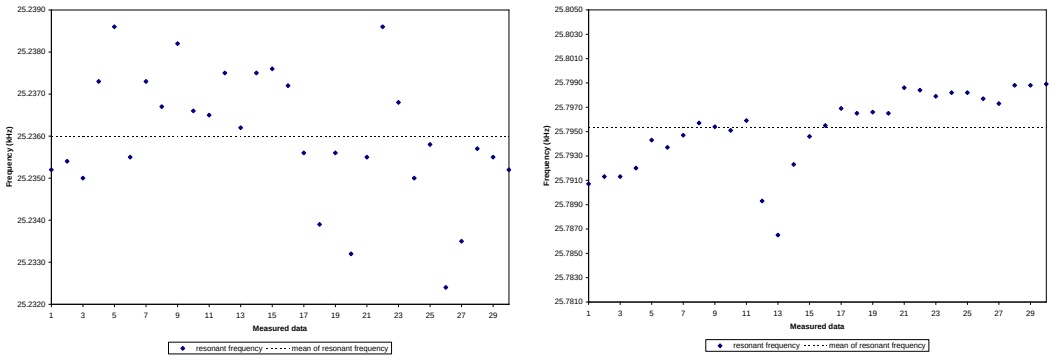

(a) at 0 Nm *(b) at 25 Nm*

Figure 5.40 Repeatability test for SL20 torque (D2).

5.1.7.3 Linearity Test

A linearity test was then undertaken in the same measuring system as the repeatability test. This test is concerned with loading/unloading of the torque transducer. The torque transducer was subjected to both clockwise and anti-clockwise torque and the resonance frequency was measured at each load for both directions for 2 cycles (Appendix A.6). The environmental temperature was also monitored during the measurement. The torque was applied approximately in ±2.5 Nm incremental steps for the range up to 25 Nm. The corresponding graphs are shown in figure 5.41-5.42 including the equation for the line of best fit.

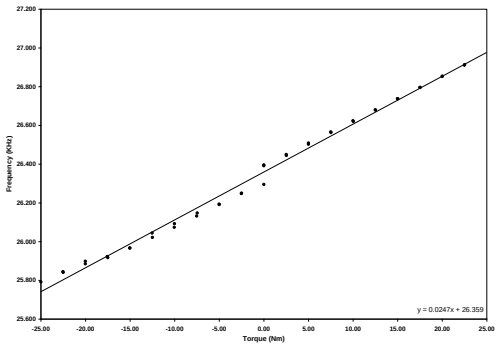

Figure 5.41 Linearity test of SL20 torque transducer (C2).

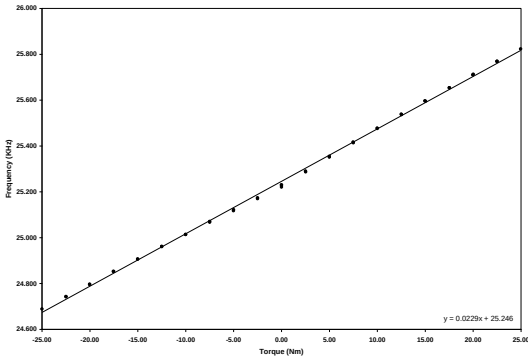

Figure 5.42 Linearity test of SL20 torque transducer (D2).

As can be seen from the graphs, the frequency is proportional to the applied torque. The results shown in Table 5.11 are a summary of typical characteristics; linearity, hysteresis including the information about the temperature variation during testing.

Table 5.11 Typical characteristics of torque transducer based on SL20 resonant sensor provided from linearity test.

TBTF	*Temperature variation (℃)*	*Sensitivity (Hz/Nm)*	*Linearity (±Hz)*	*Hysteresis (±Hz)*
C2	3.2	23.5	63.8	96.5
D2	2.1	22.7	25.4	8.5

From the results in Table 5.11, device C2 shows poor linearity and hysteresis values which could be mainly attributed to large variation in temperature during the test.

5.1.7.4 Temperature Test

The last experiment was a temperature test, which is an important test, since the torque shaft and TBTF were made from two different materials. Any error in temperature performance can be due to mismatch between the torque shaft and TBTF material's temperature coefficient. The temperature range for this experiment is between 5 to 55^{o}C. The test was carried out at zero torque in the controlled chamber as shown in figure 5.43. The temperature was heated to the highest temperature first and then it was reduced in approximate 5^{o}C steps. The resonance frequency

was monitored and recorded twice at each temperature point as shown in Appendix A.7.

Figure 5.43 Temperature test for torque transducer based on SL20 resonant sensors.

Figures 5.44-5.45 indicate the temperature results obtained from the experiment including the equation for the line of best fit.

Similar to the linearity test, both resonant sensors show linear characteristic to the temperature with a temperature coefficient approximately 2.5 Hz/^{o}C and 1.9 Hz/^{o}C and the non-linearity is 2.8Hz and 6.3Hz for C2 and D2 respectively. The temperature sensitivity of D2 is less than C2, however, it shows a more non-linear performance. The reason for this different characteristic may be due to inappropriate fitting of the sensor into the channel machined for it on the torque shaft which may lead to the sensor being twisted while being subjected to shear strain on the torque shaft.

Table 5.12 and 5.13 are the summary of the performance characteristics of torque transducer based on SL20 resonant sensor, C2 and D2 in the clockwise direction for the applied torque range 0-25Nm. The sensitivity, stability, repeatability, linearity, and hysteresis were calculated as percentage of the torque range.

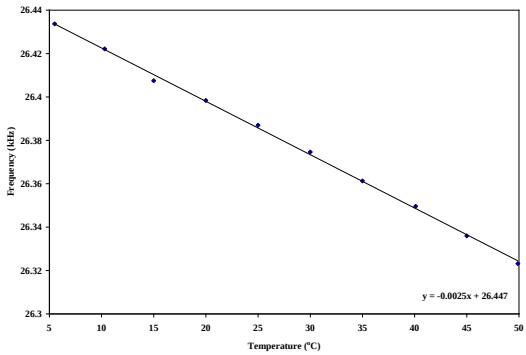

Figure 5.44 Temperature test of SL20 torque transducer (C2).

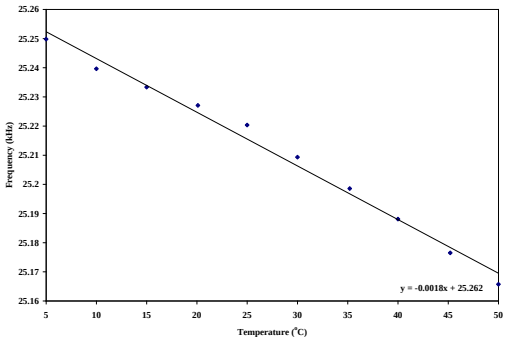

Figure 5.45 Temperature test of SL20 torque transducer (D2).

Table 5.12 Characteristics of torque transducer based on SL20 resonant sensor, C2.

Initial frequency	26.4 kHz
Q-value	1302
Span at full scale (±25 Nm)	1176 Hz
Sensitivity	23.5 Hz/N·m
Stability	0.02%
Repeatability	0.2%
Linearity	5.4%
Hysteresis	8.2%
Temperature sensitivity	2.5 Hz/^{o}C

Table 5.13 Characteristics of torque transducer based on SL20 resonant sensor, D2.

Initial frequency	25.2 kHz
Q-value	1050
Span at full scale (±25 Nm)	1134 Hz
Sensitivity	22.7 Hz/N·m
Stability	0.06%
Repeatability	0.3%
Linearity	2.2%
Hysteresis	0.7%
Temperature sensitivity	1.9 Hz/^{o}C

Both torque transducers have high Q-value (>1000) and show similar result of span (~500Hz) and sensitivity value (~24 Hz/Nm). The sensitivity of the torque transducer may be increased by either reducing cross-section of the sensor or reducing shaft diameter. However, the latter method will reduce the overload capability of the torque transducer as well.

C2 torque transducer show better results in stability and repeatability but poorer linearity and hysteresis when compare to D2 torque transducer. This may be due to temperature variation during the linearity test of C2 torque transducer, which is higher than D2. Linearity is the parameter that most affects to the performance of the torque transducer when compared to other parameters.

The temperature sensitivity of C2 torque transducer is higher than D2. This temperature characteristic is useful when considering the design on electronic circuit for temperature compensation. Using identical material for the shaft and TBTF sensor can minimise this effect.

5.1.8 Calibration of torque transducer based on SL20 resonant sensor

In order to investigate the performance of the torque transducer based on SL20 metallic TBTF resonant sensor to be implemented as torque transfer standard, the D2 torque transducer was calibrated at National

Physical Laboratory (NPL) in UK against Torque Standard Machine (Deadweight Lever-beam) as shown in figure 5.46. The room temperature was controlled at 20±1°C. NPL performed a range of calibration tests to evaluate the performance of this torque transducer based on the British Standard (BS 7882:1997) incorporating changes that will be implemented in next revision (BS 7882:2008). Parameters including repeatability, reproducibility, linearity, residual deflection, reversibility and uncertainty had been considered and classified according to the BS7882. Moreover, stability and creep test had been additionally investigated to provide more information.

Figure 5.46 NPL Torque Standard Machine (Deadweight Lever-beam).

Two adapters, one split clamp to fit square drive and one flange type both with 20 mm shaft (Fig. 5.47), were manufactured in order to fit the ETP-20 friction joints of NPL torque standard machine as shown in figure 5.48.

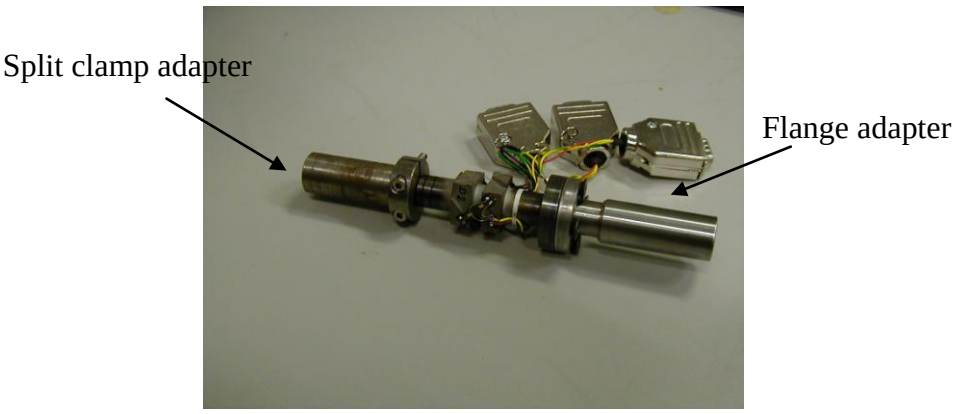

Figure 5.47 D2 torque transducer with two adapters.

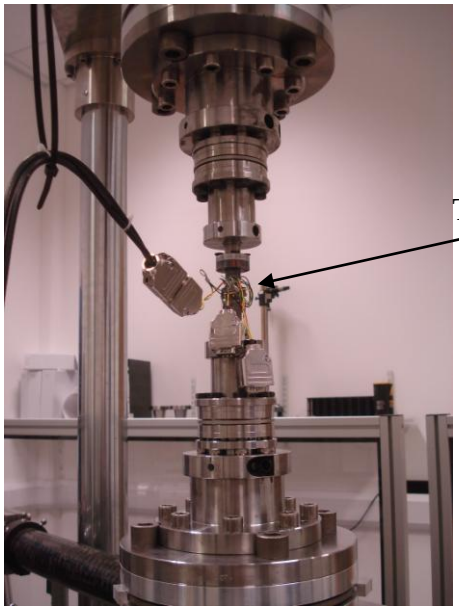

Figure 5.48 Set-up torque transducer with NPL torque standard machine.

The calibration range is up to 30Nm in clockwise direction and mode of calibration is in clockwise direction. Hewlett-Packard 894410A Vector Signal Analyser with resolution 0.5Hz and Kistler Type 5011 charge amplifier were used to monitor the resonance frequency of torque transducer during calibration. Torque value was increased and decreased for hysteresis information at 0° orientation. A one-minute waiting time was applied to stabilise the system after each change of torque increment. Torque transducer was also calibrated at 120° and 240° orientation in order to obtain the information for reproducibility. The data taken from the measurement is shown in Table 5.14.

Table 5.14 Calibration data of D2 torque transducer.

Nm	*f (Hz)*			
	0°		*120°*	*240°*
0	24984.0	24984.0	24990.8	24997.3
5	25103.6	25104.0	25111.3	25117.3
10	25216.9	25217.3	25226.0	25230.3
15	25327.0	25326.5	25336.5	25341.3
20	25436.5	25436.5	25445.0	25450.8
30	25655.5	25655.5	25661.8	25669.3
20	25436.0			
15	25325.5			
10	25215.5			
5	25103.3			
0	24984.0	24983.6	24991.3	24998.3

The calibration data was then analysed for each parameter according to BS 7882 as shown in Table 5.15. These calibration results will be used to compare with a transducer classification table in order to establish the devices classification.

Table 5.15 Calibration result of D2 torque transducer according to BS7882.

Nm	R_1	R_2	E_{it}	E_z	E_h
0				0.1490%	
5	0.3426%	0.7586%	0.3051%		-0.2842%
10	0.1339%	0.9895%	-0.0487%		-0.6162%
15	0.1459%	0.7991%	-0.2214%		-0.4365%
20	0.0000%	0.3861%	-0.0161%		-0.1105%
30	0.0000%	0.1490%	-0.0308%		

The uncertainty of calibration at 95% confidence level (k = 2) was calculated to be about 0.8% as shown in Appendix A.8.

According to BS 7882, the deflection value expressed in units other than those of torque, and increasing and decreasing torques have been applied, the following parameters; repeatability, reproducibility, error of interpolation, residual deflection, and reversibility, shall be determined for the classification of torque measuring devices. Table 5.16 is the classification result of D2 torque transducer for each parameter at each torque value.

Table 5.16 The classification result of D2 torque transducer.

Nm	R_1	R_2	E_{it}	E_z	E_h	*a*
0				1		
5	1	1	1		0.5	1
10	0.5	1	0.1		0.5	0.5
15	0.5	1	0.5		0.5	0.5
20	0.05	0.5	0.05		0.1	0.5
30	0.05	0.2	0.1			0.2

In addition, a lower limit of calibration shall be determined in order to ensure that the classification is consistent with the resolution of the torque indicator, which is the Vector Signal Analyser in this case. According to Equation 3.9 in Chapter 3, the ‘a’ value can be obtained if the resolution was known. In this case, the resolution of the indicator is 0.5Hz, and therefore the ‘a’ value was calculated based on BS 7882 as shown in Table 5.16.

From the calibration results (Table 5.16) and ‘a’ calculation, it is shown that this torque transducer meets the requirements for class 1. It is also found that the class of accuracy of torque transducer with SL20 metallic TBTF resonant sensors is limited by the resolution of the indicator (electronic display). Acquiring the indicating device with higher resolution would give a substantial benefit in improving the accuracy of this torque transducer.

Furthermore, the stability/creep test of the torque transducer was considered at 0 Nm and 30 Nm. The resonance frequencies at those two loads were recorded for 10 minutes in every 30 seconds with 1 minute

stabilisation before each measuring value. The recorded resonance frequencies were shown in Table 5.17.

Table 5.17 Stability test of D2 torque transducer at 0 Nm and 30 Nm.

Time	*f (Hz)*	
(second)	*0 Nm*	*30 Nm*
0	24998.7	25669.5
30	24998.7	25670.0
60	24999.2	25670.0
90	24999.2	25670.0
120	24999.2	25670.0
150	24999.2	25670.0
180	24999.2	25670.0
210	24998.7	25669.5
240	24999.2	25670.0
270	24999.2	25670.0

Time	*f (Hz)*	
(second)	*0 Nm*	*30 Nm*
300	24999.2	25670.0
330	24998.7	25669.5
360	24999.2	25670.0
390	24999.2	25670.0
420	24999.2	25670.0
450	24999.2	25670.0
480	24999.2	25670.0
510	24999.2	25669.5
540	24999.2	25670.0
570	24999.2	25670.0

Figure 5.49 and 5.50 illustrate the corresponding graphs of the stability test at 0Nm and 30Nm respectively. The results show that the standard deviation for both tests is less than 0.5 Hz, which is the limitation by the resolution of the indicator. For this reason, it is not possible to claim a stability value for the torque transducer unless a higher resolution indicator was used.

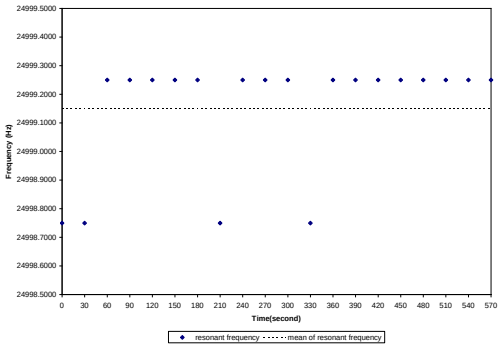

Figure 5.49 Stability test of D2 torque transducer at 0 Nm.

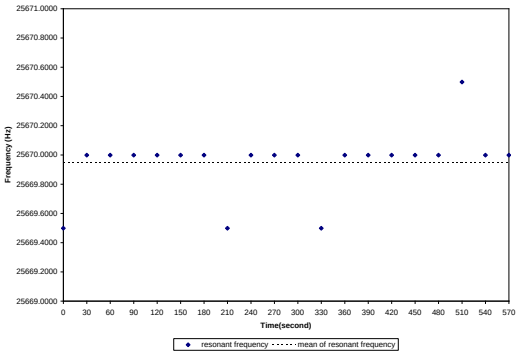

Figure 5.50 Stability test of D2 torque transducer at 30Nm.

CHAPTER 6

6. Miniturisation of Metallic TBTF Resonant Sensors (Design 2)

The latest successful miniature metallic TBTF resonant sensor, SL12, was developed and described in this chapter. The summary of key findings, configuration, characteristics, performance in a torque transducer, and the calibration result of torque transducer based on this design are also included.

6.1 Design 2 (SL12)

6.1.1 Configuration

The latest version of the miniaturised metallic TBTF resonant sensor is SL12 which has reduced the size by 70% from the original one (SL40). The configuration of SL12 is the same as SL20 sensor. Figure 6.1 shows a photo of SL12 TBTF resonant sensor. The engineering drawing of SL12 is shown in Appendix B.1.

Figure 6.1 SL40 and SL12 metallic TBTF resonant sensor.

6.1.2 Fabrication

The same material and fabrication process were applied for SL12 sensor. Figure 6.1 demonstrates a plate of SL12 sensor with 89 x 76 mm dimension. Due to the smaller size of SL12 sensors, therefore there are 30 sensors; 6 groups of 5 sensors per plate.

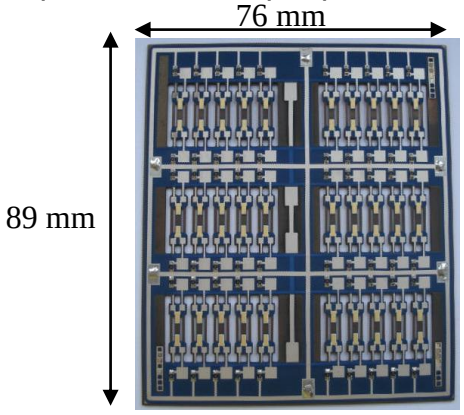

Figure 6.2 Batch production of SL12 metallic TBTF resonant sensors.

The dimension of SL12 sensors was also measured at ETC by using the microscope as shown in figure 6.3.

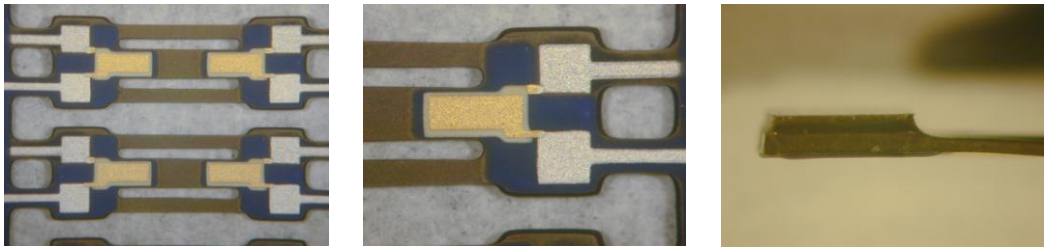

(a) sensor and tine dimension *(b) PZT dimension* (c) substrate and tine thickness

Figure 6.3 Picture of SL12 sensors taken from microscope.

The dimension of measured SL12 resonant sensor was summarised in Table 6.1.

Table 6.1 Dimension of SL12 TBTF resonant sensor.

Parameter	*Design Dimensions*	*Actual Dimensions*
Total length	12 mm	12.2±0.2 mm
Tine length	6 mm	6.0±0.1 mm
Central tine width	1.3 mm	1.3±0.1 mm
Outer tine width	0.65 mm	0.63±0.08 mm
Gap width	0.5 mm	0.5±0.1 mm
Tine thickness	0.25 mm	0.21±0.09 mm
PZT width	1 mm	1±0.1 mm
PZT length	2.5 mm	2.5±0.1 mm
PZT thickness	40 μm	38±4 μm

6.1.3 Polarisation

The method and condition of polarisation of SL12 sensors are the same as for SL20 sensors.

6.1.4 Initial Checks

Figure 6.4 illustrates the first four modes of vibrations of SL12 resonant sensor modelled by FEA.

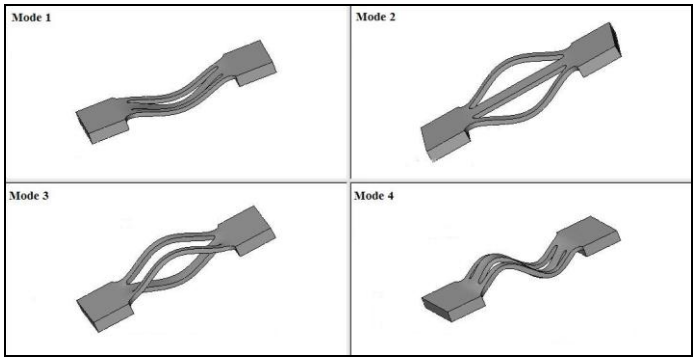

Figure 6.4 First four vibration modes of SL12 resonant sensor from FEA.

In order to confirm successful operation of the driving and sensing mechanisms, the resonant frequency of the sensors were measured in the open-loop configuration. The resonant frequencies of several plates of SL12 resonant sensors were measured as shown in the Appendix B.2. There is the variation of the resonance frequency within the same plate and between the different plates of SL12 sensors as occurred to SL20 sensors. This variation can also be attributed to the uncertainties in sensors manufacturing process described in Chapter 4. The resonance frequencies between different plates are varied from 29-40 kHz with the standard deviation of 2215. Figure 6.5-6.7 show three examples of the resonance frequency variation of plate 1, plate 2, and plate 3. The resonance frequencies of sensors on plate 1 (Fig. 6.5) are increasing from 32kHz to 35kHz for sensors 1(1) to 1(20) then, the frequency is dropped to about 33kHz for sensor 1(21) and continually increasing until 34kHz for sensor 1(30). The standard deviation of frequency variation for plate 1 is about 738. The resonance frequencies of sensors on plate 2 (Fig. 6.6) vary all over the plate whilst the sensors 2(11) to 2(15) having similar value of resonance frequency. The standard deviation of the resonance frequency variation obtained for plate 2 is 283. The resonance frequency variation of sensors on plate 3 (Fig. 6.7) is clearly divided into two groups with the first 20 sensors show higher resonance frequencies than the remaining 10 sensors. The standard deviation of the resonance frequency variation for plate 3 is 1165.

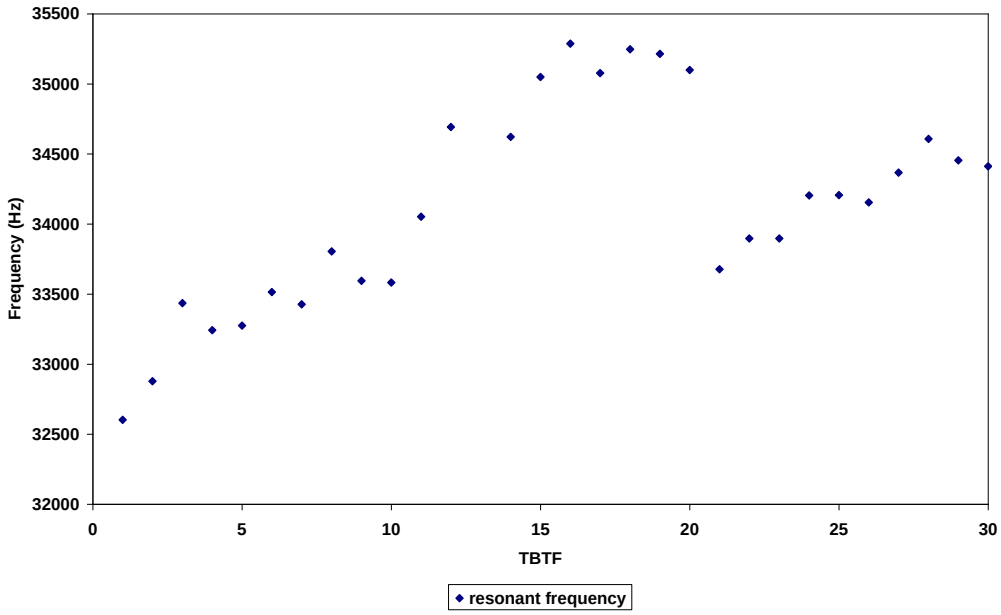

Figure 6.5 The resonance frequency of SL12 resonant sensors plate 1.

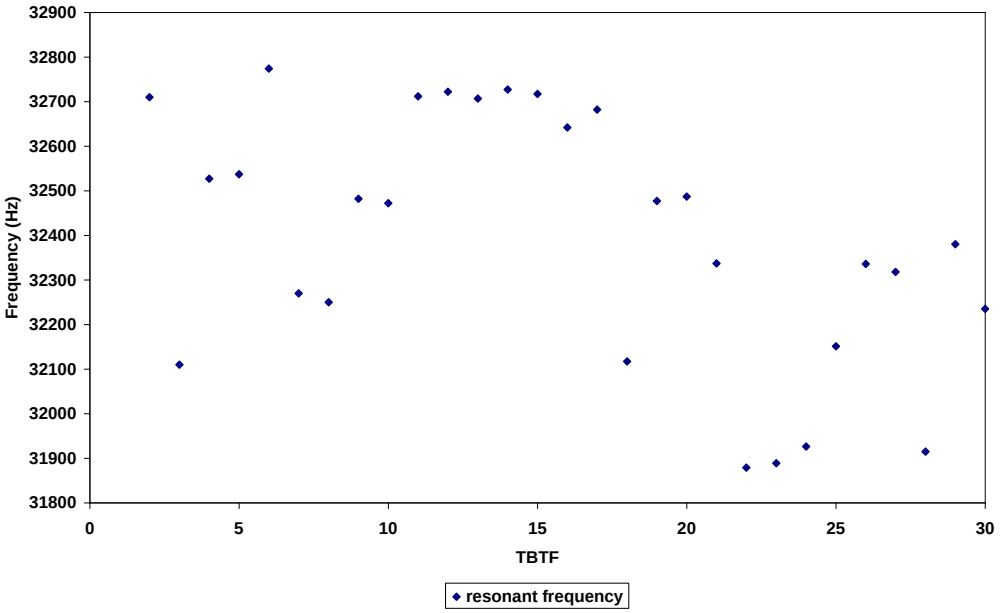

Figure 6.6 The resonance frequency of SL12 resonant sensors plate 2.

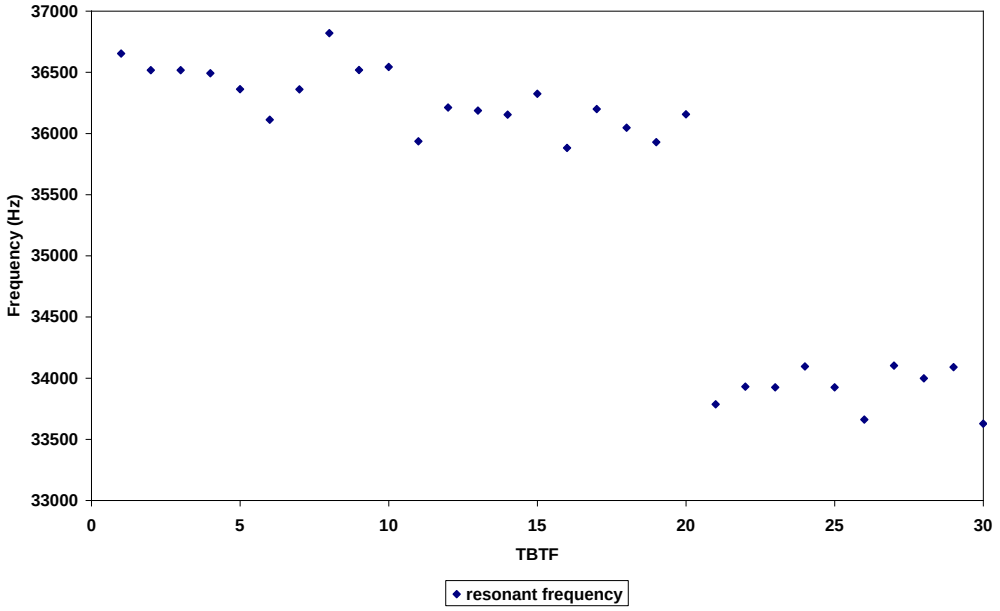

Figure 6.7 The resonance frequency of SL12 resonant sensors plate 3.

Later the Q-value variation with position was considered. Table 6.2 illustrates the Q-value of sensors from plate 3 which is varied from 86 to 1222. The Q-value of the sensor 3(8) and 3(24) can not be measured due to very low piezoelectric property of these two sensors. From the results it is shown that the Q-value of SL12 sensors on plate 3 is inconsistent as occurred to SL20 sensors on plate B. The Q-value variation of SL12 sensors on other plates shows similar result.

Table 6.2 Resonance frequency and Q-value of SL12 resonant sensors plate 3.

TBTF	*f (Hz)*	*Q-value*	*TBTF*	*f (Hz)*	*Q-value*
3(1)	36652.5	1222	3(16)	35881.0	1104
3(2)	36517.0	1124	3(17)	36198.5	254
3(3)	36517.0	664	3(18)	36046.0	627
3(4)	36492.0	417	3(19)	35928.0	575
3(5)	36362.0	1212	3(20)	36155.5	391
3(6)	36112.0	481	3(21)	33785.0	588
3(7)	36359.5	808	3(22)	33930.0	103
3(8)	36819.5	*N/A*	3(23)	33925.0	565
3(9)	36519.0	730	3(24)	34095.0	*N/A*
3(10)	36544.0	96	3(25)	33925.0	339
3(11)	35936.0	898	3(26)	33660.0	224
3(12)	36211.0	1035	3(27)	34102.5	86
3(13)	36186.0	629	3(28)	33997.5	680
3(14)	36153.5	1205	3(29)	34090.0	341
3(15)	36323.5	908	3(30)	33627.5	1121

6.1.5 Characteristics

The amplitude-frequency response for the third mode of vibration of one SL12 resonant sensor (G2) displayed on the Vector Signal Analyser is illustrated in figure 6.8. The resonance frequency (f_0) was measured to be about 40.0825 kHz and Q-value was calculated to be 1600.

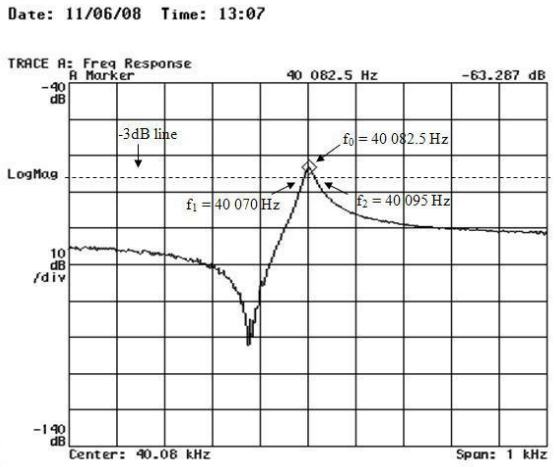

Figure 6.8 Amplitude-frequency response of SL12 resonant sensor (G2).

Other characteristics such as the stability, repeatability and temperature sensitivity of SL12 sensor were also investigated in the same condition as SL20 sensor at Brunel University.

For the stability test, the resonance frequencies of SL12 sensor were recorded over a time period of 48 hours in unequal time steps. The recorded data is shown in Table 6.3. The default frequency resolution was 0.5Hz.

Table 6.3 Stability test of SL12 resonant sensors.

Hours	*f (kHz)*
2	40.1150
4	40.1120
20	40.1210
22	40.1115
24	40.1085
26	40.1085
46	40.1095
48	40.1035

Figure 6.9 displays the stability test result of SL12 sensor. The standard deviation was found to be 5.2Hz.

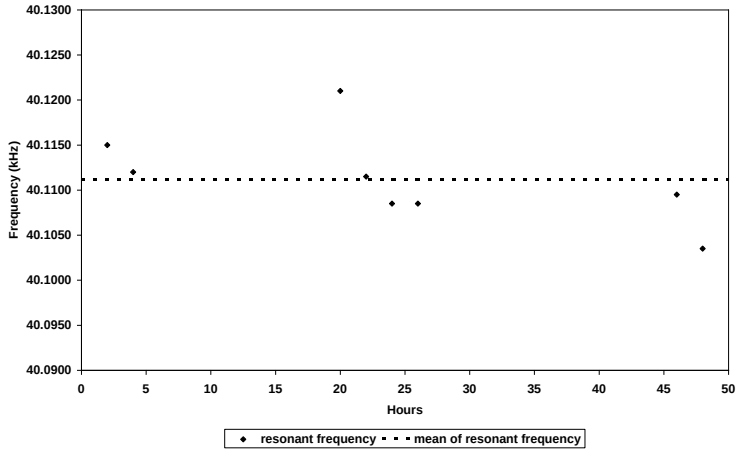

Figure 6.9 Stability test of SL12 TBTF resonant sensor for 48 hours.

Then, repeatability investigation was conducted in the same experimental set-up as for the SL20 sensor. The measured resonance frequencies are shown in Table 6.4.

Table 6.4 Repeatability test of SL12 resonant sensors.

No.	*f (kHz)*	*No.*	*f (kHz)*
1	40.1071	11	40.1068
2	40.1078	12	40.1070
3	40.1073	13	40.1063
4	40.1070	14	40.1066
5	40.1074	15	40.1076
6	40.1063	16	40.1069
7	40.1065	17	40.1074
8	40.1060	18	40.1071
9	40.1071	19	40.1074
10	40.1074	20	40.1068

Figure 6.10 shows that the standard deviation of the resonance frequency is 0.5Hz for the repeatability test.

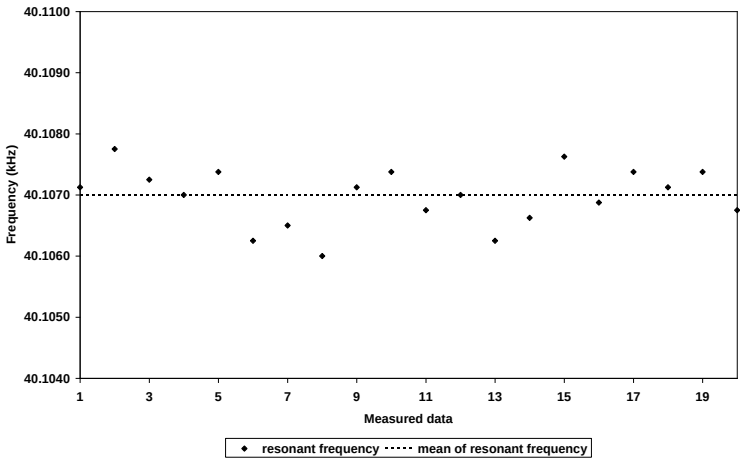

Figure 6.10 Repeatability test of SL12 TBTF resonant sensors.

Lastly, the temperature characteristic was investigated with the same experimental set-up as SL20 sensor. The frequency response of SL12 sensor at each temperature point was recorded as shown in Table 6.5.

Table 6.5 Temperature test of SL12 resonant sensors.

T (°C)	*f (kHz)*
-30	40.4070
0	40.2535
30	40.1005
60	39.9385
90	39.7805

The temperature characteristic of SL12 sensor displayed in figure 6.11 is without any kind of temperature compensation and shown that the temperature sensitivity is approximate 5.2Hz/°C in the temperature range between -30°C and 90°C.

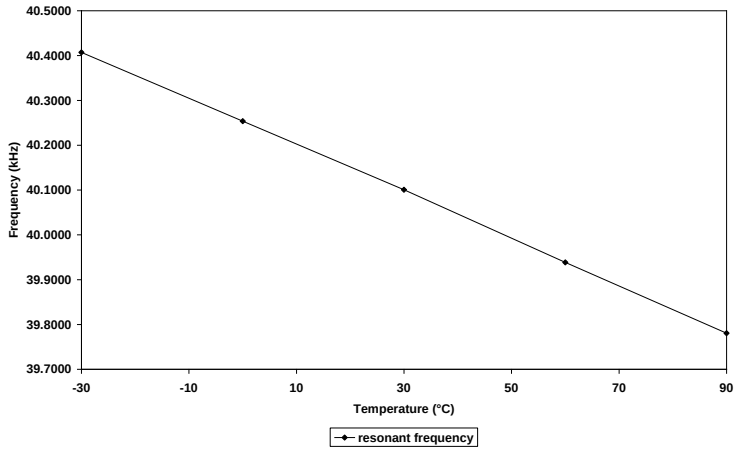

Figure 6.11 Temperature test of SL12 TBTF resonant sensors.

Table 6.6 summarises the characteristics which include the stability, repeatability, and temperature performance of SL12 TBTF resonant sensors.

Table 6.6 Characteristics of SL12 TBTF resonant sensor.

f_0 (kHz)	10% of f_0 (Hz)	Stability		Repeatability		Temperature	
		SD	%	SD	%	Hz/^oC	%
40.0825	4008.25	5.2	0.13	0.5	0.01	5.2	0.13

6.1.6 Torque Transducer Based on SL12 Resonant Sensor

The torque shaft was designed and four SL12 TBTF resonant sensors were mounted onto the torque shaft by laser-welding as shown in figure 6.12. The drawing of the torque shaft design is shown in Appendix B.3.

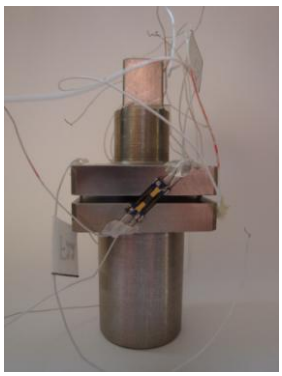

Figure 6.12 Torque transducer with SL12 TBTF resonant sensors.

One sensor was damaged at the soldering pad due to the heat from the laser during the laser-welding process because the soldering pads are very close to the edge of the slot machined for mounting. Consequently, only 3 of 4 sensors, which are F23, G1, and I5 were calibrated. Table 6.7 shows the resonant frequency and the Q-value of F23, G1, and I5 sensors before and after mounting to the torque shaft.

Table 6.7 Resonant frequency and Q-value before and after mounting to the shaft of F23, G1, and I5 sensors.

TBTF	f_0 (kHz)		Q-value	
	before	after	before	after
F23	33.4175	34.5530	1215	1501
G1	39.4750	39.7360	987	681
I5	41.2125	41.4900	916	2075

From the results in Table 6.7, it is shown that the resonant frequency was less affected from the mounting process that is contrast to the Q-value which was influenced by this process. The Q-value of F23 and I5 are increased after mounting that may be contribute to the firm mounting of the sensor results in strong vibration and also prevents the energy losses from the resonating elements into the surrounding area. Nevertheless, the Q-value of G1 sensor was reduced which could be due to many factors such as the heat from the laser affecting to the PZT performance, or the short-circuit between the seam welding and the soldering pad which may cause the loss of the energy via this path, etc.

6.1.7 Calibration of Torque Transducer Based on SL12 Resonant Sensor

Torque transducer based on SL12 metallic TBTF resonant sensor was calibrated at Brunel University against torque test rig as shown in figure 6.13. The temperature variation during the calibration is approximate 1°C. Hewlett-Packard 894410A Vector Signal Analyser with resolution 0.5Hz and Kistler Type 5011 charge amplifier were used to monitor the resonance frequency. The calibration was performed according to BS7882:2008 which includes repeatability, reproducibility, linearity, residual deflection, and reversibility parameters and then the accuracy of the torque transducer was classified. The uncertainty was also evaluated. Moreover, stability test was investigated for more information.

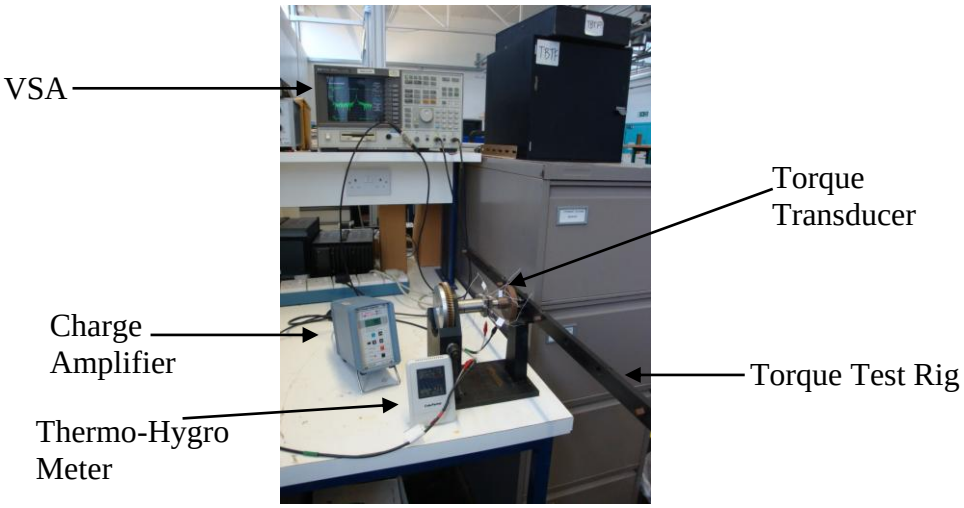

Figure 6.13 Torque calibration system.

The calibration range is up to 20Nm and the mode of operation is in clockwise direction. The calibration diagram is shown in figure 6.14.

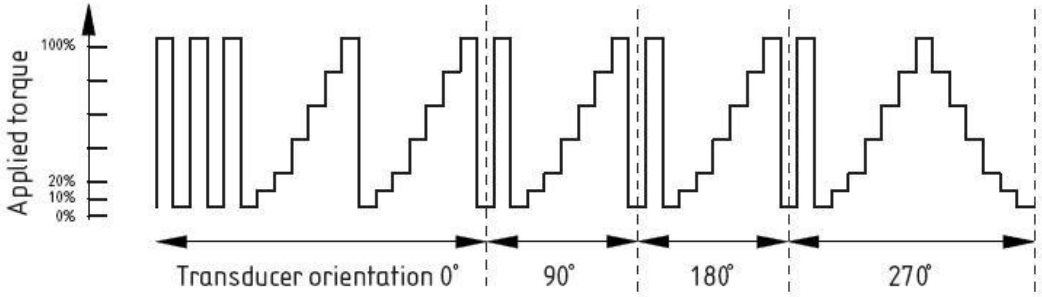

Figure 6.14 The calibration sequence of torque transducer with square drives for both increasing and decreasing torques, classes 0.05 to 5.0.

At 0° orientation, two cycles of increasing torque were carried out for repeatability evaluation. A one-minute waiting time was applied to stabilise the system after each change of torque increment. Torque transducer was also calibrated at 90°, 180° and 270° orientation in order to obtain the information for reproducibility. Moreover, torque value was increased and decreased for hysteresis information at 270° orientation.

The data taken from the calibration of 3 sensors are shown in Table 6.8-6.10.

Table 6.8 Calibration data of F23 torque transducer.

Nm	*f (Hz)*				
	0°		*90°*	*180°*	*270°*
0	34531.5	34531.5	34531.0	34530.0	34531.5
4.224	34835.9	34835.9	34834.9	34833.9	34835.9
7.218	35056.3	35056.4	35055.0	35054.5	35056.5
13.206	35503.0	35502.5	35503.5	35502.0	35504.0
16.2	35719.0	35718.2	35719.0	35718.9	35719.1
19.17	35925.5	35926.5	35927.0	35925.5	35925.5
16.2					35718.0
13.206					35502.5
7.218					35056.0
4.224					34835.5
0	34531.5	34531.0	34532.0	34530.0	34530.5

Table 6.9 Calibration data of G1 torque transducer.

Nm	*f (Hz)*				
	0°		*90°*	*180°*	*270°*
0	39730.5	39726.7	39742.3	39727.5	39731.8
4.224	40037.5	40034.5	40050.0	40037.3	40040.5
7.218	40237.5	40233.3	40247.0	40234.0	40238.0
13.206	40599.7	40597.3	40615.5	40598.8	40602.3
16.2	40758.7	40755.3	40766.8	40756.8	40759.8
19.17	40914.2	40912.3	40926.3	40909.3	40912.3
16.2					40748.5
13.206					40600.8
7.218					40240.8
4.224					40039.0
0	39729.7	39728.0	39740.3	39728.0	39732.3

Table 6.10 Calibration data of I5 torque transducer.

Nm	*f (Hz)*				
	0°		*90°*	*180°*	*270°*
0	41467.8	41467.7	41467.5	41469.7	41469.5
4.224	41714.3	41714.3	41714.3	41716.3	41716.3
7.218	41856.5	41856.0	41857.2	41859.7	41859.3
13.206	42121.8	42120.7	42123.7	42126.2	42125.2
16.2	42274.0	42275.8	42275.2	42277.3	42273.7
19.17	42449.7	42448.8	42450.2	42455.5	42455.7
16.2					42275.2
13.206					42123.7
7.218					41858.3
4.224					41715.7
0	41467.7	41467.0	41467.7	41470.0	41468.8

The calibration data of all three sensors were then analysed for each parameter according to BS 7882 as shown in Table 6.11-6.13. These calibration results will be used to compare with a transducer classification table in order to establish the devices classification.

Table 6.11 Calibration result of F23 torque transducer according to BS7882.

Nm	R_1	R_2	E_{it}	R_0	R_3	*a*
0				0.07%		
4.224	0.01%	0.176 %	0.24%		0.12%	615
7.218	0.03%	0.19%	0.17%		0.10%	1050
13.206	0.052 %	0.103 %	0.08%		0.15%	1922
16.2	0.07%	0.12%	0.01%		0.09%	2358
19.17	0.07%	0.14%	0.03%			2790

Table 6.12 Calibration result of G1 torque transducer according to BS7882.

Nm	R_1	R_2	E_{it}	R_0	R_3	*a*
0				0.1695%		
4.224	0.2448%	0.8923%	0.2179%		0.4858%	521
7.218	0.0983%	0.4456%	0.3111%		0.5434%	890
13.206	0.1440%	0.4588%	0.3522%		0.1723%	1629
16.2	0.0246%	0.4630%	0.2912%		1.0945%	1999
19.17	0.1480%	0.2956%	0.0806%			2365

Table 6.13 Calibration result of I5 torque transducer according to BS7882.

Nm	R_1	R_2	E_{it}	R_0	R_3	*a*
0				0.0763%		
4.224	0.0057%	0.1020%	0.0229%		0.2030%	434
7.218	0.1202%	0.3165%	0.0081%		0.2566%	741
13.206	0.1529%	0.3812%	0.0211%		0.2287%	1356
16.2	0.2170%	0.4340%	0.0567%		0.1865%	1663
19.17	0.1017%	0.4320%	0.0210%			1968

Then the torque transducers were classified according to BS7882 as shown in Table 6.14-6.16.

Table 6.14 Classification result of F23 torque transducer.

Nm	R_1	R_2	E_{it}	R_0	R_3	*a*
0				0.5		
4.224	0.05	0.2	0.5		0.1	0.5
7.218	0.1	0.2	0.5		0.1	0.2
13.206	0.2	0.2	0.2		0.2	0.2
16.2	0.2	0.05	0.05		0.1	0.1
19.17	0.2	0.05	0.1			0.1

Table 6.15 Classification result of G1 torque transducer.

Nm	R_1	R_2	E_{it}	R_0	R_3	*a*
0				1		
4.224	0.5	1	0.5		0.5	0.5
7.218	0.2	0.5	1		0.5	0.5
13.206	0.5	0.5	1		0.2	0.2
16.2	0.05	0.5	1		1	0.2
19.17	0.5	0.5	0.2			0.1

Table 6.16 Classification result of I5 torque transducer.

Nm	R_1	R_2	E_{it}	R_0	R_3	*a*
0				0.5		
4.224	0.05	0.2	0.05		0.2	0.5
7.218	0.5	0.5	0.05		0.5	0.5
13.206	0.5	0.5	0.05		0.2	0.2
16.2	0.5	0.5	0.2		0.2	0.2
19.17	0.5	0.5	0.05			0.2

From the classification results, it is shown that F23, and I5 torque transducers meet the requirements for class 0.5 whilst the G1 torque transducer is classified into class 1. The accuracy of the G1 torque transducer is lower may be due to the condition during the calibration was disturbed.

The uncertainties of calibration at 95% confidence level (k = 2) were calculated to be 0.5%, 0.2%, and 0.7% for I5, F23, and G1 torque transducers respectively. The calculation of the uncertainty for all torque transducers is demonstrated in the Appendix B.4.

When compare to the calibration result of SL20 torque transducer, SL12 torque transducer shows better performance in general which is corresponded to the FEA analysis in Chapter 4 that the smaller sensor is less affected from the lateral force when the torque is applied.

The stability test was also investigated at 0 Nm and 20 Nm for three torque transducers for more understanding in the performance. The resonance frequency was measured at every 30 seconds for 10 minutes with 1 minute stabilisation time before each measuring value. The resonance frequencies of all three torque transducers are shown in Table 6.17.

Figure 6.15-6.17 illustrate the corresponding graph of the stability test at 0 Nm of F23, G1, and I5 torque transducers with the standard deviation 1Hz, 2Hz, and 0.6Hz respectively.

Table 6.17 Stability test of SL12 torque transducer.

Time (minutes)	*f (Hz)*					
	F23		*G1*		*I5*	
	0 Nm	*20 Nm*	*0 Nm*	*20 Nm*	*0 Nm*	*20 Nm*
0.5	34521.0	35884.5	39723.0	41019.0	41455.3	42434.7
1	34520.5	35882.5	39728.0	41019.7	41454.3	42430.5
1.5	34522.0	35882.0	39724.5	41019.2	41454.8	42431.2
2	34522.0	35882.5	39723.0	41019.7	41454.8	42435.2
2.5	34522.0	35881.5	39724.3	41019.2	41454.3	42434.2
3	34522.0	35883.5	39720.7	41019.2	41454.3	42434.2
3.5	34521.5	35883.5	39727.0	41020.8	41454.8	42434.7
4	34522.0	35881.5	39724.3	41019.2	41454.3	42433.7
4.5	34522.5	35881.0	39723.8	41019.2	41454.8	42434.2
5	34522.5	35879.2	39726.5	41020.8	41454.3	42433.7
5.5	34522.0	35879.7	39724.8	41020.8	41453.8	42433.7
6	34522.5	35879.2	39725.8	41021.8	41453.8	42433.7
6.5	34522.5	35883.5	39723.8	41020.8	41454.3	42433.2
7	34524.0	35880.2	39725.8	41020.8	41454.3	42433.7
7.5	34524.0	35881.5	39723.0	41020.3	41454.3	42434.2
8	34523.5	35879.2	39720.2	41019.7	41453.8	42434.2
8.5	34523.0	35882.0	39722.8	41020.3	41453.8	42434.2
9	34524.0	35878.7	39725.5	41020.3	41453.8	42433.7
9.5	34523.0	35882.5	39726.3	41019.7	41452.7	42433.2
10	34523.5	35879.7	39723.3	41020.3	41453.3	42434.2

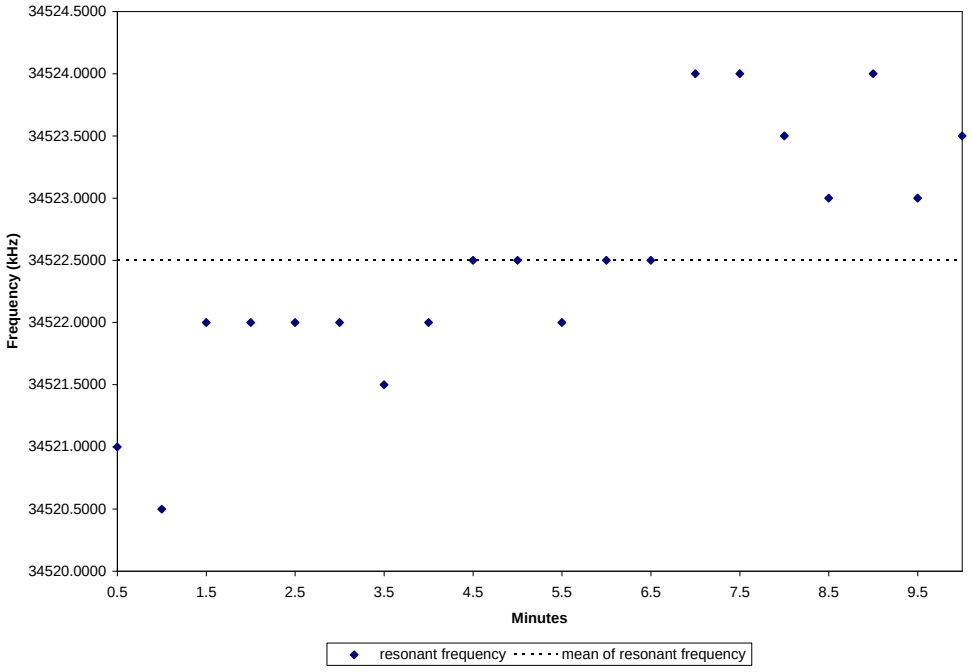

Figure 6.15 Stability test of F23 torque transducer at 0Nm.

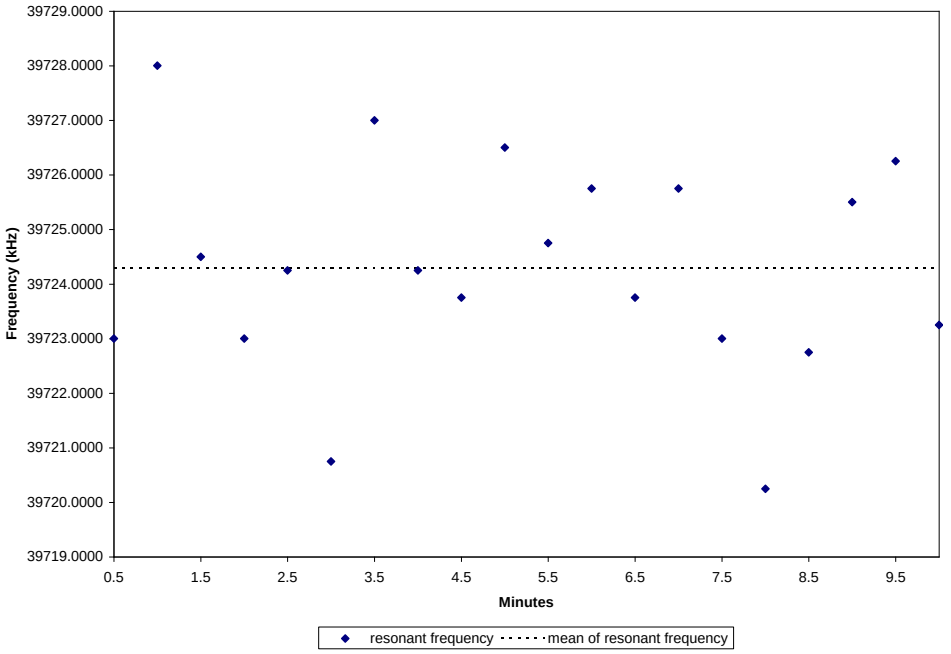

Figure 6.16 Stability test of G1 torque transducer at 0Nm.

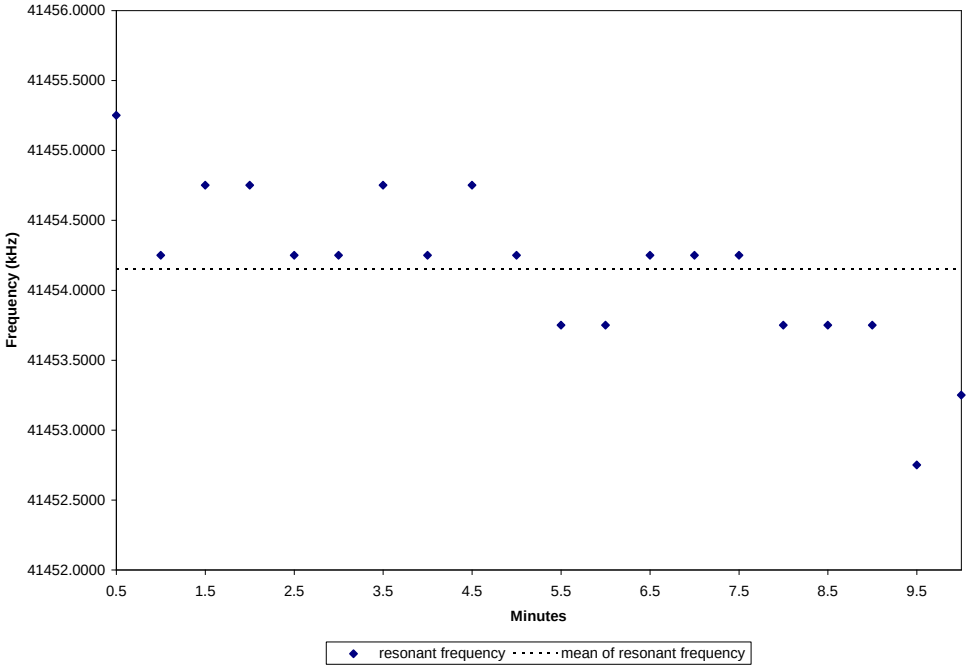

Figure 6.17 Stability test of I5 torque transducer at 0Nm.

From the results, it is found that I5 torque transducer shows the best stability performance whilst G1 torque transducer presents the poorest performance.

The corresponding stability graphs at 20Nm were shown in figure 6.18-6.20. The standard deviation was calculated to be 1.7Hz, 0.7Hz, and 1.1Hz for F23, G1, and I5 torque transducers respectively.

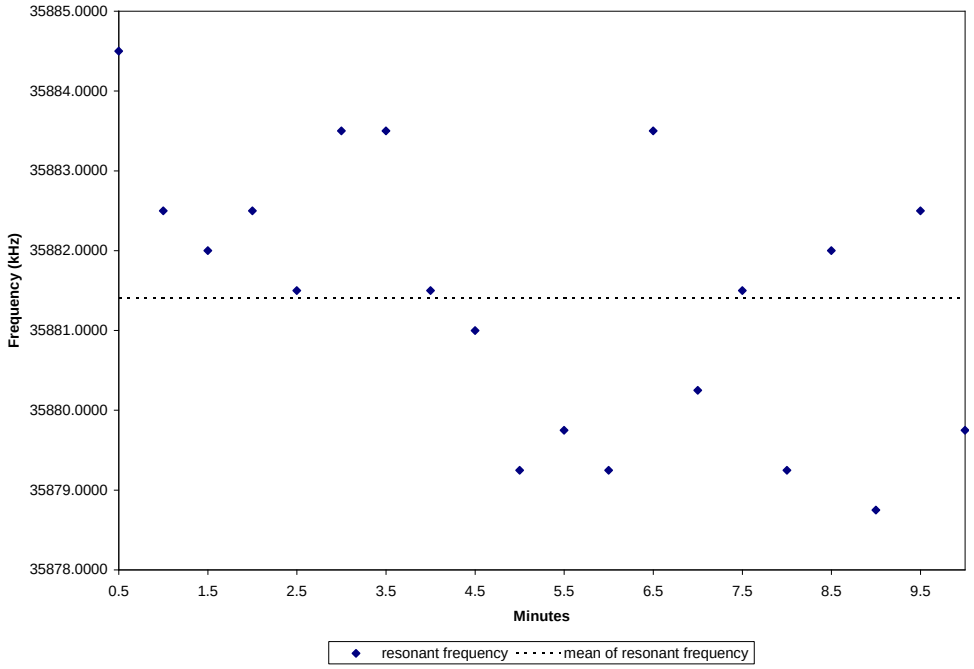

Figure 6.18 Stability test of F23 torque transducer at 20Nm.

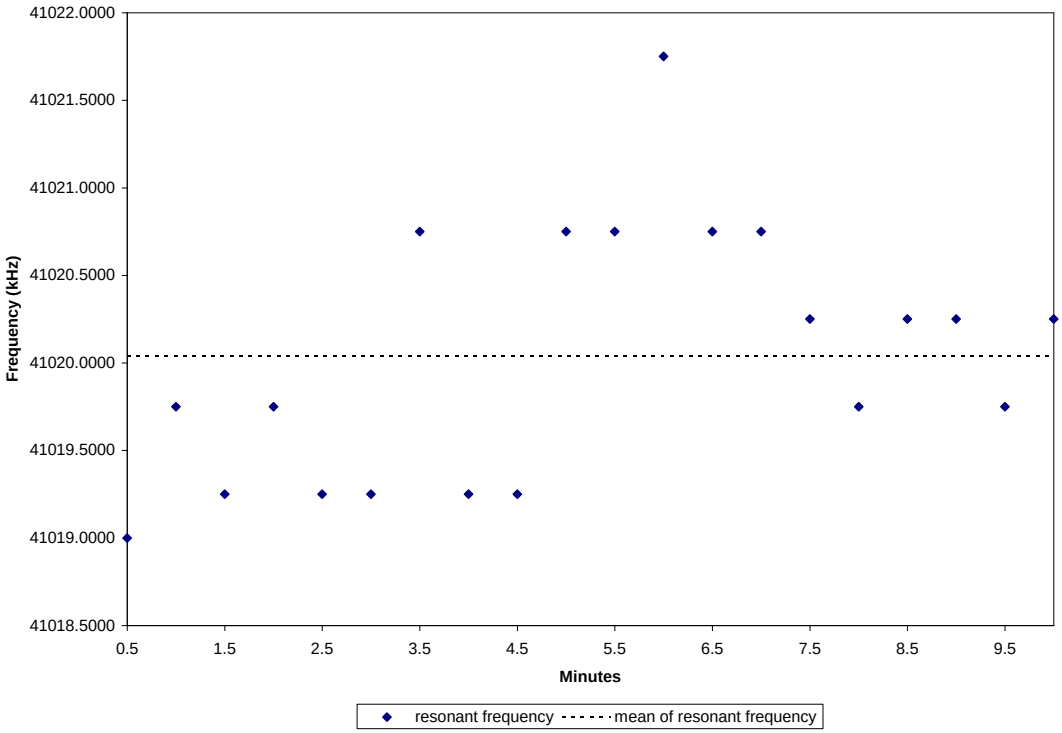

Figure 6.19 Stability test of G1 torque transducer at 20Nm.

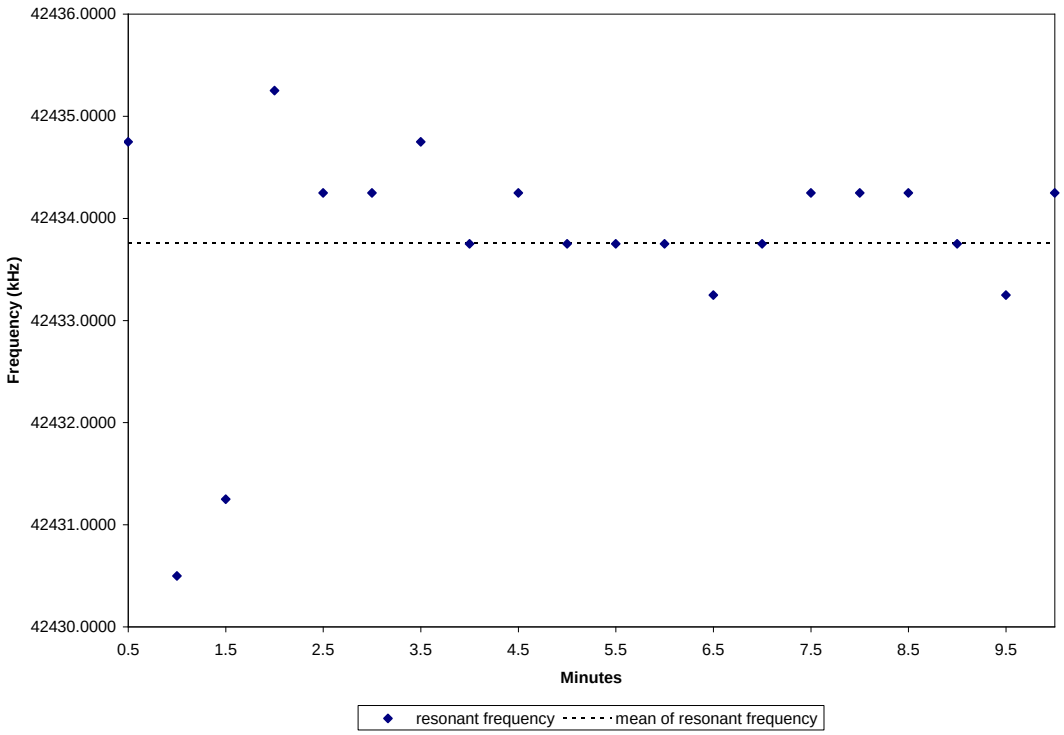

Figure 6.20 Stability test of I5 torque transducer at 20Nm.

Contrary to the stability results at 0Nm, G1 torque transducer shows the best performance among three torque transducers. I5 and F23 torque transducer show similar performance.

The standard deviations and percentages of mean value of the resonant frequency for all three torque transducers from the stability test at 0Nm and 20Nm is summarized in Table 6.18.

Table 6.18 Stability results of SL12 torque transducer.

TBTF	*SD (Hz)*		*% of mean value*	
	0 Nm	*20 Nm*	*0 Nm*	*20 Nm*
F23	1.0	1.7	0.003	0.005
G1	2.0	0.7	0.005	0.002
I5	0.6	1.1	0.001	0.003

In conclusion, the torque transducer is more stable at zero load except for G1 torque transducer. As mentioned previously about the environmental condition during the testing of G1 torque transducer, it is quite difficult to conclude the stability performance of this torque transducer at this stage.

Chapter 7

7. Conclusions and Further Work

This chapter summarises and concludes the research work carried out on a new torque transducer using metallic TBTF resonant sensors as the sensing element, for use as a torque transfer standard. Finally, suggestions for further work are also included.

7.1 Conclusions

Previous research work has shown that metallic resonant sensors offer some significant advantages over strain gauges in load and torque applications. Initial tests, however, showed that the SL40 TBTF sensor was not suitable for use in a torque transfer standard due to its size and subsequent sensitivity to parasitic lateral forces.

In order to reduce the overall length of the SL40 sensor, care had to be taken to ensure that the new design would not be detrimental to performance characteristics such as Stability, Repeatability, Temperature Sensitivity, and especially Overload Capability. During the course of this research two new smaller versions of the sensor were produced.

(a) Firstly the SL20 device was manufactured and characterised. The results were compared with previously published material and this work formed the basis of the following publication:

Intiang, J., Weidenmuller, J., Rakowski, R.T., Jones, B.E., Cheshmehdoost, A. (2007) Characteristics of 9mm Metallic Triple-Beam Tuning Fork Resonant Sensor. *Sensors and their Applications XIV,* 76, 6 pages. (see Appendix C)

Additionally, investigations were carried out of on how manufacturing processes affected yield, gain, and frequency distributions within batches and across batches, in order to better understand their impact on the next smaller version of the sensor.

(b) A torque transducer using the SL20 sensor was constructed and calibrated at the National Physical Laboratory, falling into class of accuracy 1 category, uncertainty 0.8% (Transfer Standard Classification). Analysis showed a reduction of 52% in the measurement errors due to lateral forces (compared to the large SL40 sensor). This was a significant step towards the establishment of a torque transfer standard using this technology and the results were presented as a key note lecture at:

Intiang, J., DeGolier, E., Rakowski, R.T., Jones, B.E., Cheshmehdoost, A. (2009) Use of Metallic Resonant Sensor in Torque Measurement Transfer Standard. *Sensor+Test Conference 2009*, 1, 71-76. (see Appendix D)

(c) Finally the SL12 sensor was designed. This represented the smallest size possible based on the design criteria to maintain the tine cross sectional area and from FEA analysis this showed a reduction of 80% in measurement errors due to lateral forces. A torque transducer using the SL12 sensors was made and calibration showed a class of accuracy 0.5 category, uncertainty 0.2% (Transfer Standard Classification).

(d) The author's work was awarded a £2,000 scholarship by the Worshipful Company of Scientific Instrument Makers (WCSIM), London. The research work was presented to WCSIM in SIMposium 2008 (4th March 2008). The title of the presentation was Miniaturisation of Metallic Resonant Sensors for Torque Measurement Applications. The research project and presentation were judged by the conference panel to be 'Highly Commended' and was judged to be a very close second to the winner (see Appendix E)

(e) The main difficulties encountered during the research programme stemmed from a lack of fabrication facilities at Brunel University, hence lack of full control over process step variables. Additionally, an improved class of accuracy transfer standard would have been achieved with these sensors if a more sophisticated electronic measurement and indicator system was available.

7.2 Expanded Summary

7.2.1 Introduction

The conventional resistive strain gauge-based torque transducer is widely used as the torque transfer standard in many laboratories and industries. The metallic TBTF resonant sensors-based torque transducer designed by Yan, et al (*2005a*) was proposed in order to overcome some problems associated with these conventional torque transducer based on strain gauges. The output signal obtained from the metallic TBTF resonant sensor is in frequency form, which is easily compatible to the digital circuitry, therefore the analogue-to-digital conversion unit required with strain gauges can be eliminated, resulting in more convenient and lower cost of the torque measurement system. Furthermore, the frequency signal can be measured with high accuracy so the resolution achievable from using the metallic TBTF resonant sensor would be as good as strain gauges. Moreover, the frequency signal is not dependent on the amplitude of the electrical signals and the measurement accuracy is not limited by the signal-to-noise ratio as occurs with an analogue signal obtained from the strain gauges, therefore the metallic TBTF resonant sensors provide better long-term stability. In addition, the output signal obtained from strain gauges is very low when compared to the metallic

TBTF resonant sensors at the same strain level. In order to obtain a measurable output signal, the surface strain of the strain gauges has to be designed in order to approach the elastic limit of the sensing element, hence the overload capability of the strain gauges is limited by this factor. Finally, the installation of the metallic TBTF resonant sensors is not labour-intensive as with strain gauges.

The first prototype of the metallic TBTF resonant sensor is too large for many current applications which have limited space for installing torque transducers. Therefore, further research work is required to understand the performance impact of any miniaturisation process of the sensor. Moreover, FEA analysis has shown that reducing the overall size of the sensor can minimise the error from the lateral force, which is one of the parasitic loads that affects to the accuracy of the torque measurement. Alternatively, it has been suggested that a spoke-pinned wheel configuration can also be used as the torque shaft with the sensors mounted at 90° to the shaft axis in order to experience only tensile force through the spoke. However, that design has additional size and construction problems so in this project the existing torque shaft design requires the sensors to be mounting at 45° to the shaft axis, used with the miniaturised sensors. The miniaturisation process was achieved by reducing the overall length by 50% (SL20) and 70% (SL12) from the first prototype (SL40) which has the total length of 40mm. According to the FEA analysis, the measurement errors due to lateral forces were reduced by 52% and 80% for SL20 and SL12 respectively. In addition to this advantage, the footprint of the resonant sensor is smaller so the cost of fabrication per device is lower.

In the miniaturisation process, the PZT paste thick-film printing process is a physical limitation to the size reduction because there is a danger that a smaller piezoactuator might not be able to excite the stiffer tines when the size of the sensor was reduced. The strategy adopted for this design process was to maintain the tine cross-sectional area, roughly about 0.4 mm^2, to maintain the overload capability resulting in reduced connector and mounting geometry whilst maintaining the area of the PZT elements.

7.2.2 Metallic TBTF Resonant Sensor Fabrication

The metallic TBTF resonant sensor consists of three parallel beams (tines) and joined to the substrate at each end. It was etched from stainless steel in which the vibrations are driven and detected by thick-film printed piezoelectric elements. The resonator substrate was fabricated by a photochemical etching technique and the thick-film piezoelectric elements were deposited by a standard screen-printing process. The combination of these two batch-fabrication processes provides the opportunity for mass production of the sensor and hence low cost. The optimum mode of vibration for this design is the mode when the central tine vibrates in anti-phase with the two outer tines. This mode is inherently more dynamically balanced as the shearing forces and bending moments at the decoupling zone are cancelled out, resulting in only a

little vibrational energy being dissipated into the supporting structure at each end of the resonator. This improves the Q-factor and the performance of the resonator. The substrate of the metallic TBTF resonant sensor was fabricated from 430S17 stainless steel thin sheet because this material is suitable for the deposition of the printed film and firing processes during manufacture. Thick-film standard screen printing process is implemented to print the required material on the defined driving and sensing regions

The metallic TBTF resonant sensor has both a piezoelectrical drive and picked-up elements. In order to create the piezoelectric properties, the thick-film printed PZT elements must be polarised. The poling voltage, temperature, and time, are three main parameters that should be considered for this process. The poling condition applied to SL20 resonant sensors is 285±15V, 200°C, and 2 hours. The effect of the applied poling voltage to the performance of the resonant sensor was investigated. Q-value parameter was chosen to indicate the performance of the sensors. The result shows that the Q-value is sharply increased when the poling voltage is increased from 200V to 225V then there is a dropped at 250V. After this, dip Q gradually increased when the poling voltage is up to 300V. Consequently, the applied voltage for SL20 metallic TBTF resonant sensor should be more than 250V. Nevertheless, the poling voltage should not be more than 300V because an electric breakdown event could occur if the printed thick-film has some intrinsic porosity. Increasing poling temperature can increase the piezoelectric activity, however, the maximum temperature should not be more than the melting temperature of the solder used in electrical wire connection for this process. In term of the poling duration time, if the devices are poled at higher temperature, the duration time can be reduced whilst achieving the same level of the piezoelectric properties.

Cutting the sensors from the fabrication plate is another important step that can affect to the performance of the sensors. The metallic TBTF resonant sensors can be cut by using a simple guillotine method, or by using a laser cutting machine. A skilled operator is required for cutting the sensors with the guillotine as the cutting force can cause the sensors to bend and possibly cracking the printed PZT film if the sensors were cut too close to the edge. Using the laser cutting machine provides less damage to the sensors and is more convenient though a little more expensive. Nevertheless, the cost will decrease if the sensors were cut in an automated high volume.

In electrical wiring process, temperature, soldering time, and volume of solder are three parameters that should be considered. The sensors can be damaged if too much volume of solder was applied because the gold layer would be dissolved into the solder droplet causing a broken track or a dry joint.

Moreover, care should be taken in handling the sensors to prevent damage to the printed films which will affect the piezoelectric properties as well as the sensor performance.

7.2.3 Characteristics of The Metallic TBTF Resonant Sensors

The metallic TBTF resonant sensors were designed to operate in the mode that the central tine vibrates in anti-phase with the two outer tines. The resonant frequency for this mode of operation was measured in an open-loop configuration in order to observe the successful operation of the driving and sensing mechanisms of the sensors. The PZT element at one end of the sensor was driven by an AC signal from a vector signal analyser HP89410A which swept the frequencies around the resonant frequency of the sensor. The PZT element on the other end detects the signal which was then connected to the charge amplifier and fed back to the signal analyser for frequency response analysis. The resonant frequencies obtained for SL40, SL20 and SL12 are between 5-7kHz, 20-27kHz and 29-40kHz respectively. Moreover, the Q-factor which is the value indicating the performance of the sensors, was also obtained and found to vary for each individual sensor. The variation of both resonant frequency and Q-factor occurred within the same plate as well as between different plates, and is due to dimensional variations and uncertainties in the sensor manufacturing process.

In addition, the stability, repeatability, and temperature characteristics of the metallic TBTF resonant sensors for three different sizes were investigated. Basically, the metallic TBTF resonant sensor has been designed for a 10% change in frequency at full load and therefore the stability, repeatability, and temperature characteristics were presented as the percentage of this value. Table 7.1 shows the characteristics of some metallic TBTF resonant sensors.

Table 7.1 Characteristics of SL40, SL20 and SL12 metallic TBTF resonant sensors.

TBTF	*f_0 (kHz)*	*10% f_0 (Hz)*	*Q*	*Stability*		*Repeatability*		*Temperature*	
				SD	*%*	*SD*	*%*	*Hz/^oC*	*%*
SL40	4.62	462	1847	0.27	0.06	<0.1	<0.02	0.7	0.16
SL20	26.18	2618	1310	0.60	0.02	0.35	0.01	2.8	0.11
SL12	40.08	4008	1600	5.18	0.13	0.47	0.01	5.2	0.13

The results show that the miniaturisation process has not had any significant detrimental effect on sensor performance, with only slight variations in their characteristics. The temperature sensitivity of the SL20 resonant sensor is the least sensitive to temperature when comparing the results as a percentage of full-scale operation.

7.2.4 Torque Transducers Design

In order to implement the metallic TBTF resonant sensors in torque measurement, the torque shaft was designed and then the sensors were

mounted onto the shaft. The material of the torque shaft and the sensors should be the same in order to prevent thermal expansion errors if electronic compensation is not used. The TBTF resonant sensors may be attached to the torque shaft by gluing, laser-welding, or the combination of both methods. The last method begins with pre-gluing the sensors onto the torque shaft for firm alignment that can reduce the error from misalignment during the next stage, which is the welding process. Voltage, pulse time, and focus are three main parameters for setting the operation of the laser-welding machine. A torque transducer with different materials and geometries will require different settings and, therefore, empirical work should be conducted for each application before commencing the laser-welding process.

After mounting the sensors, the resonant frequency was slightly changed whilst the Q-value was mostly increased. The increased Q-value can be determined from the effect of firmly mounting the sensors, which results in a strong vibration and prevents the lost of energy into the surrounding area and therefore improving the Q-value of the sensors. Nevertheless, some sensors had reduced Q-value which could be caused by many factors, such as the heat from the laser that affects the PZT performance, or a short-circuit occurs between the seam welding and the soldering pad which may cause loss of the energy via this path, etc.

7.2.5 Calibration of Torque Transducers

One torque transducer based on SL20 resonant sensor was calibrated against Torque Standard Machine (Deadweight Lever-beam) at NPL with the calibration range up to 30Nm. Three torque transducers based on SL12 resonant sensors were calibrated at Brunel University against the torque test rig with the calibration range up to 20Nm. The calibration method is according to the British Standard (BS 7882) and mode of calibration is in clockwise direction. The classification results and the uncertainty of calibration at 95% confidence level are summarised in Table 7.2.

Table 7.2 Classification results and the uncertainty of torque transducers based on SL20 and SL12 metallic TBTF resonant sensors.

TBTF	Class of accuracy	Uncertainty (k=2)
SL20	1	0.8%
SL12 (F23)	0.5	0.2%
SL12 (I5)	0.5	0.5%
SL12 (G1)	1	0.7%

From the results, two of three torque transducers based on SL12 metallic TBTF resonant sensors show better performance than the torque transducer based on SL20 TBTF resonant sensor which corresponds to the FEA analysis that the smaller sensor is less affected by lateral forces when the torque is applied, hence reducing the size of sensor can improve the accuracy of the torque transducer based on metallic TBTF resonant sensor.

7.3 Further Work

Research carried out provides the basis for developing a torque transfer standard in which the sensing elements are the metallic TBTF resonant sensors. However, further work will be required in order to improve the torque measurement system with the metallic TBTF resonant sensors. Some suggestions for further work are as follows:

a) The uncertainty in manufacturing process has a major influence on the performance characteristics of the metallic TBTF resonant sensors, so research has to be undertaken in order to minimise the uncertainty, improve the uniformity of sensor characteristics and to also improve the yield. At the moment achieved yield rates for the SL20 and SL12 sensors (taking only sensors with a Q>1000) is 16% and 22% respectively. For commercial qualities this would need to increase to at least 90% in the first instance.

b) Research into different PZT paste formulations material to reduce porosity, avoiding breakdown events during the polarisation process, enhancing the performance characteristics of the PZT elements, improving signal to noise and Q values.

c) Mechanical packaging for the torque transducer needs to be considered as well as special jigs to ensure consistency in manufacturing and assembly processes.

d) Evaluate precision cutting techniques: precision ultrasonic knife cutting machine and precision laser cutting machine should be compared in order to find the best solution for the cutting process in order to reduce the variations in performance due to etching.

e) An Electronic Circuit Unit should be designed for use in a closed-loop control measurement system. The frequency monitor should be high resolution, as the resolution of the indicator is one of the parameters that limit the accuracy class of the torque transfer standard. Additionally, wireless interfacing should also be considered for torque measurement in dynamic system applications.

Bibliography

Abbott, T.D. (1966) Design of a Moiré Fringe Torque Transducer. *IBM Journal*, 412-415.

Adams, L.F. (1975) *Engineering Measurements and Instrumentation*. Kent:J.W. Arrowsmith Ltd.

Antonio, P., Achille, P. and Stefano, P. (2006) An optical torque transducer for high-speed cutting. *Meas.Sci.Technol.*, **17**, 331-339.

Barthod, C., Teisseyre, Y., Gehin, C. and Gautier, G. (2003) Resonant force sensor using a PLL electronic. Sensors and Actuators A, **104**, 143-150.

Bass, H.G. (1971) *Introduction to Engineering Measurements*. Berkshire:McGraw-Hill Publishing Company Limited.

Beckley, J., Kalinin, V., Lee, M. and Voliansky, K. (2002) Non-contact torque sensors based on SAW resonators. *IEEE International Frequency Control Symposium and PDA Exhibition*, 202-213.

Beckwith, T.G., Marangoni, R.D. and Lienhard, J.H. (1993) *Mechanical Measurements*, 5th ed. USA:Addison-Wesley Publishing Company.

Beeby, S.P. and Whitehead, N.M. (2001) Silicon micromechanical resonator with thick-film printed vibration excitation and detection mechanisms. *Sensors and Actuators A*, **88**, 189-197.

Beeby, S.P., Ensell, G., Kraft, M. and Whitehead, N.M. (2004) *MEMS Mechanical Sensors*. UK:Artech House, Inc.

British Standard BS 7882:2008 Method for calibration and classification of torque measuring devices

Centro Nacional de Metrolog ía, CENAM (2006) Brochure: Force and Torque *[www.cenam.mx/fyp]* Available from: http://www.cenam.mx/fyp/Archivos%20PDF/Fuerza/boletin_fuerza_y_partorsionalENGLISH.pdf [Accessed 28th May 2007].

Cheshmehdoost, A. (1992) *High integrity bus structures for optical fibre sensors*. Thesis, Brunel University:UK.

Collett, C.V. and Hope, A.D. (1978) *Engineering Measurements*, ELBS ed. Bath:The Pitman Press.

Cucci, G.R. (1982) “Vibrating beam pressure sensor,” U.S. Patent #4,311,053, Jan. 19.

Dally, J.W., Riley, W.F. and McConnell, K.G. (1993) *Instrumentation for engineering measurements*, 2nd ed. Republic of Singapore: John Wiley & Sons, Inc.

Dargie, P., Sion, R., Atkinson, J. and Whitehead, N.M. (1998) An investigation of the effect of poling conditions on the characteristics of screen-printed piezoceramics. *Microelectronics International*, **15/2**, 6-10.

Davis, F.A. (2002) The 1st UK National Standard Static Torque Calibration Machine-New Design Concepts Lead The way. *Measurement Science Conference in Anaheim, USA*.

DeGolier, E. (2007) *Design of a retrofit power-sensing coupling for pumping systems using triple-beam tuning fork strain gauges*. Dissertation MSc Engineering Design: School of Engineering and Desing, Brunel University.

DeVoe, D. L. (2001) Piezoelectric thin film micromechanical beam resonators. *Sensors and Actuators A*, **88**, 263-272.

Doebelin, E.O. (1966) *Measurement Systems Application and Design*, International Student ed. Tokyo:Kosaido Printing Co., Ltd.

EerNisse, E. P. and Paros, J. M. (1983) Practical Considerations For Miniature Quartz Resonator Force Transducers. *IEEE*, 255-260.

Elwenspoek, M. and Wiegerink, R. (2001) *Mechanical Microsensors*. Germany:Springer-Verlag Berlin Heidelberg 2001.

Fleming, W.J. (1982) Automotive torque measurement: a summary of seven different methods. *IEEE transactions on vehicular technology*, **31(3)**, 117-124.

Gardner, J.W., Varadan, V.K. and Awadelkarim, O.O. (2001) *Microsensors MEMS and Smart Devices. West* Sussex:John Wiley & Sons Ltd.

Garshelis, I.J. (1992) A Torque Transducer Utilizing A Circularly Polarized Ring. *IEEE*, **28(5)**, 2202-2204.

Garshelis, I.J. and Conto, C.R. (1994) A Torque Transducer Utilizing Two Oppositely Polarized Rings. *IEEE*, **30(6)**, 4629-4631.

Gautschi, G. (1936) *Piezoelectric sensorics*. Germany:Springer-Verlag Berlin Heidelberg 2002.

Harada, K. and Sakamoto, H. (1976) A New Torque Transducer With Permanent Magnets And A Ring Core. *IEEE*, **12**, 807-809.

Harada, K., Sasada, I., Kawajiri, T. and Inoue, M. (1982) A New Torque Transducer Using Stress Sensitive Amorphous Ribbons. *IEEE*, **18(6)**, 1767-1769.

Hammond, J.M. and Lec, R.M. (1998) A Non-Contact Piezoelectric Torque Sensor. *IEEE International Frequency Control Symposium*. 715-723.

Herceg, E.E. (1976) *Handbook of Measurement and Control*. USA:Schaevitz Engineering.

Hoffmann, K. (1989) *An Introduction to Measurements using Strain Gages*. Germany: Hottinger Baldwin Messtechnik GmbH.

Howarth, P. and Redgrave, F. (2003) Metrology-in short, 2nd ed. Denmark:MKom Aps.

Jones, B.E. and Yan, T. (2003) Applications of metallic digital strain gauges for load and torque measurement. *The Institute of Materials, Minerals and Mining (IOM) Conference On-line measurement for quality in the metals industries: Does automated inspection meet the need? Instrumentation Series*, 1 page.

Jordan, G.R. (1985) Sensor technologies of the future. *Journal of Physics E: Scientific Instrum*ents, **18**, 729-735.

Kurowski, P.M. (2006) *Engineering Analysis with COSMOSWorks Professional 2006*. Schroff Development Corporation.

Langdon, R.M. (1987) Resonator sensors-a review. *Journal of Physics E: Scientific Instruments 1983-86*, 19-31.

Lou-Moller, R., Bove, T., Ringgaard, E. and Pedersen, A.F. (2006) Investigation of a commercial PZT thick-film composition on various substrates for high frequency ultrasonic applications. *IEEE Ultrasonics Symposium*, 926-929.

Morris, A.S. (1991) *Measurement & Calibration for Quality Assurance*. USA:Prentice Hall International (UK) Ltd.

Myrvoll, F. (2003) *Field Measurements in Geomechanics*. Lisse:Swets&Zeitlinger.

Nakra, B.C. and Chaudhry, K.K. (1985) *Instrumentation Measurement and Analysis*. New Delhi:Tata McGraw-Hill Publishing Company Limited.

Physikalisch-Technische Bundesanstalt (PTB) (2005) The world's largest facility for torque calibration *[www.ptb.de]* Available from: http://www.ptb.de/en/publikationen/news/html/news043/_index.html [Accessed 16th April 2009].

Physikalisch-Technische Bundesanstalt (PTB) (2009) *Torque Realization [www.ptb.de]* Available from: http://www.ptb.de/en/org/1/_index.htm [Accessed 14th April 2009].

Pratt, B.C. (2008) The Calibration of Torques Measuring Devices to British Standard B.S. 7882:2008. *UKASLab PaperForNCSLI July08 BCP*.

Prudenziati, M. (1994) *Handbook of Sensors and Actuators 1: Thick Film Sensors*. Natherlands: Elsevier Science B.V.

Randall, D.S., Rudkin, M.J., Cheshmehdoost, A. and Jones, B.E. (1997) A pressure transducer using a metallic triple-beam tuning fork. *Sensors and Actuators A*, **60**, 160-162.

Renganathan, S. (1999) *Transducer Engineering*. Chennai:Allied Publishers Ltd.

Robinson, A. (2007) The Design, Development and Commissioning of a 2 kNm Torque Standard Machine. *CAL LAB*, Jan-Feb-Mar, 31-35.

Sasada, I., Hiroike, A. and Harada, K. (1984) Torque Transducers With Stress-Sensitive Amorphous Ribbons of Chevron-Pattern. *IEEE*, **20(5)**, 951-953.

Schicker, R. and Wegener, G. (2002) *Measuring Torque Correctly*. Bielefeld:Hottinger Baldwin Messtechnik GmbH.

Shavezipur, M., Ponnambalam, K., Khajepour, A. and Hashemi, S.M. (2008) Fabrication uncertainties and yield optimization in MEMS tunable capacitors. *Sensors and Actuators A*, **147**, 613-622.

Sirohi, R.S. and Radha Krishna, H.C. (1991) *Mechanical Measurements*, 3rd ed. Delhi: H.S. Poplai for New Age International (P) Limited.

Stewart, M., Cain, M. and Weaver, P. (2006) Use of piezoceramics as DC actuators in harsh environments. *Actuator 2006*, 1-4.

The Centre for Metrology and Accreditation (MIKES) (2006) *MIKES Metrology Annual Report 2005 [www.mikes.fi]* Available from: http://www.mikes.fi/documents/upload/mikesmetrologyar2005www.pdf [Accessed 5th June 2007].

The Instrumentation Course Team (1986) T292 Instrumentation. Milton Keynes: The Open University Press.

Tilmans, H. A.C., Elwenspoek, M. and Fluitman, J. H.J. (1992) Micro resonant force gauges. *Sensors and Actuators A*, **30**, 35-53.

Torah, R.N., Beeby, S.P. and Whitehead, N.M. (2004) Improving the piezoelectric properties of thick-film PZT: the influence of paste composition, powder milling process and electrode material. *Sensors and Actuators A*, **110**, 378-384.

Torah, R., Beeby, S.P. and Whitehead, N.M. (2005) An improved thick-film piezoelectric material by powder blending and enhanced processing parameters. *IEEE Transactions on Ultrasonics, Ferroelectrics, and Frequency control*, **52**, 10-16.

Varadan, V.K., Jiang, X. and Varadan, V.V. (2001) *Microstereolithography and other Fabrication Techniques for 3D MEMS*. West Sussex:John Wiley & Sons Ltd.

Wakiwaka, H. and Mitamura, M. (2001) New magnetostrictive type torque sensor for steering shaft. *Sensors and Actuators A*, **91**, 103-106.

Weaver, W. JR., Timoshenko, S.P. and Young, D.H. (1990) *Vibration problems in engineering 5th edition*. Canada:John Wiley & Sons, Inc.

Westbrook, M.H. and Turner, J.D. (1994) *Automotive Sensors*. Bristol:Institute of Physics Publishing.

Whitehead, N.M., Cheshmehdoost, A., Verrall, A. and Jones, B.E. (1997) Torque sensor employing a mechanical resonator. *Sensors and Actuators A*, **60**, 29-31.

Whitehead, N.M. and Turner, J.D. (1997) Thick-film sensors: past, present and future. *Meas. Sci. Technol.*, **8**, 1-20.

Wikipedia (2009) Photochemical machining. Available at: http://en.wikipedia.org/wiki/Photochemical_machining [Accessed 6th July 2009].

Wolff, U., Schmidt, F., Scholl, G. and Magori, V. (1996) Radio Accessible SAW Sensors For Non-Contact Measurement Of Torque And Temperature. *IEEE*, 359-362.

Yan, T., Jones, B.E., Rakowski, R.T., Tudor, M.J., Beeby, S.P. and Whitehead, N.M. (2003a) Thick-film PZT-metallic triple beam resonator. *Electronics letters*, **39(13)**, 982-983.

Yan, T., Jones, B.E., Rakowski, R.T., Tudor, M.J., Beeby, S.P. and Whitehead, N.M. (2003b) Metallic triple beam resonator with thick-film printed drive and pickup. *Eurosensors XVII*, 10-13.

Yan, T., Jones, B.E., Rakowski, R.T., Tudor, M.J., Beeby, S.P. and Whitehead, N.M. (2004a) Design and fabrication of thick-film PZT-metallic triple beam resonators. *Sensors Actuators A*, **115**, 401-407.

Yan, T., Jones, B.E., Rakowski, R.T., Tudor, M.J., Beeby, S.P. and Whitehead, N.M. (2004b) Development of metallic digital strain gauges. *Applied Mechanics and Materials*, **1-2**, 179-184.

Yan, T., Jones, B.E., Rakowski, R.T., Tudor, M.J., Beeby, S.P. and Whitehead, N.M. (2005a) Stiff torque transducer with high overload capability and direct frequency output. *IMEKO 19th International Conference on Force, Mass, Torque and Density Measurements*, 5 pages.

Yan, T., Jones, B.E., Rakowski, R.T., Tudor, M.J., Beeby, S.P. and Whitehead, N.M. (2005b) Metallic resonant strain gauges with high overload capability. *Sensor review*, **25/2**, 144-147.

Appendices

Appendix A.1 Engineering drawing of SL20 resonant sensors

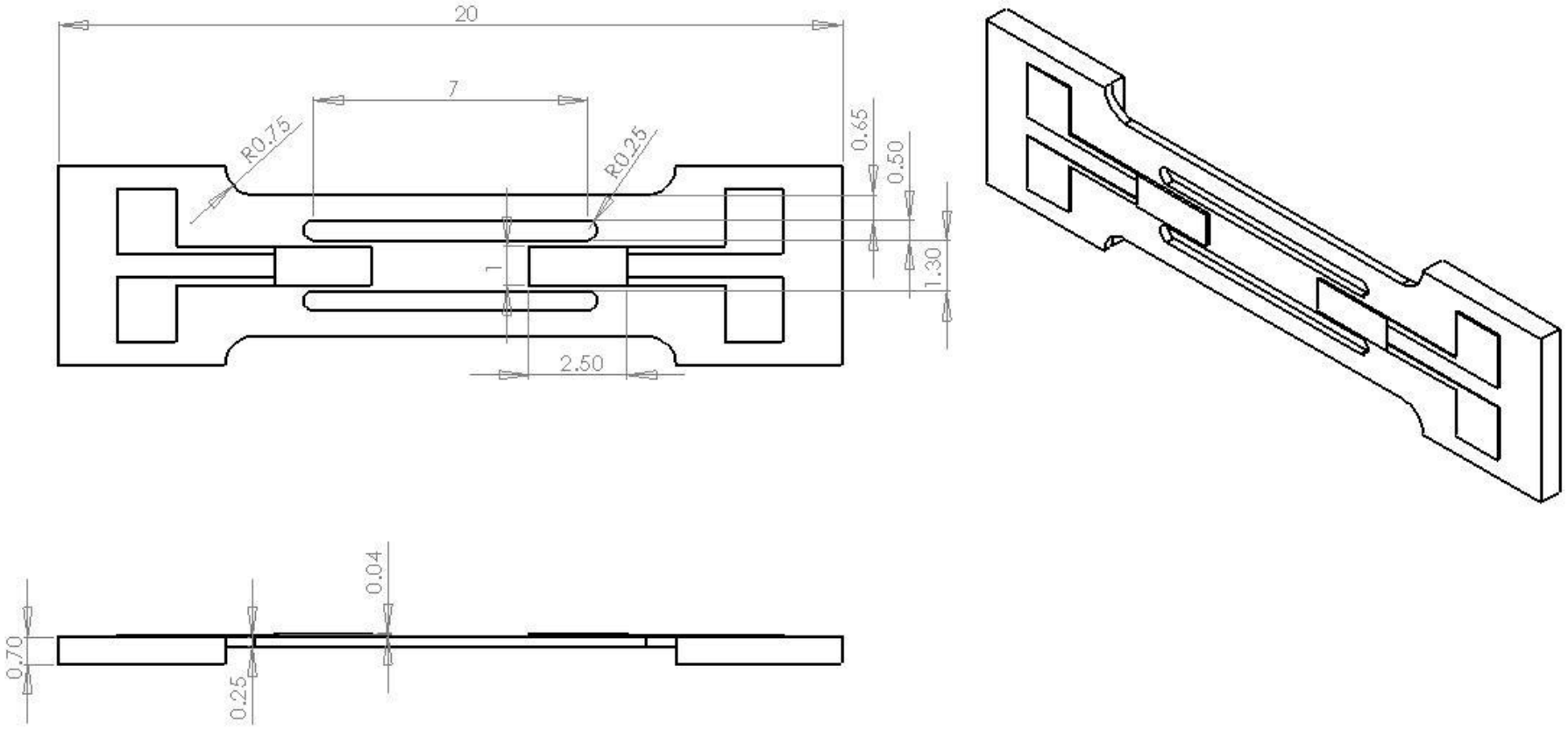

Appendix A.2 Resonance frequency of 12 plates SL20 resonant sensors

No.	*f (Hz)*											
	A	*B*	*1*	*2*	*3*	*4*	*5*	*6*	*7*	*8*	*9*	*10*
1	26060.0	22755.0	20850.0	22310.0	24670.0	N/A	N/A	23385.0	N/A	22677.5	22152.5	23712.5
2	25190.0	22850.0	21140.0	22410.0	24827.5	25607.5	21950.0	23465.0	22367.5	22895.0	N/A	23960.0
3	N/A	22707.5	20845.0	N/A	24600.0	25347.5	21950.0	23325.0	22465.0	N/A	22275.0	23417.5
4	N/A	22917.5	20890.0	22300.0	24600.0	25297.5	21777.5	23400.0	22502.5	22725.0	22290.0	23380.0
5	N/A	22947.5	21005.0	22210.0	24682.5	25005.0	21867.5	N/A	22580.0	N/A	22085.0	23300.0
6	24890.0	23307.0	21180.0	22305.0	24647.5	24722.5	21532.5	N/A	22935.0	22362.5	22392.5	23450.0
7	26740.0	23247.0	21100.0	N/A	24630.0	N/A	N/A	23435.0	N/A	N/A	22567.5	23157.5
8	27310.0	23362.0	N/A	21935.0	N/A	24495.0	21307.5	N/A	N/A	N/A	22705.0	23085.0
9	27000.0	23265.0	21055.0	22255.0	24692.5	24545.0	21480.0	23647.5	23080.0	22392.5	22675.0	23155.0
10	N/A	23300.0	21150.0	22015.0	24670.0	24575.0	21280.0	23680.0	23147.5	22520.0	N/A	N/A
11	23230.0	21090.0	21330.0	N/A	23460.0	N/A	N/A	22435.0	22805.0	N/A	23177.5	N/A
12	N/A	21040.0	21440.0	22990.0	23537.5	N/A	N/A	22467.5	22992.5	N/A	N/A	N/A
13	23490.0	21160.0	21540.0	N/A	N/A	N/A	21710.0	22467.5	23105.0	N/A	23270.0	23232.5
14	N/A	21265.0	21540.0	22925.0	23127.5	N/A	21642.5	22407.5	23155.0	N/A	23097.5	23220.0
15	23670.0	N/A	21440.0	22905.0	23080.0	N/A	N/A	N/A	23015.0	N/A	N/A	23047.5
16	23435.0	21290.0	21905.0	N/A	N/A	N/A	N/A	N/A	N/A	N/A	23132.5	N/A
17	23625.0	21245.0	N/A	22555.0	23070.0	N/A	21467.5	22262.5	N/A	22690.0	23272.5	22975.0
18	N/A	21245.0	21945.0	22680.0	N/A	24720.0	21347.5	22330.0	23365.0	N/A	23252.5	23122.5
19	N/A	21360.0	21680.0	22345.0	23125.0	24575.0	21387.5	22442.5	N/A	N/A	23212.5	23122.5
20	23470.0	21445.0	21700.0	22350.0	23105.0	N/A	21340.0	22245.0	23547.5	N/A	22870.0	22995.0

Appendix A.3 Drawing of shaft design for torque transducer based on SL20 metallic TBTF resonant sensors.

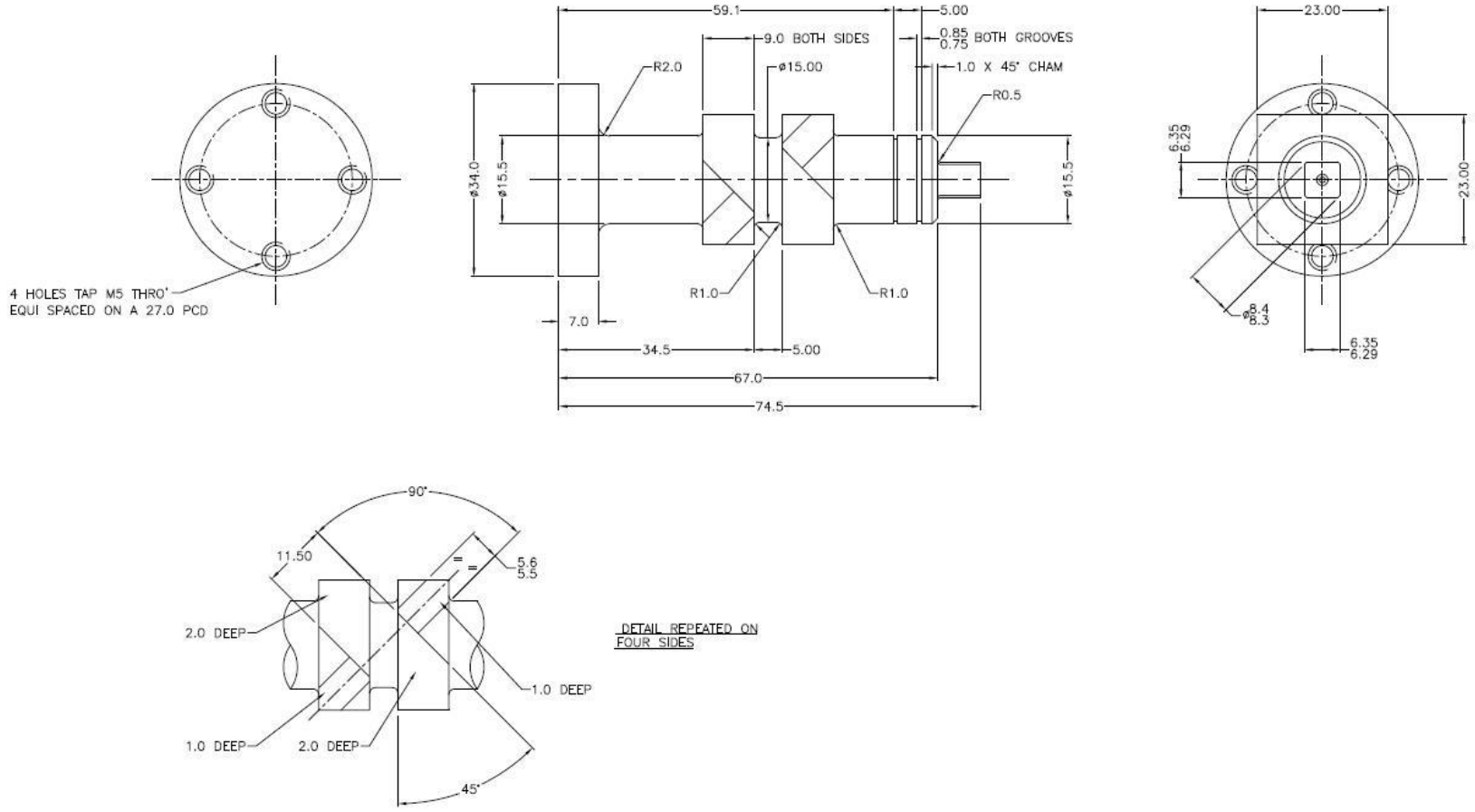

Appendix A.4 Stability test of torque transducer based on SL20 resonant sensor

Cycle 1

Minute	*f (kHz)*			
	0 Nm		*27.5 Nm*	
	C2	*D2*	*C2*	*D2*
1	26.4058	25.2331	26.9429	25.8299
2	26.4064	25.2328	26.9431	25.8292
3	26.4066	25.2336	26.9438	25.8290
4	26.4063	25.2345	26.9435	25.8281
5	26.4062	25.2368	26.9429	25.8279
6	26.4059	25.2361	26.9425	25.8284
7	26.4058	25.2353	26.9422	25.8285
8	26.4057	25.2341	26.9428	25.8295
9	26.4059	25.2339	26.9429	25.8306
10	26.4063	25.2337	26.9436	25.8310
11	26.4066	25.2327	26.9439	25.8311
12	26.4066	25.2331	26.9435	25.8308
13	26.4064	25.2325	26.9431	25.8298
14	26.4061	25.2317	26.9428	25.8290
15	26.4058	25.2324	26.9425	25.8294

Cycle 2

Minute	*f (kHz)*			
	0 Nm		*27.5 Nm*	
	C2	*D2*	*C2*	*D2*
1	26.4055	25.2358	26.9646	25.8693
2	26.4061	25.2365	26.9645	25.8691
3	26.4065	25.2354	26.9645	25.8695
4	26.4074	25.2356	26.9640	25.8685
5	26.4069	25.2339	26.9638	25.8673
6	26.4068	25.2339	26.9639	25.8671
7	26.4066	25.2341	26.9643	25.8676
8	26.4061	25.2343	26.9649	25.8684
9	26.4059	25.2351	26.9648	25.8695
10	26.4064	25.2360	26.9646	25.8698
11	26.4070	25.2369	26.9643	25.8687
12	26.4071	25.2354	26.9640	25.8677
13	26.4070	25.2347	26.9637	25.8671
14	26.4071	25.2339	26.9635	25.8664
15	26.4066	25.2336	26.9644	25.8674

Cycle 3

Minute	*f (kHz)*			
	0 Nm		*27.5 Nm*	
	C2	*D2*	*C2*	*D2*
1	26.4024	25.2308	26.9585	25.8107
2	26.4022	25.2309	26.9584	25.8116
3	26.4021	25.2296	26.9586	25.8110
4	26.4022	25.2294	26.9584	25.8107
5	26.4028	25.2285	26.9583	25.8101
6	26.4033	25.2298	26.9584	25.8098
7	26.4032	25.2310	26.9579	25.8097
8	26.4029	25.2316	26.9579	25.8089
9	26.4026	25.2313	26.9579	25.8092
10	26.4023	25.2306	26.9588	25.8090
11	26.4026	25.2300	26.9592	25.8092
12	26.4030	25.2297	26.9593	25.8089
13	26.4034	25.2320	26.9595	25.8091
14	26.4033	25.2292	26.9592	25.8087
15	26.4034	25.2296	26.9593	25.8096

Appendix A.5 Repeatability test for torque transducer based on SL20 resonant sensor.

No.	*f (kHz)*			
	C2		*D2*	
	0 Nm	*25 Nm*	*0 Nm*	*25 Nm*
1	26.4003	26.9883	25.2352	25.7907
2	26.4053	26.9889	25.2354	25.7913
3	26.4037	26.9893	25.2350	25.7913
4	26.4033	26.9893	25.2373	25.7920
5	26.4063	26.9905	25.2386	25.7943
6	26.4033	26.9917	25.2355	25.7937
7	26.4063	26.9894	25.2373	25.7947
8	26.4051	26.9896	25.2367	25.7957
9	26.4053	26.9901	25.2382	25.7954
10	26.4026	26.9904	25.2366	25.7951
11	26.4068	26.9899	25.2365	25.7959
12	26.4032	26.9890	25.2375	25.7893
13	26.4005	26.9888	25.2362	25.7865
14	26.4042	26.9885	25.2375	25.7923
15	26.4057	26.9888	25.2376	25.7946
16	26.4070	26.9912	25.2372	25.7955
17	26.4068	26.9889	25.2356	25.7969
18	26.4066	26.9889	25.2339	25.7965
19	26.4051	26.9888	25.2356	25.7966
20	26.4053	26.9888	25.2332	25.7965
21	26.4055	26.9883	25.2355	25.7986
22	26.4049	26.9878	25.2386	25.7984
23	26.4043	26.9875	25.2368	25.7979
24	26.4042	26.9877	25.2350	25.7982
25	26.4046	26.9883	25.2358	25.7982
26	26.4052	26.9884	25.2324	25.7977
27	26.4034	26.9894	25.2335	25.7973
28	26.4041	26.9888	25.2357	25.7988
29	26.4031	26.9883	25.2355	25.7988
30	26.3978	26.9850	25.2352	25.7989

Appendix A.6 Linearity test of torque transducer based on SL20 resonant sensor.

TBTF: C2

Torque (Nm)	*T (℃)*	*f (kHz)*	
		Cycle 1	*Cycle 2*
0.00	21.2	26.3960	26.3961
2.51	21.3	26.4500	26.4500
5.00	21.4	26.5089	26.5092
7.50	21.5	26.5661	26.5661
9.99	21.5	26.6233	26.6244
12.49	21.4	26.6801	26.6801
14.99	21.8	26.7382	26.7382
17.50	21.8	26.7957	26.7955
20.00	21.6	26.8525	26.8524
22.49	21.2	26.9114	26.9111
25.01	21.6	26.9680	26.9678
22.52	22.0	26.9135	26.9136
20.02	21.9	26.8546	26.8546
17.54	22.2	26.7962	26.7963
15.03	22.6	26.7374	26.7373
12.53	22.5	26.6793	26.6793
10.03	22.6	26.6204	26.6204
7.53	21.6	26.5636	26.5634
5.00	21.9	26.5028	26.5029
2.52	22.8	26.4446	26.4442
0.00	22.8	26.3915	26.3917
-2.50	22.4	26.2500	26.2507
-5.01	22.7	26.1933	26.1941
-7.47	22.8	26.1467	26.1484
-10.02	22.4	26.0904	26.0946
-12.53	22.6	26.0454	26.0425
-15.02	23.2	25.9671	25.9674
-17.50	23.0	25.9179	25.9171
-20.02	22.1	25.8861	25.8846
-22.53	22.8	25.8446	25.8451
-25.00	23.2	25.7917	25.7915
-22.50	23.1	25.8409	25.8412
-20.02	23.0	25.8990	25.8988
-17.56	23.7	25.9228	25.9229
-15.04	23.5	25.9659	25.9667
-12.49	23.7	26.0221	26.0217
-10.05	23.2	26.0742	26.0734
-7.53	24.4	26.1311	26.1328
-5.00	23.1	26.1906	26.1920
-2.52	23.4	26.2475	26.2487
0.00	23.4	26.2954	26.2949

TBTF: D2

Torque (Nm)	*T (℃)*	*f (kHz)*	
		Cycle 1	*Cycle 2*
0.00	21.5	25.2310	25.2303
2.50	21.7	25.2910	25.2908
4.99	22.2	25.3551	25.3548
7.48	22.2	25.4172	25.4169
9.99	22.3	25.4777	25.4777
12.50	22.2	25.5389	25.5391
14.96	22.3	25.5962	25.5969
17.50	22.9	25.6535	25.6538
19.97	22.9	25.7100	25.7100
22.48	22.2	25.7687	25.7685
24.96	22.2	25.8234	25.8234
22.51	22.3	25.7700	25.7697
20.02	22.3	25.7129	25.7132
17.53	22.5	25.6540	25.6540
15.03	22.7	25.5953	25.5954
12.52	22.2	25.5369	25.5371
10.00	22.2	25.4759	25.4762
7.50	22.6	25.4138	25.4134
4.99	22.2	25.3513	25.3514
2.52	22.7	25.2866	25.2870
0.00	22.5	25.2294	25.2287
-2.50	23.2	25.1740	25.1739
-5.00	22.0	25.1219	25.1219
-7.50	22.9	25.0703	25.0709
-10.00	22.7	25.0137	25.0137
-12.50	21.6	24.9608	24.9610
-15.01	22.2	24.9061	24.9062
-17.51	22.2	24.8522	24.8532
-20.03	23.2	24.7970	24.7976
-22.49	23.1	24.7417	24.7420
-25.00	23.1	24.6888	24.6892
-22.50	23.6	24.7432	24.7432
-20.03	23.6	24.7957	24.7956
-17.55	22.1	24.8525	24.8532
-15.01	23.1	24.9069	24.9068
-12.50	23.2	24.9619	24.9618
-10.02	23.3	25.0138	25.0136
-7.50	23.0	25.0675	25.0672
-5.01	22.9	25.1176	25.1177
-2.50	22.9	25.1702	25.1704
0.00	23.0	25.2205	25.2205

Appendix A.7 Temperature test of torque transducer based on SL20 resonant sensors.

TBTF: C2

T (°C)	*f (kHz)*	
	1	*2*
49.9	26.3232	26.3231
45	26.3359	26.3359
40.1	26.3495	26.3495
35	26.3613	26.3612
30	26.3746	26.3745
25	26.3869	26.3869
20	26.3983	26.3983
15	26.4074	26.4074
10.3	26.4219	26.4223
5.5	26.4333	26.4339

TBTF: D2

T (°C)	*f (kHz)*	
	1	*2*
50	25.1657	25.1657
45.2	25.1764	25.1765
40	25.1880	25.1880
35.2	25.1984	25.1986
30	25.2094	25.2092
25	25.2203	25.2203
20.1	25.2272	25.2269
15	25.2336	25.2330
10	25.2398	25.2394
5	25.2503	25.2492

Appendix A.8 Uncertainty calculation of torque transducer based on SL20 resonant sensor.

D25 torque transducer

Applied torque Nm	Uncertainty contribution									
	Applied torque u_1		Reproducibility u_2		Repeatability u_3		Resolution u_4		Residual deflection u_5	
	Value %	Uncertainty %	Value %	Uncertainty %	Value %	Uncertainty %	Value %	Uncertainty %	Value %	Uncertainty %
0										
5	0.002	0.001	0.7586	0.2682	0.3426	0.0989	0.4166	0.1701		
10	0.002	0.001	0.9895	0.3498	0.1339	0.0387	0.2139	0.0873		
15	0.002	0.001	0.7991	0.2825	0.1459	0.0421	0.1452	0.0593		
20	0.002	0.001	0.3861	0.1365	0.0000	0.0000	0.1103	0.0450		
30	0.002	0.001	0.149	0.0527	0.0000	0.0000	0.0745	0.0304	0.1490	0.0430

Applied torque Nm	Uncertainty contribution							
	Temperature u_6		Interpolation u_7		Reversibility u_8		Combined uncertainty u_c	Expanded uncertainty U
	Value %	Uncertainty %	Value %	Uncertainty %	Value %	Uncertainty %	%	%
0								
5	0.07	0.0404	0.3051	0.0623	0.2842	0.0820	0.3505	0.7011
10	0.07	0.0404	0.0487	0.0099	0.6162	0.1779	0.4061	0.8121
15	0.07	0.0404	0.2214	0.0452	0.4365	0.1260	0.3235	0.6470
20	0.07	0.0404	0.0161	0.0033	0.1105	0.0319	0.1527	0.3054
30	0.07	0.0404	0.0308	0.0063	0.0000	0.0000	0.0850	0.1700

Appendix B.1 Engineering drawing of SL12 resonant sensor.

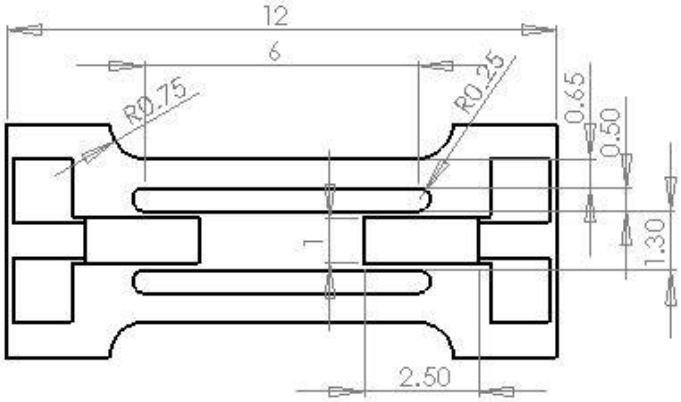

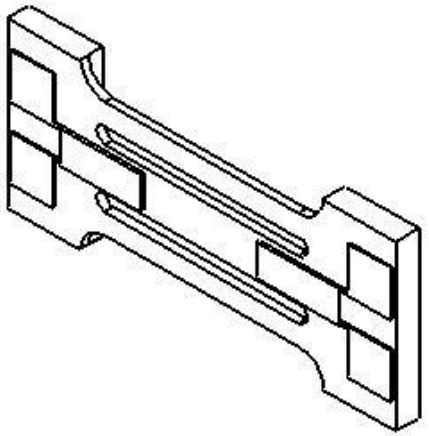

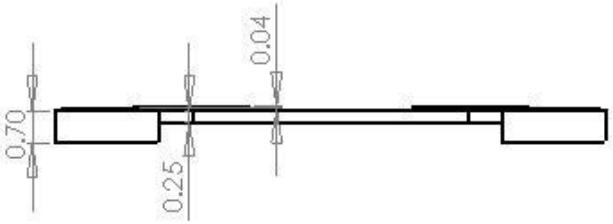

Appendix B.2 Resonance frequency of SL12 resonant sensors.

No.	*f (Hz)*				
	1	*2*	*3*	*4*	*5*
1	32602.5	N/A	36652.5	29610.0	39020.0
2	32877.5	32710.0	36517.0	31120.0	39060.0
3	33435.0	32110.0	36517.0	N/A	38975.0
4	33242.5	32527.0	36492.0	29750.0	38937.5
5	33275.0	32537.0	36362.0	N/A	39142.5
6	33515.0	32774.0	36112.0	N/A	N/A
7	33427.5	32270.0	36359.5	N/A	39070.0
8	33805.0	32250.0	36819.5	29865.0	39155.0
9	33595.0	32482.0	36519.0	N/A	39142.5
10	33582.5	32472.0	36544.0	N/A	38787.5
11	34052.5	32712.0	35936.0	30660.0	38020.0
12	34692.5	32722.0	36211.0	N/A	38407.0
13	N/A	32707.0	36186.0	30207.0	38349.5
14	34622.5	32727.0	36153.5	30187.0	38407.0
15	35049.5	32717.0	36323.5	30227.0	38494.5
16	35287.0	32642.0	35881.0	30722.0	38354.5
17	35077.0	32682.0	36198.5	N/A	38642.0
18	35247.0	32117.0	36046.0	30324.0	38299.0
19	35214.5	32477.0	35928.0	30334.0	38559.0
20	35099.5	32487.0	36155.5	N/A	38404.0
21	33677.0	32337.0	33785.0	29866.0	35194.0
22	33897.0	31879.0	33930.0	30111.0	35481.0
23	33897.0	31889.0	33925.0	30031.0	35626.0
24	34204.5	31926.5	34095.0	30023.5	N/A
25	34207.0	32151.0	33925.0	30181.0	35486.0
26	34154.5	32336.0	33660.0	30493.0	35471.0
27	34367.0	32318.0	34102.5	30160.0	35518.5
28	34607.1	31915.0	33997.5	30200.0	35856.0
29	34454.6	32380.0	34090.0	30190.0	35841.0
30	34412.0	32235.0	33627.5	29897.0	35201.0

No.	F (Hz)							
	A	B	C	D	E	F	G	H
1	30825.0	34643.5	N/A	33221.5	N/A	32843.0	39109.5	31984.0
2	30825.5	34964.0	N/A	N/A	33127.5	33038.5	39981.5	32590.5
3	N/A	34719.0	N/A	33394.5	33373.5	32677.0	39657.5	32346.5
4	N/A	34831.5	33036.5	33269.5	N/A	32693.5	39645.0	N/A
5	30758.0	34711.5	32915.0	33466.0	33368.0	N/A	N/A	N/A
6	N/A	34247.5	N/A	33535.5	N/A	N/A	39161.5	N/A
7	30094.5	34994.0	33130.5	33359.5	N/A	32412.5	39207.5	N/A
8	29957.5	N/A	N/A	33394.5	N/A	32762.0	39251.5	31856.0
9	N/A	N/A	33383.0	33847.5	33457.0	33193.5	39390.0	N/A
10	29549.0	N/A	33093.0	35687.5	33039.5	33385.5	N/A	N/A
11	31583.5	35229.5	32876.5	33635.5	N/A	33404.5	37715.0	32949.0
12	31694.0	35437.5	32951.0	34054.5	33218.5	33399.0	N/A	N/A
13	31691.5	N/A	32825.5	34062.0	33627.5	33287.0	37942.0	32940.5
14	31343.5	35542.5	N/A	34249.0	N/A	33176.5	38064.5	32995.0
15	30748.0	35227.5	32592.5	33883.0	33572.0	33234.0	37702.5	32904.5
16	31043.5	N/A	32771.5	33850.0	N/A	32674.5	37514.0	32752.5
17	30728.0	35375.0	33019.0	34170.0	33754.5	N/A	37545.0	32586.0
18	N/A	35582.5	32946.0	N/A	N/A	33408.5	37542.5	32522.5
19	30723.0	N/A	32689.0	N/A	N/A	33397.0	37712.0	N/A
20	N/A	35617.5	N/A	34169.0	33754.5	33521.5	37079.0	N/A
21	30830.0	33723.0	32378.5	N/A	32805.5	33319.5	N/A	N/A
22	31446.4	34079.0	32883.0	34758.0	32872.5	33454.5	35112.5	33078.5
23	31188.5	34019.0	32732.5	34758.0	32671.0	33223.0	N/A	33082.0
24	31120.5	33753.0	32916.0	34763.0	32760.5	33164.5	N/A	32903.5
25	N/A	33865.5	N/A	34676.5	32769.0	33320.5	N/A	N/A
26	30502.5	33835.5	32823.0	34517.5	N/A	33017.0	34800.0	32179.0
27	30209.5	34012.0	N/A	34604.5	N/A	33165.5	34962.0	32571.5
28	N/A	34007.0	32879.0	34873.5	N/A	N/A	N/A	32620.0
29	30332.0	33974.5	32771.5	34916.5	32901.0	N/A	N/A	N/A
30	30197.0	33954.5	32879.5	N/A	32808.5	N/A	34512.5	N/A

No.	f (Hz)								
	I	*J*	*K*	*M*	*N*	*O*	*X*	*Y*	*Z*
1	N/A	31340.0	36815.0	32225.0	N/A	31893.5	33670.0	N/A	31447.5
2	39287.5	31350.0	37042.5	32430.0	34662.5	31725.0	33905.0	32630.0	31867.5
3	39822.5	31175.0	N/A	N/A	34897.5	31722.5	N/A	32357.5	N/A
4	N/A	31245.0	N/A	32112.5	N/A	31725.0	33317.5	32487.5	31370.0
5	40812.5	30980.0	N/A	N/A	33930.0	31827.5	N/A	N/A	N/A
6	N/A	30815.0	36895.0	N/A	33280.0	31837.5	32895.0	N/A	N/A
7	N/A	31205.0	36820.0	32252.5	N/A	31880.0	33020.0	N/A	N/A
8	N/A	30980.0	N/A	N/A	N/A	31827.5	32625.0	N/A	30600.0
9	N/A	30972.5	36810.0	32255.0	35697.5	31957.5	33040.0	N/A	31035.0
10	N/A	N/A	36670.0	N/A	36870.0	31847.5	32882.5	32537.5	N/A
11	36502.5	N/A	35617.5	33790.0	34330.0	33000.0	N/A	32860.0	N/A
12	36895.0	32205.0	35890.0	34000.0	34970.0	32982.5	35917.5	32860.0	33175.0
13	N/A	32122.5	35895.0	33835.0	35177.5	32987.5	N/A	32767.5	N/A
14	N/A	32305.0	36130.0	33997.5	34537.5	32982.5	35782.5	32857.5	33005.0
15	38180.0	N/A	N/A	N/A	N/A	32725.0	35785.0	32867.5	32705.0
16	36760.0	32210.0	35967.5	N/A	35957.5	32955.0	35467.5	32605.0	32487.5
17	37270.0	32022.5	35462.5	34127.5	N/A	32992.5	35407.5	N/A	N/A
18	N/A	32202.5	35672.5	N/A	34750.0	32832.5	35512.5	32310.0	32545.0
19	37512.5	32197.5	35902.5	N/A	35865.0	32950.0	35415.0	32635.0	32327.5
20	37410.0	31977.5	35787.5	33997.5	36857.5	33005.0	35430.0	32282.5	32485.0
21	34982.5	31472.5	33645.0	33785.0	N/A	32767.5	36457.5	32337.5	32665.0
22	N/A	31945.0	N/A	N/A	34335.0	32717.5	N/A	32330.0	32890.0
23	36630.0	31775.0	N/A	N/A	N/A	32375.0	36910.0	32125.0	32662.5
24	36822.5	31732.5	34032.5	N/A	N/A	32680.0	36337.5	32322.5	32637.5
25	36170.0	31475.0	N/A	33712.5	N/A	32470.0	N/A	32340.0	32682.5
26	35180.0	N/A	N/A	33740.0	33582.5	N/A	N/A	N/A	32180.0
27	35800.0	N/A	N/A	33800.0	34007.5	32200.0	36515.0	N/A	N/A

28	35872.5	31327.5	N/A	N/A	35232.5	32280.0	36452.5	32352.5	N/A
29	36150.0	31482.5	N/A	N/A	35885.0	32182.5	36555.0	32192.5	31930.0
30	36000.0	31445.0	N/A	N/A	N/A	32670.0	36500.0	31710.0	31682.5

Appendix B.3 Drawing of shaft design for torque transducer based on SL12 metallic TBTF resonant sensors.

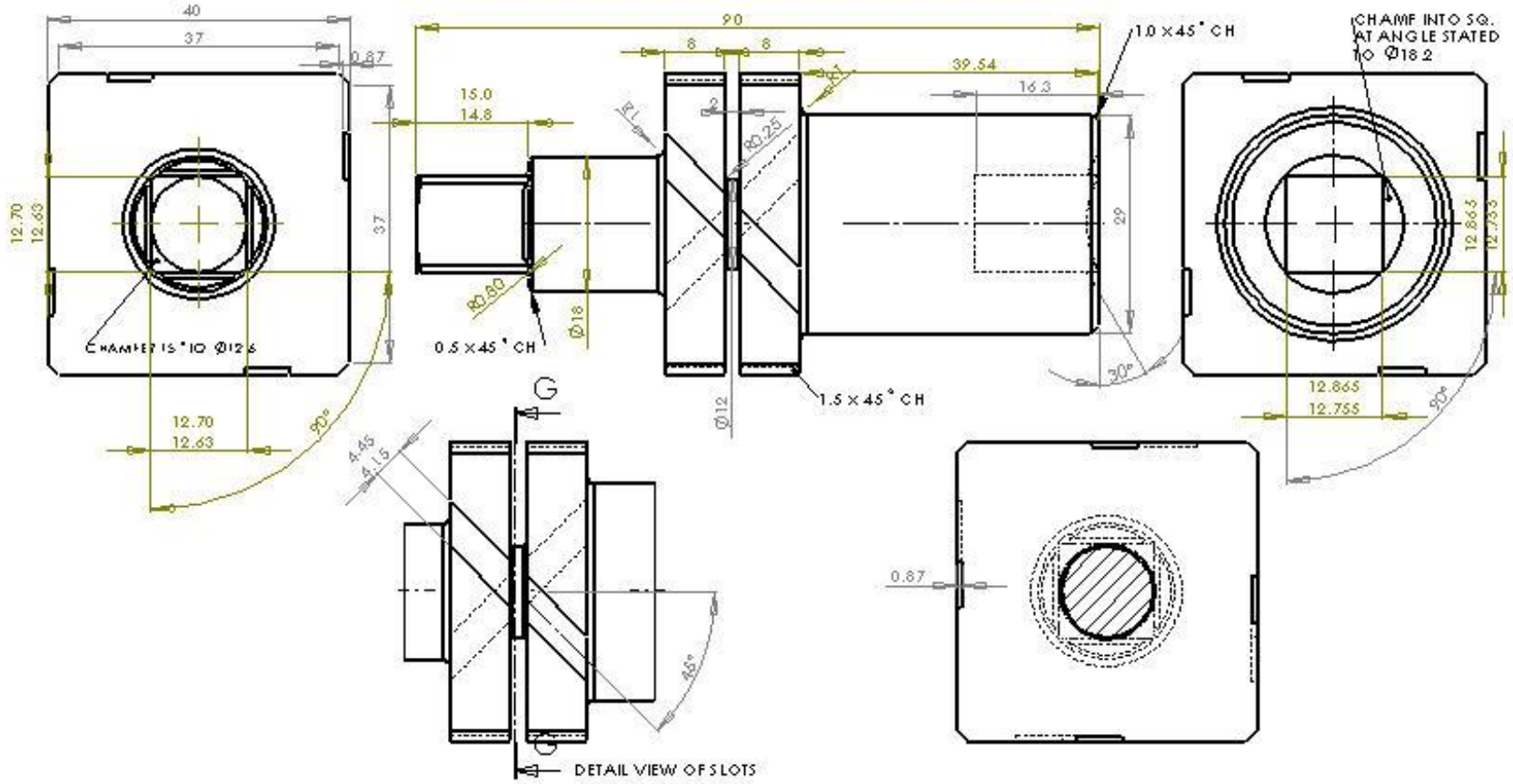

Appendix B.4 Uncertainty calculation of torque transducer based on SL12 resonant sensor.

I5 torque transducer

Applied torque Nm	Uncertainty contribution									
	Applied torque u_1		Reproducibility u_2		Repeatability u_3		Resolution u_4		Residual deflection u_5	
	Value %	Uncertainty %	Value %	Uncertainty %	Value %	Uncertainty %	Value %	Uncertainty %	Value %	Uncertainty %
0										
4.224	0.024	0.0118	0.1020	0.0361	0.0057	0.0016	0.2027	0.0828		
7.218	0.024	0.0118	0.3165	0.1119	0.1202	0.0347	0.1283	0.0524		
13.206	0.024	0.0118	0.3812	0.1348	0.1529	0.0441	0.0763	0.0311		
16.2	0.024	0.0118	0.4340	0.1534	0.2170	0.0626	0.0620	0.0253		
19.17	0.024	0.0118	0.4320	0.1527	0.1017	0.0294	0.0508	0.0207	0.0763	0.0220

Applied torque Nm	Uncertainty contribution							
	Temperature u_6		Interpolation u_7		Reversibility u_8		Combined uncertainty u_c	Expanded uncertainty U
	Value %	Uncertainty %	Value %	Uncertainty %	Value %	Uncertainty %	%	%
0								
4.224	0.53	0.1530	0.02290	0.00467	0.2030	0.0586	0.1875	0.3750
7.218	0.53	0.1530	0.00810	0.00165	0.2566	0.0741	0.2133	0.4267
13.206	0.53	0.1530	0.02110	0.00431	0.2287	0.0660	0.2214	0.4427
16.2	0.53	0.1530	0.05670	0.01157	0.1865	0.0538	0.2339	0.4677
19.17	0.53	0.1530	0.02100	0.00429	0.0000	0.0000	0.2206	0.4412

F23 torque transducer

Applied torque Nm	Uncertainty contribution									
	Applied torque u_1		Reproducibility u_2		Repeatability u_3		Resolution u_4		Residual deflection u_5	
	Value %	Uncertainty %	Value %	Uncertainty %	Value %	Uncertainty %	Value %	Uncertainty %	Value %	Uncertainty %
0										
4.224	0.024	0.0118	0.1756	0.0621	0.0147	0.0042	0.1644	0.0671		
7.218	0.024	0.0118	0.1905	0.0674	0.0303	0.0087	0.0953	0.0389		
13.206	0.024	0.0118	0.1030	0.0364	0.0515	0.0149	0.0514	0.0210		
16.2	0.024	0.0118	0.1180	0.0417	0.0664	0.0192	0.0421	0.0172		
19.17	0.024	0.0118	0.1434	0.0507	0.0716	0.0207	0.0358	0.0146	0.0718	0.0207

Applied torque Nm	Uncertainty contribution							
	Temperature u_6		Interpolation u_7		Reversibility u_8		Combined uncertainty u_c	Expanded uncertainty U
	Value %	Uncertainty %	Value %	Uncertainty %	Value %	Uncertainty %	%	%
0								
4.224	0.14	0.0323	0.24420	0.04985	0.1245	0.0359	0.1155	0.2310
7.218	0.14	0.0323	0.16910	0.03452	0.0952	0.0275	0.0962	0.1924
13.206	0.14	0.0323	0.07720	0.01576	0.1542	0.0445	0.0735	0.1470
16.2	0.14	0.0323	0.01310	0.00267	0.0927	0.0268	0.0657	0.1313
19.17	0.14	0.0323	0.02910	0.00594	0.0000	0.0000	0.0697	0.1394

G1 torque transducer

Applied torque Nm	Uncertainty contribution									
	Applied torque u_1		Reproducibility u_2		Repeatability u_3		Resolution u_4		Residual deflection u_5	
	Value %	Uncertainty %	Value %	Uncertainty %	Value %	Uncertainty %	Value %	Uncertainty %	Value %	Uncertainty %
0										
4.224	0.024	0.0118	0.8923	0.3155	0.2448	0.0707	0.1622	0.0662		
7.218	0.024	0.0118	0.4456	0.1575	0.0983	0.0284	0.0988	0.0403		
13.206	0.024	0.0118	0.4588	0.1622	0.1440	0.0416	0.0574	0.0234		
16.2	0.024	0.0118	0.4630	0.1637	0.0246	0.0071	0.0487	0.0199		
19.17	0.024	0.0118	0.2956	0.1045	0.1480	0.0427	0.0423	0.0173	0.1695	0.0489

Applied torque Nm	Uncertainty contribution							
	Temperature u_6		Interpolation u_7		Reversibility u_8		Combined uncertainty u_c	Expanded uncertainty U
	Value %	Uncertainty %	Value %	Uncertainty %	Value %	Uncertainty %	%	%
0								
4.224	0.42	0.0727	0.21790	0.04448	0.4858	0.1402	0.3688	0.7375
7.218	0.42	0.0727	0.31110	0.06350	0.5434	0.1569	0.2476	0.4953
13.206	0.42	0.0727	0.35220	0.07189	0.1723	0.0497	0.2041	0.4082
16.2	0.42	0.0727	0.29120	0.05944	1.0945	0.3160	0.3688	0.7377
19.17	0.42	0.0727	0.08060	0.01645	0.0000	0.0000	0.1454	0.2908

Appendix C

Characteristics of 9mm Metallic Triple-Beam Tuning Fork Resonant Sensor

J Intiang, J Weidenmüller, R T Rakowski, B E Jones, A Cheshmehdoost[1]

Brunel Design, School of Engineering and Design, Brunel University, Kingston Lane, Uxbridge, UB8 3PH, UK
[1] ForceSenSys Ltd., BEC, Kingston Lane, Uxbridge, UB8 3PH, UK

E-mail: Richard.Rakowski@brunel.ac.uk

Abstract. This paper describes the design and testing of the first miniaturised metallic triple-beam tuning fork resonant sensors for use in force, pressure and torque measurement applications. The new devices with 9mm length vibrating tines have resulted in over a 40% in size when compared to previously tested resonators. The four fold increase in operating frequency to 26 kHz, with Q factors in air up to 4000, provides additional benefits for resolution, accuracy, range and overload capability. Measurement repeatability of at least 0.02% of span levels for torque transducers employing the sensors are quoted. Results of characterisation over the temperature range -30^{o}C to +90^{o}C are given.

1. Introduction

Resonant sensors have been used in a wide range of sensing applications, such as load, pressure, torque and fluid flow characteristics [1]. The key element of these sensors is the resonator, an oscillating structure, which is designed such that its resonance frequency is a function of the measurand. The most common sensing mechanism is for the resonator to be stressed as a force sensor. The applied stress effectively increases the stiffness of the resonator structure, which results in an increase in the resonator's natural frequency. The resonator provides a virtual digital frequency output, which is less susceptible to electrical noise and independent of the level and degradation of transmitted signals, offering good long-term stability. The frequency output is also compatible with digital interfacing and no analogue-to-digital conversion is required, therefore maintaining inherent high accuracy and low cost.

The first successful metallic triple-beam tuning fork (TBTF) resonant sensor with thick-film drive/pickup elements [2, 3, 5] has a resonating 'tine' element length of 15.5mm and an overall sensor length of 23.5mm, a thickness of 0.25mm and beam widths of 1mm, 2mm and 1 mm. The gap between the

beams was 0.5mm. However, this device is too large for current force/torque and pressure sensing applications. The challenge has been to reduce the sensor dimensional footprint and if possible enhance sensor performance.

2. Design and Fabrication

The combination of processes used in the resonator fabrication, photo-etched TBTFs with drive and pick-up piezoelectric elements printed directly onto the device surface, presents low-cost manufacturing opportunities for mass batch production. Figure 1 shows a plan view of the resonator structure with PZT drive and detection elements. The thick-film screen-printing process deposits relatively thick layers of material, typically between 50 and 100μm. The magnitude of the output of the lead zirconate titanate (PZT) element depends upon the piezoelectric properties of the deposited layer, its thickness and the stress or voltage applied. In trying to reduce the size of the sensor there is a danger that the piezoactuator might not be able to excite the stiffer tines, so PZT printing is a physical limitation in size reduction. Finite element analysis (FEA) was employed to simulate the modal behaviour and stress distribution of the resonator in order to optimise the positioning of the thick-film PZT elements on the structure.

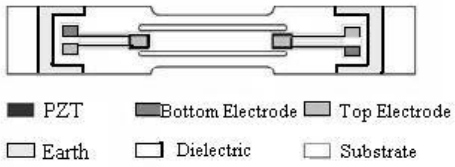

Figure 1. Plan view of the resonator structure with PZT drive and detection elements.

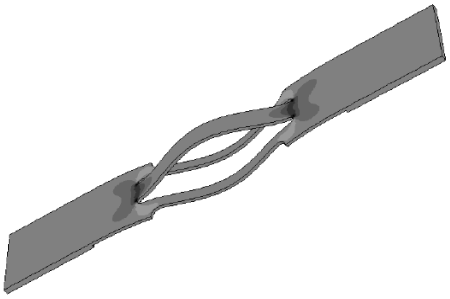

Figure 2. Stress contour plot for the resonator in mode 3.

The triple beam tuning fork has a planer structure and is inherently more dynamically balanced when compared to a single beam or an out-of- plane double beam structure vibrating in flexural modes. Balanced structures dissipate less energy through their supports and therefore possess an intrinsically higher mechanical quality factor. The sensor is designed to oscillate in a differential mode, where the central beam vibrates in anti-phase with the outer beams (mode 3) to minimise mechanical energy losses from the resonator. Figure 2 shows the operational modal behaviour of the sensor modelled by FEA.

Frequency of operation is proportional to $1/L^2$, where L is the tine length, thus a reduction in length will lead to an increase in operating frequency (in this case from 5-6 kHz to 25-27 kHz). However, the reduction in size allows a larger application range-ability (i.e. 9mm tine device could be used for torque applications from 10 Nm to 1000 Nm, depending on the torque shaft diameter). It is true to say that longer tines are more sensitive than shorter

tines. However, when comparing the old 15.5mm device with new 9mm device in terms of sensitivity and other performance characteristics, care was taken to make sure that both devices were compared under the same micro-strain conditions, that means to consider total frequency excursions, designed usually at 5-10% of workable range [5].

3. Resonator Operation

3.1. Open-loop configuration

The aim of the experiments was to compare the performance of resonators designed with different beam lengths. One resonator is 23.5mm long with a tine length of 15.5mm (Type 1) and a natural frequency between 5 – 7 kHz and the new resonator is 15.5mm long (Type 2) with a tine length of 9mm with a natural frequency between 25-27 kHz. Both resonating elements have the same beam thickness of 0.25mm and beam widths of 2mm for the middle beam and 1mm for each of the outer beams.

The first tests on the resonators are realised in an open-loop configuration. The PZT element at one end of the resonator is driven by a periodic chirp signal of 1V peak-peak from a Hewlett-Packard 89410A Vector Signal Analyser, which swept the frequencies around the resonant frequency. The PZT element on the other end of the resonator was connected to a Kistler 5011 Charge Amplifier, which has an adjustable low pass filter, and the output from the charge amplifier was fed back to the signal analyser for frequency response analysis of the resonator. Figure 3 shows the amplitude-frequency response for the third mode of vibration for both resonator types.

From these results the values for the centre frequencies and quality factor (Q) for the two devices are as follows: resonator Type 1 has a centre frequency of 6,411Hz and Q-factor of 870, while resonator Type 2 has a centre frequency of 26.220kHz and Q-factor of 4002.

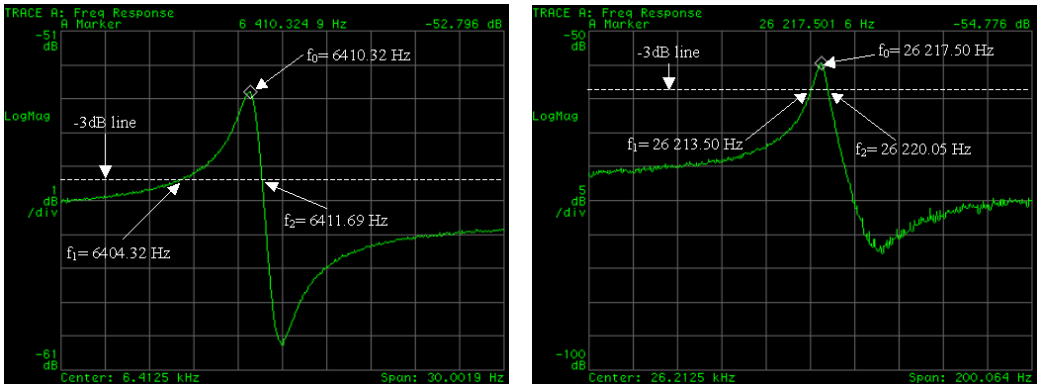

(a) Resonator Type 1 (b) Resonator Type 2

Figure 3. Resonator frequency response from HP89410A Vector Signal Analyser

3.2. Closed-loop configuration

The custom-built electronics for the TBTF resonators operates in a feedback closed loop mode. The receiving PZT element is connected to a charge amplifier circuit, followed by a digital 90° phase shift circuit. For optimised performance the feedback signal passes through a second adjustable phase shifter and a second stage of amplification all on one circuit board. The output from the second stage amplification is fed back to the driving PZT element. The resonant frequency is displayed on the Agilent 54621A oscilloscope, which is connected to the output of a Phased Locked Loop circuit. Additionally the frequency output can be connected to an analogue input of the data acquisition card DAQ6035E that imports the data to the LabView software. In this software the Fourier transformation is obtained for the amplitude-frequency analysis of the resonators.

4. Characteristics

4.1. Stability

Stability is the ability of a measuring system to maintain constant its measurement characteristic with time. For this investigation the environmental conditions, such as temperature, humidity and pressure, have to be constant. This was achieved by using a climatic test chamber Montford Mini-Mech-B set to 25°C. The resonators were operated in the open-loop configuration. Over a time period of 48h the amplitude-frequency response was recorded in unequal time steps. The default frequency resolution for this experiment was 0.5Hz.

Figure 4a displays the test result of resonator Type 1 over a time period of 48h. The maximum deviation from the mean value of 4,620.75Hz was 0.25Hz. In practical terms, for a measured torque sensitivity of 40 Hz/Nm [4] for this resonator type, the maximum error converted to torque is 0.00625 Nm, hence the stability for a torque range of 0-20 Nm is 0.03 percent.

The maximum deviation for resonator Type 2 (figure 4b) from the mean value 26.187kHz was 1Hz. The torque sensitivity of this new designed resonator, tested under static torque conditions, with an expanded torque range of 0-100 Nm, is 26.6 Hz/Nm. Hence the maximum error converted to torque is 0.0375Nm or, calculated for this torque range, gives a stability of 0.04 percent.

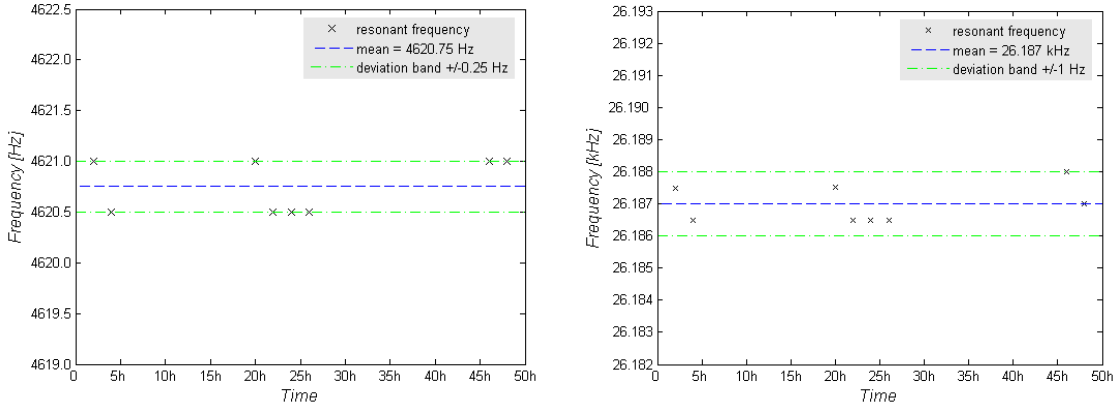

(a) Resonator Type 1 (b) Resonator Type 2

Figure 4. 48h Stability test results

4.2. *Repeatability*

This investigation illustrates the measurement precision under conditions of repeated measurements over a short period of time. The experimental set-up was similar to that for the stability investigation, except that the period of measurement was shortened to about 5 minutes and the resolution was adjusted to 0.1Hz.

Figure 5a shows, that the deviation of the resonance frequency of resonator type 1 is less than the resolution of 0.1Hz. Hence the maximum error converted to torque is less than 0.0025Nm as the torque sensitivity is 40 Hz/Nm. The repeatability for the measurement range 0-20 Nm, is better than 0.01 percent.

The maximum deviation for resonator Type 2 (figure 5b) is 0.62Hz with respect to the mean value 26.190kHz. Hence the error in torque is 0.023Nm at the torque sensitivity of 26.6 Hz/Nm and the repeatability for the expanded torque range 0-100 Nm is 0.02 percent.

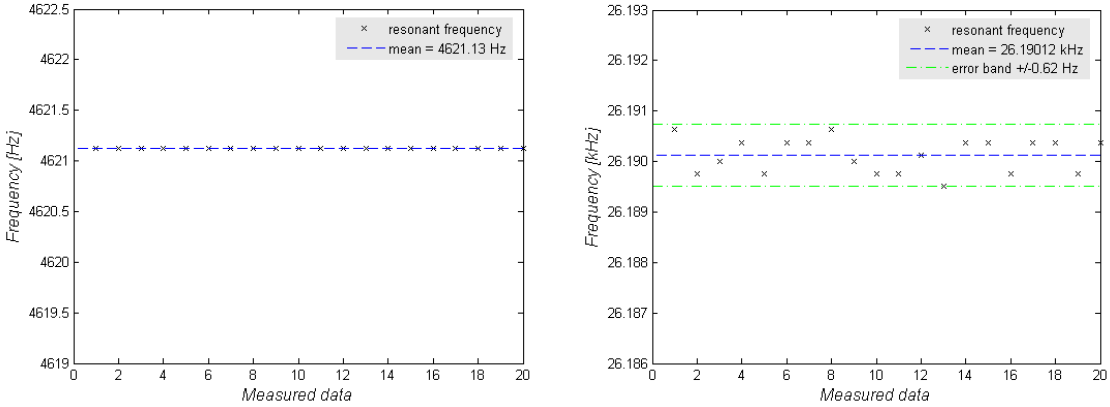

(a) Resonator Type 1 (b) Resonator Type 2

Figure 5. Repeatability Test Results

4.3. Temperature

Industrial monitoring applications require a satisfactory measurement capability over a temperature range of -30°C up to 85°C. To increase the application field of the resonant sensor by having even larger temperature ranges requires that the compensated temperature range should be as large as possible. On account of this the temperature characteristic needs to be known so that strategies for temperature compensation can be employed.

The experimental set-up was similar to that for the stability and repeatability tests. The drive and pickup PZT elements of the sensor were connected by two coaxial cables to the open-loop electronics outside the climatic test chamber. The temperature was increased from -30°C to 90°C in steps of 30°C. At each temperature point the frequency response of the respective resonator was recorded after two hours delay, required to establish stable conditions inside the climatic test chamber.

The temperature characteristic of resonator Type1 is displayed in figure 6a. Without any kind of temperature compensation the maximum deviation from the mean 4,615.0Hz is 45Hz in the temperature range between -30°C and 90°C (approximately 0.75Hz/^{o}C). Converted to torque it is 1.125Nm or 5.6 percent for the torque range of interest. After fitting a quadratic polynomial (see equation f(t) in figure 6a), the maximum deviation could be reduced to 1.5Hz. This is 0.038Nm or 0.2 percent of the maximum torque value.

Figure 6b shows the characteristic of resonator Type 2. The trend of this resonator is similar with a maximum deviation from the mean 26.1525kHz of 172.5Hz (approximately 2.5Hz/^{o}C). Converted to torque it is 6.48Nm or 6.48 percent. After fitting a quadratic polynomial f(t), (figure 6b), the maximum deviation is 10Hz or in torque 0.385Nm. This is about 0.4 percent deviation in the complete temperature range.

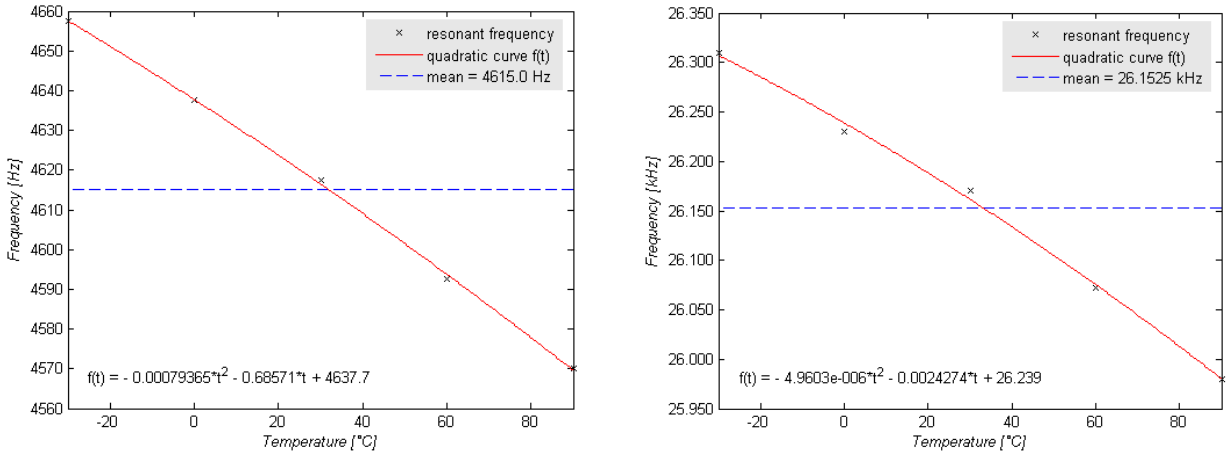

(a) Resonator Type 1 (b) Resonator Type 2

Figure 6. Temperature test results

5. Discussion of Results

The 9mm tine TBTF has a performance comparable to the 15.5mm device. However, the 9mm device under test has a 500Hz frequency excursion (range or span) for every +/- 25Nm, which is only 2% of the base frequency. Therefore, under the same strain conditions as tested on the 15.5mm device [5], the 9mm element could measure up to 1000Nm.

Range is approximately 500Hz for 50 Nm (+/- 25 Nm).
Sensitivity is better than 25 Hz/Nm.
Linearity is better than 2% of the range (worse case)..
Repeatability (Max/Min. load) is +/- 0.04% of the range (maximum change 2Hz): given that the temperature during the tests was varying by +/- 1^{o}C, this is a good result.
Stability is better than +/- 0.04% of the range (though temperature effect must be considered).
Max. Hysteresis is less than 1%

The temperature coefficient of these 9 mm devices is approximately 2.5 Hz/^{o}C, which translates to 0.08Nm torque. There are several reasons for this effect, which should be investigated further: (a) material of TBTF, stainless steel 430 S17 with a temperature coefficient of 12 ppm; (b) temperature mismatched between TBTF and shaft material (stainless steel 17-4 Ph hardened), which has a temperature coefficient of 16 ppm; (c) temperature characteristic of the PZT paste and dielectric is not known (there is an effect although not quantified).

6. Conclusion

Reduced size metallic triple-beam tuning fork resonant devices, resulting in a 42% reduction in critical dimensions, have been successfully fabricated and tested. The main characteristics can be summarised as follows:

(a) The stiffer 9mm device are less sensitive than the longer 15.5 mm device but they have an increased operating range.
(b) Unstressed frequency of operation occurs at 26 kHz, with a variation of +/-5% in the resonant frequency, from device-to-device through all fabricated batches, due to etching tolerances and variations printed PZT activity factor.
(c) Unstressed frequency variation within a given batch is less than +/-2%.
(d) Q-factors are generally greater than 2,000 (maximum of 4,000 although some are as low as 1500).
(e) Robust devices with good stability and repeatability, having high overload capability and suitable for laser spot welding to transducer structures.
(f) Performance characteristics of the 9mm devices are encouraging, so that future plans for further miniaturization can be implemented.
(g) Improvements in yield (etching results, and printing PZT drive and pick-up) will lead to better device performance and further cost reduction.

7. References

[1] Lanngdon R M, 1987. Resonant Sensors- a review. *Current Advances in Sensors*, ed B E Jones (Bristol: Adam Hilger) pp 19-31

[2] Jones B E, White N M, Tudor M J and Beeby S P: Metallic Resonators GB0302585.5 (filed on 05.02.03)

[3] Jones B E, White N M, Tudor M J and Beeby S P: Resonant Sensor Assembly US 2006/0170311 A1 (filed on 03.08.06) and W02004070335 Resonant Sensor Assembly

[4] Yan T, Jones B E, Rakowski R T, Tudor M J, Beeby S P and White N M, 2003. Metallic triple-beam resonant force sensor with thick-film printed piezoelectric vibration excitation and detection mechanisms. *Sensors and Their Applications XII*, Ed. S J Prosser and E Lewis, Bristol: Institute of Physics Publishing, pp 77-82

[5] Yan T, Jones B E, Rakowski R T, Tudor M J, Beeby S P and White N M, 2005. Stiff torque transducer with high overload capability and direct frequency output, IMEKO 19th Int. Conf. on Force, Mass, Torque and Density Measurements, February, Cairo, 5 pages

Appendix D

Use of Metallic Resonant Sensor in Torque Measurement Transfer Standard

Intiang J, DeGollier E, Rakowski R T, Jones B E, Cheshmehdoost[1] A.
Brunel University
[1](ForceSenSys Ltd., Brunel Commercialisation Office)
Kingston Lane, Uxbridge, UB8 3PH, UK

Abstract

This paper will describe progress in the development of miniature metallic resonant Triple Beam Tuning Fork (TBTF) sensors for torque measurement applications. For high accuracy any torque transducer using these sensors ought to have low sensitivity to parasitic influences such as bending moments and lateral forces, which can only be achieved with reduced sizes. Compared to the original 15.5mm length vibrating tine, the lateral forces are reduced by 52% for a 9mm tine length and by 80% for 6mm tine. High stiffness of these metallic resonant sensors will additionally reduce the occurrence of wrong measurement values as a result of overload damage. To support the use of these sensors in industrial applications a transfer standard using this technology is recommended.

Key Words: Torque Measurement, Calibration, Resonant Sensor, Transfer Standard

1. Introduction

Quality of measurement in industry requires the measured value to be compared to reference standards, which are traceable to the base SI unit. This can be achieved by using transfer standards. The most common torque transfer standard, widely used in laboratories and in industry, is based on strain gauge sensors. Low sensor output signals require surface strain on the sensing elements to approach the elastic limit in order to obtain a measurable signal over a wide measuring range. As a result, the overload capability of strain gauge torque transducers is limited to about 20% of full range; this is too low for many applications. To overcome this problem, i.e. to increase overload capability whilst maintaining accuracy and resolution, work has been started to develop a new torque transfer standard using metallic resonant sensors [1]. Additionally, metallic resonant sensors give a frequency signal compatible with digital circuitry, so that analogue-to-digital conversion can be eliminated. Moreover, the resonant sensor provides better long-term stability, since the frequency signal is not dependent on the amplitude of the electrical signals and hence accuracy is not limited by signal-to-noise ratio.

In 2005, Yan *et al* [1] showed that the metallic resonant sensor based on TBTF design showed high overload capability in the measurement of torque. Full scale operation is achieved with less than 400 microstrain, which is about five times stiffer than for resistance strain gauge torque transducers. However, the TBTFs used in this research were 40mm long (characteristics shown in Table 1). Finite Element Analysis (FEA) indicated that the TBTF not only measures the changes in tensile/compressive strain at a 45° angle to the axis of the shaft caused by torque but also experiences some shear strain and twist that will affect the final accuracy of the torque transducer. This effect could be minimized if it was possible to reduce the overall size of the TBTFs, whilst maintaining the stiffness of the resonant sensors. Figure 3 shows the sensors spot-welded onto the outer shoulders of the torque transducer at ±45° relative to the neutral axis of the shaft (one on either side), i.e. the resonators are set perpendicular to each other.

2. Design and Fabrication

The combination of processes used in resonator fabrication, photo-etched TBTFs with drive and pick-up piezoelectric thick-film elements printed directly onto the device surface, presents low-cost manufacturing opportunities for mass batch production [1]. Figure 1a shows a plan view of the resonator structure with PZT drive and detection elements. The magnitude of the output of the lead zirconate titanate (PZT) element depends upon the piezoelectric properties of the deposited layer, its thickness and the stress or voltage applied. In trying to reduce the size of the sensor there is a danger that the piezoactuator might not be able to excite the stiffer tines, so PZT printing is a physical limitation in size reduction. Finite

element analysis (FEA) was employed to simulate the modal behaviour and stress distribution of the resonator in order to optimise the positioning of the thick-film PZT elements on the structure.

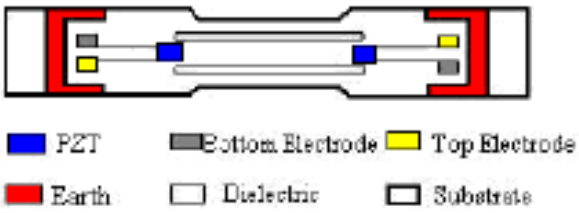

Figure 1a Plan view of the resonator structure with PZT drive and detection elements.

Figure 1b Stress contour plot for the resonator in mode 3.

The triple beam tuning fork has a planer structure and is inherently more dynamically balanced when compared to a single beam or an out-of-plane double beam structure vibrating in flexural modes. Balanced structures dissipate less energy through their supports and therefore possess an intrinsically higher mechanical quality factor. The sensor is designed to oscillate in a third harmonic differential mode, where the central beam vibrates in anti-phase with the outer beams (mode 3) to minimise mechanical energy losses from the resonator. Figure 1b shows the operational modal behaviour of the sensor modelled by FEA.

The first phase of the miniaturisation process was achieved by simply reducing the overall length by 50% from 40mm (T15, 15.5mm tine) to 20mm (T9, 9mm tine) [2]. The latest version of the sensor T6 has reduced the size by 70% from the original, as shown in figure 2. For the latest embodiment of the resonant sensor FEA analysis showed that a further reduction of 50% in the overall size was not possible due to the requirements of the PZT geometry and increased difficulty in exciting the short tine length.

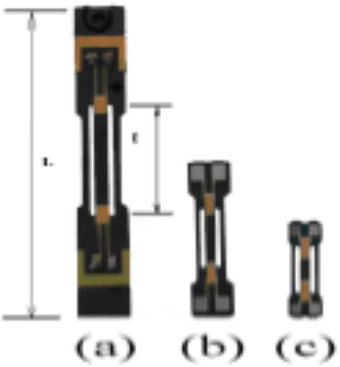

Figure 2 Miniaturisation of the metallic TBTF resonant sensors (a) T15 (b) T9 (c) T6

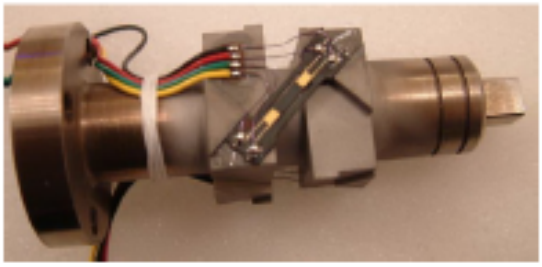

Figure 3 Torque transducer with metallic TBTF resonant sensor

The strategy adopted for the miniaturisation process was to maintain the tine cross-sectional area, roughly at 0.4 mm^2, reduce the connector and mounting geometry but maintain the area of the PZT elements. Fundamental resonator operation and characteristics of the three miniaturized metallic TBTF resonant sensors are summarized in table 1.

Table 1 Resonator operation and characteristics of the three miniaturized metallic TBTF resonant sensors (* Results previously published [2])

SENSOR	Length L (mm)	Tine t (mm)	f_o (kHz)	Q	Stability	Repeatability	Temperature Sensitivity Hz/°C
T15*	40	15.5	6	870	0.03%	< 0.01%	0.75
T9*	20	9	26	4002	0.04%	0.02%	2.5
T6	12	6	40	1600	0.02%	< 0.01%	5.2

3. FEA Analysis of Torque Transducer

3.1 Introduction

The transducer in figure 3 was modelled in FEA and the results were compared with actual test measurements. Operating at 5Nm, a 100 microstrain reading compares with a level of 1800 microstrain usually required for torque transducers based on resistance strain gauges, this will give a major advantage in application where high overload capability is required

3.2 Parasitic Influences

When torque is applied, it is expected that there will be a small amount of twist in the TBTF sensor when the shaft strain is in shear, creating different amounts of tension in the outer tines and the middle tine. These differences would have an effect on the accuracy of any torque reading. When the sensor is loaded with a one-directional force, as in a load cell, the sensor shows a small variation across three tines [3] as shown in figure 4a. Because the angle actually changes from 45 degrees as the material strains, the sensor will have several different forces acting on it. There will be tensile strain, which is the quantity being measured but there also will be a shear strain, as the once co-linear sides of the mounting surfaces move away from each other. The structure will also undergo a small degree of twist, disproportionally raising the strain in the side tines in relation to the central tine. The resulting distortions in the sensor in torque measurement can be seen in figure 4b, amplified 1000 times. While the shear is quite obvious, it can be seen that there is also some twist in the structure. This effect could be minimized if it was possible to reduce the overall size of the metallic TBTF resonant sensor, whilst maintaining the stiffness of the resonant sensors.

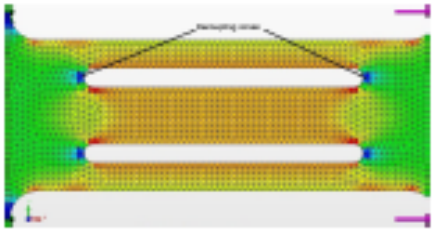

Figure 4a TBTF with 1 directional force along its axis (load cell configuration)

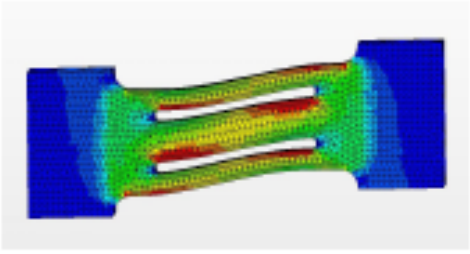

Figure 4b TBTF with distortion configuration

3.3 Stress Distribution Averaging across Resonant Tines

Figure 5a shows an example FEA result for the three metallic TBTF resonant sensors T15, T9, T6 in the same condition of mounting and loading with a 20N shear force at one end. The average difference in stress distribution between the 3 tines compared to the T15 sensor is a reduction of 52% for the T9 sensor and reduced by 80% for T6 sensor.

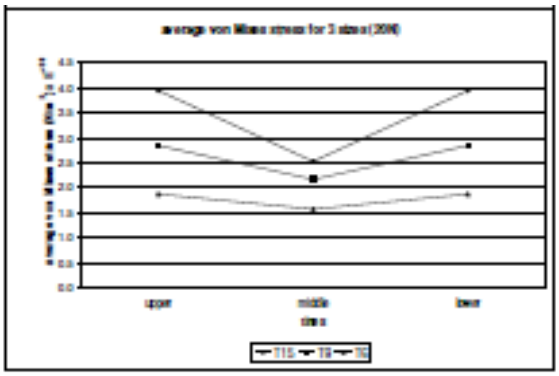

Figure 5a FEA results of the average von Mises stress on three tines for the T15, T9, and T6 sensors with an applied 20N shear force

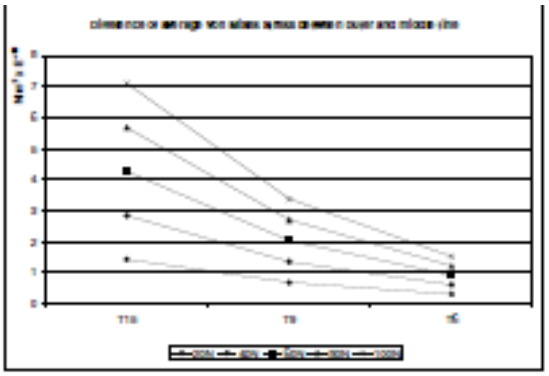

Figure 5b FEA results of the difference of the average von Mises stress between the outer and middle tines for the T15, T9, and T6 sensors for applied 20 - 100N shear force

Figure 5b illustrates a further FEA analysis on the three resonant sensors for applied shear loads from 20N to 100N. It is clearly seen that when the size of the sensor is reduced, the difference in the average stress distribution on three vibrating tines is decreased, concluding that reducing the overall size can satisfy the requirement to improve the accuracy of the torque transducer with the metallic TBTF resonant sensors.

4. Characteristics of T6 Resonant Sensor

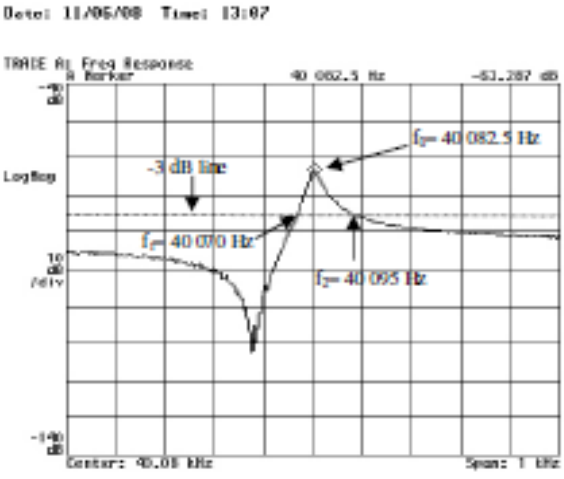

Figure 6 Resonant frequency signal of T6 sensor

Figure 6 illustrates the amplitude-frequency response from the first manufactured batch of T6 sensors and shows the third mode of vibration characteristic. From the result the value for the centre frequency is about 40kHz and the quality factor (Q) obtained from this characteristic is calculated to be about 1600.

For the repeatability measurement of T6 sensor, the default frequency resolution was 2.5Hz, the standard deviation from the mean value of the resonant frequencies was found to be ±1.6Hz. The standard deviation for the stability test was found to be ±5.2Hz. Finally, the temperature coefficient of the resonator was measured at 5.2Hz/ºC.

5. Overload Capability

Strain gauge transducers produce low amplitude output signals, thus the surface strain is generally designed to approach the elastic limit of the sensing element in order to obtain a measurable value. As a result, the overload capability of the strain-gauge-based torque transducer will be limited by this factor [1]. The overall accuracy of the torque measuring system is determined by mechanical disturbance variables and the uncompensated thermal and humidity effects. In addition any overloading or damage to the torque transducer is a significant factor in obtaining the wrong measurement values [5] during testing or use in industrial applications. Such errors in measurement values might not be detected until the next calibration event. From the torque measurement point of view, the overload is the quantity that is actually

of interest in normal operation, as it is usually an indicator of a developing fault or failure in a manufacturing application. It is additionally very hard to predict the level or nature of such a overload fault. In most cases the manufacturing system will have the appropriate overload protection to prevent damage to the plant and possibly the transducer, such as switching off the drive part when the overload is built up. However, such mechanical overload protection devices respond with a certain time delay, as the occurrence of the overload peaks is highly dynamic [4], so it is not enough to simply protect the transducer with these protective measure and hope that no damage occurs.

This problem with overload capability is one of the factors which could lead to the development of the new torque transfer standard using sensors with high stiffness. Evidence shows that the TBTF resonant sensor, fabricated with stiff metallic structures will provide better overload capability than strain gauges, at the same time as increasing the torque measuring range [1].

6. Transfer Standard

In metrology, traceability to the base SI unit is very important to ensure that the measured value is accurate. From the definition of torque, which is the product of force and distance, it can be traceable to the fundamental units of mass, length and time. The hierarchy of metrology is as follow; primary standard, secondary standard, calibration machine and measuring instrument.

In torque calibration, the measured quantity (torque) is disseminated or transferred from the National Standard to a reference standard, then to working standards and finally to test devices for applications by using torque transfer standard. Importantly, the transfer transducer should not have incorrect measurement properties. The damage to the transducer by overloading, which results in an error in the measurement value, can not be detected from an incorrect zero signal but only during recalibration [5].

The T9 TBTF torque transducer was evaluated at the National Physical Laboratory (NPL) in UK against the Torque Standard Machine (Deadweight Lever-beam). Calibration was carried out to British Standard (BS) 7882. Parameters measured included repeatability, reproducibility, linearity, residual deflection, reversibility and uncertainty. Moreover, stability and creep test had also been investigated to obtain more information on the transducer.

A series of ten readings were taken at each calibration point to minimise the influence of any fluctuations in the reading. A one-minute waiting time enabled the system to stabilise after each change of torque increment. The calibration result is shown in Table 2.

Table 2 Calibration result of torque transducer according to BS7882

Torque (N.m)	Relative error of repeatability R_f	Relative error of reproducibility R_2	Relative error of Interpolation E_g	Relative error of zero E_z	Relative error of reversibility E_h
0				0.15%	
5	0.34%	0.76%	0.31%		-0.28%
10	0.13%	0.99%	-0.05%		-0.62%
15	0.15%	0.80%	-0.22%		-0.44%
20	0.00%	0.39%	-0.02%		-0.11%
30	0.00%	0.15%	-0.03%		

The uncertainty of calibration at 95% confidence level (k = 2) is about 0.002%.

Table 3 is the classification result of the torque transducer with 9mm metallic TBTF resonant sensor. It shows that this torque transducer meets the requirements for a class 1 transfer standard.

Table 3 The classification result of torque transducer with metallic TBTF resonator

Relative error of repeatability R_f	Relative error of reproducibility R_2	Relative error of Interpolation E_g	Relative error of zero E_z	Relative error of reversibility E_h	Uncertainty	a
1	1	1	1	0.5	0.05	1

From the calibration result, it is found that the class of accuracy of the torque transducer is limited by the resolution of the system display/indicator, shown as column 'a' in Table 3, where 'a' is a coeffficient which determines the lower limit of calibration when multiplied by the indicator resolution. Incorporating a display/indicating device with higher resolution would give aditional benefit in improving the accuracy of this torque transducer, possibly to the 0.5 or even 0.2 classification.

7. Conclusion

The metallic TBTF resonant sensor gives a direct frequency signal output, which has an advantage over conventional resistive strain gauges. The frequency signal is compatible with digital circuitry, so the analogue-to-digital conversion unit needed for strain gauges can be eliminated for this kind of torque transducer. Using metallic TBTF resonant sensors in a torque transfer standard is more convenient as the cost of the torque measurement system will be reduced compared to strain gauges. In addition, the resolution achievable using metallic resonant sensors would be as good as strain gauges, as frequency can be measured with quite high accuracy, which is very important for transfer standards. Moreover, resonant sensors provide better long-term stability since the frequency signal is not dependent on the amplitude of the electrical signals and the measurement accuracy is not limited by the signal-to-noise ratio, as occurs with an analogue signal.

The most common torque transfer standard is based on strain gauge sensors, where the overload capability is too low for many applications. A new torque transfer standard using metallic TBTF resonant sensors is proposed to overcome this problem, whilst maintaining accuracy and resolution. Measurement errors due to lateral forces, which would degrade the accuracy of such a torque transducer, were reduced by 80% when using the latest embodiment of the TBTF sensor. The new T6 sensor design, whose overall size has been reduced by 70%, has maintained the high stiffness of the original T15 metallic resonant sensor. This paper shows the first test results for the T6 sensor, whose overall length is only 12mm. The stiffness of these metallic structures will reduce the occurrence of wrong measurement values due to any overload damage, which might occur in practical applications. Calibration results show that the a TBTF torque transducer incorporating the T9 sensors would be classified as a class 1 torque transfer standard . A torque transducer, incorporating the T6 sensors, is currently under construction and will be evaluated against national standards.

References

[1] Yan T, Jones B E, Rakowski R T, Tudor M J, Beeby S P and White N M. (2005) *Stiff torque transducer with high overload capability and direct frequency output*, IMEKO 19th Int. Conf. on Force, Mass, Torque and Density Measurements, February, Cairo.

[2] Intiang J, Weidenmuller J, Rakowski R T, Jones B E, Cheshmehdoost A. (2007) *Characteristics of 9mm Metallic Triple-Beam Tuning Fork Resonant Sensor.* Sensors and their Applications XIV, Ed. S J Prosser and A Al-shamma'a: Institute of Physics Publishing.

[3] Eric D. (2007) *Design of a retrofit power-sensing coupling for pumping systems using triple-beam tuning fork strain gauges.* Dissertation MSc Engineering Design: School of Engineering and Desing, Brunel University.

[4] Rainer, S. and Georg, W. (2002) *Measuring Torque Correctly*. Germany:HBM.

[5] Sven, K. (2008) *High Precision Torque Measurement System.* [www] Available from: http://www.hbm.com/fileadmin/mediapool/techarticles/2008/2008_kuhn-highprecision_torque_en.pdf [Accessed 5th Jan 2009]

Appendix E.1 Specification of Stainless Steel 430S17

Category	Steel
Class	Stainless steel
Type	Ferritic standard
Common Names	Chromium steel
Designations	France: AFNOR Z 8 C 17 Germany: DIN 1.4016 Italy: UNI X 8 Cr17 Japan: JIS SUS 430 Sweden: SS 2320 United Kingdom: B.S. 430 S 15 United States: AMS 5503 , AMS 5627 , ASME SA182 , ASME SA240 , ASME SA268 , ASME SA479 , ASTM A176 , ASTM A182 , ASTM A240 , ASTM A268 , ASTM A276 , ASTM A314 , ASTM A473 , ASTM A479 , ASTM A493 , ASTM A511 , ASTM A554 , ASTM A580 , ASTM A651 , FED QQ-S-763 , FED QQ-S-766 , FED QQ-W-423 , FED STD-66 , MIL SPEC MIL-S-862 , SAE 51430 , SAE J405 (51430) , UNS S43000

Composition

Element	Weight %
C	0.12
Mn	1.00
Si	1.00
Cr	16.0-18.0
P	0.04
S	0.03

Mechanical Properties

Properties		Conditions	
		T (°C)	Treatment
Density (×1000 kg/m^3)	7.8	25	
Poisson's Ratio	0.27-0.30	25	
Elastic Modulus (GPa)	200	25	
Tensile Strength (Mpa)	480	25	annealed, hot finished (plate, sheet, strip) more
Yield Strength (Mpa)	275		
Elongation (%)	20		
Reduction in Area (%)	45		
Hardness (HRB)	88 (max)	25	annealed (plate, sheet, strip)

Thermal Properties

Properties		Conditions	
		T (°C)	Treatment
Thermal Expansion (10^{-6}/ºC)	10.4	0-100 more	
Thermal Conductivity (W/m-K)	26.1	100 more	
Specific Heat (J/kg-K)	460	0-100	

Electric Properties

Properties		Conditions	
		T (°C)	Treatment
Electric Resistivity (10^{-9} -m)	600	25	

Appendix E.2 Specification of Stainless Steel 17-4PH

Category	Steel
Class	Stainless steel
Type	Precipitation-hardening standard
Designations	United States: AMS 5342 , AMS 5343 , AMS 5344 , AMS 5355 , AMS 5604 , AMS 5622 , AMS 5643 , AMS 5825 , ASME SA564 , ASME SA705 , ASTM A564 , ASTM A693 , ASTM A705 , MIL SPEC MIL-C-24111 , MIL SPEC MIL-S-81506 , MIL SPEC MIL-S-81591 , SAE J467 (17-4PH) , UNS S17400

Composition

Element	Weight %
C	0.07
Mn	1.00
Si	1.00
Cr	15.5-17.5
Ni	3.0-5.0
P	0.04
S	0.03
Cu	3.0-5.0
Nb+Ta	0.15-0.45

Mechanical Properties

Properties		Conditions	
		T (°C)	Treatment
Density (×1000 kg/m^3)	7.7-8.03	25	
Poisson's Ratio	0.27-0.30	25	
Elastic Modulus (GPa)	196	25	
Tensile Strength (Mpa)	1070	25	H1025 (bar, plate, sheet, strip) more
Yield Strength (Mpa)	1000		
Elongation (%)	12		
Reduction in Area (%)	45		
Hardness (HRC)	35-42	25	H1025 (bar, plate, sheet, strip) more

Thermal Properties

Properties		Conditions	
		T (°C)	Treatment
Thermal Expansion (10^{-6}/ºC)	10.8	0-100 more	
Thermal Conductivity (W/m-K)	18.3	100 more	
Specific Heat (J/kg-K)	460	0-100	

Electric Properties

Properties		Conditions	
		T (°C)	Treatment
Electric Resistivity (10^{-9}□-m)	800	25	

Appendix E.3 Specification of PZT29

FERROPERM
PIEZOCERAMICS A/S

Pz29

A very soft PZT with high sensitivity

Pz29 is a very soft piezoceramic material with very high coupling factors and piezoelectric charge coefficients. It is specially optimised for applications where high sensitivity, or high displacements are required.

Typical applications are:

- 1D, 2D, 3D Medical arrays for imaging systems
- Inkjet printheads
- Actuators for medical, electronic or optical control systems
- NDT sensors with high sensitivity

Main Characteristics of Ferroperm Pz29

	Symbol	Unit	Pz29
Electrical Properties			
Relative dielectric permittivity at 1 kHz	K_{33}^T		2900
Dielectric dissipation factor at 1 kHz	$\tan\delta$	10^{-3}	19
Curie temperature	$T_C >$	°C	235
Recommended working range	<	°C	150
Electromechanical Properties			
Coupling factors	k_p		0,64
	k_t		0,52
	k_{33}		0,75
Piezoelectric charge coefficient	d_{33}	pC/N	575
Mechanical Properties			
Mechanical Quality Factor	Q_{mP}		90
Density	ρ	g/cm³	7,45

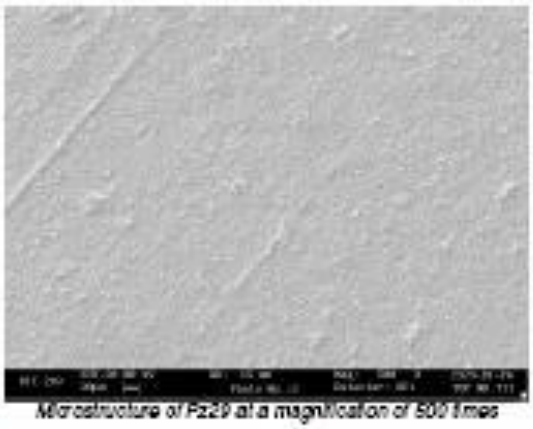

Microstructure of Pz29 at a magnification of 500 times

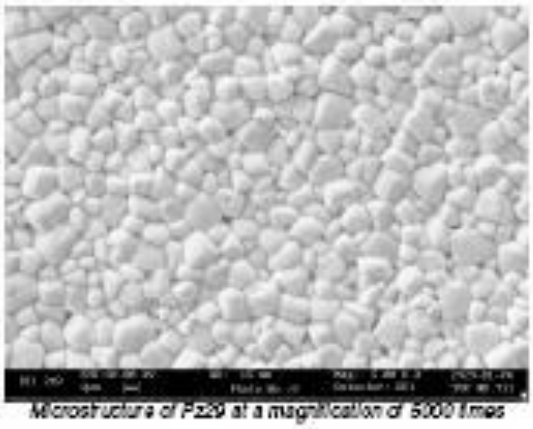

Microstructure of Pz29 at a magnification of 5000 times

Hejreskovvej 18 • DK-3490 • Kvistgaard • Denmark • Tel +45 - 49 12 71 00 • Fax +45 - 49 13 81 88
E-Mail: pz@ferroperm-piezo.com • Internet: www.ferroperm-piezo.com

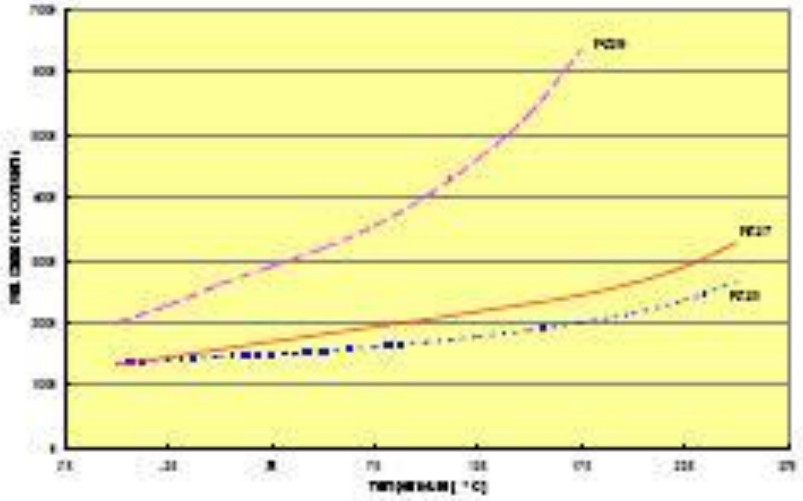

Temperature dependence of the free dielectric constant of Pz29 in comparison with other soft PZT materials from Ferroperm.

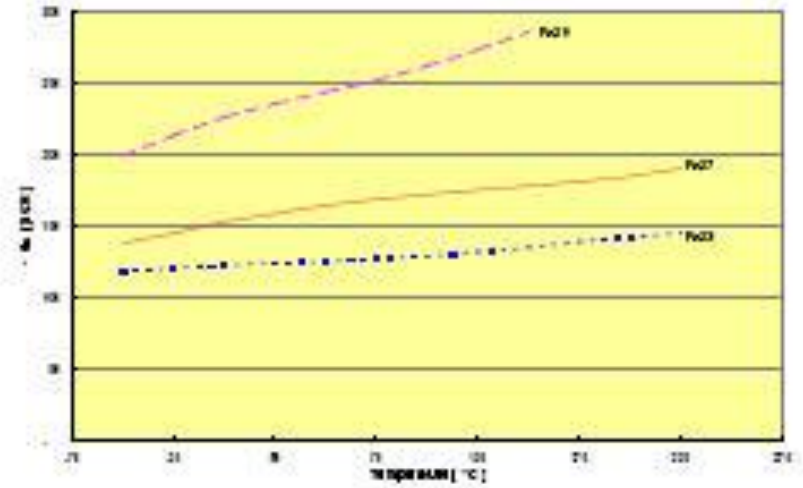

Temperature dependence of the piezoelectric charge coefficient, d_{31}, for Pz29 in comparison with other soft PZT materials from Ferroperm.

Ferroperm Piezoceramics A/S is a company completely dedicated to the production of high quality piezoelectric ceramics for our main strategic markets: Vibration sensors, flow-meters, medical diagnostics, underwater acoustics, and NDT.
We have more than 45 years of experience in production of advanced piezoelectric ceramics, and employ today more than 50 motivated people in management, production, development and research. We have extensive experience in development and improvement of products, which can fulfil customers' individual needs.

For more information on Ferroperm and our materials please visit our internet page
http://www.ferroperm-piezo.com

Appendix E.4 SIMPosium (WCSIM)

From the Master

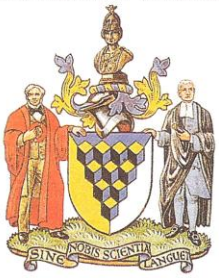

The Worshipful Company of Scientific Instrument Makers
9, Montague Close, London, SE1 9DD.
Tel: 020 7407 4832 Fax: 020 7407 1565

05 March 2008

Jittakant Intiang
Brunel University
School of Engineering and Design
Kingston Lane
Uxbridge
UB8 3PH

Dear Jittakant,

SIMPosium

At the end of yesterday's inaugural SIMPosium proceedings it was my pleasant duty to chair the judging panel and present the Medal, Certificate and cheque to the winner. In my remarks I made a special mention of your presentation because, in the opinion of the judges, it was 'Highly Commended' and was a very close second to the winner, Michael Schwertner from Oxford. Had there been a second prize to award then you would certainly have won it.

I congratulate you on your first class performance and wish you every success in your future studies and in your career.

Yours sincerely

David W Smith

David W Smith
Master

cc Carl Saunders Singer, The Clerk

e-mail: theclerk@wcsim.co.uk Internet: http://www.wcsim.co.uk
Registered Charity No. 221332